RADAR AND AIRGLOW STUDIES OF F-REGION

COMPOSITION AND DYNAMICS AT LOW LATITUDES

A Dissertation

Presented to the Faculty of the Graduate School

of Cornell University

in Partial Fulfillment of the Requirements for the Degree of

Doctor of Philosophy

by

Michael James Nicolls

August 2006

RADAR AND AIRGLOW STUDIES OF F-REGION COMPOSITION AND

DYNAMICS AT LOW LATITUDES

Michael James Nicolls, Ph.D.

Cornell University 2006

This thesis presents a series of studies investigating the composition and dynamics of the low latitude F-region ionosphere using airglow imagers and the Arecibo and Jicamarca incoherent scatter radars (ISRs), along with supporting instrumentation.

Some dynamical aspects of the low latitude ionosphere are investigated. The effects of a large-scale traveling ionospheric disturbance (TID) are studied. The TID characteristics are consistent with an atmospheric disturbance caused by high latitude Lorentz forcing associated with periodic substorms. Plasmaspheric coupling is necessary to explain the observed electron densities and airglow intensities.

Evidence is presented for post-midnight uplifts during which the low latitude ionosphere is lifted by tens of kilometers in mild events and by over a hundred kilometers in severe events. The uplifts are not caused by a reversal of the zonal electric field, instead occurring as a response to a decreasing westward field in conjunction with sufficient recombination and plasma flux. The midnight pressure bulge may play a role in the dynamics and the disturbance dynamo may enhance the uplifts.

The spectral properties of daytime penetration fields are analyzed using ground-based magnetometer data. The spectrum deviates from a power law under disturbed conditions, and the integrated power is a strong function of geomagnetic activity. The transfer function of the system is estimated using simultaneous interplanetary

electric field data. Case studies support the notion of long-duration responses and of a weakly resonant system.

Models of the airglow emission rates are used to investigate the nighttime F-region ion composition. The intensities calculated including the molecular ions given by the International Reference Ionosphere (IRI) model are much higher than measurements indicate, implying that IRI overestimates the molecular ion fraction. A revision of the IRI ion composition is needed, which could be constrained with airglow measurements.

The neutral thermosphere over Arecibo is investigated using ion energy balance to estimate the neutral density and temperature. The so-called Burnside factor, associated with errors in the O^+-O collision cross section, is estimated. In contrast to ion momentum studies, which typically lead to a Burnside factor greater than one, ion energy balance studies tend to result in low values for the Burnside factor. However, the ratio derived here is close to theoretical simulations of the collision cross section and may be a first step in reconciling the discrepancy between momentum and energy balance results.

BIOGRAPHICAL SKETCH

Michael James Nicolls was born on March 17, 1981 in San Jose, California, son of Margaret and Chris, and younger brother to Melissa. His family migrated to Port Moody, British Columbia, a suburb of Vancouver, when he was only a few months old. Mike attended French immersion schools (remember, this is Canada) until Grade 6 when he transferred to St. George's School in Vancouver, where he completed his high school degree. Mike decided to go east for college to Cornell University, where he started out studying French literature and computer science. In his Sophomore year, Mike transferred to Electrical Engineering. One day, he saw an advertisement in an elevator for the Arecibo Observatory Research Experience for Undergraduates program. Mike got excited and applied to the program, and by a small bit of confusion over Mike's knowledge of the programming language ASP, Mike was accepted. Mike had a wonderful summer working for Drs. Nestor Aponte and Sixto González in Puerto Rico, who put him in touch with a professor at Cornell, Mike Kelley. Mike K. sent Mike N. to places like Alaska and Greece as an undergraduate, thereby enamoring him with the field and hooking him in. Thus, Mike N. stayed at Cornell University to pursue a Ph.D., and now looks forward to returning to the West, and hopefully eventually to Vancouver.

Dedicated to my family - Dad, Mom, Melissa, and Nanny -

and to the memory of Adele Nicolls (1923 - 2005).

ACKNOWLEDGEMENTS

I would first of all like to acknowledge my advisor, Mike Kelley, for his continuous support and guidance throughout my time at Cornell. Mike has encouraged me to be active and to pursue diverse interests, yet has also pushed me to be independent, giving me a somewhat unique graduate experience. I look forward to continue working with Mike as I pursue my career. Secondly, I should thank the folks at Arecibo - Nestor, Sixto, and Mike Sulzer - for initiating my interest in space physics, educating me, supporting me, encouraging me, and collaborating with me. Next, I would like to acknowledge Michael Vlasov at Cornell for teaching me about the physics of space plasmas, for working closely with me, and for always being willing to discuss problems with me. Much of the work in this thesis is close collaborative work with Michael, so I am very grateful to him. I also acknowledge my other committee members, Don Farley and Dave Hysell, for useful discussions and guidance, Dave Hammer for sparking my interest in plasma physics and for being a really nice guy, the other space physics students for enduring the common plight, and Laurie for always being willing to explain the rules of hyphenation to me (which, alas, I seem to have forgotten again...).

I owe a special thanks to certain colleagues and friends who have either been extremely helpful in my educational process or have given me something to do outside of work. These people include Sixto, Nestor, Diego, Dianna, Zev, Bryan, Ryan,

TABLE OF CONTENTS

LIST OF TABLES

LIST OF FIGURES

Chapter 1

Introduction

A highbrow is a person educated beyond his intelligence. - Brander Matthews, <u>Epigrams</u>

1.1 Motivation

To a meteorologist, the upper atmosphere is probably the region above the troposphere. To my uncle, the upper atmosphere is just, you know, above us. In either case, it is not obvious why we care to study the upper atmosphere in an electrical engineering department, or perhaps even at all. But the reasons are actually plentiful, and pretty good.

For a long time, human perception of the upper atmosphere was based solely on observations of the aurora. Early on, humans of course did not know what the aurora was, and religious and mythological significance was often attached to those majestic lights. Later, scientific efforts associated the aurora with weather patterns, with temperature fluctuations, with mountains and volcanos*. When Kristian Birkeland finally associated the aurora with magnetic field fluctuations and those magnetic field fluctuations with sunspot activity in his 1901 book, his theories were largely

---

*See <u>The Northern Lights</u> by Lucy Jago.
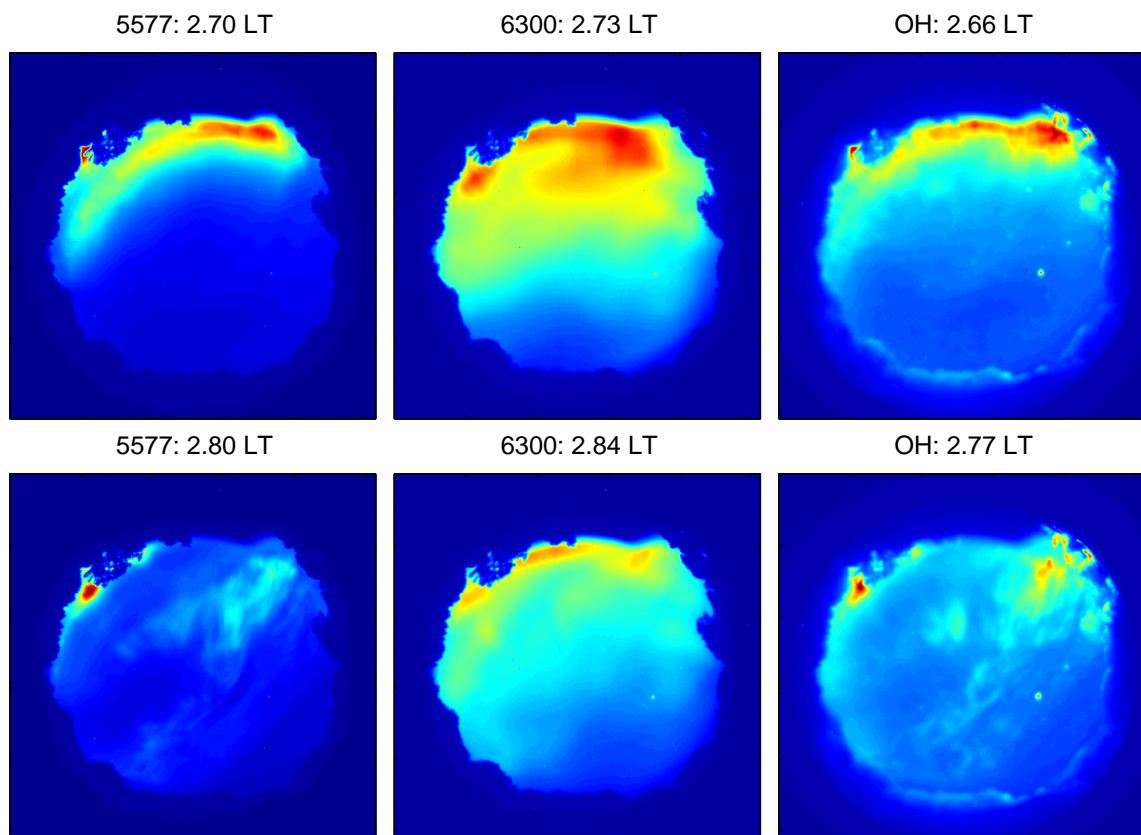
Figure 1.1: All-sky images from Oneida, NY of an auroral event on September 10-11, 2005 coincident with a major flare and geomagnetic storm. Plotted are two series of images (557.7 nm, 630.0 nm, and OH) separated by about 6 minutes. North is towards the top of the images.

dismissed by the Royal Society and its president, Lord Kelvin (see quote in the heading of Chapter 5). Birkeland's ideas on the Sun-Earth connection and of field-aligned currents proved to be correct, firmly establishing critical links between the environs of the Earth and that of the Sun. An example of an auroral event captured on September 10-11, 2005 by the Cornell all-sky imager in Oneida, NY is shown in Figure 1.1, where we show a series of six images in three different emission lines. In the first set (near 0240 LT), we see the diffuse aurora in the red (630.0 nm) and green (557.7 nm) emissions, as well in the hydroxyl images (which are shorter exposures - about 8 seconds as compared to 90 seconds, because of the larger bandwidth of the

filters). The 557.7-nm (green line) volume emission rate peaks in a region near 95 km, and the OH emission peaks somewhat lower, near 86 km. The 630.0-nm (red line) emission comes from the F region. In the first set of images, it is probable that the broadband OH filter is dominated by the red line emission, since it is unlikely that the diffuse aurora reached altitudes less than 90 km. In the second set of images, only 6 minutes later, we see green discrete arcs directly overhead and structured red aurora. We see an arc in the OH emission as well, which is not obvious in the red line filter but looks similar to the green line image. This entire night was very dynamic.

Shortly after Marconi in the early 1900's showed that radio waves propagated around the earth, Heaviside and Kennelly suggested the presence of an ionized layer up there. About 20 years later, Appleton proved with radar experiments that this layer existed, and in fact found a couple of them (e.g., *Appleton*, 1927). These pioneering discoveries led to practical investigations of the Earth's ionosphere and interest in new scientific fields, including radio wave propagation, solar-terrestrial physics, and plasma physics. Soon after, *Chapman* (1931) explained how the ionosphere could be formed via the absorption of solar extreme ultraviolet radiation by neutral constituents, which will be reviewed in the next section.

While many developments followed these pioneering investigations, and a review of those is meant for a history book, not a thesis, one notable advancement critical to this thesis and this graduate student's career was the discovery of incoherent scatter by *Gordon* (1958). Gordon, who received his Ph.D. in Electrical Engineering at Cornell and later became a professor there (here), suggested that the free electrons in the ionosphere should scatter high frequency radio waves, and that this scatter could be used as an ionospheric diagnostic. His idea was verified by *Bowles* (1958). Gordon's theory led to the building of several huge ionospheric observatories, including the Arecibo Observatory (commissioned in 1963, located at 18.34°N,

66.75°W) and the Jicamarca Radio Observatory (commissioned in 1961, located at 11.95°S, 76.87°W at the geomagnetic equator), in a testament to efficient planning and the paucity of bureaucracy (see *Farley and Hagfors*, 2006, for a more detailed history). Gordon's theory of incoherent scatter was somewhat flawed and the correct theory of incoherent scattering was developed shortly thereafter by many independent scientists (*Dougherty and Farley*, 1960; *Fejer*, 1960; *Salpeter*, 1960; *Hagfors*, 1961; *Rosenbluth and Rostoker*, 1962). The observatories are still in use today and are the most powerful instruments for studying the ionosphere using the technique of incoherent scattering. Refinements and developments are still being made to the theory, and new observations continue to be made.

Thus, to return to the question posed in the first paragraph, we can now identify what the upper atmosphere is and why we study it (particularly within an electrical engineering department). The upper atmosphere (consisting of the upper mesosphere, the thermosphere, and the ionosphere) is the region of the atmosphere where the energy input is dominated by solar extreme ultraviolet radiation, electric fields and currents, and energetic (auroral) particles, and it is the region where the motion of the neutral atmosphere is strongly influenced by the motion of the plasma. The history of ionospheric and plasma studies is strongly tied to that of electromagnetics, to the propagation of radio waves, and to general radar studies. Interest in the upper atmosphere has grown in the space age - it is the region of the atmosphere where satellites fly and space tourists will be sipping their bubbly space cola. Thus, understanding the forces on spacecraft (charging, drag, etc.), space radiation, and communication is very important. For different but overlapping reasons, investigating the weather of space has become of interest - understanding how the day-to-day variations in our upper atmosphere relate to those of the sun and those of the lower atmosphere is a daunting but noble scientific endeavor. Predicting ionospheric insta-
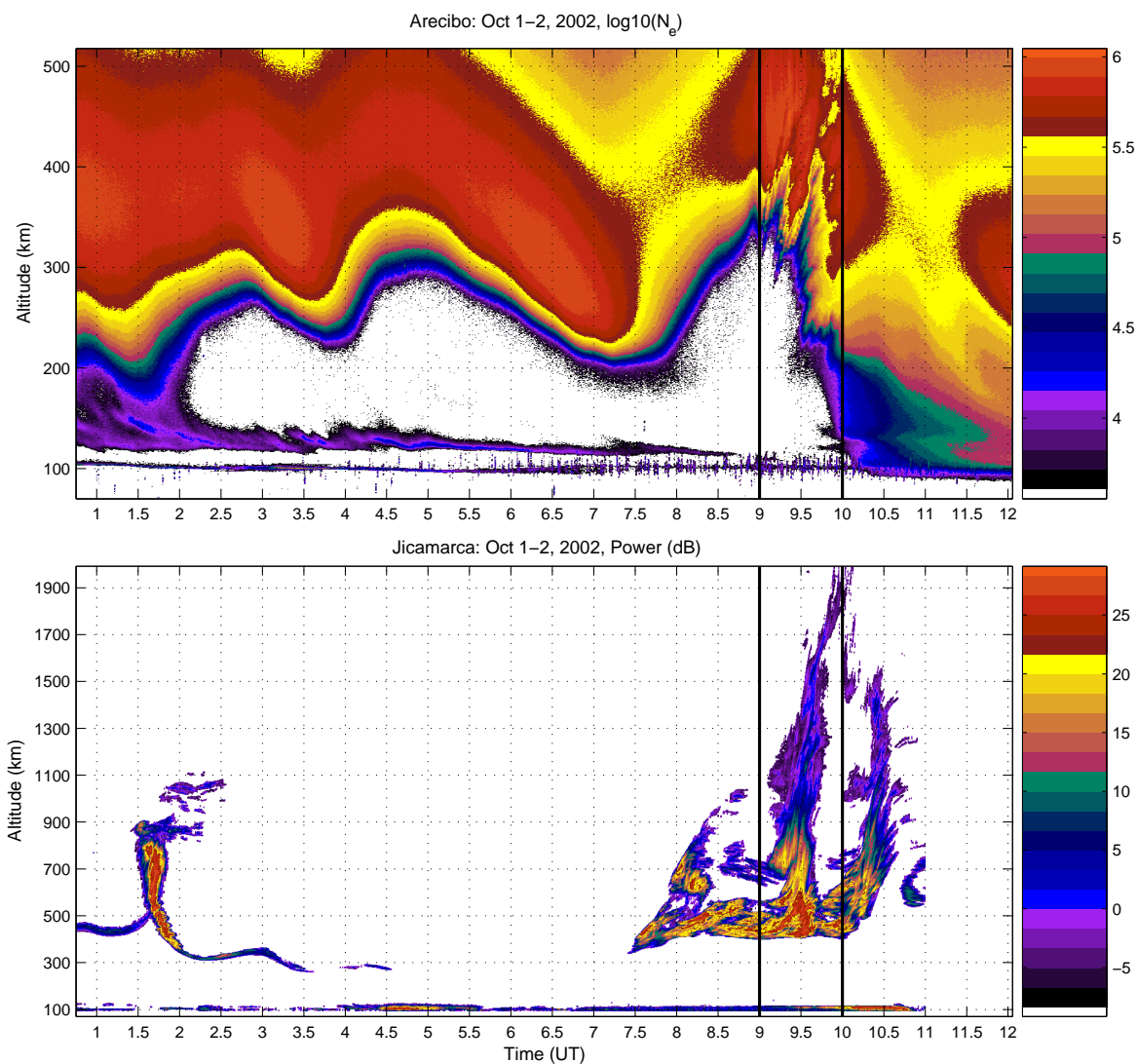
Figure 1.2: Example of some observations of plasma instabilities at Arecibo (top, where the electron density is plotted) and at Jicamarca (bottom, where the power coherently scattered from irregularities is plotted).

bilities and storms is of particular interest. An example of an ionospheric instability in which the ionosphere over Arecibo went unstable at nearly the same time as the ionosphere over Jicamarca (at the geomagnetic equator) is shown in Figure 1.2. Although the instabilities occur at about the same time, and the Arecibo flux tubes cross the geomagnetic equator above 2000 km, there is probably not much flux-tube coupling between the two systems as the Jicamarca bubbles at those high altitudes are largely stagnant. It is likely, however, that the ionospheric conditions that drove one system unstable also drove the other unstable. This event is discussed more in Chapter 3. This figure is also a good example of the different dynamical layers over Arecibo, showing large-scale F-region fluctuations, smaller-scale intermediate layer fluctuations, and a thin sporadic-E layer.

1.2   Formation and Structure of the Ionosphere

Here we review and develop a simple model for the F-region ionosphere. The continuity equation for an ionic species j is,

$$\frac{\partial n_j}{\partial t} + \nabla \cdot (n_j \mathbf{v}_j) = P_j - L_j \tag{1.1}$$

where n_j is the species density, $\mathbf{v}_j$ is the species velocity (due to say diffusion, electric fields, and neutral winds), and P_j and L_j are production and loss terms, respectively.

The production term P_j is crucially dependent on the ionization rate during the daytime. The ionization rate for a given species at a given altitude is a strong function of the wavelength of the incoming radiation. Calculating the ionization rate can be done as outlined in many atmospheric texts (e.g., *Banks and Kockarts*, 1973; *Rees*, 1989; *Rishbeth and Garriott*, 1969; *Schunk and Nagy*, 2000). The total ionization rate

for a given species is

$$Q_j(z, \chi) = \sum_i q_j(z, \lambda_i, \chi) \quad \text{cm}^{-3}\text{s}^{-1} \tag{1.2}$$

where the summation is over wavelength, z is altitude, χ is solar zenith angle, and $q_j(z, \lambda_i, \chi)$ is the ionization rate as a function of wavelength. At a specific wavelength, it is given by

$$q_j(z, \lambda, \chi) = n_j(z)I(z, \lambda, \chi)\sigma_{ion,j}(\lambda) \quad \text{cm}^{-3}\text{s}^{-1} \tag{1.3}$$

where n_j is the neutral species density, $I(z, \lambda, \chi)$ is the photon flux, and $\sigma_{ion,j}$ is the ionization cross section. The photon flux as a function of altitude, wavelength, and solar zenith angle can be calculated using the Lambert-Beer exponential absorption law (*Rees*, 1989),

$$I(z, \lambda, \chi) = I_\infty(\lambda)e^{-\tau(z,\lambda,\chi)} \quad \text{photons cm}^{-2}\text{s}^{-1} \tag{1.4}$$

where $I_\infty(\lambda)$ is the flux at the top of the atmosphere as a function of wavelength and τ is the optical depth of the atmosphere.

The optical depth is defined as (e.g. *Rees*, 1989; *Schunk and Nagy*, 2000)

$$\tau(z, \lambda, \chi) = -\sum_j \sigma_{abs,j}(\lambda) \int_z^\infty n_j(z)ds \quad \text{cm}^2 \tag{1.5}$$

where ds is the incremental path length and $\sigma_{abs,j}$ is the absorption cross section for neutral species j. For solar zenith angles less than 90°, the integration over slant path can be converted to one over altitude using some geometry (*Rees*, 1989),

$$\tau(z, \lambda, \chi) = \sum_j \sigma_{abs,j}(\lambda) \int_z^\infty n_j(z') \left[1 - \left(\frac{R_e + z}{R_e + z'}\right)^2 \sin^2 \chi\right]^{-1/2} dz' \quad \text{cm}^2 \tag{1.6}$$

where R_e is the radius of the Earth, Note that there are some approximations that can be made (the plane-stratified approximation or the Chapman grazing incidence function (*Chapman*, 1931; *Rishbeth and Garriott*, 1969)) but the equation can be easily numerically integrated instead.
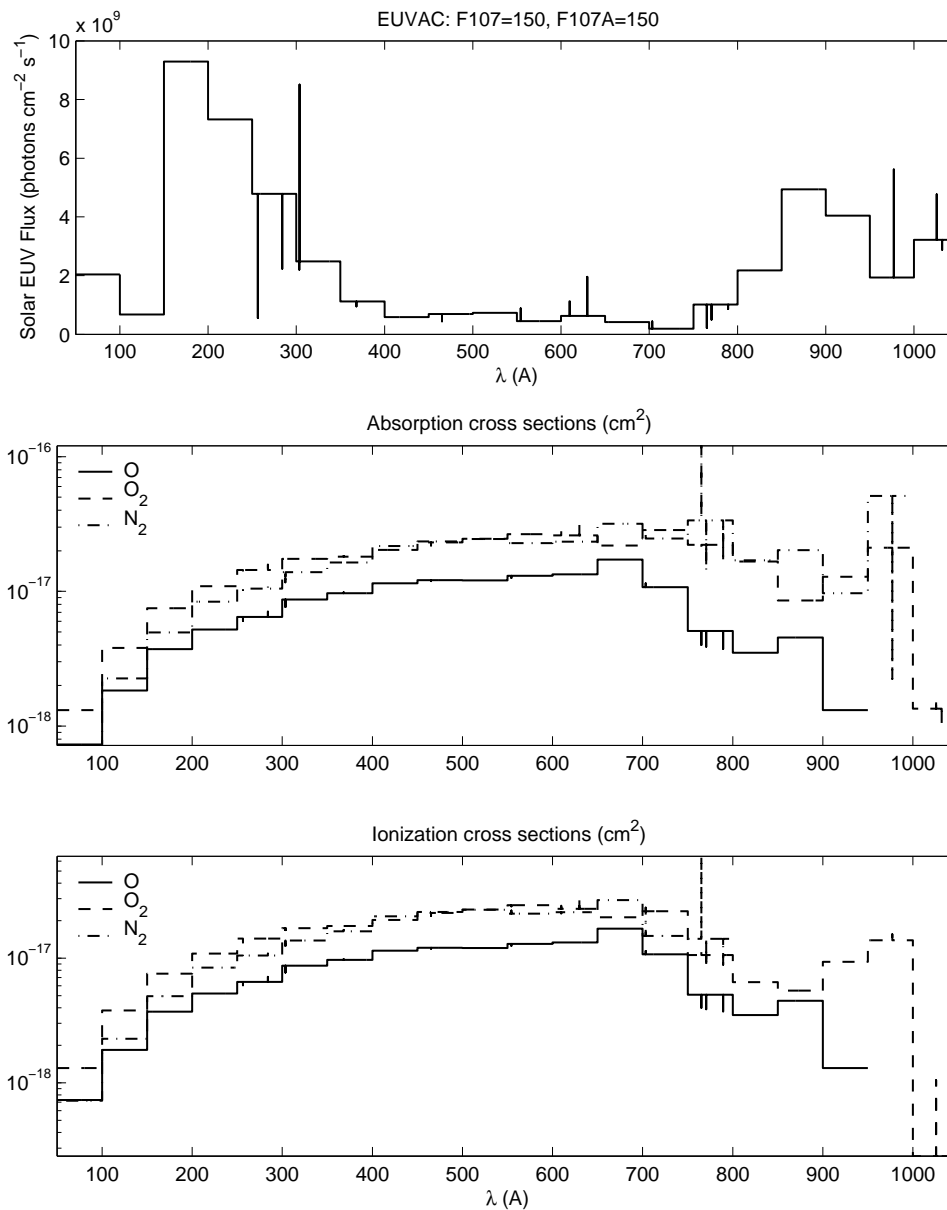
Figure 1.3: Example of output from the EUVAC model. The top panel is the flux at the top of the atmosphere, the middle panel shows the absorption cross sections, and the bottom panel shows the ionization cross sections.

Thus, in order to calculate the total ionization rate for an ionic species, the problem has been reduced to a function of the solar zenith angle, the neutral densities, the photon fluxes, and the absorption and ionization cross sections. There are many models for the fluxes and cross sections, although measurements especially of the fluxes are fairly difficult and rare. Figure 1.3 shows an example from the EUVAC model (*Richards et al.*, 1994), which specifies the $F74133$ reference flux in 37 wavelength bins from 50-1050 Å. To obtain the EUV flux as a function of solar activity, a simple scaling is used,

$$I_\infty(\lambda_i) = F74113_i[1 + A_i(P - 80)] \tag{1.7}$$

where A_i is a wavelength-dependent scaling, $P = (F10.7A + F10.7)/2$ where $F10.7$ is the daily $F10.7$ index and $F10.7A$ is the 81-day average $F10.7$ index centered on the day of interest, and i denotes wavelength bin. *Richards et al.* (1994) also report absorption and ionization cross sections at these wavelengths, as computed from the review by *Fennelly and Torr* (1992). Direct measurements of the solar spectral irradiance, for example by the Solar EUV Experiment (SEE) instrument on the NASA Thermosphere Ionosphere Mesosphere Energetics Dynamics (TIMED) spacecraft (e.g., *Woods et al.*, 2005) will no doubt improve our characterization of the EUV input into the upper atmosphere.

Further sources and sinks are associated with the various chemical reactions that occur in the ionosphere. These reactions include ion-atom interchange, atom-atom interchange, charge transfer, dissociative recombination, and collisional deactivation (quenching) (*Rees*, 1989). While we will not go into detail here on those reactions, simple photochemical models can be developed which equate the production and losses that occur in the ionosphere under the assumption that transport is negligible
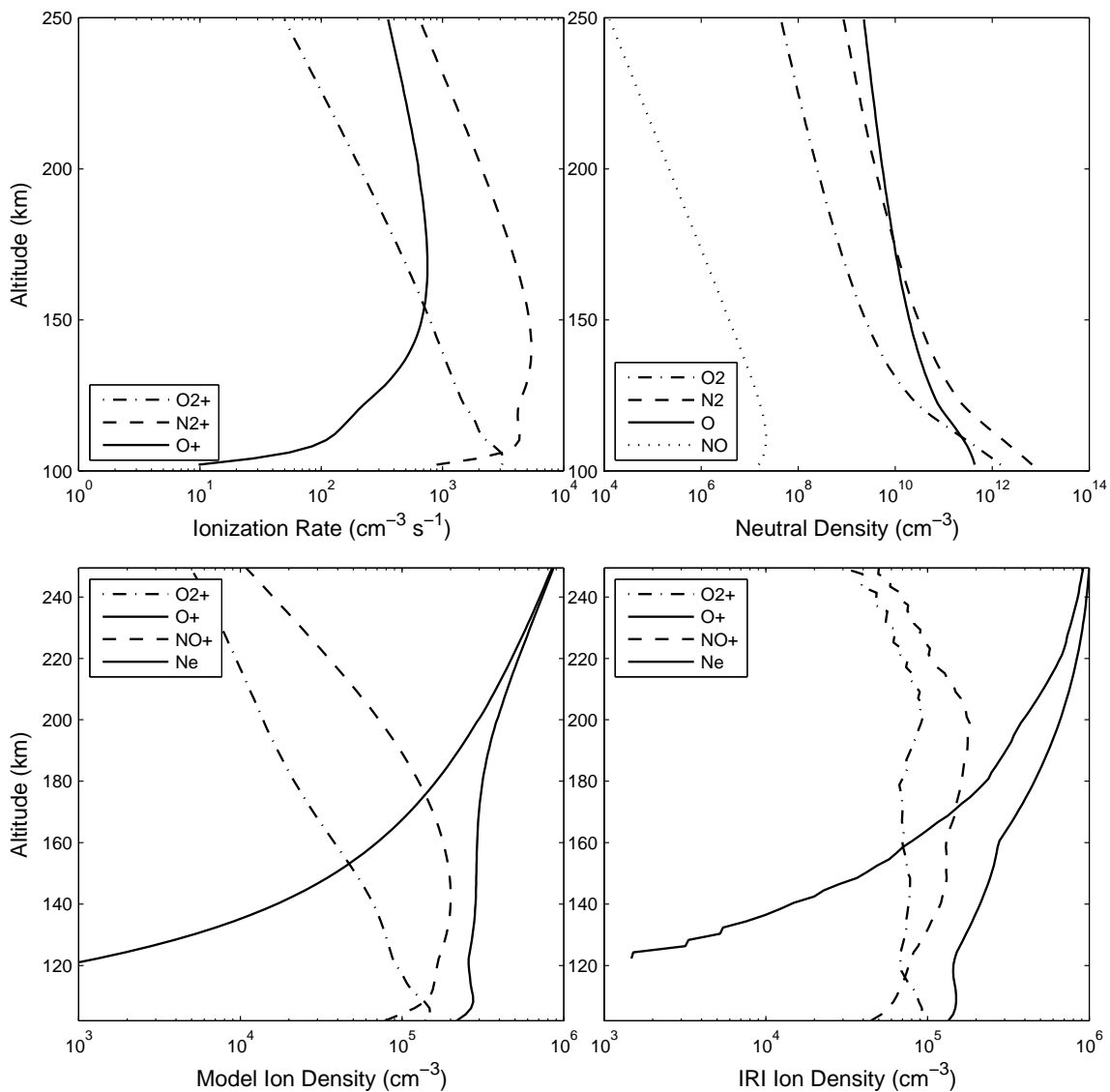
Figure 1.4: Example of the production of the ionosphere, from ionization rates to densities. The top left panel shows the ionization rates, the top right panel shows the MSIS neutral densities for these conditions, the bottom left panel shows the ion densities calculated using the ionization rates, and the bottom right panel shows the ion densities from the IRI model.

(valid in the lower F region and E region),

$$P_j \approx L_j. \tag{1.8}$$

These major reactions for O_2^+, O^+, N_2^+, and NO^+ in the lower F region include

$$O^+ + N_2 \quad \rightarrow \quad NO^+ + N \tag{1.9}$$

$$O^+ + O_2 \quad \rightarrow \quad O_2^+ + O \tag{1.10}$$

$$N_2^+ + O \quad \rightarrow \quad NO^+ + N \tag{1.11}$$

along with the dissociative recombination of O_2^+ and NO^+.

An example that carries through with these calculations (including the reactions listed above along with many other more minor reactions) is shown in Figure 1.4, where we plot the ionization rates calculated as described above, the MSIS neutral densities (*Hedin*, 1991a), the resulting ion densities, and a comparison to the ion densities given by the International Reference Ionosphere (IRI) model (*Bilitza*, 2001). Note that MSIS does not give NO densities so we have used the empirical model of *Titheridge* (1997). We have also included secondary ionizations as described by *Titheridge* (1996). This type of calculation works only where transport is negligible - near the F-region peak, diffusion is important and leads to the decrease of electron density with altitude. The transport term in the continuity equation must be kept. To be self-consistent, the velocity must be solved using a momentum equation for the ionic species, which will in turn depend on the momentum equation for the neutrals (through ion drag terms) and to the electron momentum equation (through electric field terms).

The heating of the thermosphere is dominated by the absorption of solar radiation. At high latitudes, electric currents along with the impact of energetic particles are additional sources of energy input. Photoelectrons (suprathermal electrons) heat the

electron gas (ambient electrons), which then pass some of their energy to the ion and neutral gases. Because of the high frequency of collisions at low altitudes, the ion and neutral gases are at nearly the same temperatures in the E region and lower F region. At higher altitudes, where the collision frequency is lower, the thermal coupling between ions and neutrals decreases whereas the thermal coupling between electrons and ions increases. *Banks* (1967) derived an approximate expression relating the ion temperature to the neutral and electron temperatures from the steady state ion energy budget,

$$T_i = \frac{T_n + (\alpha n_e/n_n)T_e^{-1/2}}{1 + (\alpha n_e/n_n)T_e^{-3/2}} \tag{1.12}$$

where $\alpha \approx 6 \times 10^6$, n_n is the neutral density, n_e is the electron density, T_n is the neutral temperature, and T_e is the electron temperature. This expression clearly shows the transition from a temperature near the neutrals at low altitudes and a temperature near the electrons at higher altitudes.

1.3 Organization

This thesis consists of a series of individual studies designed to address certain ionospheric problems. It is thus barely coherent from chapter to chapter, but carries a uniform theme within the general context of F-region dynamics and composition at low latitudes using radar and airglow measurements.

Chapter 2 reviews the models we have developed for the study of low latitude airglow, and presents some zenith airglow observations coincident with Arecibo incoherent scatter measurements. This work is based on the publications *Vlasov et al.* (2005) and *Nicolls et al.* (2006e). Chapter 3 presents multi-instrument observations and studies of a large-scale traveling ionospheric disturbance during a geomagnetic storm. This chapter is based mainly on the works *Nicolls et al.* (2004) and *Nicolls*

and Kelley (2005). Chapter 4 presents observations, modeling, and explanations for phenomena we have termed post-midnight uplifts that occur near the geomagnetic equator, based on the work of *Nicolls et al.* (2006c). Chapter 5 presents an analysis of four years of magnetometer data designed to study the effects of penetration electric fields, based on the work of *Nicolls et al.* (2006b). Chapter 6 presents a study of the nighttime molecular ion composition in the F region using airglow volume emission rates, based on the work of *Nicolls et al.* (2006e). Finally, Chapter 7 presents an ion energy balance study using Arecibo incoherent scatter radar data investigating the F-region neutral composition and temperature, based on *Nicolls et al.* (2006a). We have also included in Appendix A a short paper (*Nicolls et al.*, 2005) summarizing some observations of a stable auroral red arc over sunny Ithaca.

Chapter 2

Low Latitude Airglow: Instrumentation and Theory*

You can't have a light without a dark to stick it in. - Arlo Guthrie

2.1 Introduction

Ariglow refers to the natural luminosity of the Earth's atmosphere, and is typically divided into three categories. Dayglow refers to daytime airglow resulting from excitation due to the absorption of solar radiation. Dayglow is, of course, much weaker than the intensity of direct sunlight and is therefore difficult to study, however sensitive satellite instrumentation (such as the GUVI instrument on the TIMED satellite) can be used to monitor various dayglow emissions to study important thermospheric parameters like the solar extreme ultraviolet (EUV) flux and the O/N_2 ratio (e.g., *Strickland et al.*, 1995). Twilight airglow refers to emission processes induced during twilight, when the upper atmosphere is still sunlit but the lower atmosphere is in

---

*Some of this chapter is based on the publications *Vlasov et al.* (2005) and *Nicolls et al.* (2006e), which is joint collaborative work with M. N. Vlasov and M. C. Kelley. Reproduced by permission of the American Geophysical Union.

darkness. Twilight airglow measurements can be used, for example, to extract height profiles of neutral densities, such as atomic oxygen (e.g., *Melendez-Alvira et al.*, 1995; *Meriwether et al.*, 1978). Finally, nightglow refers to airglow processes that occur when the entire atmosphere is in darkness. The processes leading to nightglow are dominated by chemical reactions involving neutral constituents and/or the recombination of ionic species that have been ionized during the daytime. The nightglow is the focus of this chapter, and from here on we simply refer to it as airglow.

Like the aurora (which is caused by the impact of energetic precipitating electrons leading to excitation of some neutral species - atomic oxygen, molecular oxygen, or molecular nitrogen), the nighttime airglow has strong (when compared to the background) emissions at specific, discrete wavelengths. Commonly studied emissions include the atomic oxygen red and green lines at 630.0 nm and 557.7 nm, respectively, the sodium yellow emission at 589.2 nm, the near-infrared hydroxyl emissions, the O_2 Herzberg bands (300-400 nm), the $N(^2D)$ emission at 520.0 nm, the emission caused by radiative recombination of O^+ at 777.4 nm, and various metallic emissions.

Studies of the nighttime airglow have their origins in the pioneering work of Anders Angstrom (*Angstrom*, 1868), who made spectroscopic measurements of the green line in aurora. *Campbell* (1895) recognized that the green line emission was present even when there were no active auroral displays. Lord Rayleigh (the son, not the Nobel prize-winning father) made the first absolute measurements of the green line in aurora (*Rayleigh*, 1930). Later, Sidney Chapman (*Chapman*, 1931) explained the importance of recombination in generating airglow emissions.

The atomic oxygen red and green lines (630.0 and 557.7 nm, respectively) are the strongest features in the visible nighttime airglow spectrum at low and mid-latitudes. The main source of these emissions in the nighttime thermosphere is the dissociative recombination of O_2^+. Variations in the intensities of both emissions

are closely connected with variations in electron density and neutral composition at $F2$-region altitudes. Additionally, a major source of the green line emission is the three-body excitation of atomic oxygen in the mesosphere.

The usual approach for the calculation of the nighttime red and green line airglow excited in the $F2$ region is based on the single ion approximation, $[\mathrm{O}^+]=n_e$, where n_e denotes electron density (e.g., *Bates*, 1992; *Link and Cogger*, 1988; *Solomon*, 1991; *Vlasov et al.*, 2005). In this case, the green line intensity in the $F2$ region is proportional to electron density because $\mathrm{O}(^1S)$ deactivation by collisions is negligible in the thermosphere (the emission rate is also proportional to the O_2 neutral density, giving the volume emission rate a sensitive dependence on the height of the ionosphere). However, it is very difficult to infer electron density variations from green line measurements because of the significant and complicated contribution to the emission intensity from the mesosphere. The red line intensity is proportional to electron density, but strongly depends on the altitude of the $F2$ peak. This dependence is a result of the importance of $\mathrm{O}(^1D)$ quenching by neutral constituents in the thermosphere. Thus, the connection between the emission intensities and the ionospheric parameters is complicated. In addition, the usual approach mentioned above needs to be modified to consider the fact that the molecular ion density can be significant on the bottomside of the $F2$ region, which is where the red and green line volume emission rates are the highest.

In this chapter, we discuss our models for the airglow volume emission rates and compare them to some measurements. We discuss the red and green line emissions, including modifications involving the role of molecular ions. We also discuss the mesospheric green line emission. Some of this work has recently been published by *Vlasov et al.* (2005) and *Nicolls et al.* (2006e), and more details on the scientific applications can be found in Chapters 3 and 6. We conclude this chapter by discussing the instru-

mentation necessary to make airglow measurements and the processing techniques applied to the measurements. We also show and discuss some measurements of the integrated volume emission rate.

2.2 Airglow Models

In this section, we review our approach for calculating the airglow intensity from ionospheric parameters. We include discussions of our models for the $F2$-region red and green line emissions, the mesospheric green line emission, and briefly the $F2$-region 777.4-nm near-infrared emission. The effect of molecular ions is considered in our analysis of the red and green line emissions. The role of this modification is considered in detail in Chapter 6. This modification was considered because during conditions where the ionosphere is low, like those on October 1-2, 2002 which will be discussed in Chapter 3, it is possible that the increased molecular ion density on the bottomside of the F layer may become important. Some of these results follow the work of *Vlasov et al.* (2005) and *Nicolls et al.* (2006e).

2.2.1 $F2$-region Red and Green Line Emissions

The red and green line optical emissions are radiated by atomic oxygen excited in the ^1D and ^1S metastable states, respectively. The red line is a doublet, resulting from the forbidden atomic oxygen transition $^3P_{2,1} - {}^1D_2$ (actually it is a triplet, but the third line, $^3P_0$, is very weak). The $^1D_2$ state (630.0 nm) is 1.97 eV above the ground state and has a radiative lifetime near 110 s. The long lifetime leads to significant deactivation by collisions below the F region, which will be discussed later when we formulate the expression for the volume emission rate. The second line occurs at a
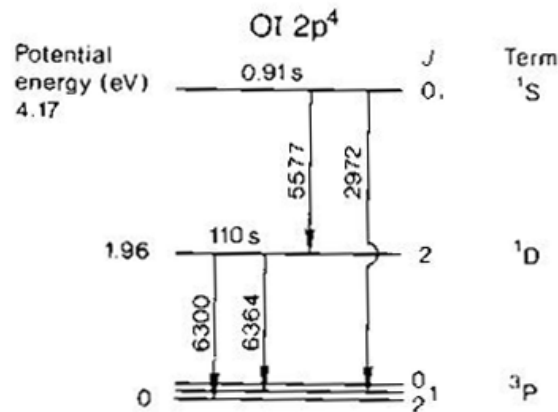
Figure 2.1: Partial energy level diagram for atomic oxygen, from *Rees* (1989).

wavelength of 636.4 nm. The red line doublet emission thus occurs via the reaction

$$O(^1D_2) \rightarrow O(^3P_{2,1}) + h\nu(630.0, 636.4 \text{ nm}). \tag{2.1}$$
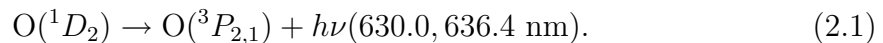
The F-region green line, $O(^1S_0)$, has a much shorter lifetime near 0.91 s and is 4.17 eV above the ground state. Emission of a photon leaves the atom in either the $^1D_2$ or $^3P_1$ state via the reactions

$$O(^1S_0) \rightarrow O(^1D_2) + h\nu(557.7 \text{ nm})$$

$$O(^1S_0) \rightarrow O(^3P_1) + h\nu(297.2 \text{ nm}).$$
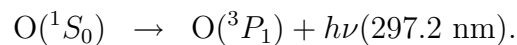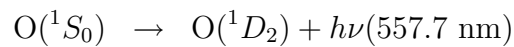
Thus, the emission of every 557.7-nm photon leaves an O atom in the $^1D_2$ state giving rise to an additional source of $O(^1D)$. An energy level diagram is shown in Figure 2.1 summarizing the transitions.

The main source of the metastable atoms $O(^1D_2, {}^1S_0)$ in the nighttime thermosphere is the dissociative recombination of O_2^+,

$$O_2^+ + e^- \rightarrow O(^3P) + O(^1D, {}^1S). \tag{2.2}$$
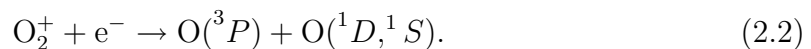
The rate coefficient of this reaction has been given most recently by the formula

(*Sheehan and St.-Maurice*, 2004)

$$\alpha_{O_2^+}^* = 1.95 \times 10^{-7}(300/T_e)^{0.7} \quad \text{cm}^3\text{s}^{-1} \tag{2.3}$$

where T_e denotes electron temperature. The production rate of $O(^1D)$ and $O(^1S)$ atoms in Reaction 2.2 is thus given by

$$\mu_j \alpha_{O_2^+}^* [O_2^+] n_e \tag{2.4}$$

where μ_j is the quantum yield for state j and n_e is electron density.

The quantum yields of $O(^1D)$ and $O(^1S)$ in Reaction 2.2 are very different. The $O(^1D)$ yield, μ_D, is in the range 1-1.3 (*Torr and Torr*, 1982; *Guberman*, 1988; *Link and Cogger*, 1988). The $O(^1S)$ yield, μ_S, does not exceed 10% (*Torr and Torr*, 1982; *Guberman*, 1987; *Peverall et al.*, 2000). *Sobral et al.* (1992) inferred an $O(^1S)$ yield of 8% from a rocket measurement. Laboratory measurements (e.g., *Peverall et al.*, 2000) indicate that the value of μ_S is between 3% and 4% for dissociative recombination of O_2^+ vibrationally unexcited ions for electron temperatures between 800 K and 1500 K. Theoretical calculations (e.g., *Guberman*, 1987; *Peverall et al.*, 2000) also provide very strong support for the laboratory measurements.

According to the laboratory investigation of *Kella et al.* (1997), the dissociative recombination of O_2^+ in the lowest vibrational levels leads to a higher yield of $O(^1S)$ than had been anticipated by theory (*Guberman and Giusti-Suzor*, 1991). Thus, there is a significant discrepancy between the yields inferred from rocket (8%) and laboratory (3-4%) measurements. However, it is very difficult to control the vibrational population of the ions in a laboratory plasma, and for this reason we use the 8% value deduced from rocket measurements. There is clearly some uncertainty in this parameter.

Table 2.1: Reactions and rate coefficients used in the red and green line airglow model.

Reactions	Rate coefficients, $\mathrm{cm}^3\mathrm{s}^{-1}$, s^{-1}, or $\mathrm{cm}^6\mathrm{s}^{-1}$	Reference
$\mathrm{O}(^1D) + \mathrm{N}_2 \rightarrow \mathrm{O}(^3P) + \mathrm{N}_2$	$k_1 = 2 \times 10^{-11} \exp{(107.8/T_n)}$	*Langford et al. (1986)*
$\mathrm{O}(^1D) + \mathrm{O}_2 \rightarrow \mathrm{O}(^3P) + \mathrm{O}_2$	$k_2 = 2.9 \times 10^{-11} \exp{(67.5/T_n)}$	*Streit et al. (1976)*
$\mathrm{O}(^1D) + \mathrm{O} \rightarrow \mathrm{O}(^3P) + \mathrm{O}$	$k_3 = (3.730 + 1.1965 \times 10^{-1} T_n^{0.5}$	*Sun and Dalgarno (1992)*
	$-6.5898 \times 10^{-4} T_n) \times 10^{-12}$	
$\mathrm{O}(^1D) + \mathrm{e}^- \rightarrow \mathrm{O}(^3P) + \mathrm{e}^-$	$k_4 = 1.6 \times 10^{-12} T_e^{0.91}$	*Link and Cogger (1988)*
$\mathrm{O}(^1D) \rightarrow \mathrm{O}(^3P) + h\nu(630.0 \text{ nm})$	$A_{1D} = 7.1 \times 10^{-3}$	*Froese-Fischer and Saha (1983)*
$\mathrm{O}(^1D) \rightarrow \mathrm{O}(^3P) + h\nu(636.4 \text{ nm})$	$A_{2D} = 2.2 \times 10^{-3}$	*Froese-Fischer and Saha (1983)*
$\mathrm{O} + \mathrm{O} + \mathrm{M} \rightarrow \mathrm{O}_2(c^1\Sigma_u^-) + \mathrm{M}$	$k_5 = 1.4 \times 10^{-34}(300/T_n)^2$	*Torr et al. (1985)*
		Lopez-Gonzalez et al. (1992a,b)
$\mathrm{O}_2(c^1\Sigma_u^-) + \mathrm{O}_2 \rightarrow \mathrm{O}_2(b^1\Sigma_g^+) + \mathrm{O}_2$	$k_6 = 3.0 \times 10^{-14}$	*Kenner and Ogryzlo (1983)*
$\mathrm{O}_2(c^1\Sigma_u^-) + \mathrm{O} \rightarrow \mathrm{O}_2 + \mathrm{O}$	$k_7 = 6.0 \times 10^{-12}$	*Kenner and Ogryzlo (1983)*
$\mathrm{O}_2(c^1\Sigma_u^-) + \mathrm{O} \rightarrow \mathrm{O} + \mathrm{O}(^1S)$	$k_8 = 0.2 k_7$	*Kenner and Ogryzlo (1983)*
$\mathrm{O}_2(c^1\Sigma_u^-) \rightarrow \mathrm{O}_2 + h\nu$	$A_\Sigma = 0.02$	*Kenner and Ogryzlo (1983)*
$\mathrm{O}(^1S) + \mathrm{O}_2 \rightarrow \mathrm{O}(^3P) + \mathrm{O}_2$	$k_9 = 4.3 \times 10^{-12} \exp{(-850/T_n)}$	*Slanger et al. (1972)*
$\mathrm{O}(^1S) \rightarrow \mathrm{O}(^1D) + h\nu(577.7 \text{ nm})$	$A_{1S} = 1.215$	*Baluja and Zeippen (1988)*
$\mathrm{O}(^1S) \rightarrow \mathrm{O}(^3P) + h\nu(297.2 \text{ nm})$	$A_{2S} = 0.076$	*Baluja and Zeippen (1988)*

Common Approach, Neglecting Molecular Ions

The common approach (e.g., *Bates*, 1992; *Link and Cogger*, 1988; *Solomon*, 1991) for the calculation of the 630.0- and 557.7-nm intensities is based on the assumption that O^+ is the main ionospheric constituent in the nighttime $F2$ region and that the O_2^+ ions are only produced through the ion-molecular reaction,

$$O^+ + O_2 \rightarrow O_2^+ + O. \tag{2.5}$$

By equating the production rate of Reaction 2.2 to the loss rate of Reaction 2.5, the O_2^+ concentration can be written as

$$\left[O_2^+\right] = \frac{\gamma_2\left[O_2\right]}{\alpha_{O_2^+}^* n_e}\left[O^+\right] \tag{2.6}$$

where γ_2 is the rate coefficient of Reaction 2.5 given by (*St.-Maurice and Torr*, 1978)

$$\begin{aligned}
\gamma_2 &= 2.82 \times 10^{-11} - 7.74 \times 10^{-12}(T_{eff}/300) + 1.073 \times 10^{-12}(T_{eff}/300)^2 \\
&\quad -5.17 \times 10^{-14}(T_{eff}/300)^3 + 9.65 \times 10^{-16}(T_{eff}/300)^4 \quad \text{cm}^3\text{s}^{-1} \tag{2.7}
\end{aligned}$$

and $T_{eff} = 2T_i/3 + T_n/3$. The values given by Equation 2.7 are in good agreement with the rate coefficients measured by *Hierl et al.* (1997) for typical nighttime ionospheric temperatures. Usually, the O_2^+ concentration is much less than the O^+ concentration because the $\gamma_2[O_2]$ term in Equation 2.6 is much less than $\alpha_{O_2^+}^* n_e$ in the $F2$ region. Plugging in reasonable numbers for $F2$-region altitudes, $\gamma_2[O_2]$ is less than 10^{-3} s^{-1} and $\alpha_{O_2^+}^* n_e$ is larger than 10^{-2} s^{-1}; then, clearly $[O_2^+] \ll [O^+]$ and $[O^+] \approx n_e$. In this case, according to Equation 2.6, the production rate of $O(^1D)$ via Reaction 2.2 can be written as $\mu_D \gamma_2[O_2]n_e$. Given this description, the volume emission rate for airglow at 630.0 nm would be simply

$$I_R = \frac{A_{1D}}{A_{1D} + A_{2D}}\mu_D \gamma_2[O_2]n_e \tag{2.8}$$

where A_{1D} corresponds to the transition coefficient for spontaneous emission of a photon at wavelength of 630.0 nm, and A_{2D} corresponds to the transition coefficient for spontaneous emission at 636.4 nm (the Einstein coefficients).

However, we have not considered collisional deactivation (quenching), which is important because of the highly metastable nature of the ^1D state. The quenching reactions are additional loss mechanisms (competing with radiative deactivation) resulting from deactivation due to collisions with other species. These reactions have the form

$$O(^1D) + X \rightarrow O(^3P) + X \tag{2.9}$$
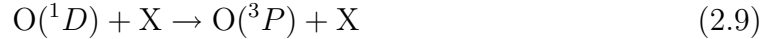
where X is typically a neutral species, but could also represent deactivation due to a collision with an electron. In our model for the 630.0-nm volume emission rate, we consider the quenching due to interactions with neutral constituents N_2, O_2, and O as well as electrons. The reactions and rate coefficients are summarized in Table 2.1.

In addition to the main source given by Reaction 2.2, it has been theorized that there is a small additional contribution to the production of $O(^1D)$ atoms resulting from the dissociative recombination of NO^+. This channel involves the reactions (*Rusch et al.*, 1978)

$$NO^+ + e^- \rightarrow N(^2D) + O \tag{2.10}$$

$$N(^2D) + O_2 \rightarrow NO + O(^3P, {}^1D) \tag{2.11}$$

with a rate coefficient of (*Sheehan and St.-Maurice*, 2004)

$$\alpha^*_{NO^+} = 3.5 \times 10^{-7}(300/T_e)^{0.69} \quad \text{cm}^3\text{s}^{-1}. \tag{2.12}$$

It is actually controversial whether $N(^2D)$ is important in 630.0-nm photochemistry, especially at auroral latitudes (*Chakrabarti*, 1999), as some authors have claimed that it is necessary to account for observed intensities (e.g., *Rusch et al.*, 1978) and others have claimed that it is unnecessary (e.g., *Link and Swaminathan*, 1992). *Link*

and Swaminathan (1992) found that the yield of the O(^1D) atoms in Reaction 2.11 does not exceed 0.1. However, *Rusch et al.* (1978) identified Reaction 2.11 as an important source of auroral O(^1D). In any case, this channel seems to be a minor source of O(^1D) at night at low and mid-latitudes. Nevertheless, we will include this branch for completeness, however we will not give values for the reaction rates because they are uncertain. We should mention that recent laboratory measurements (*Miller and Hunter*, 2004) seem to show agreement with the low yield estimated by *Link and Swaminathan* (1992).

The production rate of O(^1D) atoms via this channel is given by

$$\beta \gamma_D [\text{N}][\text{O}_2] \tag{2.13}$$

where β is the yield of the N(^2D) atoms in Reaction 2.10 and γ_D is the rate coefficient of Reaction 2.11. A simple model of the N(^1D) density can be developed by assuming that the only other mechanism for N(^2D) loss is via deactivation by atomic oxygen,

$$\text{N}(^2D) + \text{O} \rightarrow \text{N} + \text{O}, \tag{2.14}$$

with rate coefficient γ_O. Then, with Reactions 2.10 and 2.11, we can write the N(^2D) density as

$$[\text{N}] = \frac{\alpha^*_{\text{NO}^+}[\text{NO}^+]n_e}{\gamma_O[\text{O}] + \gamma_D[\text{O}_2]}. \tag{2.15}$$

If we further assume that NO$^+$ is only produced via the ion-molecular reaction,

$$\text{O}^+ + \text{N}_2 \rightarrow \text{NO}^+ + \text{N}(^2D) \tag{2.16}$$

with rate coefficient (*St.-Maurice and Torr*, 1978)

$$\gamma_1 = 1.53 \times 10^{-12} - 5.92 \times 10^{-13}(T_{eff}/300) + 8.6 \times 10^{-14}(T_{eff}/300)^2 \quad \text{cm}^3\text{s}^{-1}, \tag{2.17}$$

then we can write the density of N(^2D) atoms as

$$[\text{N}] = \frac{\gamma_1[\text{O}^+][\text{N}_2]}{\gamma_O[\text{O}] + \gamma_D[\text{O}_2]}. \tag{2.18}$$

Finally, again letting $[O^+] = n_e$ as is typically done, the volume emission rate of the red line emission induced by recombination in the $F2$ region is given by the formula (*Vlasov et al.*, 2005)

$$I_R = \frac{A_{1D}\left\{\mu_D\gamma_2[O_2]n_e + \frac{\beta\gamma_1[N_2]n_e\gamma_D[O_2]}{\gamma_D[O_2]+\gamma_O[O]}\right\}}{k_1[N_2] + k_2[O_2] + k_3[O] + k_4n_e + A_{1D} + A_{2D}} \tag{2.19}$$

where k_1, k_2, k_3, and k_4 are the rate coefficients of $O(^1D)$ quenching by N_2, O_2, O, and electrons, respectively, and A_{1D} and A_{2D} are the $^1D \rightarrow {}^3P$ transition coefficients. The rate coefficients for the collisional and radiative deactivation of the $O(^1D)$ atoms are summarized in Table 2.1.

Then, the integrated intensity of the red line emission is given by

$$J_R = \int_{z_1}^{z_2} I_R dz, \tag{2.20}$$

where z_1 and z_2 are the lower and upper boundaries of the emission layer, respectively. J_R increases when the $F2$-peak altitude decreases because the numerator in Equation 2.19 increases more quickly than the denominator due to the low efficiency of quenching by O_2.

By the exact same procedure, the volume emission rate of the green line in the $F2$ region can be written as

$$I_G = \frac{A_{1S}\mu_S\gamma_2[O_2]n_e}{A_{1S} + A_{2S}}. \tag{2.21}$$

There are no quenching terms in the denominator of Equation 2.21 because $O(^1S)$ deactivation by collisions with neutral constituents (and other sources) is negligible in the $F2$ region because of the short lifetime of the ^1S state. The rate coefficients and rate constants are again summarized in Table 2.1. The integrated intensity of the green line emission is given by

$$J_G = \int_{z_1}^{z_2} I_G dz, \tag{2.22}$$

where z_1 and z_2 are the lower and upper boundaries of the emission layer, respectively. The integrated volume emission rates are typically reported in units of Rayleighs, corresponding to 10^6 photons $\text{cm}^{-2}\text{s}^{-1}$.

Consideration of Molecular Ions

As can be seen from Equation 2.6, the $[O_2^+]/[O^+]$ ratio increases with decreasing electron density and decreasing altitude (the O_2 density increases at lower altitudes). Thus, the typical approach above, described by Equations 2.19 and 2.21, can be applied only when the O_2^+ density is negligible with respect to the O^+ density. In the case where this condition is not met, the volume emission rates of the red and green line intensities are given by the formulae (*Vlasov et al.*, 2005)

$$I_R^{\triangle} = \frac{A_{1D}\left\{\mu_D \alpha_{O_2^+}^*[O_2^+]n_e + \frac{\beta \alpha_{NO+}^*[NO^+]n_e \gamma_D[O_2]}{\gamma_D[O_2]+\gamma_O[O]}\right\}}{k_1[N_2] + k_2[O_2] + k_3[O] + k_4 n_e + A_{1D} + A_{2D}} \tag{2.23}$$

$$I_G^{\triangle} = \frac{A_{1S}\mu_S \alpha_{O_2^+}^*[O_2^+]n_e}{A_{1S} + A_{2S}} \tag{2.24}$$

where we have simply not made some of the approximations that went into Equations 2.19 and 2.21.

Neglecting the second term in the numerators of Equations 2.19 and 2.23 and using the relationship $n_e = [O^+] + [O_2^+]$, the ratio $I_R/I_R^{\triangle}$ can be written as

$$P = \frac{I_R}{I_R^{\triangle}} = \frac{\gamma_2[O_2]}{\alpha_{O_2^+}^*[O_2^+]} = 1 + \frac{[O_2^+]}{[O^+]}, \tag{2.25}$$

which is equal to 1 when $[O_2^+] \ll [O^+]$. This result indicates that Equation 2.19 gives unrealistically high intensities when the O_2^+ density becomes comparable to the O^+ density. Additionally, we can take into account the NO^+ ions produced by Reaction 2.16 and lost via Reaction 2.10,

$$[NO^+] = \frac{\gamma_1[N_2]}{\alpha_{NO+}^* n_e}[O^+]. \tag{2.26}$$

Using the relation $n_e = [\mathrm{O^+}] + [\mathrm{O_2^+}] + [\mathrm{NO^+}]$, we obtain for the same ratio

$$P = \frac{I_R}{I_R^\triangle} = 1 + \frac{\gamma_1 [\mathrm{N_2}]}{\alpha_{\mathrm{NO^+}}^* n_e} + \frac{\gamma_2 [\mathrm{O_2}]}{\alpha_{\mathrm{O_2^+}}^* n_e}. \tag{2.27}$$

The height distribution of $I_R^\triangle$ can be written by assuming a barometric distribution for the neutral constituents and a Chapman layer for the electron density (a good approximation on the bottomside of the $F2$ region). Thus, the neutral density is given by

$$[\mathrm{M}] = [\mathrm{M}]_0 e^{z/H_\mathrm{M}} \tag{2.28}$$

where M is the neutral constituent, $[\mathrm{M}]_0$ is the density of the neutral constituent at the F peak, H_M is the neutral scale height,

$$H_\mathrm{M} = \frac{k_B T_n}{m_\mathrm{M} g}, \tag{2.29}$$

and z is 0 at the F peak and increases with decreasing altitude. The electron density is given by

$$n_e = n_{e0} \exp \left[\frac{1}{2} \left(1 + \frac{z}{H_{Ch}} - e^{z/H_{Ch}} \right) \right] \tag{2.30}$$

where n_{e0} is the density at the F peak ($N_m F2$) and H_{Ch} is the Chapman scale height. Then, using these descriptions, the height distribution of the red line emission can be written using Equation 2.19 and 2.27 as

$$
\begin{aligned}
I_R^\triangle &= \frac{I_R}{P} \\
&= \frac{A_{1D} \mu_D \gamma_2 [\mathrm{O_2}]_0}{\ell P} n_{e0} \exp \left[\frac{z}{H_{\mathrm{O_2}}} + \frac{1}{2} \left(1 + \frac{z}{H_{Ch}} - e^{z/H_{Ch}} \right) \right]
\end{aligned} \tag{2.31}
$$

where

$$
\begin{aligned}
\ell &= k_1 [\mathrm{N_2}]_0 \exp \left(z/H_{\mathrm{N_2}} \right) + k_2 [\mathrm{O_2}]_0 \exp \left(z/H_{\mathrm{O_2}} \right) \\
&\quad + k_3 [\mathrm{O}]_0 \exp \left(z/H_\mathrm{O} \right) + A_{1D} + A_{2D}
\end{aligned} \tag{2.32}
$$

and

$$P = \frac{I_R}{I_R^{\triangle}}$$

$$= 1 + \frac{\gamma_1 [\mathrm{N}_2]_0}{\alpha_{\mathrm{NO}^+}^* n_{e0}} \exp\left[\frac{z}{H_{\mathrm{N}_2}} - \frac{1}{2}\left(1 + \frac{z}{H_{Ch}} - e^{z/H_{Ch}}\right)\right]$$

$$+ \frac{\gamma_2 [\mathrm{O}_2]_0}{\alpha_{\mathrm{O}_2^+}^* n_{e0}} \exp\left[\frac{z}{H_{\mathrm{O}_2}} - \frac{1}{2}\left(1 + \frac{z}{H_{Ch}} - e^{z/H_{Ch}}\right)\right]. \tag{2.33}$$

We should note that in formulating these expressions we have ignored the quenching due to deactivation by electrons (k_4), which is typically much smaller than the other quenching terms.

We remind the reader that $z = 0$ at the altitude of the $F2$ peak and z increases below $h_m F2$. We can restrict our consideration to altitudes below $h_m F2$ because that is where the volume emission rate peaks, and the influence of molecular ions is significant only on the bottomside of the $F2$ region. Using Equations 2.31-2.34 it is possible to calculate the altitude distribution of the 630.0-nm volume emission rate in two ways: including the molecular ions, $I_R^{\triangle}$, and neglecting the molecular ions, I_R. These profiles, calculated with $H_{Ch} = H_{\mathrm{O}}$ (H_{O} is the atomic oxygen scale height), $N_m F2 = 5 \times 10^5$ cm^{-3}, and $h_m F2 = 360$ km, and using $[\mathrm{N}_2]_0$ and $[\mathrm{O}_2]_0$ as given by the MSIS-90 model (*Hedin*, 1991a) for the geophysical conditions on the night of October 1-2, 2002, are shown in Figure 2.2a. As can be seen from the figure, the difference between the two profiles is very small, and their integrated intensities are very close. However, this difference increases as the electron density gradient decreases on the bottomside of the $F2$ layer. Thus, the height profiles of I_R and $I_R^{\triangle}$, calculated with $H_{Ch} = 1.5 H_{\mathrm{O}}$ and shown in Figure 2.2b, are very different and in this case it is necessary to take into account the molecular ions. However, according to the IRI model (*Bilitza*, 2001) and much experimental data (e.g., *Emery et al.*, 1981), the gradient scale on the bottomside of the nighttime $F2$ region does not typically exceed the H_{O} value at mid-latitudes. A typical scale of the bottomside gradient
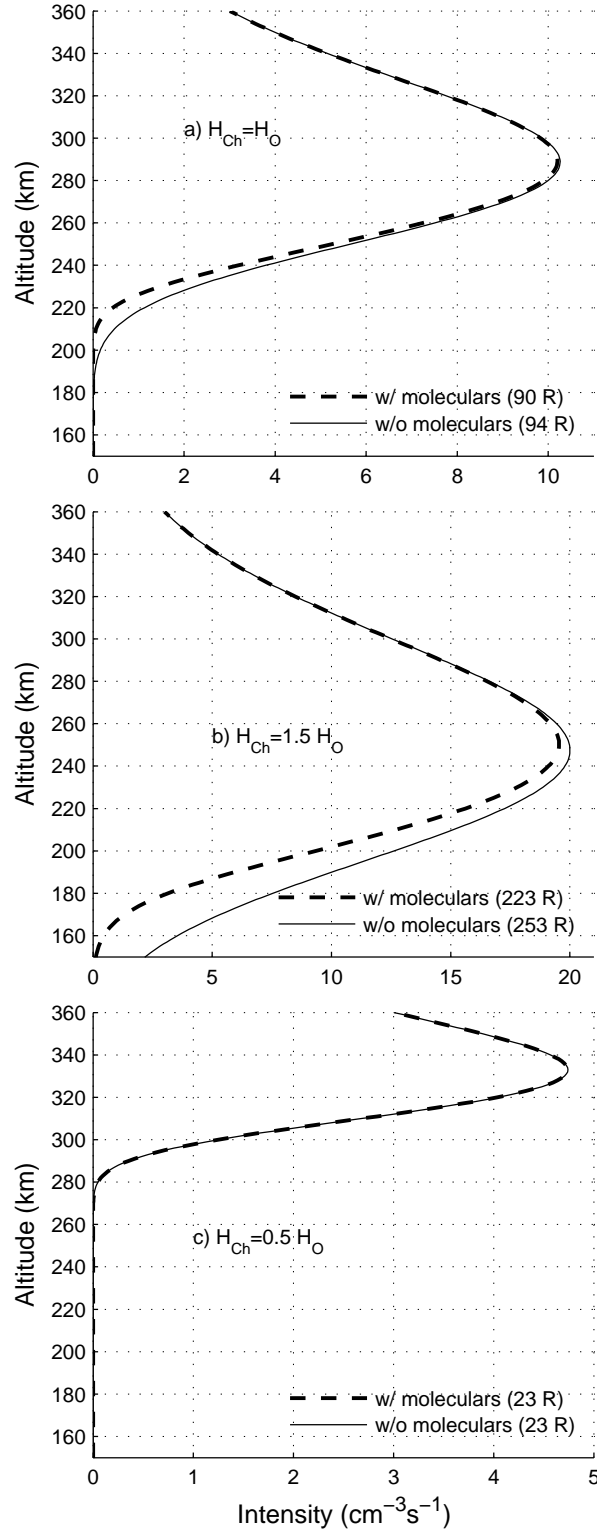
Figure 2.2: Height distributions of the red line intensity calculated with (dashed) and without (solid) molecular ions for three different scales heights. Here, $[O]_0=3.9 \times 10^8$ cm^{-3}, $[O_2]_0=7.4 \times 10^5$ cm^{-3}, $[N_2]_0=2.65 \times 10^7$ cm^{-3}, $T = 1000$ K, $N_mF2 = 5 \times 10^5$ cm^{-3}, $h_mF2=360$ km, $H_O \approx 58$ km. The integrated intensity for each curve is also indicated.
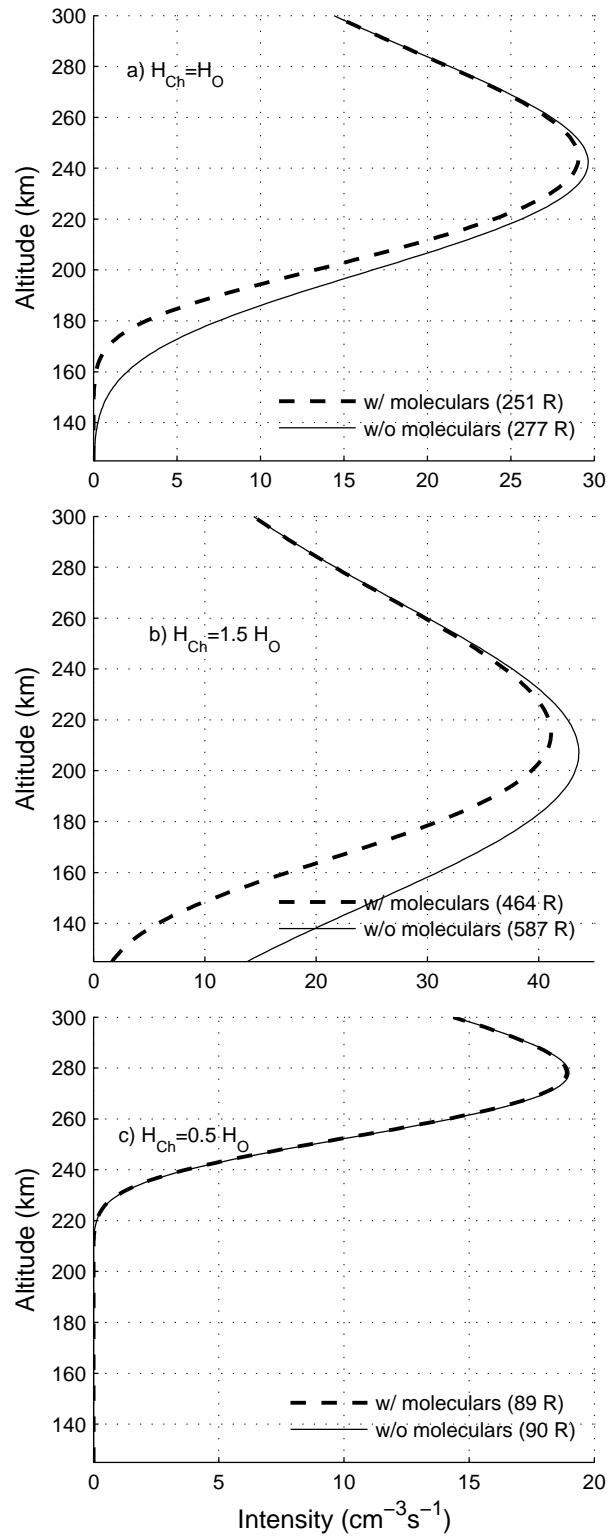
Figure 2.3: Same as Figure 2.2 except with $h_m F2$=300 km and $[O]_0 = 1.1 \times 10^9$ cm^{-3}, $[O_2]_0 = 5.8 \times 10^6$ cm^{-3}, $[N_2]_0 = 1.6 \times 10^8$ cm^{-3}.

is about $H_O/2$. As can be seen from Figure 2.2c, the difference between the height profiles with and without moleculars calculated with $H_{Ch} = H_O/2$ is negligible (the two curves overlap almost exactly on this plot). This means that using the ionospheric parameters and Equations 2.19 and 2.21, it is possible to calculate the intensities of the red and green lines. These conclusions, of course, strongly depend on the value of $h_m F2$. For this reason, a second example is shown in Figure 2.3 where we have reduced $h_m F2$ to 300 km.

Thus, we have shown that even when the F layer is low, it is still possible to use the one-ion approximation for the F-region airglow given in Equations 2.19 and 2.21, provided that the scale height is sufficiently close to H_O. If the scale height is large, then $h_m F2$ must be sufficiently high in order for the one-ion approximation to be valid. The formulation developed in this section may be useful at times when these conditions are not valid. We revisit the nighttime molecular ion composition in Chapter 6.

2.2.2   Mesospheric Green Line Emission

The observed intensity of the green line also includes mesospheric radiation, which makes estimating the ionospheric influence on the volume emission rate difficult. The mesospheric radiation occurs from the region of the ionosphere that includes the highest concentration of atomic oxygen, which occurs between 95-100 km. In this region, the mesospheric green line emission is excited by a two-step mechanism (*Barth*, 1961, 1964):

$$\mathrm{O} + \mathrm{O} + \mathrm{M} \rightarrow \mathrm{O}_2^* + \mathrm{M} \tag{2.34}$$

$$\mathrm{O}_2^* + \mathrm{O} \rightarrow \mathrm{O}_2 + \mathrm{O}(^1S) \tag{2.35}$$

where O_2^* refers to an excited intermediate state and M can be any third species, atomic or molecular (but is probably N_2). The first reaction, Reaction 2.34, yields excited O_2 in the $A^3\Sigma_u^+$, $A'^3\Delta_u$, and $c^1\Sigma_u^-$ states. The first state leads to emission in the Herzberg band and the second in the Chamberlain band (see, for example, *Rees* (1989) for details). The important step is the one that converts the O_2 in the $c^1\Sigma_u^-$ state to the $X^3\Sigma_g^-$ state via Reaction 2.35. Radiative deactivation then occurs as previously described. There is some uncertainty regarding the identity of the O_2^* state (*McDade et al.*, 1986; *Meriwether*, 1989). The $c^1\Sigma_u^-$ state is considered to be the most probable, but excitation of the second vibrational level of this state is necessary to remove the energy deficit (*Bates*, 1988).

The reactions for production and loss of $O(^1S)$ in the mesosphere are listed in Table 2.1. $O_2(c^1\Sigma_u^-)$ is produced by Reaction 2.34 with rate coefficient k_5, with a production rate

$$k_5[O]^2[M]. \tag{2.36}$$

The various loss reactions give rise to a loss rate that can be written as,

$$k_6[O_2] + k_7[O] + A_\Sigma. \tag{2.37}$$

Equating these production and loss rates gives rise to a density,

$$\left[O_2(c^1\Sigma_u^-)\right] = \frac{k_5[O]^2[M]}{k_6[O_2] + k_7[O] + A_\Sigma}. \tag{2.38}$$

The production rate of $O(^1S)$ atoms via Reaction 2.35 with rate coefficient k_8 will be

$$k_8[O_2(c^1\Sigma_u^-)][O] \tag{2.39}$$

and the volume emission rate will be

$$I_G^{mes} = \frac{A_{1S}k_8[O_2(c^1\Sigma_u^-)][O]}{k_9[O_2] + A_{1S} + A_{2S}} \tag{2.40}$$
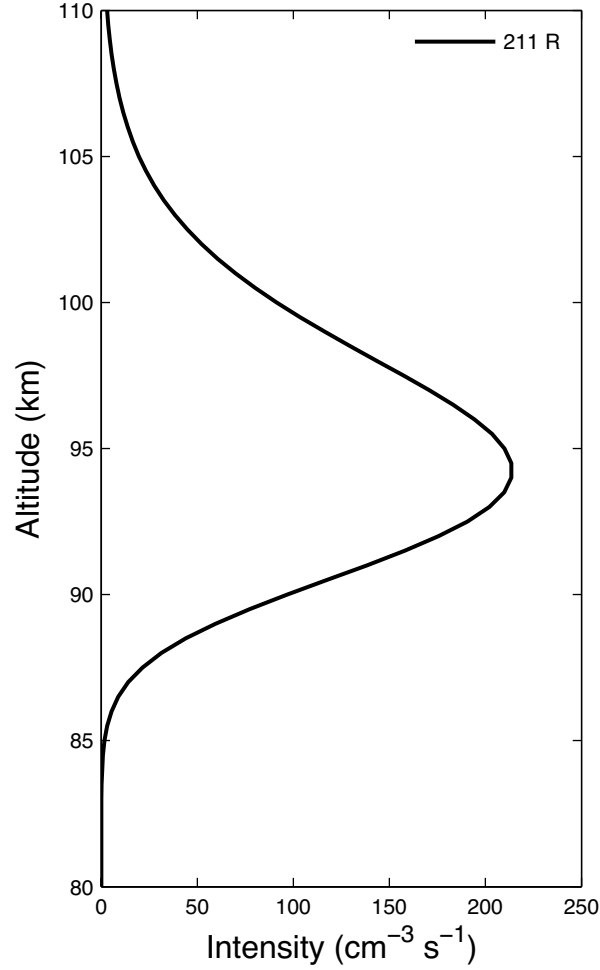
Figure 2.4: Example of a mesospheric green line volume emission rate profile for typical atmospheric conditions. The integrated volume emission rate is denoted in the upper right.

where we have included quenching due to collisions with O_2 with rate coefficient k_9. Substituting in Equation 2.38, we obtain for the volume emission rate (*Vlasov et al.*, 2005),

$$I_G^{mes} = \frac{k_5 k_8 A_{1S}[O]^3[M]}{(k_6[O_2] + k_7[O] + A_\Sigma)(k_9[O_2] + A_{1S} + A_{2S})}. \qquad (2.41)$$

The maximum of the volume emission rate is at about 95 km and the typical half-layer thickness is about 10 km. An example of a volume emission rate profile is shown in Figure 2.4 for typical nighttime atmospheric conditions from the MSIS model (using $[M]=[N_2]$). Typical green line emission intensities observed over Arecibo

are about 100 R with variations of about 40% (*Schubert et al.*, 1999). These variations are closely connected with variations of the atomic oxygen density at about 95 km, where the [O] peak is situated. The importance of atomic oxygen and mesospheric temperature variations on the green line emission will be discussed in Chapter 3 for a specific case study. In general, these variations are complex and difficult to understand.

2.2.3 777.4-nm Oxygen Emission

The emission at 777.4 nm is reviewed here briefly because of its usefulness as an F-region diagnostic. The reaction has been studied in depth by *Tinsley et al.* (1973) and reviewed by *Makela* (2003) and *Makela et al.* (2001a, 2003). The emission is due to radiative recombination of O^+, which leaves O in an excited state,

$$O^+(^4S) + e^- \rightarrow O^* \tag{2.42}$$

and the excited atom cascades to the ground state. The cascade leading to emission at 777.4 nm is caused by the transition from the $^5P_{3,2,1}$ state (a quintet) to the $^5S_2^0$ state, i.e.

$$O^+(^5P) \rightarrow O(^5S) + h\nu(777.4 \text{ nm}). \tag{2.43}$$
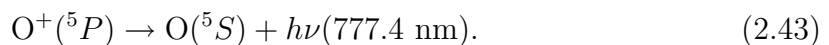
The rate coefficient (*Sahai et al.*, 1981; *Melendez-Alvira et al.*, 1999) of this reaction is approximately

$$\alpha_{O^+}^* = 7.8 \times 10^{-13} \text{ cm}^3\text{s}^{-1} \quad (T = 1000 \text{ K}) \tag{2.44}$$

although there is some uncertainty (*Tinsley et al.*, 1973). The volume emission rate is then simply

$$I_{7774} = \alpha_{O^+}^* n_e[O^+]. \tag{2.45}$$

There is an additional source of the emission due to a radiative attachment reaction (e.g., *Tinsley et al.*, 1973) but the major source is the one given. Clearly, since near

the $F2$-region peak $[\text{O}^+] \approx n_e$, the emission rate is proportional to the square of the electron density, making the integrated volume emission rate a nice tracer for the peak density. However, the emission is fairly weak, with typical integrated intensities in the range of tens of Rayleighs.

2.3 Instrumentation and Processing

Airglow data presented in this thesis come from two types of airglow measurements. One type of measurement is calibrated, absolute zenith intensities as measured by an imager operated by Boston University at the Arecibo Observatory. The other measurement type is all-sky images taken by cameras operated by Cornell University and using image processing software developed at Cornell. Here we discuss briefly these systems and analysis procedures.

2.3.1 Boston University Imager

This system and processing details have been discussed most recently in *Vlasov et al.* (2005). The Boston University (BU) all-sky imaging system (*Baumgardner et al.*, 1993; *Smith et al.*, 2000) has been operating at Arecibo since May, 2002. It utilizes a bare 1024×1024-pixel charge-coupled device (CCD), thermoelectrically cooled to -50°C. A rotating filterwheel houses up to six narrow-band (1.2-1.8-nm FWHM) filters, three of which record the nighttime mesospheric emissions: $\text{O}(^1S)$ near 96 km in altitude (557.7 nm), Na near 90 km (589.3 nm), and the OH Meinel bands in the near-infrared (695-950 nm) originating from near 87 km. The fourth position has an $\text{O}(^1D)$ filter for 630.0-nm studies of the thermosphere. Of the remaining two, a filter centered at 644.4 nm is used to monitor continuum emission and the other houses a dark filter for calibration purposes. The system can record intensity variations of

less than 0.5-1% of the mean level and has a pixel resolution at 90 km at zenith corresponding to 0.3 km. During multi-emission observing modes, images at each emission wavelength can be obtained sequentially about every 5 minutes. For the data presented later, 557.7-nm images were taken about every 6 minutes and 630.0-nm images were taken about every 30 minutes.

Measured photon counts are converted into Rayleighs using the BU standard analysis, a process that is independent of any other measurements. Several parameters intrinsic to the imaging systems are used in the calibration, including the filter bandwidth and transmission along with the integration time used to obtain the images. Other factors, such as atmospheric absorption of the airglow emission between the layer and the ground, are also accounted for. The imager was shown a C^{14} standard source in which the spectral emissivity in $RÅ^{-1}$ over the visible region was known. As well as providing a standard photometric source, the brightness of the source at various zenith distances in the imager's field of view was measured to derive the off-axis brightness response of the imaging system, i.e., the vignetting function, which drops off with increasing zenith angle. The effect of vignetting was removed by dividing the sky images by the normalized vignetting function.

2.3.2   Cornell University Imagers

The Cornell University imaging systems and software have been discussed in detail in two other theses, *Garcia* (1999) and *Makela* (2003), and we refer the reader to those documents for further details on the airglow instrumentation. Details of the image processing have been discussed in *Garcia et al.* (1997) and *Garcia* (1999). We essentially use the same processing techniques described in those documents, except a new star removal algorithm that is quick and simple is employed. This algorithm works by applying a median filter to the image, creating a "blurred" image (typical
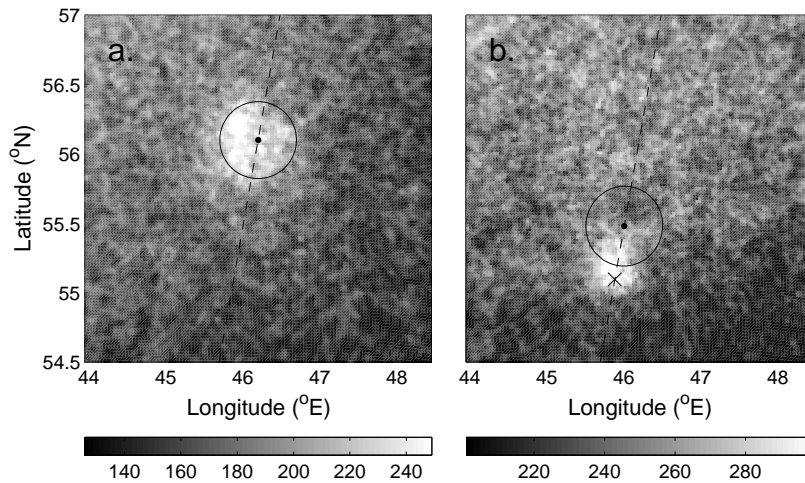
Figure 2.5: Measurements of uncalibrated 630.0-nm intensities at the heating facility in SURA, Russia for two different orientations of the heater beam.

filter widths are 10 pixels by 10 pixels). The algorithm then creates a difference image by subtracting the blurred image from the true image. The algorithm then looks for spikes above a certain threshold, assumes those are stars, and fills those spots in with the blurred image.

An example of the algorithms applied to images is shown in Figure 2.5, which are measurements of the 630.0-nm integrated intensity, unwarped and de-starred but uncalibrated. The measurements are from a heating campaign at the SURA heating facility in Russia during the summer of 2004 (*Kagan et al.*, 2005). The left panel corresponds to the heater beam directed vertically, and the right panel corresponds to the heater beam being directed slightly to the south, along the magnetic meridian.
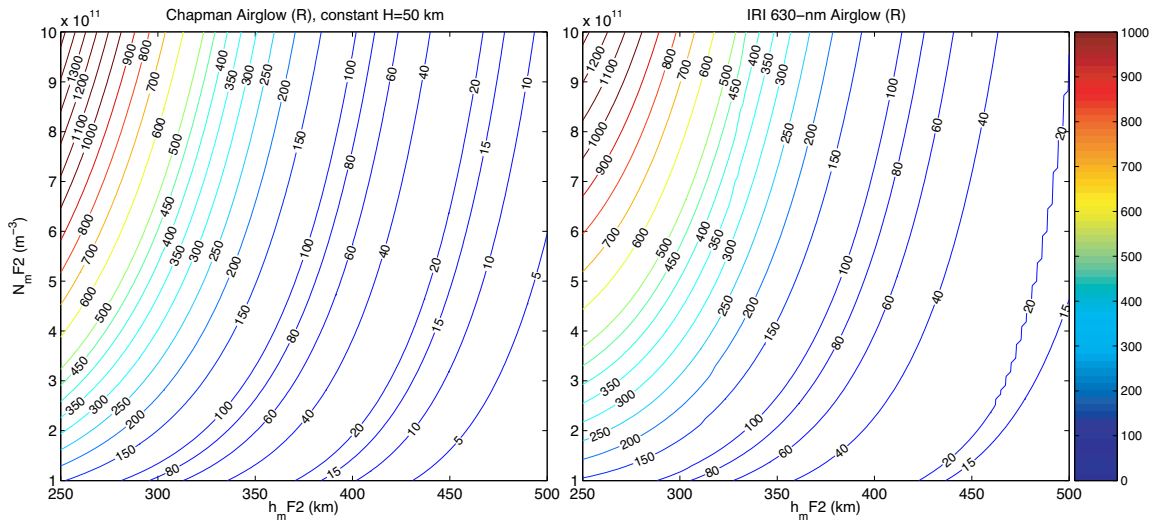
Figure 2.6: Red line intensity contours as a function of h_mF2 and N_mF2 using (left) a Chapman profile with constant scale height and (right) IRI density profiles.

2.4 Airglow Relationship to Ionospheric Parameters

The F-region airglow emissions are good tracers of ionospheric behavior. The red line emission, as we have shown, depends on both the height of the $F2$ layer as well as the density. The 777.4-nm emission depends almost exclusively on the electron density. *Makela et al.* (2001a) was able to successfully combine these two emissions to create topographic maps of the ionosphere.

The left panel of Figure 2.6 shows contours of the integrated red line intensity in Rayleighs as a function of N_mF2 and h_mF2 assuming a Chapman profile for the electron density with scale $H = 50$ km. The right panel shows the same type of plot except using the IRI electron densities. The curves are qualitatively similar. Curves like those shown in Figure 2.6 imply that it may be possible to extract quantitative information about the peak height and density of the ionosphere from integrated red line measurements. Such an approach is beneficial because an all-sky imager has a
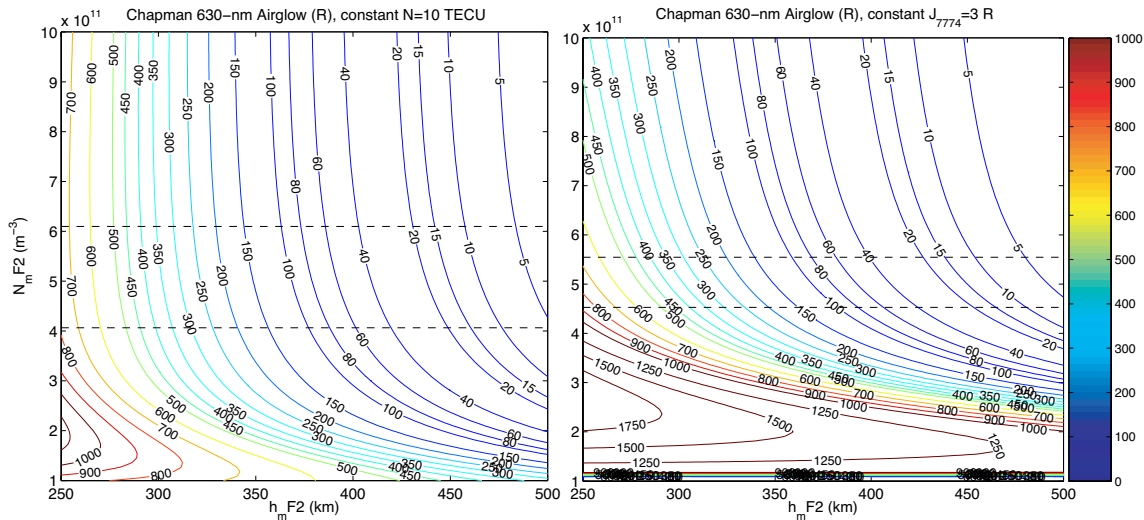
Figure 2.7: Same as Figure 2.6 except for a constant TEC value (left) and a constant 777.4-nm value (right). The dashed lines are Chapman scale heights corresponding to $H=40$ km and $H=60$ km.

field of view of about 1000 km by 1000 km, and the approach can thus give a large-scale view of F-region dynamics. Given a measurement of an integrated red line intensity, the height and density is given by the appropriate contour in Figure 2.6. For high densities, the intensity is nearly independent of h_mF2 and therefore h_mF2 and N_mF2 can be inferred from the measurements.

The approach described in the previous paragraph assumes either a given Chapman scale height or assumes that the IRI profile shape is correct. Both of these assumptions are questionable. Given a measurement of a second ionospheric parameter, this assumption can be relaxed. In Figure 2.7 the same types of curves are plotted except for a given total electron content (TEC) value or a given 777.4-nm intensity value. Thus, given a measurement of either of these parameters, it seems possible to make a plot like those in Figure 2.7 and possibly extract the ionospheric parameters with some uncertainty. An example of this approach will be given in the next section.

2.5 Observations of Zenith Airglow Intensities at Arecibo in October, 2002

This section shows some examples of measurements of zenith airglow measurements made at Arecibo in October of 2002, as presented by *Vlasov et al.* (2005). We consider the nighttime variations of the red and green line intensities together with the variations of the ionospheric parameters under quiet conditions. The typical behavior of the $F2$ region over Arecibo under quiet geomagnetic conditions is characterized by the "midnight collapse" of h_mF2 accompanied by an N_mF2 increase (e.g., *Emery et al.*, 1981; *Crary and Forbes*, 1986; *Macpherson et al.*, 1998). To illustrate these typical variations, in Figure 2.8 we show data from three nights in October, 2002, measured using the Arecibo ISR. Although these were dual-beam experiments, the data shown in Figure 2.8 are from the line feed antenna. The top row of the figure shows color images of the electron density, and the lower two panels show h_mF2 and N_mF2, respectively, smoothed over about 7 minutes. The "striations" that are observed are due to beam-swinging and are the result of fairly typical gradients in electron density over about 150 km in horizontal distance.

All three nights show fairly typical and similar behavior. An h_mF2 increase is seen before midnight, which is caused by an equatorward wind. The altitude of the $F2$ peak must decrease when the equatorward wind decreases and then turns northward. This decrease and wind reversal induces a collapse in h_mF2. One would expect that the h_mF2 fall should induce a decrease in electron density due to the increase in the recombination rate at lower altitudes; however, an increase in electron density is observed temporarily during the period before the decrease (see Figure 2.8). This increase in density is the result of plasmaspheric flux, and will be discussed more in Chapter 3.
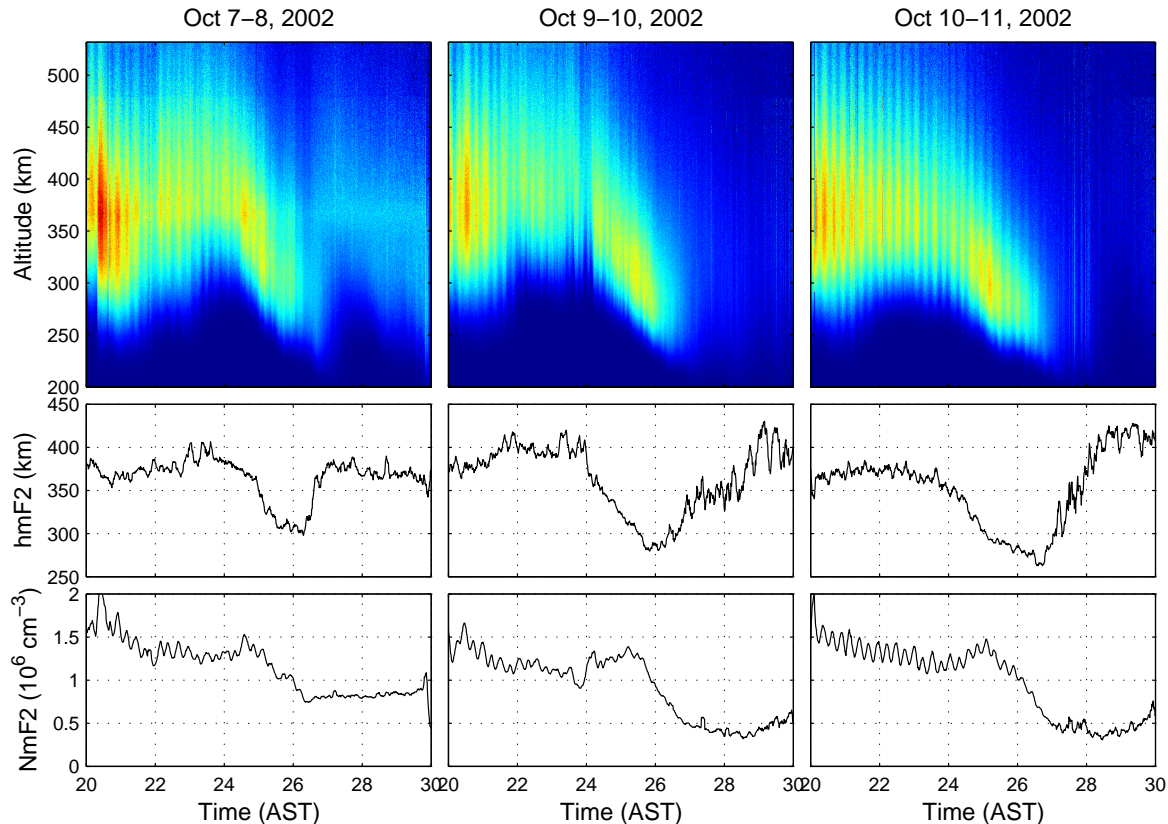
Figure 2.8: Color images of electron density (top) along with variations in $h_m F2$ (middle) and $N_m F2$ (bottom) for three nights in October, 2002.

Using the height profiles of the electron density shown in Figure 2.8, and using the neutral densities from MSIS, it is possible to calculate the typical variations of the red line intensity over Arecibo under quiet geomagnetic conditions for this period. These intensities, calculated for the three nights shown in Figure 2.8, are plotted in Figure 2.9. For the purposes of this plot, we have averaged the electron density over 30 minutes. The "midnight" collapse clearly induces a peak in both the 630.0-nm and 557.7-nm integrated intensities. The 630.0-nm intensity peaks about 0200 LT at an intensity of 500-600 R, at which time the 557.7-nm intensity peaks near 150 R.

The red and green line intensities measured by the BU imager during several nights between October 1 and 11 are shown in Figure 2.10. Also plotted in gray are
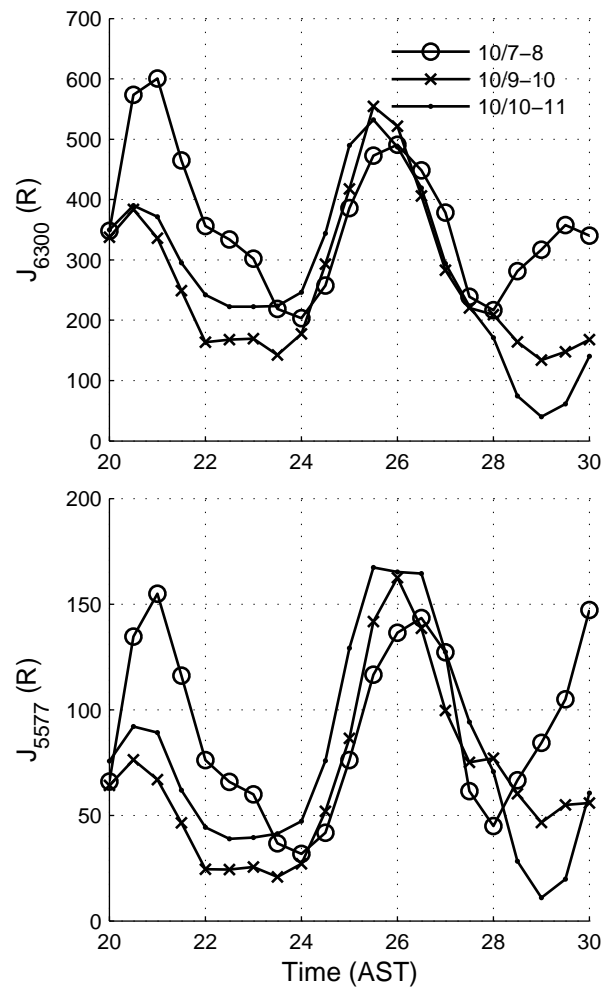
Figure 2.9: Red and green line intensities calculated by Equations 2.19 and 2.21 using the electron densities shown in Figure 2.8 for three nights in October, 2002.
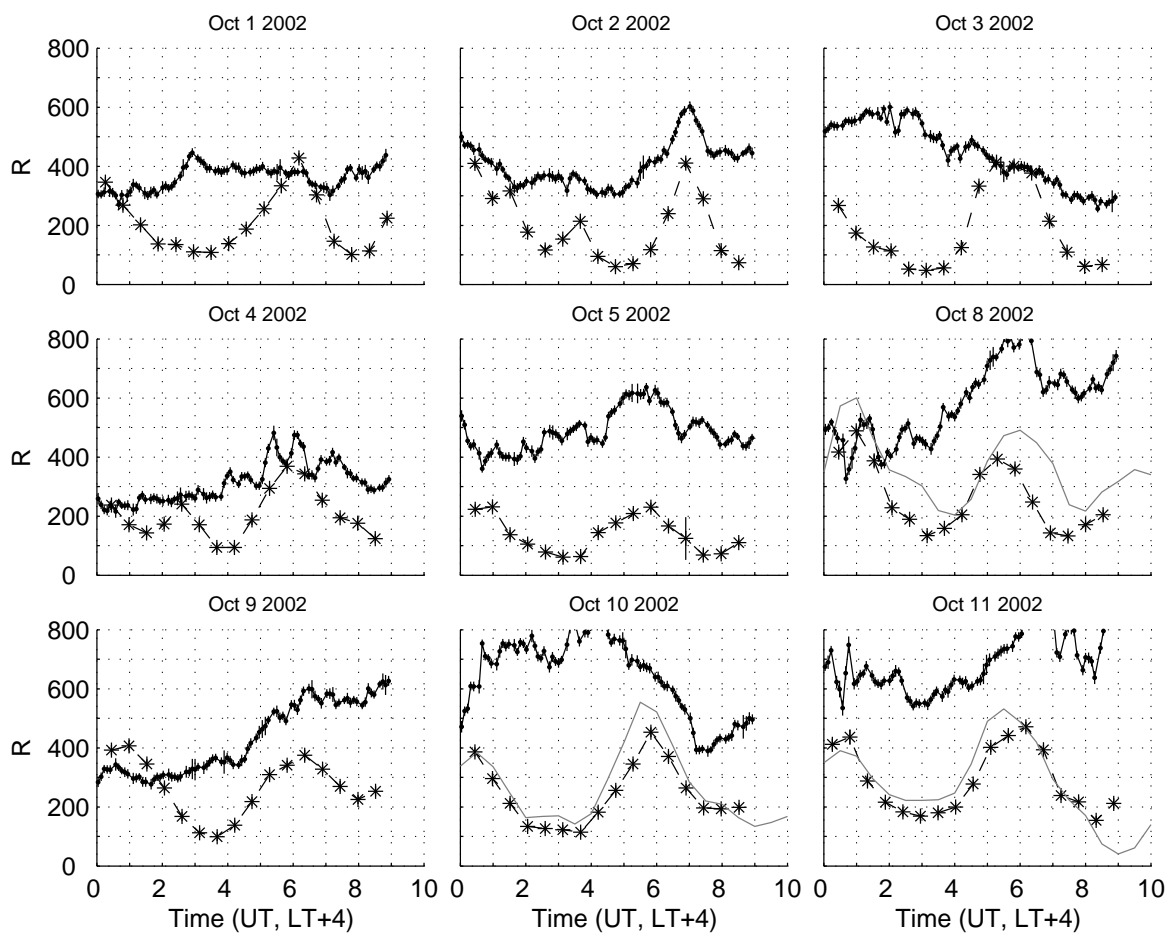
Figure 2.10: Intensities of the red (dashed, stars) and green lines (solid) measured by the BU imager during several nights in October 2002. The gray lines in three of the plots correspond to the 630.0-nm model calculations of Figure 2.9.

the red line calculations for the three nights (October 7-8, 9-10, and 10-11) shown in Figures 2.8 and 2.9. The comparisons between the measured and calculated results show generally very good agreement, especially on the last two nights. As can be seen by comparing the intensities measured on different nights in Figure 2.10, the red line behavior over Arecibo during the whole period is, in general, similar to the behavior indicated in Figure 2.9. These typical variations are characterized by a minimum before midnight and a maximum after midnight. This behavior is the result of the typical h_mF2 and N_mF2 variations shown in Figure 2.8. The green line intensity is quite variable, but from the calculations shown in Figure 2.9 and the observations shown in Figure 2.10 it seems as though about 15-25% of the emission is coming from the F region. The bulk of the emission is a result of the mesospheric radiation. The absolute green line intensities are quite high as compared to previously published results (e.g., *Schubert et al.*, 1999). We should note a potential source of error in the calibration procedure that could lead to an overestimate of the green line intensity. The method requires knowledge of the continuum levels at 557.7 nm and the off-band (644.4 nm) wavelength. The off-band filter was originally chosen for 630.0-nm work, and is about 850 Å away from the 557.7-nm line. The continuum is not constant over this range, and the calibration procedure uses the most recently obtained ratio between the continuum value at 630.0 nm and that at 557.7 nm to calibrate the green line measurements. This ratio was obtained at the Millstone Hill Observatory, and if the ratio is different at lower latitudes, then this could explain intensity values that are higher than expected.

It is easy to estimate the influence of N_mF2 on the red line intensity because the red line intensity is proportional to electron density, according to Equation 2.19. The influence of h_mF2 is more complicated because it depends on the neutral composition. An example of an approach to estimate h_mF2 and N_mF2 from the measured airglow

on October 9-10 is shown in Figure 2.11 using the methodology described in the previous section. Here, we used vertical TEC computed from the dual-frequency GPS station at St. Croix (17.75°N, 64.58°W) to constrain the density, along with normalized IRI density profiles. We have also plotted the measured parameters from Figure 2.8, and we see good agreement between the values derived from the airglow data and the measured results, especially for h_mF2. In fact, it seems likely that the discrepancy is in large part due to the fact that the GPS station is a couple of hundred kilometers away from Arecibo and the method of computing vertical TEC is complicated by the estimated receiver bias and the thin-shell ionosphere assumption. Because there is a trade-off between the effects of the density and the height, an error in one (namely, TEC) will cause an error in the estimated height as h_mF2 is adjusted to match the observed intensity. The dashed line in this figure shows the IRI-predicted parameters, and we see that the midnight collapse is not reproduced by that model; there is little h_mF2 collapse and no N_mF2 increase.

On some nights (for example, October 4-5, 2002), the peak of the red line intensity does not exceed 200 R during the midnight collapse (see Figure 2.10). In such cases, it seems that the N_mF2 variation (increase) is not present or not as large. On other nights, when the peak of the red line intensity reaches over 400 R, an N_mF2 increase, together with an h_mF2 collapse, is needed to obtain the observed intensities. For example, the variations of the red line intensity observed on the night of October 8-9 correspond to $N_mF2=3.5\times10^5$ cm^{-3} and $h_mF2=320$ km at 0300 UT; $N_mF2=5.5\times10^5$ cm^{-3} and $h_mF2=300$ km at 0500 UT; $NmF2=6.6\times10^5$ cm^{-3} and $h_mF2=280$ km at 0700 UT. Thus, the peak of the red line intensity regularly observed after midnight is a result of a collapse in h_mF2, together with either an increase in N_mF2 or the maintenance of a high N_mF2 value. Neither a collapse in h_mF2 nor an increase in N_mF2 alone can provide intensities higher than the 300-400 R typically observed.
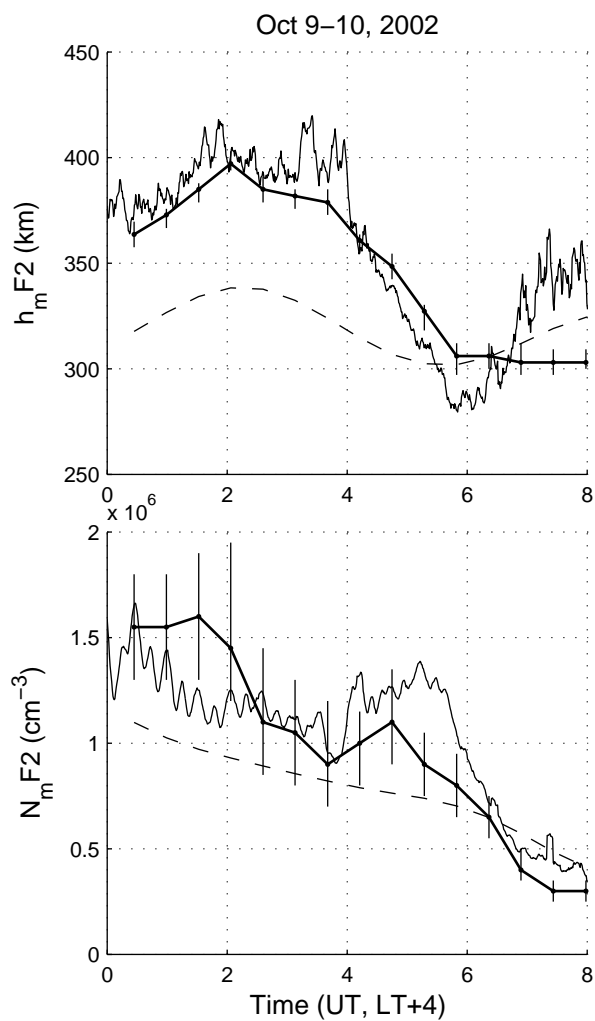
Figure 2.11: Inferred h_mF2 (upper) and N_mF2 (lower) from the airglow intensities on the night of October 9-10, 2002. TEC information (from GPS) and IRI profile shapes were used to help constrain the problem. The dashed lines in each plot correspond to the IRI values for these conditions.

2.6   Conclusions

In this chapter, we have presented our models for the airglow intensities, discussed briefly the instrumentation necessary for making those measurements, and showed some examples of measurements from the Arecibo Observatory made in October 2002, as discussed in detail in *Vlasov et al.* (2005).

The main feature of the ionospheric behavior, inferred from the emission data from nights in October 2002 and shown by ISR measurements, is an N_mF2 increase in conjunction with an h_mF2 decrease near midnight. According to the modern theory of the $F2$ region, the nighttime electron density is maintained by plasma flux from the plasmasphere, which provides a slower decrease in electron density in comparison with loss due to recombination.

Similarly, the variations of the red line intensity measured during nights in October 2002 are characterized by a minimum before midnight and a peak after midnight under quiet geomagnetic conditions. The calculations indicate that these variations correspond to a decrease in the electron density together with an increase in h_mF2 after sunset, followed by a peak in electron density together with a collapse in h_mF2 after midnight. This behavior has been observed often over Arecibo. Taking into account these features of the nighttime variations of the ionospheric parameters, it becomes possible to infer N_mF2 and h_mF2 values from the measured intensities.

Acknowledgements

Chapter 3

Multi-Instrument Study of a Large-Scale Traveling Ionospheric Disturbance*

The ships hung in the sky in much the same way that bricks don't.
   - Douglas Adams, in The Hitchhiker's Guide to the Galaxy

3.1   Abstract

On October 1-2 2002, a moderate magnetic storm took place with the 3-hour K_p index exceeding 5^- for 24 hours and reaching 7^+ twice. The Arecibo incoherent-scatter radar (ISR) operated through the night and recorded remarkable activity in the overhead ionosphere, which we report in this chapter. The Arecibo data, when combined with all-sky airglow observations in the Puerto Rican and Hawaiian sectors, ionosonde measurements in North and South America, total electron content data,

---

*Some of this chapter has been adapted from the published works, *Nicolls et al.* (2004), *Nicolls and Kelley* (2005), and *Vlasov et al.* (2005). Reproduced by permission of the American Geophysical Union.

and magnetometer and satellite recordings, provide excellent coverage of a global disturbance that modulated the Arecibo ionosphere over 150 km and provided a source for mid-latitude and equatorial instabilities (spread F). We report 630.0-nm and 557.7-nm airglow enhancements of over 300 R in 2 hours, which we show can be explained by the ionospheric disturbance and can give insight into the neutral density perturbation associated with the traveling atmospheric disturbance. We provide evidence that the generation of the disturbances is caused by the atmospheric response to periodic westward current enhancements in the high latitude ionosphere associated with a series of periodic substorms. We explore the gravity wave features of the thermospheric disturbances and report a horizontal phase velocity of around 750 m/s. We also investigate the dynamics of the local ionosphere on this night.

3.2   Introduction

Auroral currents and precipitating particles are an important energy source in the polar region. During magnetic storms, associated with intense magnetospheric energy inputs, enhanced atmospheric heating in the auroral zone can set up large amplitude atmospheric gravity waves (AGWs), which travel equatorward in the form of traveling atmospheric disturbances (TADs) in the lower atmosphere or thermosphere, caused by the thermal expansion of the neutral atmosphere. TADs are manifested in the ionosphere as traveling ionospheric disturbances (TIDs), suggested first by *Hines* (1960), and are formed in the polar atmosphere through direct heat deposition from precipitating particles or fluctuations in the auroral electrojet. This latter mechanism leads to the dissipation of energy via Joule heating or Lorentz forcing, and is in general more important than the direct effects of precipitating particles (e.g., *Fuller-Rowell et al.*, 1997; *Hunsucker*, 1982). However, the dominance of either the Joule or Lorentz

mechanisms is not as clear, as demonstrated in early modeling studies by, for example, *Chimonas and Hines* (1970). Waves produced by Joule heating, however, have been shown to be more effective in propagating to low latitudes (*Richmond*, 1979), although other results suggest that the Lorentz term should be the most dominant except in very strong storm conditions (*Hunsucker*, 1982). Joule heating is generated via ionization in the auroral region causing enhanced conductivity in conjunction with electric fields of magnetospheric origin. In the Lorentz case, electric fields set the plasma into motion and this momentum is transferred into the neutral atmosphere through collisions, which can cause intense wind surges and neutral heating through viscous forcing. Recent reviews on magnetic storms include *Buonsanto* (1999), *Fuller-Rowell et al.* (1997), *Prölss* (1997), and *Rees* (1995).

Low and mid-latitude disturbances are created by the transport of energy from high latitudes, in the form of TADs and changes in global wind patterns (*Prölss*, 1997). According to models, TADs are created during substorms and propagate at very high velocities to lower latitudes. The wind perturbations that accompany them, typically an equatorward then poleward wind enhancement, can lead to compression and heating of the low and mid-latitude ionosphere, causing plasma motion along the field lines. The perturbations are more effective during the nighttime because they add to the background circulation (*Buonsanto*, 1999) and because of dissipation on the dayside due to enhanced ion drag (*Fuller-Rowell et al.*, 1997). The AGWs can in principle be observed as fluctuations in the neutral constituents, but in reality are studied indirectly through ionospheric fluctuations. Changes in N_mF2 and h_mF2 can be detected using ionosondes or incoherent scatter radars (ISRs), total electron content (TEC) variations deduced using GPS receivers, or airglow fluctuations using imagers. Two relatively recent reviews on AGWs and TIDs generated in the high latitude ionosphere are *Hocke and Schlegel* (1996) and *Hunsucker* (1982). The quasi-

periodic nature of some observed TID events have been normally associated with either a periodic source (i.e., a series of bursts) that leads to gravity waves with the same periodicity (and possibly resonance) or a single source whose impulse response generates a train of waves (e.g., *Hocke and Schlegel*, 1996; *Lewis et al.*, 1996).

AGWs are characterized by large periods, which can be in excess of 3 hours, and large wavelengths, greater than 100 km, so that the buoyancy, inertial, gravitational, and pressure gradient forces are all important (*Hocke and Schlegel*, 1996). The TADs/TIDs associated with AGWs can be classified into groups based on velocity and period. Large-scale TIDs, propagating in the thermosphere, have velocities in the range 400-1000 m/s, scale sizes greater than 1000 km, and periods from 30 minutes to several hours (*Hocke and Schlegel*, 1996). Large-scale disturbances in the presence of gravity wave activity have been observed at Arecibo (e.g., *Harper*, 1972; *Thome*, 1966, 1968) and other mid-latitude stations (e.g., St. Santin, by *Testud and Vasseur*, 1969), manifesting themselves as temperature fluctuations on the order of 50-100 K in association with ion velocity, plasma density, and altitude perturbations. Recently, *Shiokawa et al.* (2002, 2003), using an impressive array of instrumentation including the MU radar in Japan, observed large-scale TIDs associated with storm-time activity, manifested as airglow enhancements, intense poleward wind pulsations, and TEC fluctuations. These authors attempted to locate the source of the TIDs associated with a Joule heating enhancement in the Northern Hemisphere using the assimilative mapping of ionospheric electrodynamics (AMIE) technique, however they could not conclusively state the causative mechanism. *Ho et al.* (1996, 1998) have used the global GPS network to make a global map of large-scale TIDs, and *Tsugawa et al.* (2003) recently studied the damping of large-scale TIDs using GPS TEC, concluding that ion drag is the most important dissipative mechanism.

Many attempts to numerically model the large-scale TIDs have been made since

the early 70's (e.g., *Richmond*, 1978, 1979; *Richmond and Matsushita*, 1975). *Richmond and Matsushita* (1975) modeled the thermospheric response to a 2-hour magnetic substorm using a plasma density enhancement in the auroral E region, which led to strong Joule heating. The energetic particles that caused the increased ionization were also modeled to add heat to the neutral atmosphere in a manner proportional to the density perturbation and inversely proportional to the neutral gas density. An interesting feature of the simulation was the generation of thermospheric disturbances propagating both poleward and equatorward at a speed of roughly 750 m/s. The model calculations showed good qualitative agreement with the Arecibo data of *Harper* (1972). More advanced numerical models have since been developed (e.g., *Fuller-Rowell et al.*, 1994, 1996, 1997; *Millward et al.*, 1993a,b) which shed light on ionospheric storm effects and on the global thermospheric wind response, including seasonal, daytime-nighttime, and hemispheric differences, in addition to the transport of "composition bulges" equatorward. Another interesting result of these simulations is low and mid-latitude behavior when the wind surges from the two poles interact, as the responses of the two poles can be quite different. We should note that modeling studies to illustrate the different causative mechanisms in the formation of TIDs - including AGWs (TADs), particle precipitation fluctuations, ionospheric return currents, and disturbed plasma convection patterns - have also been performed (e.g., *Kirchengast*, 1996, 1997), emphasizing that while the AGW-TID relationship is indisputable, other mechanisms for the generation of TIDs also exist with different tracers in ionospheric data.

There have not been very many low and mid-latitude observations of the vertical structure of large-scale TIDs, nor have there been many airglow and GPS observations. In this chapter, we show results from a multi-period TID event that the Arecibo ISR recorded during a magnetic storm on the night of October 1-2, 2002, and show

evidence for AGWs as the causative mechanism of the TID. We use TEC maps of North America, ionosonde observations, and airglow data from the Hawaiian sector to characterize the scale size and speed of the equatorward propagating TIDs. Airglow data from the Arecibo Observatory show enhancements relating to the storm in both the $O(^1D)$ (630.0-nm) and $O(^1S)$ (557.7-nm) airglow emissions. These enhancements are consistent with the passage of the large-scale gravity wave, as we discuss. Our observations are quite similar to those of *Shiokawa et al.* (2002, 2003) of large-scale TIDs, and, like in those works, can be related to equatorward and poleward wind enhancements. We further consider possible sources of the TID in the high latitude region using the AMIE technique. We also show that the TID event contributed to mid-latitude and equatorial spread F, demonstrating that such events can drive plasma instabilities at low latitudes.

3.3   Geomagnetic Conditions on October 1-2, 2002

Conditions during the first two days of October 2002 are indicated in Figure 3.1, where we have plotted the K_p and D_{st} indices, the $\hat{z}$-component of the IMF as measured by the ACE satellite, the northward magnetic field component measured by the GOES-8 satellite, and a representative auroral zone magnetometer signal obtained in Leirvogur, Iceland. D_{st} and K_p indicate that a storm commenced mid-day on October 1st, and that a series of substorms took place until early morning on the 2nd when the recovery phase commenced. The D_{st} reached around -175 nT and the K_p peaked at 7^+, reaching that level twice. B_z went southward at about 0800 UT on the 1st until about 0800 UT on the 2nd.

The GOES-8 satellite is relevant to the Puerto Rican sector since it is in a geosynchronous orbit at a longitude of about 75°W. Typical values of H_p are about 100 nT,
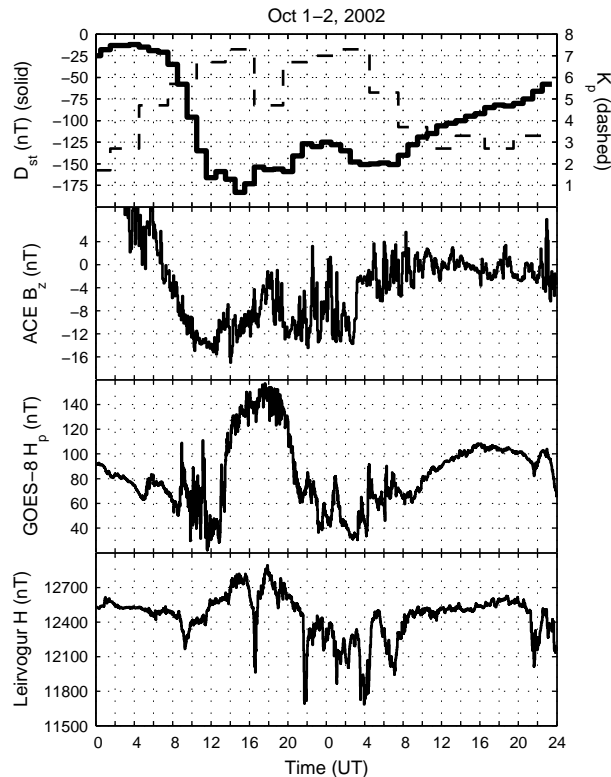
Figure 3.1: Geomagnetic indices and fields: K_p and D_{st} (top), B_z from the ACE satellite (second), the northward component of B measured by the GOES-8 satellite (third), and the H component at Leirvogur, Iceland (bottom).

so during the storm we see about 50 nT oscillations about this value. When the oscillation is in the negative direction (i.e. less than 100 nT), this implies that the tail of the Earth's magnetic field has become extended, and we see a corresponding enhancement (meaning negative trend) in the D_{st} associated with a ring current build-up and increased energy input into the high latitude region (*Kelley*, 1989). This peaks at around 1300 UT on the 1st at the pinnacle of the storm, when the energy is released via Poynting flux towards the Earth. Energy build-up began again at about 2000 UT on the 1st and this energy was released through a series of substorms evident in the Leirvogur and GOES data.

In addition, according to images from the UV imager on POLAR, auroral activity was very dynamic with expansion down to lower than 60° at some times. Particle pre-

cipitation data from POES shows intense, fluctuating activity at these low latitudes (D. Evans, personal communication, 2003).

The Arecibo ISR observations described in this paper were during the night of October 1-2, local time, or about 0000-1200 UT on October 2nd. This is many hours after the commencement of the storm, during the period of high substorm activity, which is good timing because of the propagation time for TIDs from high to low latitudes. Arecibo airglow observations were made during a similar time range, whereas Hawaiian airglow observations were made from about 0500-1500 UT on the 2nd. Ionosonde and TEC observations are of course theoretically available for all local times.

3.4 Evidence for a Large-Scale TID in Arecibo ISR Observations

On October 1-2, 2002, the Arecibo ISR was operating in the TOPSIDE mode (see *González et al.* (2004) for details), which gives plasma parameters, including densities, light-ion composition, and electron and ion temperatures up to very high altitudes (~ 2500 km) with $\sim$38-km altitude resolution and several-minute time resolution. In addition, raw power profiles were taken, which give E- and F-region electron densities with about 10-second time resolution and 600-m altitude resolution from about 60 to 520 km. During this experiment, the radar remained in the vertical position, with data only being taken by the line feed antenna, and hence the line-of-sight velocity measurements reflect vertical motions and cannot be resolved into vector drifts as can be done during beam-swinging experiments. The density data were carefully corrected for range-squared variations and near-field gain effects, and calibrated using an on-site ionosonde. However, the ionosonde did not operate properly for the bulk
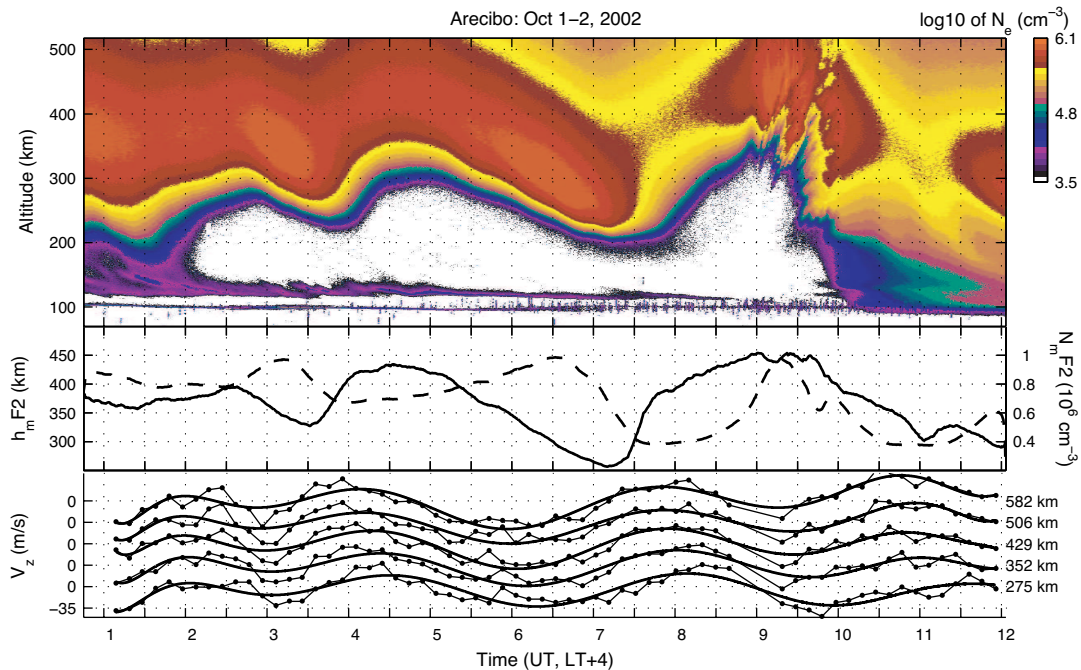
Figure 3.2: Summary of Arecibo ISR data for the night of October 1-2, 2002. The top panel is $\log_{10}$ of electron density, the middle panel is $h_m F2$ (solid) and $N_m F2$ (dashed), smoothed over 12 minutes, and the bottom panel is vertical ion velocity (points) with polynomial fits (solid). The tick marks in the V_z panel are separated by 35 m/s.

of the night, nor did the digisonde located in nearby Ramey, Puerto Rico. Only one or two points over the course of the night were able to be used for the calibration, and thus there is likely a rather high error in the calibrated peak density, which we estimate to be around 20-30%. The relative density variations should be unaffected. Airglow modeling results and TEC comparisons, however, imply that the calibration is consistent with other datasets.

Observations of the plasma density as a function of height and time from the Arecibo ISR are presented in Figure 3.2, along with line plots of $h_m F2$ and $N_m F2$ (middle panel). At least three and possibly four oscillations of the F layer were recorded on this evening with the final one near dawn driving the F peak to nearly 450 km. Unlike the previous cycles, this final uplift resulted in violent height oscillations

with very short periods. The long-period component of the signal, about 3 hours, is well within the gravity wave regime, but the pre-dawn high frequency components exceed the Brunt-Vaisala frequency and are likely associated with plasma instabilities rather than neutral atmospheric waves. Although ionosonde data is not available in the Puerto Rican sector, it is certain that such an instrument would have recorded mid-latitude spread F between 0800 and 1000 UT (0400 to 0600 LT).

Although the oscillatory behavior shown in Figure 3.2 certainly suggests a gravity wave wind field, the possibility of penetrating electric fields associated with rapid changes of the high latitude fields and currents must be discussed. Indeed, there was a magnetic substorm lasting about an hour over Iceland with a magnetic perturbation exceeding 500 nT beginning at about 0300 UT (see lower panel of Figure 3.1). This is a bit earlier than the second rapid uplift of the base of the F layer over Arecibo which began at about 0330 UT. But, more crucial is the fact that the magnetosphere was very quiet in the time period from 0800 UT to 1200 UT when the most severe oscillation of the F layer occurred over Arecibo. It is very unlikely that penetrating electric fields caused the observed ionospheric behavior and for the remainder of this chapter we explore the effects of high latitude energy and momentum input and the launching of atmospheric waves into the atmosphere as the primary cause for the disturbed low latitude activity on this night.

Evidence for the role of gravity waves in generating these periodicities is presented in the lower panel of Figure 3.2, where we show the vertical ion velocity as a function of time and altitude. Oscillations in the velocity at the same 3-4 hour period can be seen, and a clear downward phase progression occurs. The wave phase at higher altitudes is expected to precede the phase at lower altitudes (e.g., *Richmond*, 1978). Also included in this plot are polynomial fits to the curves from 0230 to 1000 UT. In order to estimate the vertical phase velocity, we cross-correlate the velocities from the

polynomial fits from the height ranges shown in Figure 3.2. Inspection of the plasma-density data in Figure 3.2 also indicates a downward phase progression of iso-density contours, although these are much more difficult to interpret. The velocity analysis yields a downward phase progression of 200-300 m/s. The pulse around 0400 UT appears to have a higher downward phase velocity then the pulse at around 0800 UT, and also a shorter period. These differences must be associated with either changes in the source or dissipative effects. These phase velocities and frequencies (periods of 2.5-4 hours) yield a vertical wavelength of several thousand kilometers, which is many times the atmospheric scale height, H. Such large vertical wavelengths have been observed at Arecibo before (e.g., *Miller*, 1996; *Thome*, 1968) and are thought to be due to the high viscocity of the thermosphere which acts to surpress vertical variations.

The full linearized dispersion relation for AGWs can be written as (e.g., *Andrews et al.*, 1987; *Garcia*, 1999)

$$\frac{\omega^2}{c^2} - \left(\frac{N_b^2 - \omega^2}{f_{cor}^2 - \omega^2}\right) k_x^2 - k_z^2 - \frac{1}{4H^2} = 0 \qquad (3.1)$$

where $N_b = \frac{R_g g}{H C_p} = \frac{2\pi}{\tau_b}$ is the Brunt-Vaisala frequency assuming that the temperature is constant with altitude; $c = \sqrt{\gamma R_g T_n}$ is the speed of sound; f_{cor} is the Coriolis term, equal to $2\Omega \sin\theta$ where Ω is the rotational frequency of the Earth and θ is latitude; $R_g = 287$ Jkg^{-1}K^{-1} is the real gas constant, g is gravity, $\gamma = C_p/C_v \approx 1.402$ is the heat capacity ratio, and $C_p = 1005$ Jkg^{-1}K^{-1} is the specific heat capacity at constant pressure; k_x and k_z are the horizontal and vertical wavenumbers, respectively ($k_{x,z} = \frac{2\pi}{\lambda_{x,z}}$); and $H = \frac{k_b T_n}{mg}$ is the neutral scale height where k_b is Boltzmann's constant, T_n is neutral temperature, and m is mass. If we take the atmosphere to be incompressible ($c^2 \to \infty$), then we get the relation

$$\omega^2 = \frac{N_b^2 k_x^2 + (k_z^2 + \frac{1}{4H^2}) f_{cor}^2}{k_z^2 + k_x^2 + \frac{1}{4H^2}}. \qquad (3.2)$$

The Coriolis term for large-scale waves may be important, but let us proceed by assuming we can neglect it, attributing this to the relatively high frequency of the oscillations observed ($\omega \gg f_{cor}$). Then,

$$\omega^2 = \frac{N_b^2 k_x^2}{k_z^2 + k_x^2 + \frac{1}{4H^2}}. \tag{3.3}$$

For $\lambda_z, \lambda_x \gg H$ and $\omega \ll N_b$ we find

$$\frac{\omega}{k_x} = 2N_b H = \sqrt{2gH}. \tag{3.4}$$

This result is very reminiscent of shallow water and tidal waves in which the phase velocity depends on the square root of the depth of the water. Substituting for N_b corresponding to a 16-minute period and H=59 km yields a phase velocity of 772 m/s, which is quite similar to that found by data and models (e.g., *Harper*, 1972; *Richmond and Matsushita*, 1975; *Thome*, 1968), generally in the range of velocities 400-1000 m/s (*Hocke and Schlegel*, 1996). The phase velocity components found in the analysis are such that the Doppler shift due to a mean wind is negligible. If we naively solve Equation 3.4 for λ_x using a two-hour period, then the horizontal wavelength comes out to quite a large value, about 6000 km, or around 50° latitude. This number may be unreasonably large. For reference, the simulation by *Richmond and Matsushita* (1975) resulted in a horizontal wavelength of 30° latitude (3300 km), so our simple estimate is not completely outrageous.

3.5   North American TEC Observations

We turn now to TEC observations from the North and South American GPS network, consisting of over 500 receivers (*Coster et al.*, 2003). Slant TEC (STEC) is computed for each observation after individual receiver and satellite biases have been removed. GPS satellite biases are calculated by JPL and GPS receiver biases are estimated

as described in *Sardon et al.* (1994) and *Wilson et al.* (1999). STEC is converted to vertical TEC (VTEC) using a simple mapping function that assumes a thin-shell ionosphere at 350 km. A pierce-point position (latitude and longitude) of the satellite track at 350 km is also computed. Data are available with a time resolution from 30-60 s, and data over 5 minutes are used to produce a single map. The data are binned into uniformly gridded 1° latitude and longitude bins. There are typically tens to several hundred points in a single bin in a 5-minute map, with the highest numbers over the continental US.

Because ISRs give electron densities as a function of time and altitude, it is possible to compute the ISR TEC and compare this to the VTEC from GPS at a nearby station. In some cases, however, it may be difficult to separate ionospheric spatial gradients from local changes in density over the observing station. One must be cautious of this effect if one wishes to compare absolute TEC, and alternate procedures may be needed to study perturbations (e.g., *Makela et al.*, 2000, 2001b). Indeed, the TEC perturbation (TECP) at mid-latitudes caused by the ionospheric fluctuations associated with the neutral wind of a large-scale TAD is not expected to be large. As the F layer falls (poleward wind) the peak density increases temporarily (Figure 3.2 shows a factor of ∼2 peak-to-peak density change) due to strong plasmaspheric flux. But, the layer also becomes narrower (due to recombination), so there is expected to be little variation in TEC. In fact, the observations described below show a nighttime TECP of ∼1-2 TECU (1 TECU=10^{16} el/m^2). We can conclude that any attempt to compare absolute TEC will not be useful in examining the perturbations associated with the TID since the TECP is quite small and could be lost in errors in the biases or in spatial gradients, making the conversion from STEC to VTEC error prone.

Instead, we use a method similar to that described in *Saito et al.* (1998) which was used to study TECP over Japan. This was successfully applied by *Shiokawa et al.*

(2002, 2003) and *Tsugawa et al.* (2003) to study large-scale TIDs. *Ho et al.* (1996) have looked at global TEC perturbations, however they used a significantly different method with much lower temporal and spatial resolution. Our method detrends the VTEC data by subtracting a 4-hour running average in each latitude-longitude bin thus producing a map of the TECP. The technique differs from that of *Saito et al.* (1998), who detrend the STEC before mapping. Here, we make the VTEC map and detrend the mapped values. As long as the bias estimation has little error, we expect our method to produce better results (smaller error) with shorter processing time.

The TECP is a useful method for studying the horizontal structure of the TID. To reiterate, the logic for the method is as follows. As a TAD, characterized by wind pulses, propagates at low and mid-latitudes, it drives the ionosphere up (equatorward wind pulse) and down (poleward wind pulse). As the layer falls, one would expect the density to decrease due to enhanced recombination at the lower altitudes. However, the layer motion induces an increase in plasmaspheric pressure, causing flux from the plasmasphere. Depending on the magnitude of this flux, a density enhancement and perhaps a TEC enhancement can be observed. The source of this flux is an interesting problem. Large fluxes have been observed at Arecibo before (e.g., *Vlasov et al.*, 2003) and were required to explain the observed density fluctuations. On October 1-2, 2002, when the layer falls, we see large density enhancements (see Figure 3.2). The source of this density must be downward plasmaspheric flux, and we will show that this plasma can be supplied to the plasmasphere during the equatorward wind phase of the TAD.

In the top panel of Figure 3.3, we show the VTEC from the St. Croix site (17.76°N, 295.32°E), about 250 km from Arecibo. We have plotted the data from the 1st to the 2nd to show the markedly different TEC behavior on the two days, indicating a negative ionospheric storm on the 2nd. Increased density and height gradients,
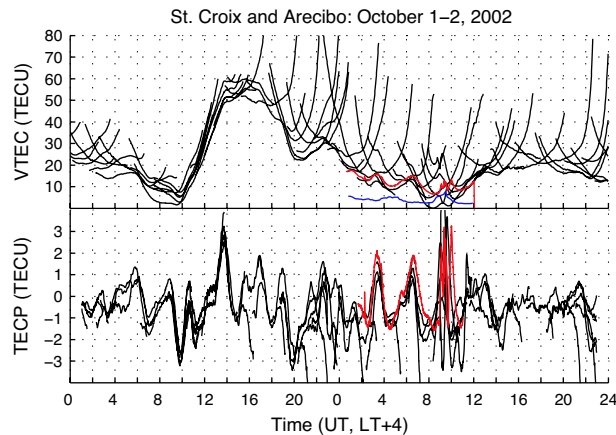
Figure 3.3: The top panel shows St. Croix VTEC from GPS for all receiver-satellite pairs (black) and the TEC calculated from Arecibo ISR data below 520 km (red) and from 500-1000 km (blue). The bottom panel shows the TEC perturbation for GPS (black) and Arecibo (red).

characteristic of a TID passage or other anomalies (e.g., *Foster et al.*, 2002), occur during the storm period, as seen in the VTEC after storm commencement ($\sim$1300 UT) that show the characteristic STEC "u" shape. Overplotted (red curve) is the TEC calculated from Arecibo ISR power profile data on October 2nd, i.e. up to 520 km. Note that we have not normalized the St. Croix TEC to the ISR data, so the two datasets independently show excellent agreement. We should note that there may at some times be significant TEC above 520 km, which has been observed at higher latitude ISRs such as Millstone Hill (*Coster et al.*, 2003). We have estimated the TEC from 500-1000 km and 1000-2000 km using the topside data on this night. The former contribution is plotted in blue and is generally $\leq$5 TECU, except near 0500 UT and 0930 UT on the 2nd when we see an increase to $\sim$7-8 TECU. This behavior is interesting in that the increases correspond to a TEC decrease in the F region, and we discuss this more later. The TEC contribution from 1000-2000 km is not included but it is small, $\leq$1 TECU.

In the lower panel of Figure 3.3, we show the TECP calculated from the GPS data.
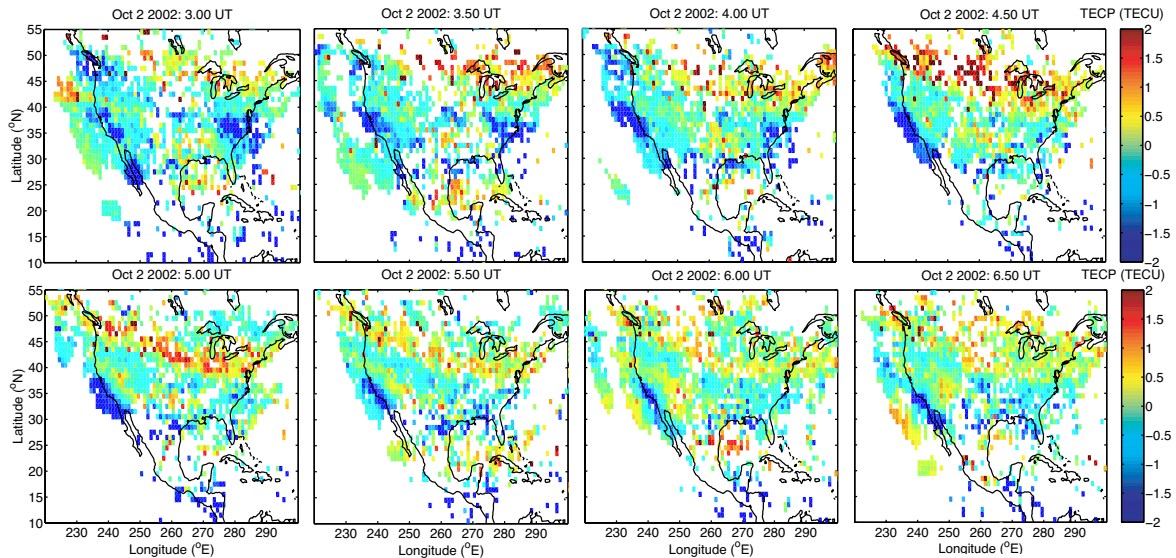
Figure 3.4: Examples of TECP images produced by the GPS mapping technique described in the text.

Overplotted in red is the TECP calculated from Arecibo data using the same running average technique. The datasets are in good agreement, within ∼0.1 TECU for all the oscillations save the last one. We see positive perturbations corresponding to the times when the layer falls (and the densities increase) of 1-2 TECU. This is consistent with the TECP observed by *Shiokawa et al.* (2002, 2003). The outlying points are a result of satellites whose ionospheric pierce-points do not encounter the TIDs, again indicative of gradients associated with the TID passage. We must be cautious in interpreting all TECP fluctuations as a disturbance. For example, midday on the 1st we see large perturbations that appear to be associated with the typical density enhancements at sunrise.

In Figure 3.4 we show sample TECP images over North America, computed using the method described above. The data shown are from 0300-0630 UT where we have plotted every 6th image (every 30 minutes). A positive TECP band at ∼40-50° N (∼50-60° geomagnetic) is seen developing during this period which we speculate may be associated with increased auroral activity ($D_{st} \approx 150$ nT, $K_p = 7^+$). The negative
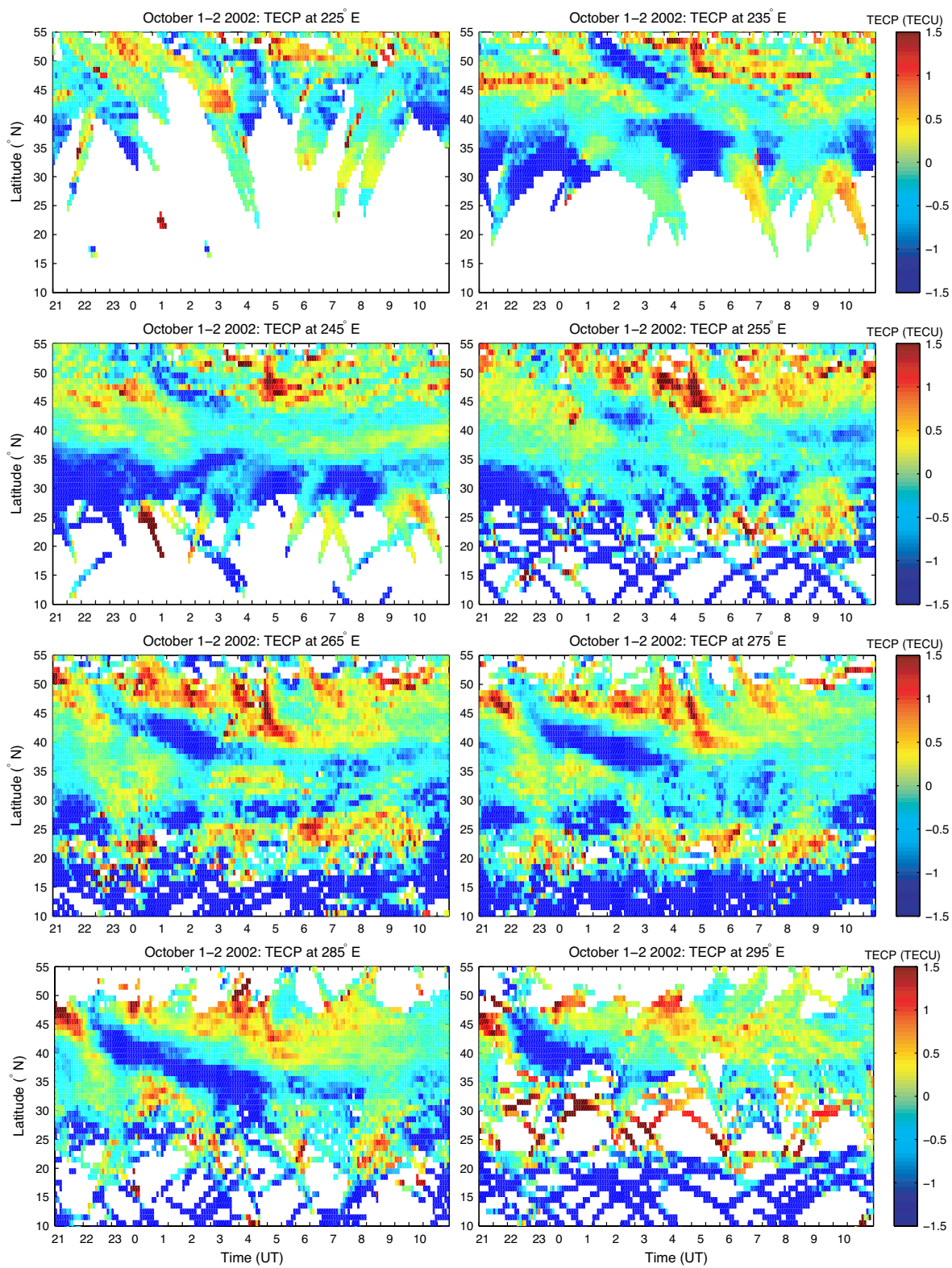
Figure 3.5: TECP as a function of latitude and time for 5 different longitudes over North America. The images represent $\pm 5°$ averages about the given longitude.

TECP band below this diffuse aurora appears to be the low density trough, which has been confirmed using DMSP data (not shown). We see these two regions moving southward over this period, and possibly associated fluctuations in the lower latitude TECP can also be seen. This relationship is shown more explicitly in Figure 3.5. Here, we show latitudinal cuts of the maps shown in Figure 3.4 at 8 different longitudes. White portions indicate that no data were available in that map; the best coverage is over the center of North America. Distinct, alternating positive and negative TECP pulses are observed at Arecibo-like latitudes, which are clearly the manifestation of the passing wave. Enhanced diffuse aurora can be seen as positive TECP and southward motion at high latitudes. The trough region on the edge of the diffuse aurora fills in later in the morning. Regions of large TECP at mid-latitudes ($\sim20°$N) can be seen at ~0300, 0600, and 0800 UT which are clearly the TEC signatures of the pulses. In addition, using this TECP imaging technique, these pulses can be associated with activity within the auroral region. For example, the mid-latitude pulse at ~0530-0600 UT appears to be related to auroral activity between ~0400-0500 UT. The propagation of the pulses is approximately 600 m/s which is consistent with models and other measurements (e.g., *Hocke and Schlegel*, 1996). The scale size of the disturbances is ~600 km which is consistent with the *Shiokawa et al.* (2002, 2003) observations as well as Japanese TECP observations on this night, which also show propagating large-scale TIDs (A. Saito, personal communication).

At first glance the explanation of the sign of the TECP relative to the vertical motion of the local ionosphere is not obvious. During a poleward wind pulse it makes sense that h_mF2 would decrease, but by itself this would not change the TEC. However, such a layer motion increases the plasma pressure and a net inward flux results, increasing the VTEC due to the finite dip angle, an effect that is enhanced at mid-latitudes. Such fluxes have been observed at Arecibo before (e.g., *Vlasov*

et al., 2003). Indeed, the blue line in Figure 3.3 shows that the topside TEC was ~180° out of phase with the *F*-region TEC variations. Plasma exchange between the plasmasphere and the *F* region can thus explain the phase relationship between winds and VTEC. A 1 TECU increase during a 2-hour period requires a plasmaspheric flux of about 2×10^8 cm^{-2}s^{-1}, which is consistent with the Arecibo data on this night. In short, we believe a local explanation for the exchange of plasma is credible in such events. The effect may be enhanced if the equatorial fountain effect is well-developed due to increased daytime eastward penetrating electric fields (e.g., *Foster et al.*, 2002; *Vlasov et al.*, 2003).

3.6 Airglow Observations

Airglow measurements provide further evidence for the structure of the TIDs. In Hawaii, Cornell University operates two imagers - one all-sky imager and one narrow-field imager, which is pointed south along the geomagnetic meridian (*Kelley et al.*, 2002; *Makela and Kelley*, 2003). Plotted in Figure 3.6 are north-south and east-west keograms (emission intensity as a function of meridional or zonal distance and time) from the all-sky imager in Hawaii, for two emissions - the 630.0-nm emission and the 777.4-nm emission. The images have been processed as described in Chapter 2 and projected onto a plane at 250 km and 350 km for 630.0 nm and 777.4 nm, respectively. As discussed in Chapter 2, these two emissions together can give significant information about the dynamics of the *F* region, with the 777.4-nm emission being a tracer for the electron density and the 630.0-nm emission depending on the ionospheric *F*2-layer height and density. Hawaii is 10 hours behind universal time, and so the first few pulses of the train of TIDs are not captured. The peak in the 630.0-nm emission near 0700 UT is a result of the TID poleward wind motion that has driven
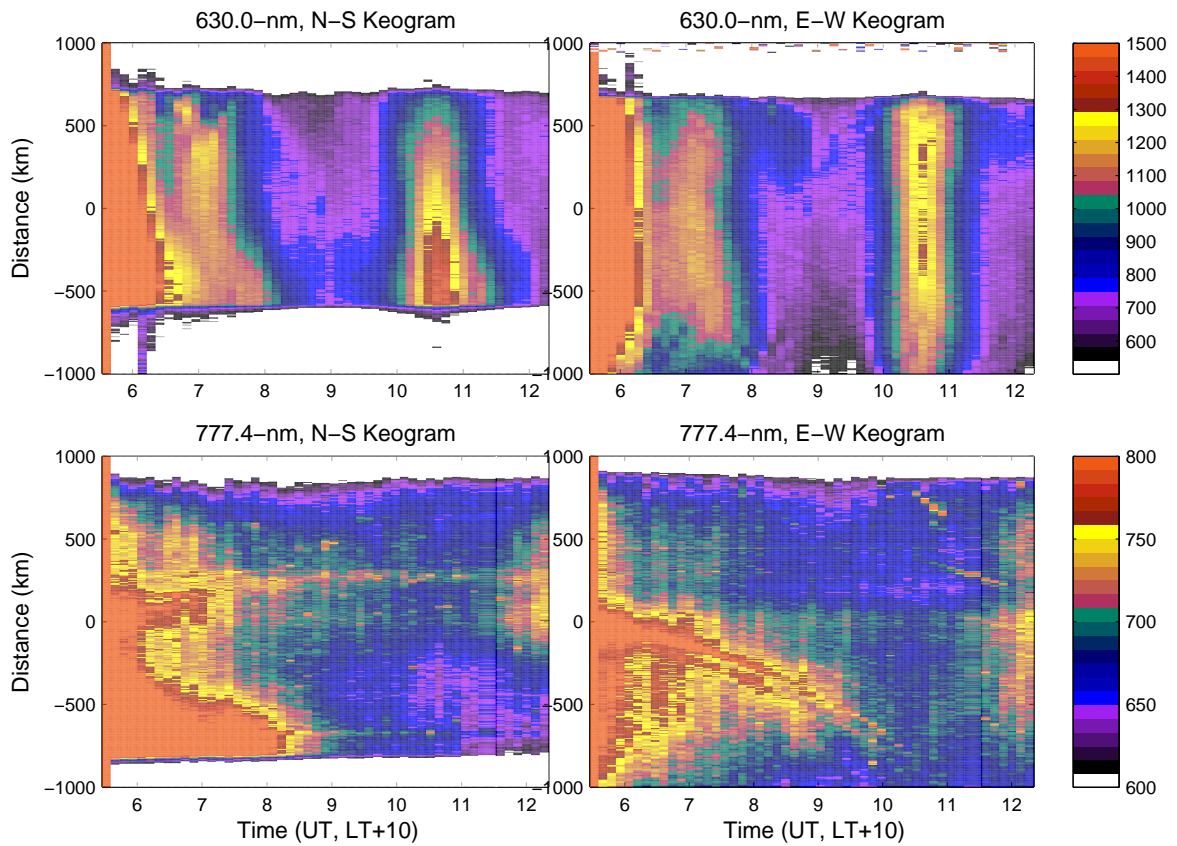
Figure 3.6: Keograms in the Hawaiian sector, measured by CASI. The upper row are 630.0-nm keograms, and the bottom row are 777.4-nm keograms. The left column shows north-south geographic cuts, and the right column shows east-west geographic cuts. The units are unnormalized intensities, proportional to Rayleighs.

the ionospheric F layer down, enhancing that emission. This corresponds well to the Arecibo data presented earlier. We do not see a corresponding strong enhancement in the 777.4-nm emission data, implying that the major effect was ionospheric motion rather than a density enhancement. We do see enhancement on the lower edge of the 777.4-nm keogram, which probably corresponds to the anomaly to the south of Hawaii.

The TID near 0700 UT clearly propagates from north to south, and from the keogram we can estimate its meridional propagation speed. The TID decreases in velocity to the south of Hawaii, perhaps because it enters the higher density anomaly region. The average speed of the TID deduced from the keogram is over 500 m/s, but it appears to be faster to the north and slower to the south. These numbers are in reasonable agreement with the dispersion relation estimates done earlier. In the east-west keogram for this phase of the TID, we see that it appears overhead slightly earlier than it appears to either the east or west. This is consistent with the idea of curved wavefronts, which makes sense for an approximately symmetric source in the high latitude region. In addition to the pulse at 0700 UT, there is a second pulse at about 1030 UT which occurs after sunrise at Arecibo. This TID is also seen to propagate to the south at a slightly faster speed. This disturbance, in addition to sunrise production, may explain the drastic change in ionospheric behavior right after sunrise observed at Arecibo.

At Arecibo, the all-sky imager did not take images with a high enough time resolution for the keograms to give meaningful information on the structure of the TIDs. Plotted in Figure 3.7 are the 557.7-nm and 630.0-nm zenith intensities measured by the imager, calibrated to Rayleighs as described in Chapter 2. We will discuss the characteristics of these measured intensities in the next section, however the manifestation of the passage of the TIDs is clear, especially in the 630.0-nm emission, where
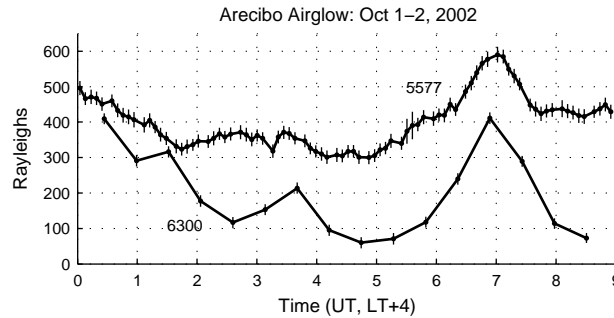
Figure 3.7: Zenith 557.7-nm and 630.0-nm airglow intensities measured by the BU imager at Arecibo on the night of October 1-2, 2002.

we see three pulses corresponding to the times when the ionosphere was pushed down by the poleward wind phase of the TID. While the first two fluctuations are not clear in the 557.7-nm emission, the final pulse near 0700 UT is certainly evident.

3.7   Discussion

We believe the data presented in the previous sections are in good agreement with the notion that a sequence of magnetic substorms over the 9-hour period from 0000-0900 UT on October 2, 2002 generated a train of neutral atmospheric perturbations which propagated equatorward, most likely in both hemispheres. At our primary site, the Arecibo Observatory, very substantial altitude modulations of the F layer occurred, culminating near dawn with the F peak reaching as high as 430 km. Similar variations were observed at mid-latitudes over Brazil, which will be discussed in Chapter 4. Low and mid-latitude airglow observations show evidence of these modulations, and North American TEC and ionosonde data have shed light on the equatorward propagating disturbances.

We note that properties of the disturbances are in good qualitative agreement with predictions made by models, such as that of *Richmond and Matsushita* (1975). They modeled the local and propagating disturbances created by a single magnetic

substorm. In less than two hours, the neutral disturbance had propagated to a position well southward of Arecibo's latitude. For reference, they find an equatorward wind pulse of 200 m/s followed by a reversal to poleward flow lagging in spatial phase by several hundred kilometers. This wind field was accompanied by a temperature perturbation of 100 K at mid-latitudes. Although we are not aware of any simulation of the effects of multiple substorms, it seems likely that a series such as those which occurred during this event would launch the multiple wave-like pulses perhaps from both hemispheres. In addition, we observe ion temperature and electron temperature variations associated with the passage of the gravity wave. The T_i variations (indicative of neutral temperature variations) are on the order of 50-100 K out of phase with the velocity oscillations by about one-quarter of a cycle, which is consistent with AGW theory. One expects the density fluctuations to be delayed by about one-quarter to one-half cycle with respect to the velocity fluctuations and the ion temperature fluctuations to be advanced by about one-quarter of a cycle with respect to the velocity fluctuations (*Kirchengast*, 1996, 1997). The electron temperature fluctuations are not as easy to interpret. The data seem to be consistent with this theory, providing very strong evidence for an AGW-induced TID.

3.7.1   Auroral Source

It is generally accepted that Lorentz forcing and Joule heating in the auroral electrojet, along with energy deposited by precipitating particles, are the main energy sources for large-scale disturbances in the neutral atmosphere that propagate to low latitudes as TADs. Lorentz forcing is caused by magnetospheric electric fields that set the plasma into motion, which subsequently transfers energy to neutrals via collisions. Thus, the $\mathbf{J} \times \mathbf{B}$ term is proportional to the conductivity (either Hall or Pedersen), the magnetic field strength, and the electric field strength. *Richmond* (1978) found

that Lorentz forcing from Hall currents is less effective in generating gravity wave activity than the Pedersen currents. The Pedersen currents are also the source of the Joule heating ($\mathbf{J} \cdot \mathbf{E}$) mechanism, which is proportional to the Pedersen conductivity and the square of the electric field strength. *Richmond* (1978) also finds that the efficiency of wave generation (AGW energy divided by energy input) is independent of the electric field strength for the Lorentz mechanism but proportional to the square of the electric field for the Joule mechanism (i.e., proportional to the heating rate). It can thus be expected that the major contributing factor when comparing the relative importance of the Joule and Lorentz mechanisms will be the electric field strength. Note that the Pedersen conductivity is proportional to density, so that ionization induced by particle precipitation should manifest itself in these other mechanisms as well (*Hunsucker*, 1982).

These ideas can be put into a more quantitative form. The rate of frictional heating (Joule heating) can be written as (e.g., *Rees*, 1989)

$$Q_E = n_i m_i \nu'_{in} |\mathbf{v} - \mathbf{u}|^2 \tag{3.5}$$

where n_i is the ion density, m_i is the ion mass, ν'_{in} is the ion-neutral energy transfer collision frequency, $\mathbf{v}$ is an ion velocity, and $\mathbf{u}$ is a neutral wind speed. This friction of course heats the neutral gas, which is manifest in the neutral energy balance equation. This heating term would then affect the neutral momentum equation through pressure gradient forcing. The corresponding neutral heating rate would be

$$Q_E = n_n m_n \nu'_{ni} |\mathbf{v} - \mathbf{u}|^2 \tag{3.6}$$

under the assumption that $n_i m_i \nu'_{in} = n_n m_n \nu'_{ni}$. Further assuming that the relative drift velocity is dominated by an electric field,

$$\mathbf{v} - \mathbf{u} \approx \frac{e\mathbf{E}}{m_i \nu_{in}}, \tag{3.7}$$
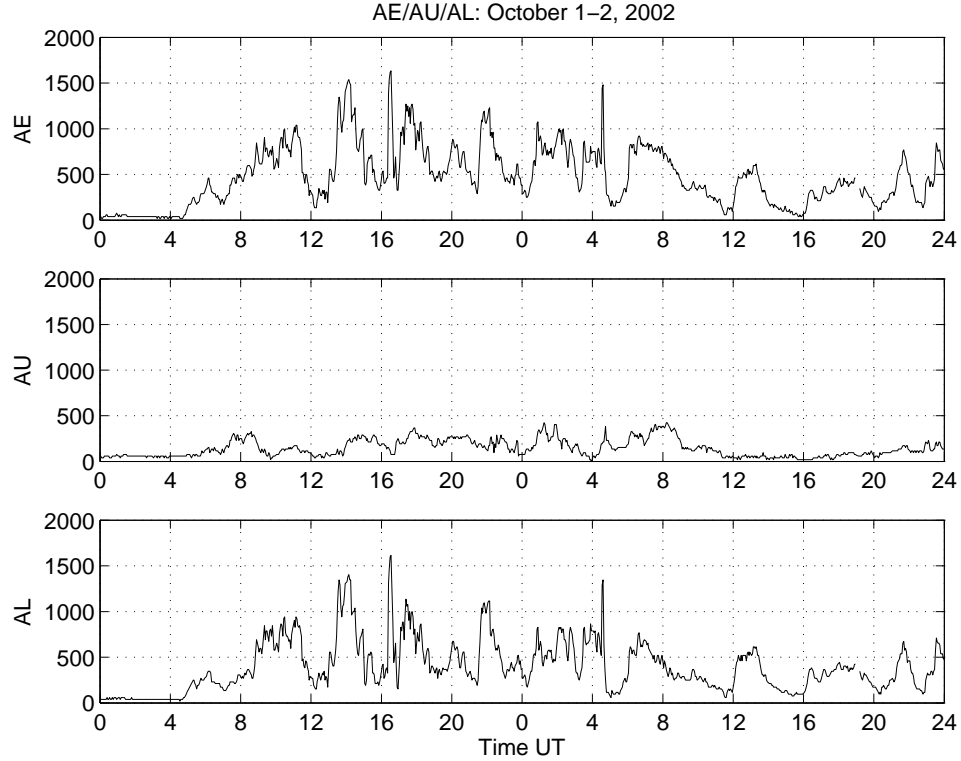
Figure 3.8: AE, AU, and AL indices on October 1-2, 2002.

we see that the heating rate is proportional to the magnitude squared of the electric field. The Lorentz mechanism is more directly seen in the neutral momentum equation. The $\mathbf{J} \times \mathbf{B}$ force can be written as,

$$\mathbf{F_{J \times B}} = \frac{1}{\rho}\mathbf{J} \times \mathbf{B} = \frac{1}{\rho}\left(\sigma_P\mathbf{E}' + \sigma_H\mathbf{E}' \times \hat{\mathbf{b}}\right) \times \mathbf{B} \qquad (3.8)$$

where $\mathbf{E}'$ is the electric field in the reference frame moving with the neutral wind.

The source of the disturbances seen at low and mid-latitudes on the night of October 1-2, 2002 is somewhat ambiguous. The metrics shown in Figure 3.1 and discussed previously give a general idea of the substorm activity on this night. Quick-look $AU/AL/AE$ indices (from the Kyoto World Data Center) plotted in Figure 3.8, the effects of which can be seen in the Leirvogur magnetometer data in the bottom panel of Figure 3.1, show periodic westward current enhancements (corresponding to negative pulses in AL and increased AE, or negative ΔH over Iceland), with maxima

at about 1000 UT, 1400 UT, 1730 UT, 2000 UT, and 2200 UT on the 1st and 0100 UT, 0230 UT, 0400 UT, and 0700 UT on the 2nd. Qualitatively, it seems quite likely that this quasi-periodic substorm activity is related to the launching of the series of TADs that have been presented here and observed with similar periods at low latitudes. The waves would be generated by Hall currents in the auroral electrojet. Such periodic substorm activity and its role in the generation of periodic bursts of AGWs/TADs have been examined before, as mentioned in the introduction (e.g., *Hocke and Schlegel*, 1996; *Lewis et al.*, 1996). In fact, some modeling work (*Millward*, 1994) has even shown a resonance effect where TADs/TIDs can be enhanced by electric field bursts of a certain interval. The efficiency of this mechanism peaks, however, at a period of about 45 minutes, whereas the intervals associated with the magnetic activity on this night are more like 2-3 hours. The current enhancements are indicative of the Lorentz mechanism (via Hall currents) dominating the forcing. This is in disagreement with the conclusion of *Richmond* (1978) that Pedersen currents are the dominant mechanism.

On the other hand, the periodic behavior at low latitudes can perhaps also be explained by a single electric field enhancment leading to say Joule heating and causing an impulse-like response in the neutral atmosphere. This is very similar to the effects of earthquakes (e.g., *Davies and Baker*, 1965; *Kelley et al.*, 1985) and nuclear explosions (e.g., *Row*, 1967) which can generate very large-scale ionospheric responses. Indeed, models (e.g., *Millward et al.*, 1993a,b; *Richmond and Matsushita*, 1975) have shown that such an input can set up a disturbance that propagates to low latitudes much like a shallow water wave, an analogy that was drawn earlier. However, such an input tends to generate only a single response at low and mid-latitudes, as the wave-train is heavily damped (*Hocke and Schlegel*, 1996). Thus, it seems far more likely that the observations relate to a periodic source.
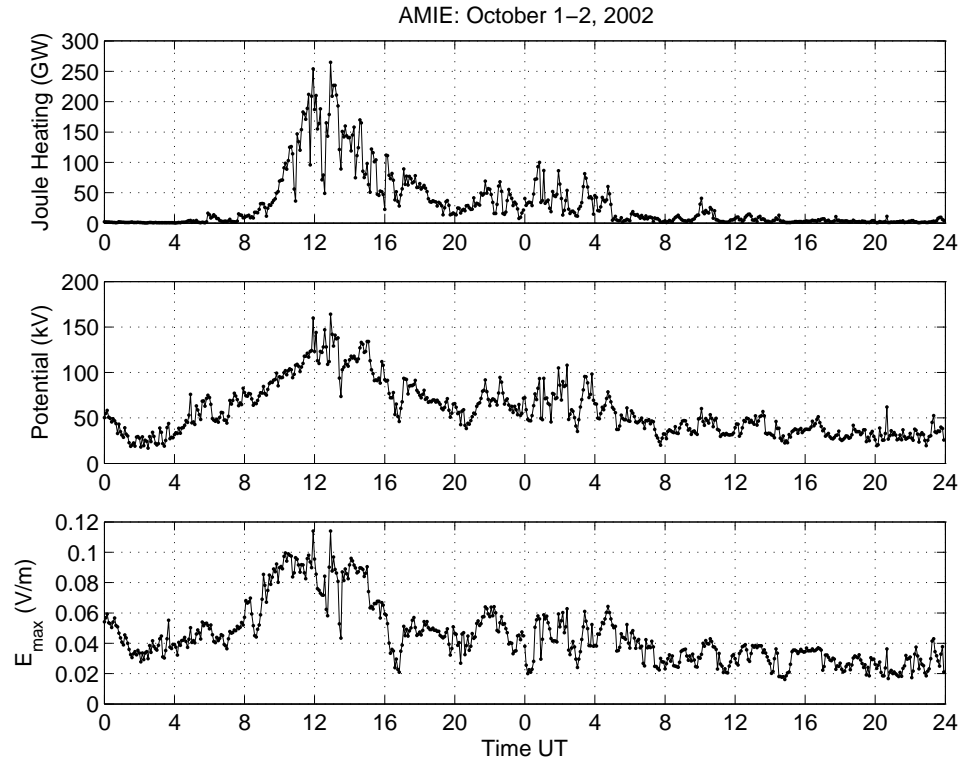
Figure 3.9: Joule heating (top), cross-cap potential (middle), and maximum electric field (bottom) on October 1-2, 2002 using the AMIE technique.

To further investigate the high latitude source, we have used the AMIE (assimilative mapping of ionospheric electrodynamics) method (*Richmond and Kamide*, 1988) to estimate Joule heating rates and cross polar cap potentials for October 1st and 2nd, 2002. The AMIE procedure is a constrained, least-squares fit of electric potential distribution to a diverse collection of datasets (in our case we used mainly magnetometer data). A summary of these data are shown in Figure 3.9, where we show the Joule heating integrated over the polar cap, the cross-cap potential, and the maximum electric field. As shown in Figure 3.9, there is a clear enhancement in the cross-cap potential and Joule heating between 1200 and 1300 UT on the 1st. Referring back to Figure 3.1, this corresponds to the peak of the storm when the energy built up in the tail is released, as discussed earlier. The cross-cap potential

at this time peaks at about 160 kV and is generally more than 100 kV during the main phase of the storm. Similarly, the Joule heating rate increases to over 250 GW. Early on the 2nd, the high latitude region is also quite active, associated with the substorm activity already discussed. Between 0000 and 0500 UT, the cross-cap potential fluctuates between 50 and about 110 kV several times and the Joule heating fluctuates between about 50 and 100 GW. Periodic electric field behavior is also seen. However, these Joule heating rates are modest and not in general significant enough to drive the neutral atmospheric disturbances that we observe. The fact that there are no strong fluctuations in the Joule heating rate and that the fluctuations in the electric field are rather modest favor the interpretation that Lorentz forcing by Hall currents is the dominant mechanism during this event.

3.7.2   Arecibo Airglow and Dynamics

Airglow and Plasma Flux

In this subsection, we investigate some aspects of the dynamics over Arecibo using airglow and ISR data. In Figure 3.10, we compare the measured and calculated red line airglow intensities. The calculations utilize the ISR data and the MSIS neutral densities, using the model described in Chapter 2. The ISR data have been binned into 15-minute averages for this calculation. The calculated peak intensity at 0700 UT is slightly higher than the observed intensity. This discrepancy could be due to unrealistic MSIS neutral composition under the disturbed geomagnetic conditions. The most significant discrepancy between the calculated and measured intensities is at 0500 UT when the minimum intensity occurs. There is the possibility that the 630.0-nm airglow observations are contaminated by the OH emission that is found near the 630.0-nm line. *Burnside et al.* (1977) found that the errors on 630.0-nm
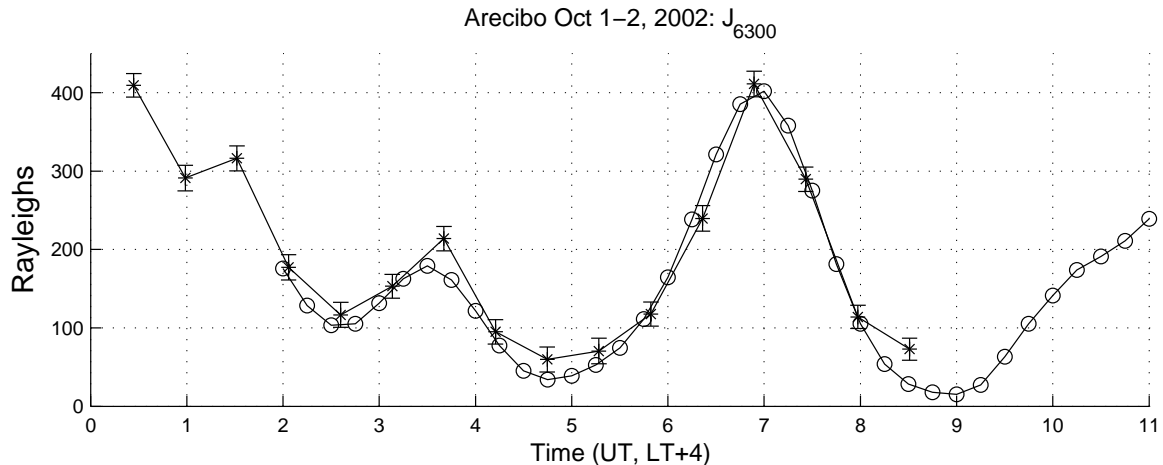
Figure 3.10: The calculated and measured red line intensities on the night of October 1-2, 2002. The circles are the calculated intensities from the ISR data, averaged over 15 minutes, and the stars are the measured zenith intensities with the imager, with error bars corresponding to the standard deviation around the zenith bin.

intensity measurements are less than 10% if the bandwidth of the instrument is less than 5 Å and if the emission intensity is greater than 20 R. We are using an instrument with a bandwidth of 12 Å. According to the spectrum of the 630.0-nm region shown in Figure 1 of *Burnside et al.* (1977), the intensity of the OH emission in the wavelength region 628.5 nm to 631.0 nm does not exceed 9 R. This means that OH contamination of 630.0-nm measurements can be significant for the low intensities observed around 0500 UT on October 2. This is also the point at which the imager is the least sensitive and the calibration to absolute intensity may be problematic. In addition, according to the ISR measurements of the electron density, the gradient scale on the bottomside of the $F2$ region is very large and the ion composition may be important in this case, the effects of which will be discussed in Chapter 6. Nevertheless, the agreement between the calculation and the observations is in general very good.

One of the main features of the nighttime ionospheric behavior, inferred from the emission data from nights in October 2002 and shown by ISR measurements (see Chapter 2), is an N_mF2 increase in conjunction with an h_mF2 decrease near midnight.

According to the modern theory of the $F2$ region, the nighttime electron density is maintained by plasma flux from the plasmasphere, which provides a slower decrease in electron density in comparison with loss simply due to recombination. When the recombination increases due to a decrease in h_mF2 at night, the downward flux must increase if N_mF2 is to remain constant or increase. This effect is clearly shown in Figure 3.3 where the TEC fluctuations are the signature of the plasmaspheric flux. Inspection of these curves show that the TEC increases coincide with h_mF2 decreases and N_mF2 increases. If there were no flux, and the layer was simply being modulated up and down with the N_mF2 changes being due to changes in the profile shape, then there would be no TEC change (except due to recombination). Using the model developed by *Vlasov et al.* (2003), it is possible to estimate the plasma flux required to maintain the high electron density measured at 0700 UT on October 2. We find the downward flux to be $\sim 1.6 \times 10^9$ cm^{-2}s^{-1}. This value is very large in comparison with the normal flux of $\sim 1\text{-}2 \times 10^8$ cm^{-2}s^{-1} typically observed at Arecibo (*Vickrey et al.*, 1979). Also, this flux is larger than the flux of 7×10^8 cm^{-2}s^{-1} estimated by *Vlasov et al.* (2003) using ISR measurements of the ionospheric parameters at Arecibo during a storm on the night of September 16-17, 1999. However, in that case the collapse in h_mF2 was accompanied by an N_mF2 decrease and the peak of the red line intensity did not exceed 250 R.

The plasma quantity transported from the plasmasphere during one hour due to fluxes higher than 10^9 cm^{-2}s^{-1} is comparable to the plasmaspheric plasma content of the short magnetic flux tubes corresponding to the location of Arecibo. Thus, the plasmasphere needs an additional source of plasma before midnight in order to provide the large plasma flux after midnight. In studying the September 16, 1999 storm, *Vlasov et al.* (2003) concluded that two sources can provide the increase in plasma flux. The first possibility is an enhanced fountain effect at the equator together with

northward motion of the Appleton anomaly. The second possibility is the creation of additional plasma content in the plasmasphere before midnight due to upward motion induced by an equatorward neutral wind. This plasma is returned to the ionosphere after midnight.

September 16, 1999 was marked by a minor magnetic storm with a maximum K_p of 6. A very strong eastward electric field was observed at Jicamarca (*Makela et al.*, 2003). This electric field induces an upward plasma drift at the equator, which lifts the plasma to high altitudes where it can flow along magnetic flux tubes to mid-latitudes. As a result, the Appleton anomaly should be much farther north than usual. This mechanism can work in the ionosphere over Arecibo 2-3 hours after sunset because eastward electric fields (upward plasma drifts) are observed at the equator during the daytime and are absent after sunset (except for the pre-reversal enhancement right after sunset) (*Kelley*, 1989). The time of plasma transport from the equatorial region to Arecibo latitudes is about 3 hours.

A strong southward wind was observed during the 3 hours before midnight on the night of September 16-17, 1999. This wind can induce plasma transport from the topside ionosphere to the plasmasphere. *Macpherson et al.* (1998) showed that a significant increase in the O^+-H^+ transition altitude, i.e., the altitude where $[O^+]=[H^+]$, as observed over Arecibo under quiet geomagnetic conditions, can be explained by an equatorward neutral wind. An increase in the transition altitude means that the plasma content in the plasmasphere has increased. The equatorward wind inferred by *Macpherson et al.* (1998) from Arecibo ISR data is a factor of three higher than the wind predicted by the horizontal wind model, HWM90 (*Hedin*, 1991b).

Using the h_mF2 variations and N_mF2 values observed on the night of October 2 it is possible to estimate the upward velocity at midnight (0400 UT) and the plasma flux from the ionosphere to the plasmasphere induced by this upward motion. This

flux is found to be $\sim 1.3 \times 10^9$ cm^{-2}s^{-1}, which is in good agreement with the downward plasma flux estimated earlier.

Thus, the ionospheric plasma transported to the plasmasphere due to an equatorward wind returns to the ionosphere when the wind ceases or changes direction. It should be noted that a decrease in the H$^+$ fraction in the topside ionosphere and plasmasphere is evidence for plasma transport in the plasmasphere due to an equatorward wind, as the Appleton anomaly moves to more northern latitudes. When the $F2$ layer is uplifted to higher altitudes and the plasma flows from the ionosphere to the plasmasphere, the red line intensity decreases. When the $F2$ layer falls to lower altitudes and the plasma flows to the ionosphere from the plasmasphere, the intensity increases. The lower the minimum intensity, the higher the plasma flux from the ionosphere. The higher the peak intensity, the higher the plasma flux to the ionosphere. As such, measurements of the red line intensities can be used for a rough estimate of the plasma exchange between the ionosphere and plasmasphere.

The Shape of the $F2$ Layer

However, the red line intensity also depends on the shape of the $F2$ layer. As can be seen from the height profiles of the electron density measured at 0500 UT, 0700 UT, and 0800 UT in Figure 3.11, the shape of the $F2$ layer changes significantly during the upwelling. First of all, we are interested in the bottomside of the $F2$ layer because the maximum red line volume emission rate is always below $h_m F2$. The sharp bottomside profile measured at 0700 UT is formed by very strong downward motion and recombination. Our estimate indicates that the downward velocity due to ambipolar diffusion together with the velocity due to the gravity field is much smaller than the downward velocity induced by the poleward wind just before 0700 UT. In
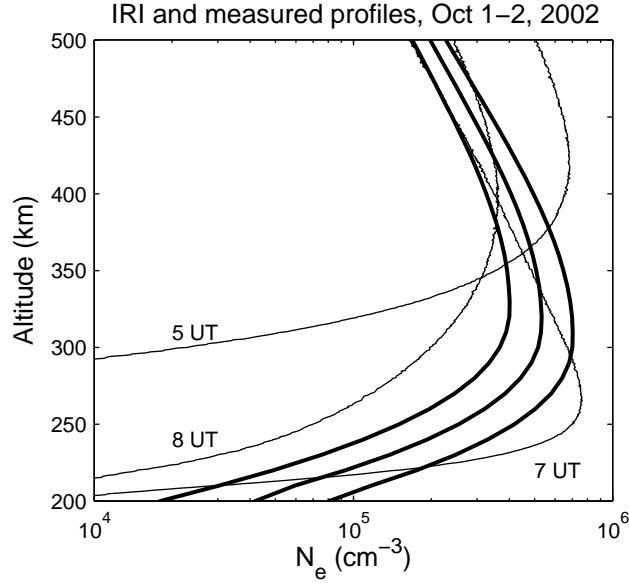
Figure 3.11: IRI (dark) and measured (light) height profiles of electron density on the night of October 1-2, 2002. The highest density IRI profile corresponds to 5 UT (1 LT) and the lowest density IRI profile corresponds to 8 UT (4 LT). The measured profiles have been averaged over 30 minutes.

this case, the continuity equation reduces to

$$\frac{\partial(n_e V)}{\partial z} = -\beta n_e \tag{3.9}$$

where n_e is electron density, V is downward velocity, and β is the recombination coefficient. Then, letting $z = 0$ at $h_m F2$ and $\beta = \beta_0 \exp(z/H_R)$ where H_R is the recombination coefficient scale, and also assuming $V = V_0 \exp(-z/H_V)$, the solution to Equation 3.9 can be written as

$$n_e = n_{e0} \exp\left[\frac{z}{H_V} + \frac{\beta_0 H_R H_V}{V_0(H_R + H_V)} \left(1 - e^{z(H_V + H_R)/H_R H_V}\right) \right] \tag{3.10}$$

where $n_{e0} = N_m F2$. A comparison of a profile calculated by Equation 3.10 with a measured profile is shown in Figure 3.12a. This excellent agreement is obtained for $V_0 = 30$ m/s corresponding to the average downward velocity inferred from the $h_m F2$ change between 0600 UT and 0700 UT, along with H_V=42 km. Other parameters (β_0 and H_R) are quite close to the values given by MSIS, implying that the total

recombination does not differ significantly from that of MSIS. However, the height profile given by the solution is sensitive to variations in these parameters.

The profile measured at 0500 UT corresponds to an h_mF2 of about 400 km where recombination is not important and the main processes are ambipolar diffusion and plasma motion along the magnetic field line induced by the southward wind and the gravity field. In this case, the steady-state continuity equation for the electron density is given by

$$\frac{\partial}{\partial z}\left[-D\sin^2 I\left(\frac{\partial n_e}{\partial z}+\frac{n_e}{H_p}\right)+n_e U\cos I\sin I\right]=0 \qquad (3.11)$$

where n_e is an electron density, $D=2T_p/m\nu$ is the ambipolar diffusion coefficient, H_p is the plasma scale height, T_p is the plasma temperature, $\nu=\nu_0\exp(-z/H)$ is the collision frequency, H is the atmospheric scale, U is the southward component of the neutral wind, and I is the magnetic inclination. The left side of this equation is the derivative of plasma flux and this flux does not change with altitude. If we assume that the flux is equal to zero, then the solution to Equation 3.11 is

$$n_e=n_0\exp\left[-\frac{z}{H_p}-\frac{U\nu_0\cos I}{\alpha g\sin I}\left(e^{-z/H}-1\right)\right] \qquad (3.12)$$

where n_0 is the electron density at the lower boundary, ν_0 is the collision frequency at the lower boundary, g is gravity, and $\alpha=H_p/H$. Using this solution, it is possible to determine the altitude of the $F2$ peak corresponding to equilibrium conditions. The derivative, $\partial n_e/\partial z$, is equal to zero at the altitude of the $F2$ maximum and we have the expression

$$\frac{1}{H_p}=\frac{\nu_0 U\cos I}{\alpha H g\sin I}\exp(-z_m/H). \qquad (3.13)$$

Then, using Equation 3.12, the altitude of the $F2$ maximum can be written as

$$z_m=H\ln\left(\frac{\nu_0 U\cos I}{g\sin I}\right). \qquad (3.14)$$

The height profile of the electron density calculated by Equation 3.12 with $n_0\approx 5\times 10^4$ cm^{-3} at the lower boundary of 310 km at 0500 UT, H=52 km, and U=70 m/s, along
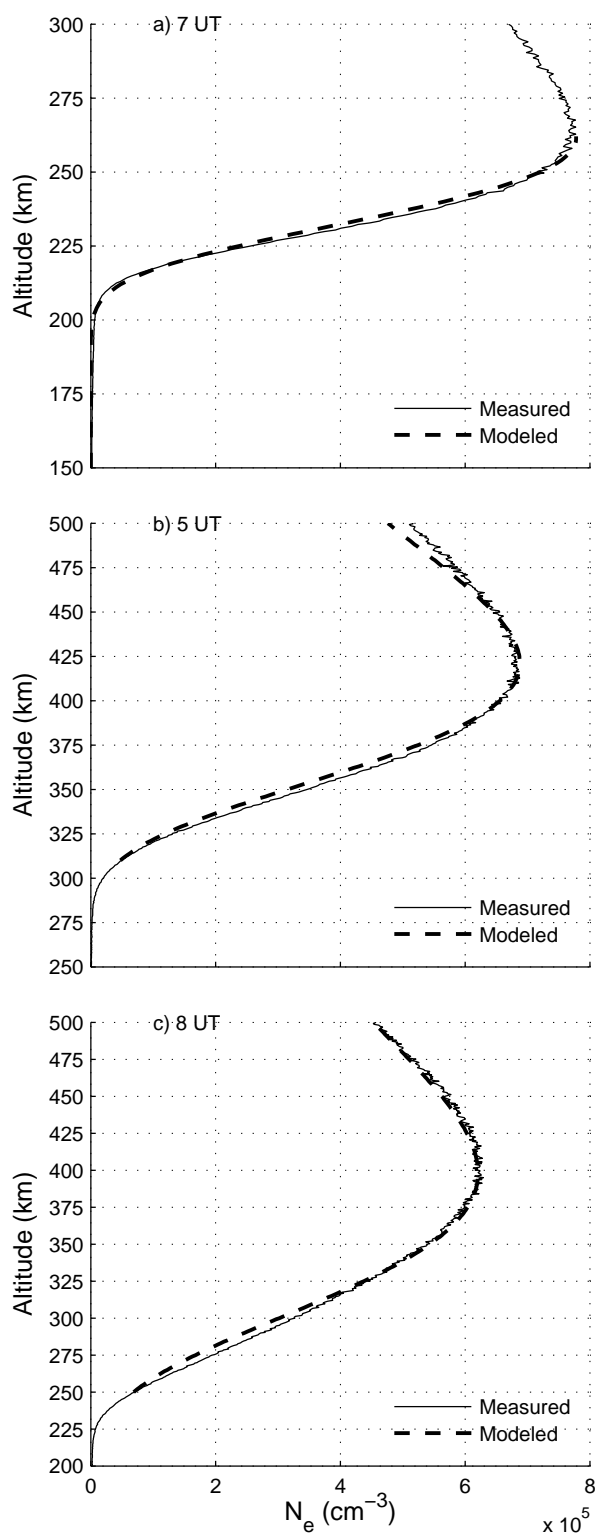
Figure 3.12: The measured (solid), averaged over 20 minutes, and modeled (dashed) height distributions of the electron density on October 2, 2002 at a) 0700 UT, b) 0500 UT, and c) 0800 UT. See text for details on the model profiles.

with $\nu_0 \approx 1 \ \mathrm{s}^{-1}$ according to the MSIS-90 model, is shown in Figure 3.12b. This profile is in good agreement with the measured profile. Thus, the strong change of the $F2$ layer as a result of the upward motion can be explained by the transition from recombination to diffusion. This conclusion is confirmed by the excellent agreement of the profile calculated by Equation 3.12 with the measurements at 0800 UT (Figure 3.12c).

The very strong change of the $F2$ layer shape on the bottomside can be described by simple solutions to the continuity equation, taking into account the main physical processes. Considering the close connection between the red line intensity and the ionospheric parameters, it is possible to conclude that variations of the red line intensity can be an indicator of the effect of the neutral wind on the ionosphere.

It is necessary to emphasize that the IRI model does not show either the collapse in $h_m F2$ or the increase in $N_m F2$ that occurs after midnight. According to the IRI model, the $N_m F2$ value decreases and the $h_m F2$ value does not change throughout the night. Our calculations of the 630.0-nm intensity using the electron density and ion composition corresponding to the IRI model give unrealistic intensities under different nighttime conditions at mid-latitudes, and this is discussed in more detail in Chapter 6.

Green Line Intensities

Let us now briefly consider the behavior of the green line emission on this night. The 557.7-nm intensities change from night to night, as shown in the zenith intensities plotted for many days in October 2002 in Figure 2.10. A comparison of the calculated and measured intensities on October 2 is shown in Figure 3.13, using the model for the F-region green line volume emission rate described in Chapter 2. One clearly sees the effect of the TID on the green line intensity, as the large decrease in height at
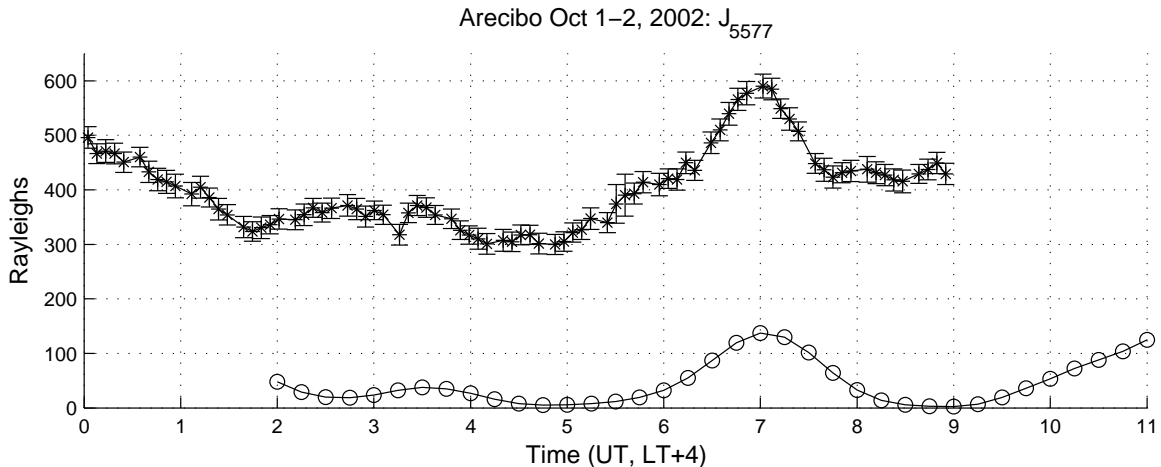
Figure 3.13: Calculated and measured green line intensities on the night of October 1-2, 2002. The circles are the calculated F-region intensities from the ISR data, averaged over 15 minutes, and the stars are the zenith intensities (from both the E and F regions) measured with the imager, with error bars corresponding to the standard deviation around the zenith bin.

about 0700 UT induces an increase in the F-region green line intensity of about 150 R. The previous oscillations cause much smaller fluctuations. Subtracting the calculated 557.7-nm $F2$-region intensities from the measured intensities, it is possible to estimate the 557.7-nm intensities radiated by the mesospheric layer. These estimates are plotted in Figure 3.14. The intensities are about 300 R at 0500 UT and 450 R at 0700 UT, and are much higher than the values of 100-140 R typically observed at Arecibo (*Schubert et al.*, 1999). The solid line in this figure is the green line integrated volume emission rate calculated using the MSIS neutral densities, but with the MSIS [O] scaled by a factor of 1.3 (note as derived in Chapter 2, the green line volume emission rate is proportional to the cube of the atomic oxygen density). We have not modified the MSIS neutral temperatures in these calculations. A 557.7-nm intensity fluctuation of about 50 R during the period 0100 LT to 0300 LT is comparable to typical fluctuations observed at Arecibo (*Schubert et al.*, 1999). According to observations (*Schubert et al.*, 1999), the temperature fluctuations are much smaller than
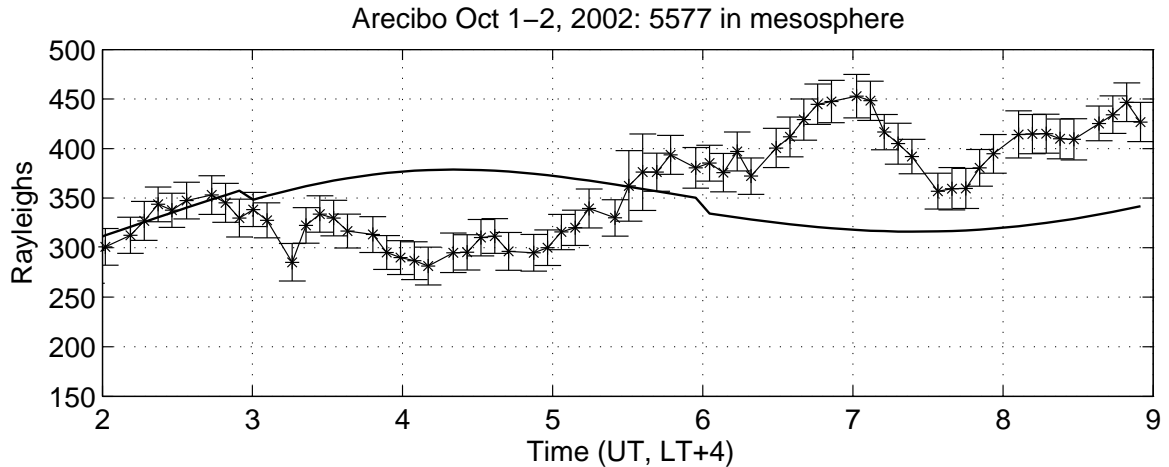
Figure 3.14: Estimated mesospheric contribution to the green line intensity, computed from the curves in Figure 3.13. The solid line is the green line intensity estimated from the MSIS neutral densities, with the MSIS [O] scaled by a factor of 1.3.

the intensity fluctuations, meaning that atomic oxygen density fluctuations are likely the main cause of the intensity fluctuations (again note the strong dependence of the intensity on the atomic oxygen density).

The O density in the mesosphere is determined by three-body recombination (see Chapter 2) and transport due to eddy diffusion and mass averaged motion. Eddy diffusion is characterized by two main parameters: the maximum value of the eddy diffusion coefficient and the altitude of this maximum. A neutral composition model (*Vlasov and Davydov*, 1993) has shown that eddy diffusion parameters strongly affect the O density. A decrease of the eddy diffusion coefficient induces an increase in the atomic oxygen density. Simultaneously, a decrease in the eddy turbulence induces a temperature decrease (*Gordiets et al.*, 1982; *Vlasov and Korobeinikova*, 1991). Such an effect of eddy diffusion on the mesospheric parameters can provide the change of $O(^1S)$ airglow observed during the period 0500-0700 UT. Approximate estimates show that an [O] increase of 13% and a temperature decrease of 6% are needed. It is reasonable to assume that gravity waves can induce these variations (*Ebel*, 1980;

Schubert et al., 1999).

It is very difficult to explain the day-to-day variations in the green line intensity (see Figure 2.10). In some cases, a sharp decrease in the green line intensity is observed, together with a strong increase in the red line intensity, as can be seen from the variations on the nights of October 1, 3, and 10, shown in Figure 2.10.. We have no explanation for this behavior, although some of the slower variations may be the result of tidal motions.

3.7.3 Mid-Latitude Plasma Instability in the F Region

In this section, we present some evidence for wave seeding of the plasma instabilities that we have suggested occurred in the pre-dawn period on October 2. The notion that gravity waves can seed plasma instabilities has been around for nearly 30 years (e.g., *Rottger*, 1973; *Klostermeyer*, 1978; *Kelley et al.*, 1981). These papers all dealt with the seeding of equatorial spread F (ESF). This idea was extended to the mid-latitude zone by *Kelley and Fukao* (1991), who conjectured that the Perkins instability (*Perkins*, 1973) could be seeded. These speculations concerning the seeding of plasma instabilities have relied strictly on an observed spatial periodicity in a trans-equatorial HF signal delay or a temporal periodicity in a coherent scatter radar (CSR) signal, with only the signal periodicity as evidence for the seeding waves themselves. The need for seeding is due to the low growth rates of these plasma processes. Consequently, growth from thermal noise is simply not feasible. Rather, geophysical noise pre-conditions the plasma and the structures thus have a head start.

In this approach, a perturbation neutral wind field due to a gravity wave impacts the bottomside of the ionosphere. Once there, it creates either electric field or Pedersen conductivity variations with the same wavelength. The former creates plasma density/conductivity variations via $\mathbf{E} \times \mathbf{B}$ drifts and, in each case, the resulting diver-

gence of some zero-order current leads to perturbation electric fields and to growth. The gravity wave generated electric field process has been successfully modeled at the equator (*Huang and Kelley*, 1996) and at mid-latitudes (*Huang et al.*, 1994). The perturbation wind generated conductivity process was suggested by *Miller* (1997) and has yet to be modeled.

At dawn on October 2, the height of the F peak in the ionosphere exceeded 450 km, one of the highest dawn excursions ever reported at Arecibo. Clearly, the plasma went unstable at this high altitude with three distinct localized uplifts occurring and considerable smaller-scale structure. This is more evident in Figure 3.15 in which the unstable region is enlarged in the top panel. Some cuts in electron density are plotted in the lower panel. Notice that with increasing time the wedges/uplifts grow larger. As the sun rises, the structure abruptly fades away. This is most likely due to the filling in of the irregularities due to production and the fact that the E-region conductivity shorts out the perturbation electric fields. The rapid variations in the contours are almost certainly caused by spatially varying electric fields. Their complexity in form is most likely due to a mixture of temporal development due to $\mathbf{E} \times \mathbf{B}$ drifts and structure motion across the fixed radar field of view.

The series of plasma density profiles in Figure 3.15 shows how structured the bottomside plasma was. The fourth and fifth profile in this series are the least ambiguous in terms of irregularity scale size since they were obtained along what seems to be a vertical wall of ionization. The dominant scale is about 40 km. Although measured in the vertical, such small features would rapidly diffuse away if there existed any gradients parallel to the magnetic field. They are thus most likely oriented perpendicular to $\mathbf{B}$ and hence closer to 30 km across the field. If we hypothesize that the bottomside contour variations between 0500 and 0530 LT were purely spatial and of the same scale size, then the associated velocity across the beam is about 50 m/s,
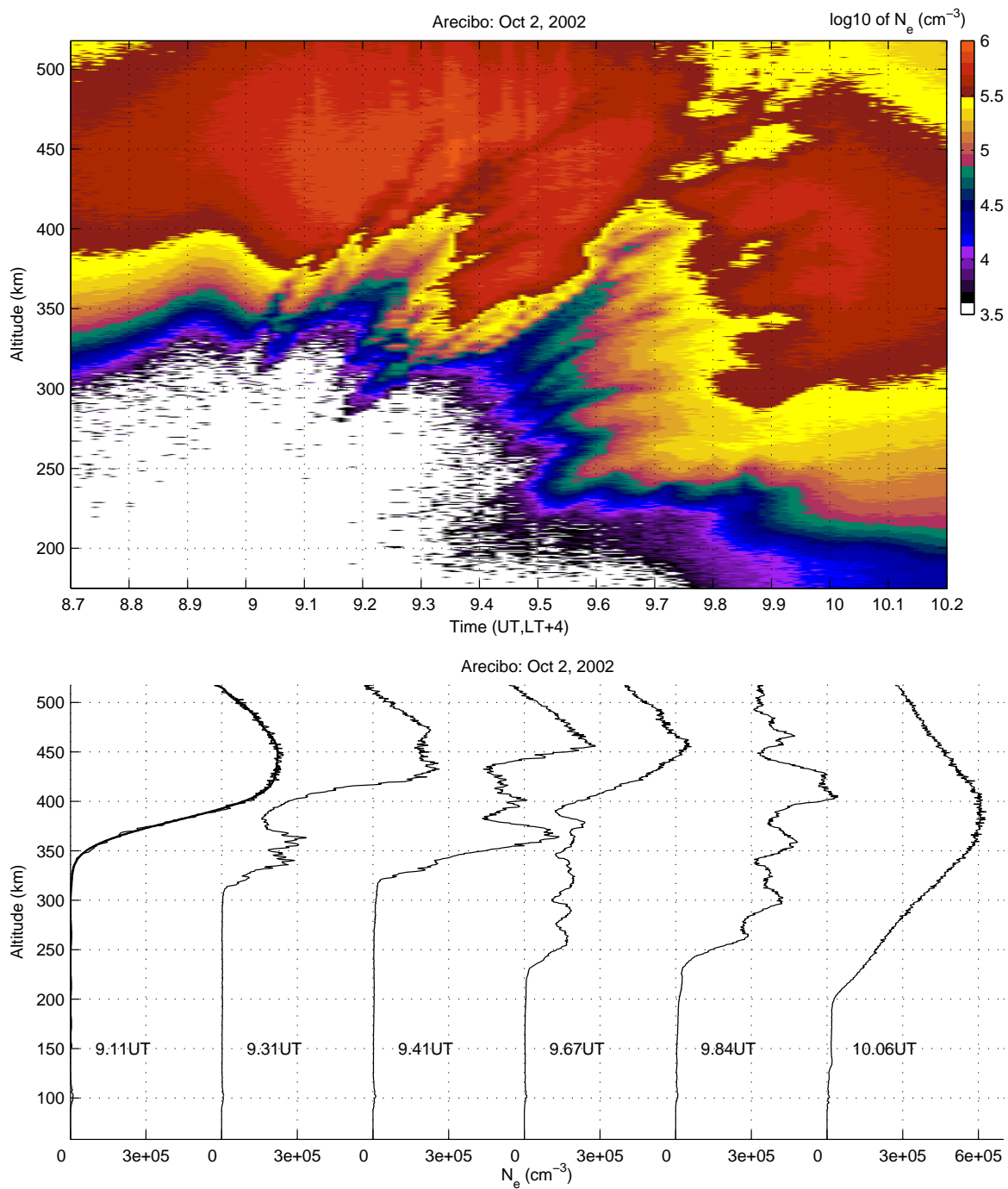
Figure 3.15: (Top) Measured electron density at Arecibo, zoomed in on the predawn period. (Bottom) Altitude cuts of the electron density.
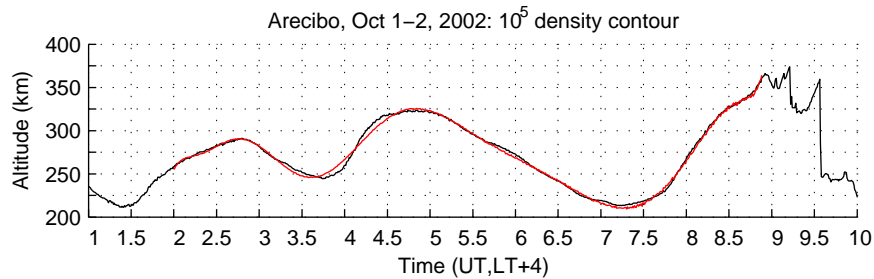
Figure 3.16: Measured density contour at $n_e = 10^5$ cm^{-3} (black line) along with a polynomial fit (red line). The polynomial order was adjusted to match the spectrum decay (see Figure 3.17).

which is consistent with typical $\mathbf{E} \times \mathbf{B}$ drifts over Arecibo.

The base of the ionosphere is a marker for the dynamics. To take advantage of this we have taken a specific density contour (10^5 cm^{-3}) and replotted it in Figure 3.16 along with a polynomial fit to the data. Inspection shows a steepened few-hour component and a weak $\sim$50-minute modulation that is present all night. To verify this, we have Fourier analyzed this time-dependent signal. We plot the spectrum in Figure 3.17 along with the spectrum of the polynomial fit. Deviations from the polynomial spectrum are interesting. The first two peaks (which the polynomial reproduces) are at the fundamental and the first harmonic of the steepened structure. The next peak is at about 50 minutes. To inspect the high frequency components, we have subtracted the polynomial fit from the data and plotted the result in Figure 3.18 for seven different contour levels. A clear downward phase progression is observed with a downward phase velocity of about 50-60 m/s. This velocity was estimated at a time when the altitude of the layer was approximately constant. The modulation is about 8 km peak-to-peak in the 10^5 cm^{-3} contour. We interpret the electron density signature to be due to advection of the bottomside gradient by the gravity wave neutral wind projection along $\mathbf{B}$. A wind of a few meters per second is sufficient to create the observed effect. Note that the period of the 50-minute wave seems to
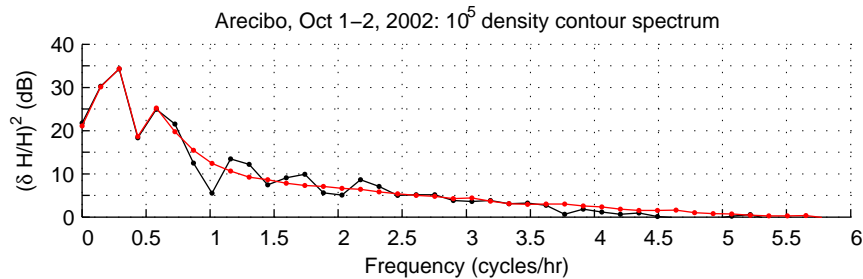
Figure 3.17: Normalized fluctuation spectrum of the density contour in Figure 3.16 (black) and of the polynomial fit (red). To avoid contamination from the irregularities, only the portion of the curve indicated by the polynomial in Figure 3.16 was analyzed.

increase somewhat as time goes on. This may be indicative of a Doppler-shifting effect due to neutral winds.

A downward phase velocity of 55 m/s and a period of 50 minutes implies a vertical wavelength of about 165 km. Note that this is consistent with Figure 3.18 - there is a little bit less than a $180°$ phase shift from the 10^4 cm^{-3} contour to the $10^{5.5}$ cm^{-3} contour, implying that the contours should be spaced by about $\lambda/2 = 82.5$ km. By inspection of the contour heights at the appropriate time, we see that this distance is about right (see figure caption). Plugging these numbers into the linear dispersion relation for atmospheric gravity waves in the reference frame of the neutral wind (*Hines*, 1960), using a Brunt-Vaisala period of 13 minutes and a scale height of 50 km, we find a horizontal wavenumber near 10^{-5} rad/m, corresponding to a horizontal wavelength near 600 km. This is approximately consistent with the region of vertically propagating modes predicted by *Hines* (1960); including viscous effects, he finds a very small region where waves with periods greater than 40 minutes can propagate with vertical wavelengths of a few hundred kilometers.

Even smaller-scale structures can be seen from the spectrum in Figure 3.17, as there appear to be spikes at about 1.75 cycles/hour and 2.25 cycles/hour. We have high-pass filtered the data to remove the large-scale and 50-minute waves. The result
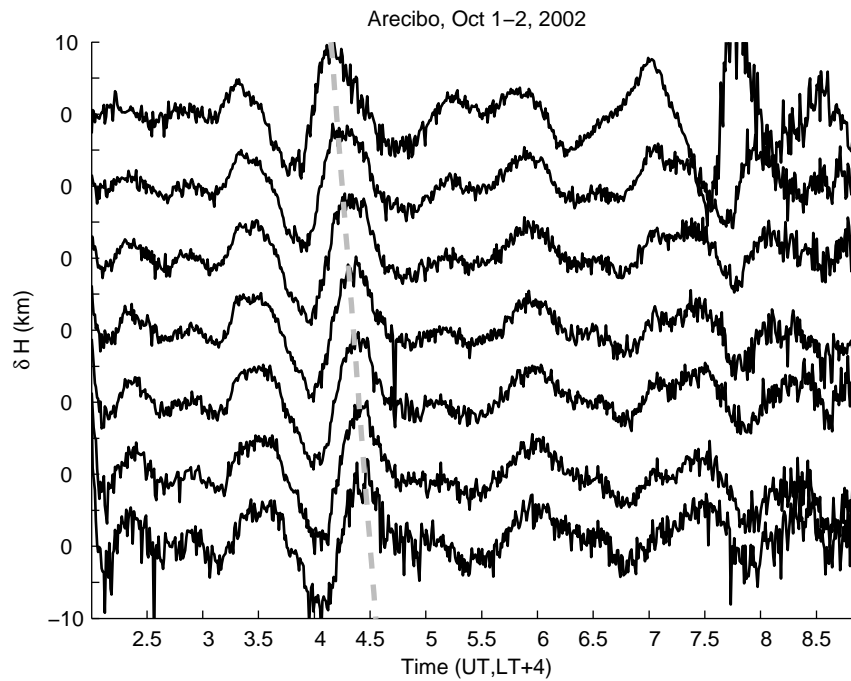
Figure 3.18: δH contours at several different densities, ranging from $\log n_e = 4$ to $\log n_e = 5.5$. Each tick mark represents a δH of 5 km. The dashed line shows the clear downward phase progression. Note that the y-axis is δH, not H. For reference, at about 0430 UT, the $10^{5.5}$ cm^{-3} contour is at about 350 km and the 10^4 cm^{-3} contour is at about 280 km.
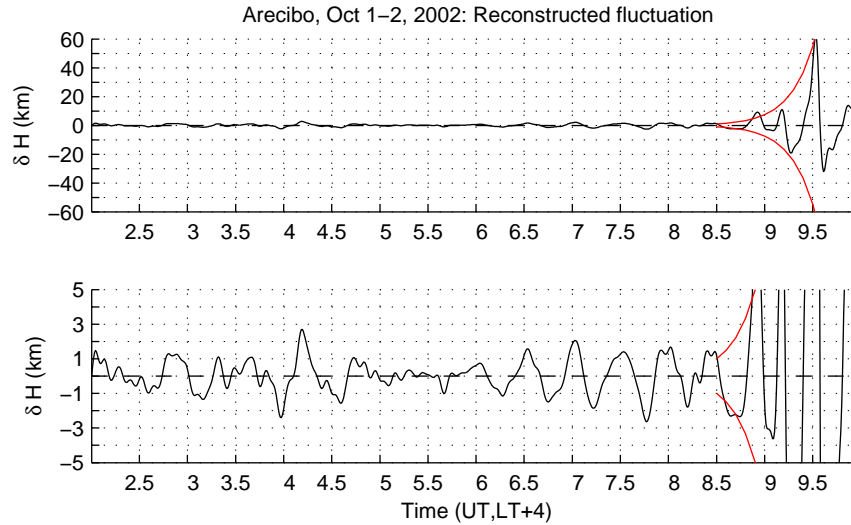
Figure 3.19: Shorter period fluctuations observed in the 10^5 cm^{-3} density contour. The two plots are the same except on different scales. The black line is reconstructed from the filtered signal, which was cutoff at 1.5 cycles/hour. The red line is an exponential fit to demonstrate the exponential growth.

is shown in Figure 3.19. The ∼30 minute wave is seen to grow exponentially as the layer rises. The ever increasing altitudinal extent of the irregularities gives a measure of the e-folding time and we find it to be about 15 minutes, as shown by the red line in Figure 3.19. Growth can be observed in the 50-minute wave, but the growth rate is more difficult to determine because of the longer period. Although we do not have a measurement of the vertical wavelength of the 30-minute wave, there is a much larger range of wavelengths allowed by the linear dispersion relation for this period than for the 50-minute wave (*Hines*, 1960).

We claim these data provide very strong evidence for gravity wave seeding. The 4-km amplitude seed grows to 20 km when the ionosphere is very high. To test the growth rate, we need to identify the instability. At first, we consider the generalized $\mathbf{E} \times \mathbf{B}$ process, in which winds and electric fields drive Pedersen currents that amplify any corrugations on the vertical bottomside gradient. But the ionospheric motion is downward during the growth time, most likely due to a southward wind component

in the large-scale TID, which is a stabilizing effect on the bottomside. The flow direction could be due to a westward electric field causing a downward/southward drift perpendicular to $\mathbf{B}$ or a northward wind pushing plasma downward/poleward parallel to $\mathbf{B}$. But in both cases, the associated Pedersen currents are westward, the direction for which an upward density gradient is stable.

We propose here an idea not previously considered but which might play a role in this unusual situation. Classically, linear instability theory rests on perturbation of an equilibrium situation. At the magnetic equator the equilibrium associated with the Rayleigh-Taylor instability is a balance between the downward gravitational force and the upward $\mathbf{J}_g \times \mathbf{B}$ force, where $\mathbf{J}_g$ is the gravitational current. Off the equator, the $\mathbf{J}_g \times \mathbf{B}$ force makes an angle to the vertical and thus cannot balance the gravitational force and no equilibrium exists. However, Figure 3.2 shows that in the time period 0500 to 0530 LT the height of the bottomside of the F layer did not change by more than 20 km. During this time, which might be called a quasi-equilibrium, gravitational current certainly flowed in the eastward direction. The magnitude of this current is related to a wind-driven Pedersen current by a ratio,

$$R = \frac{g}{U\nu_{in}} \cot I \qquad (3.15)$$

where ν_{in} is the ion-neutral collision frequency, U is the meridional wind, and I is the dip angle. For low values of ν_{in}, the ratio R can exceed unity. For example, at a bottomside height of 400 km and the MSIS neutral density for this date and time we find $R = 1.4$ for $U = 50$ m/s. Thus, even for stable directions of U, the eastward gravitational current could lead to bottomside instability. The gravitational current is stabilizing on the topside but $\mathbf{E} \times \mathbf{B}$ is destabilizing there so the effects tend to cancel. Also, $\mathbf{g} \times \mathbf{B}$ becomes small as the dip angle decreases.

Perturbation of such a quasi-equilibrium condition by this current system makes

sense only if the instability growth rate has a time scale faster than the time scale for the layer height change. The ratio of these two time scales is essentially identical to the reciprocal of R above and suggests that the bottomside would be unstable to the Rayleigh-Taylor instability. The growth rate for the instability is on the order of

$$\frac{g}{\nu_{in}L}\cos I \sin I \qquad (3.16)$$

where L is the vertical density gradient scale length. Just before the irregularities break out we find $L = 60$ km at 400 km, which yields an e-folding time of 28 minutes. This is fairly close to the estimate of the e-folding time estimated from the density fluctuations. It is interesting to note that the three major perturbations seen between 0500 and 0540 LT were progressively larger in altitude extent. The third mini-plume was at least larger by an e-fold than the first one detected, so the growth rate estimated for the gravitational process is consistent with the observation.

To reiterate, when the F layer is high, as it was during the outbreak of irregularities over Arecibo, the Pedersen conductivity is low. This fact also argues against the $\mathbf{E}\times\mathbf{B}$ instability since that instability is generated by F-region Pedersen currents, which must be large enough to support the electrical load of the E region and conjugate F region. This effect is not so pronounced for gravitational currents, since the effective conductivity for such currents is much larger than the Pedersen conductivity. This can be seen as follows. The gravitational current is given by $J_g = (nMg/B)\cos I$. The equivalent electric field for this current source is $(Mg/e)\cos I$ and hence the corresponding field-line integrated conductivity is Ne/B, where N is the field-line integrated plasma density. For a plasma density of 10^5 cm^{-3} and an integration over 100 km, this conductivity is 40 mho. This is more than an order of magnitude higher than the field-line integrated conductivity calculated using the Arecibo data during the period 0800-1000 UT. Thus, the gravitational process is capable of controlling the

electrodynamics during this period. Just after 1000 UT the build up of plasma as the sun rose dramatically increased the conductivity and the irregularities disappeared.

We should mention another possibility for producing F-region structure is electrical coupling from the E region to the F region (e.g, *Haldoupis et al.*, 2003; *Kelley et al.*, 2003a). This seems unlikely in this case for three reasons. First of all, quasi-sinusoidal E-region perturbations must have been present all night to give the oscillations we observe, which seems unlikely. Secondly, near the time when we see the unstable F region, the layers in the E region and hence their conductivity are the smallest all night. Finally, if the oscillations observed in the F region were due to quasi-sinusoidal E-region fluctuations, we would expect their amplitudes to be largest at the time when the ratio of the E-region conductivity to the F-region conductivity is the highest. However, the largest amplitudes occur near 0330-0400 UT when the F-region conductivity has its highest value for the entire evening due to the low altitude and the high electron density. As mentioned, near the time that the F region goes unstable, the E region basically disappears. Thus, it is possible that the decreased damping by the E region during this time period may have contributed to the breakout of the instability.

3.8   Conclusions

We have presented a mapping technique using the American network of GPS receivers to examine the TECP associated with large-scale TIDs and other disturbances. Using an example from the October 1-2, 2002 storm, we have shown that the method can reveal information on the horizontal and temporal structure of the disturbances. Comparing the TECP from the Arecibo ISR and the St. Croix GPS receiver, we find very good agreement, showing a TECP of $\pm$1-2 TECU associated with wind

pulses driving the F layer up and down. Maps using the method described here are produced every 5 minutes with 1° latitude-longitude resolution. Comparing this to the Japanese system (*Saito et al.*, 1998), these temporal and spatial resolutions are fairly crude, as in Japan nearly 1000 receivers are available in a small area, allowing a time resolution of 30 s and a spatial resolution of 0.15°. However, we should note that while we have fewer receivers in North America, they cover a much larger area, which is advantageous for imaging large-scale irregularities and their sources.

The TECP maps from October 1-2, 2002 indicate that multiple TIDs were launched from the auroral zone. This is consistent with other data from the Arecibo ISR, ionosondes, and imagers. The observed oscillations may be associated with a series of quasi-periodic substorms. The TECP maps, consistent with inferred neutral winds and F-layer motion, show the propagation of TEC bulges that appear to be associated with localized sources at high latitudes. We have presented evidence that the launching of the TIDs may be caused by Lorentz forcing resulting from westward current enhancements (Hall currents) in the auroral region. We have also shown that Joule heating rates are relatively modest during the storm and likely cannot account for the generation of the TIDs. Some oscillations were observed in the Joule heating rates, however.

Turning to the local Arecibo observations, we have analyzed the details of the ionospheric dynamics measured by the ISR and supporting instrumentation. Electron density enhancements are reported as the layer falls as a result of the TID poleward wind. The electron density enhancements are caused by plasma flux from the plasmasphere, which has been verified by the TEC measurements. The plasma flux from the plasmasphere can be estimated using the peak red line intensity after midnight. Our estimates indicate that the plasmaspheric flux could have exceeded 10^9 cm^{-2} s^{-1} at 0700 UT on October 2 when the $F2$ layer fell to 250 km and N_mF2 exceeded

10^6 cm^{-3}. This flux is very large and the plasmasphere needs an additional source of plasma before 0700 UT. The upward plasma motion induced by the equatorward wind phase of the TID at 0500 UT on October 2 seems to be this source.

The variations of the 630.0-nm nighttime intensity during the storm on October 1-2, 2002 are characterized by an additional peak before midnight. These fluctuations are a result of the winds associated with the passage of the large-scale gravity wave wind field. The red line intensities calculated by the model using ionospheric parameters measured by the ISR are in good agreement with the measured intensities around both peaks.

The height profile of the electron density of the $F2$ layer, uplifted to high altitudes, can be described by an analytical solution to the continuity equation including plasma motion induced by the equatorward wind, ambipolar diffusion, and gravity. We have found good agreement between the calculated and measured profiles at 0500 UT and 0800 UT using this approach. The gradient on the bottomside sharply increases when the $F2$ layer falls to about 250 km at 0700 UT on October 2. This electron density profile can be described by a different analytical solution to the continuity equation that includes recombination and downward motion induced by a northward wind. The calculated and measured profiles at 0700 UT are in good agreement.

The final uplift induced by the TID occurred near 0900 UT and caused the local ionosphere to go unstable. We have presented experimental evidence for the seeding of this plasma instability by a gravity wave. Previous publications in this area (e.g., *Kelley et al.*, 1981; *Kelley and Fukao*, 1991) only stated seeding as a hypothesis in an attempt to explain how the development of irregularities could occur given the low growth rate of the processes. We observe at least two potential seed waves for many hours, one with an observed amplitude excursion at the base of the ionosphere of about 4 km and a period of about 50 minutes, and the other with a fluctuation of

about 1 km and a period of about 30 minutes. Analysis of the larger-amplitude wave shows clear downward phase progression providing strong evidence for gravity waves and consistency with the linear theory. Near dawn, the shorter-period oscillations are found to grow rapidly to about 30 km in amplitude in a time of one hour, but only when the ionosphere is high. Our analysis precludes a bottomside $\mathbf{E} \times \mathbf{B}$ instability, which is stabilizing; but, the gravitational Rayleigh-Taylor process can overcome this. The large-scale TID in this case created conditions suitable for a smaller-scale plasma instability. We do not consider this to be a seeding mechanism. Rather, it played a similar role to that of the pre-reversal enhancement in the equatorial ionosphere, creating conditions conducive to instability.

Acknowledgments

Chapter 4

Observation and Modeling of Post-Midnight Uplifts near the Magnetic Equator*

When a dog bites a man that is not news, but when a man bites a dog that is news.
   - John Bogart

4.1   Abstract

We report here on post-midnight uplifts near the magnetic equator. We present observational evidence from digital ionosondes in Brazil, a digisonde in Peru, and other measurements at the Jicamarca Radio Observatory that show that these uplifts occur fairly regularly in the post-midnight period, raising the ionosphere by tens of kilometers in the most mild events and by over a hundred kilometers in the most severe events. We show that in general the uplifts are not the result of a zonal electric field reversal, and demonstrate instead that the uplifts occur as the ionospheric response

---

*This chapter based on the original published work, *Nicolls et al.* (2006c). Reproduced by permission of the European Geosciences Union.

98

to a decreasing westward electric field in conjunction with sufficient recombination and plasma flux. The decreasing westward electric field may be caused by a change in the wind system related to the midnight pressure bulge, which is associated with the midnight temperature maximum. In order to agree with observations from Jicamarca and Palmas, Brazil, it is shown that there must exist sufficient horizontal plasma flux associated with the pressure bulge. In addition, we show that the uplifts may be correlated with a secondary maximum in the spread-F occurrence rate in the post-midnight period. The uplifts are strongly seasonally dependent, presumably according to the seasonal dependence of the midnight pressure bulge, which leads to the necessary small westward field in the post-midnight period during certain seasons. We also discuss the enhancement of the uplifts associated with increased geomagnetic activity, which may be related to disturbance dynamo winds. Finally, we show that it is possible using simple numerical techniques to estimate the horizontal plasma flux and the vertical drift velocity from electron density measurements in the post-midnight period.

4.2   Introduction

It is well-known that the height of the F-region ionosphere is the major parameter in controlling the onset of equatorial spread F (ESF) (*Farley et al.*, 1970). This relationship is due to the fact that the growth rate for the generalized Rayleigh-Taylor instability is inversely proportional to the ion-neutral collision frequency, which decreases exponentially with altitude (*Kelley et al.*, 1979a). A second term in the growth rate depends on the eastward electric field, which is destabilizing after F-region sunset and stabilizing during the night as dictated by the nominal F-region electric fields driven by the dynamo wind systems (e.g., *Fejer et al.*, 1979).

Thus, it is no surprise that most observations of ESF are associated with the evening pre-reversal enhancement, during which the altitude of the ionosphere increases due to an increasing eastward electric field. The onset of ESF during this time period typically leads to a continuation of ESF throughout the post-sunset period, often beyond midnight, with an occurrence rate that decreases steadily throughout the night (*Kil and Heelis*, 1998; *Hysell and Burcham*, 2002). However, studies of post-midnight/pre-sunrise ESF have been fewer (e.g., *MacDougall et al.*, 1998), since ESF during this time period is in general much weaker and occurs much less frequently. Most statistical studies of the occurrence rates of ESF (e.g., *Abdu et al.*, 1983; *MacDougall et al.*, 1998) use ionosondes, where the instabilities produce a measurable spreading in range or frequency on an ionogram trace.

In this chapter, we discuss what could be a source for a secondary post-midnight maximum in the ESF occurrence rate that has been reported by *MacDougall et al.* (1998), who observed eastwardly convecting irregularity patches coincident with "bottomside bulges". Such a maximum was also observed by *Hysell and Burcham* (2002). We show observational evidence from digital ionosondes in Brazil and a digisonde at Jicamarca, Peru for what we term "post-midnight uplifts", which may be the same phenomenon as the bottomside bulges. The term "uplift" refers to the observed increase in height of the F-region ionosphere. We note here that such a "lifting" does not say anything about the sign of the electric field because of other terms in the continuity equation.

We explain these uplifts in terms of phenomena associated with the midnight pressure bulge (e.g., *Fesen*, 1996). This pressure bulge is associated with a convergence of meridional thermospheric winds near the equator (e.g., *Faivre et al.*, 2006), which produces interesting features such as the midnight temperature maximum (e.g., *Sastri et al.*, 1994) and the midnight density maximum (e.g., *Arduini et al.*, 1997).

We show that the uplifts are associated with a decrease in magnitude, but not a reversal, of the zonal electric field. A decrease in the magnitude of the westward electric field causes a waning of the reverse fountain effect (*King*, 1968). Using numerical simulations of the continuity equation, we show how the uplifts can occur despite the fact that the electric field does not change sign. We also focus on an extremely disturbed night during which the uplifts were amplified, and discuss how the uplifts may be enhanced by magnetic activity, which may be related to disturbance dynamo wind systems (e.g., *Blanc and Richmond*, 1980; *Richmond et al.*, 2003). We also show some ESF statistics from Brazil that seem to support the idea that these uplifts could be the source of a secondary maximum in ESF occurrence rates.

4.3 Observational Evidence

On the geomagnetically disturbed night of October 1-2, 2002, a series of large-scale traveling ionospheric disturbances (LSTIDs) propagated from high to low latitudes, causing large fluctuations in N_mF2 and h_mF2 as observed at the Arecibo Observatory (18.34°N, 66.75°W, dip 46°). This event has been reported and discussed by *Nicolls et al.* (2004) and *Vlasov et al.* (2005). *Nicolls and Kelley* (2005) also showed that the final LSTID before sunrise caused the Arecibo ionosphere to rise to over 450 km, and subsequently led to plasma structuring presumably due to some sort of instability mechanism. See Chapter 3 for more details.

In Figure 4.1 we show observations from two digital ionosondes in Brazil on this interesting night along with the previous night (October 1). The panels are iso-density contours from Sao Jose dos Campos (23.2°S, 45.9°W, dip -32°) and Palmas (10.2°S, 48.2°W, dip -11°) in Brazil. On October 2, at the low latitude station (Sao Jose dos Campos - SJC) we see oscillations in the height of the ionosphere induced
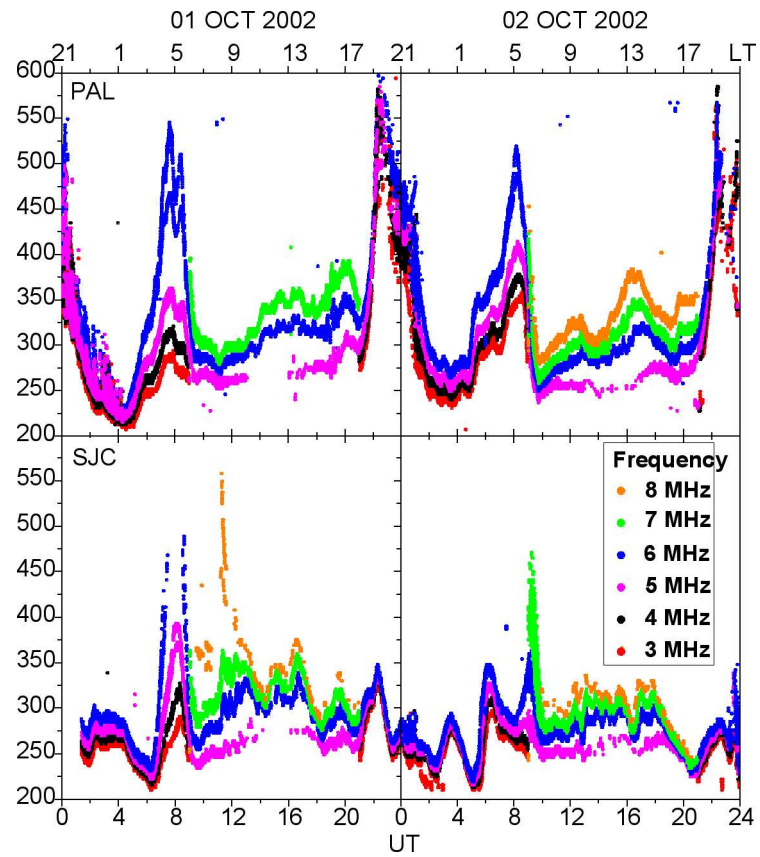
Figure 4.1: Virtual height contours as measured in Sao Jose dos Campos and Palmas, Brazil, on October 1 and 2, 2002.

by the propagating LSTID. These observations are very similar to those observed at Arecibo and are caused by the TID neutral winds coupled with a sufficient dip angle. At the equatorial station (Palmas - PAL) on this night we do not see these oscillations because of the much smaller dip angle. Instead, we see a large uplift of over 100 km between about 0500 and 0900 UT (0200 - 0600 LT). On the previous night (September 30-October 1), we do not see the oscillations associated with the LSTID. However, we do see an uplift at the equatorial station. It should be noted that on both October 1 and October 2 there was significant auroral electrojet (AE) activity, which could be a major cause of these height increases through disturbance electric fields. We discuss this possibility later.

In Figure 4.2 we show observations from instruments at the Jicamarca Radio Observatory (11.95°S, 76.87°W, dip 1°) on the night of October 1-2. The upper panel shows iso-density contours measured by the Jicamarca digisonde, and the lower panel shows coherent backscatter as measured by the JULIA radar (*Hysell and Burcham*, 1998). A large uplift of over 100 km is observed in the ionosphere. During the uplift, strong post-midnight irregularities were observed with plumes reaching up to 2000 km. It is interesting to note that the highest plume at about 0430 LT coincides with the time that the irregularity structure was observed at Arecibo (*Nicolls and Kelley*, 2005). However, the apparent simultaneity of the events might be misleading because post-midnight ESF at Jicamarca normally occurs during this time period (*Hysell and Burcham*, 2002) and any disturbed electric fields, caused for example by the TID, could enhance pre-existing irregularities.

The event on the night of October 1-2, 2002 was anomalous and coincident with a geomagnetic storm (*Nicolls et al.*, 2004). However, the uplifts occur fairly regularly in the equatorial ionosphere with no strong correlation to K_p. This is illustrated by the fact that the uplifts occurred on the previous night of September 30-October
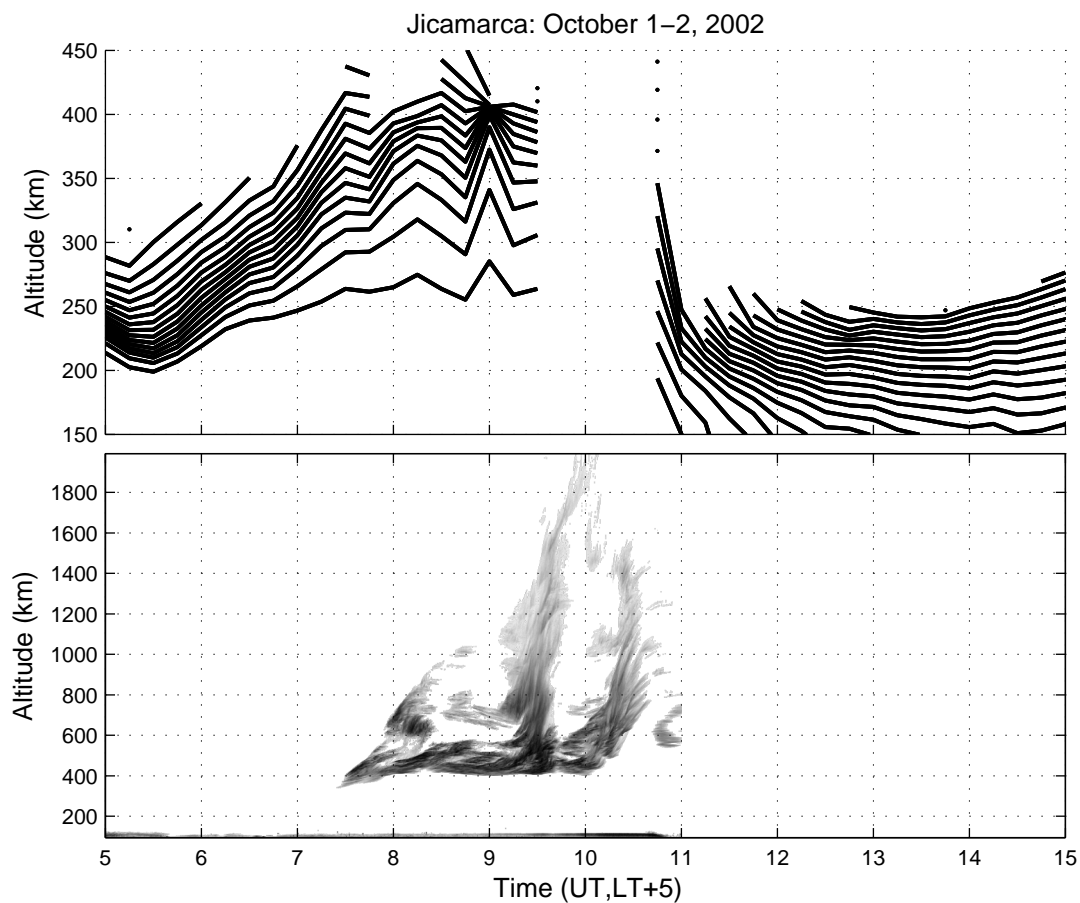
Figure 4.2: Isodensity contours as measured by the Jicamarca digisonde on October 2, 2002 and measurements of coherent backscatter from the JULIA radar at Jicamarca.
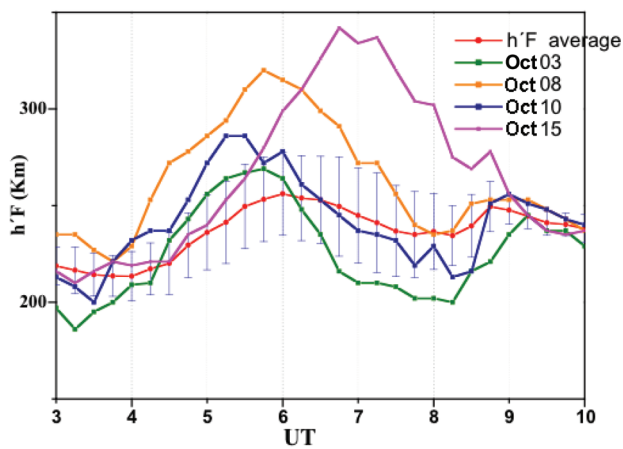
Figure 4.3: Virtual height of the F peak for several days in October 2002 along with the monthly average as measured at Palmas, Brazil.

1 as well, which was a much quieter night (see Figure 4.1). Figure 4.3 shows the virtual height of the F peak for several other days in October along with the monthly average with errorbars corresponding to the standard deviation. We should note that while relatively quiet, these nights were all disturbed to some degree, as dictated by the auroral electrojet indices, especially several hours preceding the layer uplift. The quietest of the days, October 15, was preceded by weak AE activity on the previous day. We discuss the potential influence of auroral activity later, however we should emphasize that the uplifts appear to be a quiet-time phenomenon but strongly sensitive to auroral activity. The monthly average indicates an average uplift of about 50 km in the month of October 2002, with significant variations on that curve as noted by the example days.

The averages for many months between 2002 and 2004 are shown in Figure 4.4. We have binned them here in terms of season into equinox and winter/summer, and we show f_0F2 on the bottom and $h'F$ data on the top (the virtual height of the F peak). In the virtual height data, the uplifts are evident at equinox, and are especially pronounced during a couple of months (dark blue and orange curves) which correspond to October of 2003 and October of 2002, respectively. The uplifts are evident, however, in most of the equinox curves. In the winter/summer curves, the uplifts are not present except for a weak one in June of 2002 (red curve). The signature of the uplifts can also be seen in the f_0F2 data for equinox. After midnight, the density decreases relatively constantly at a rate of about 2 MHz per hour as a signature of the reverse fountain effect. However, during the time of the uplifts, a slowing of the density decrease is observed to about 1 MHz per hour, which should be expected. This is a result of a decrease in the recombination rate as the ionosphere rises. The seasonal variation of the uplifts and the role of the reverse fountain effect will be discussed later.
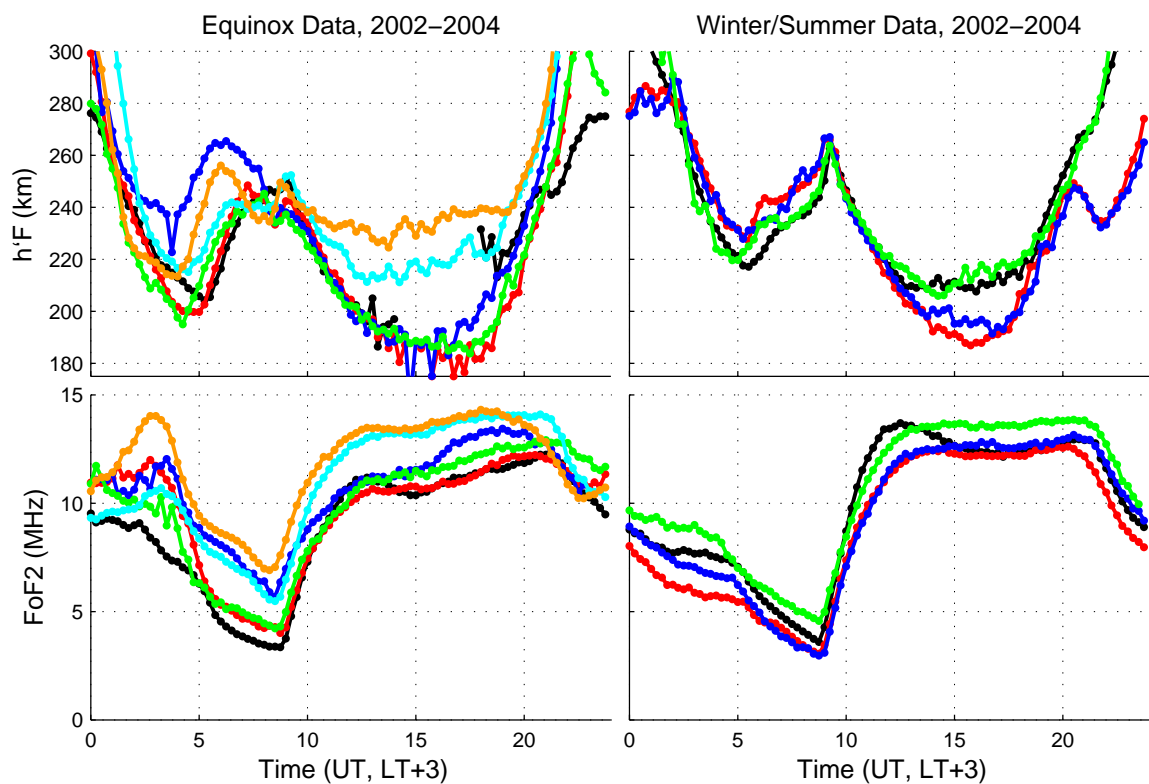
Figure 4.4: Monthly averages of f_0F2 (left) and $h'F$ binned into equinox and winter/summer months as measured in Palmas, Brazil.
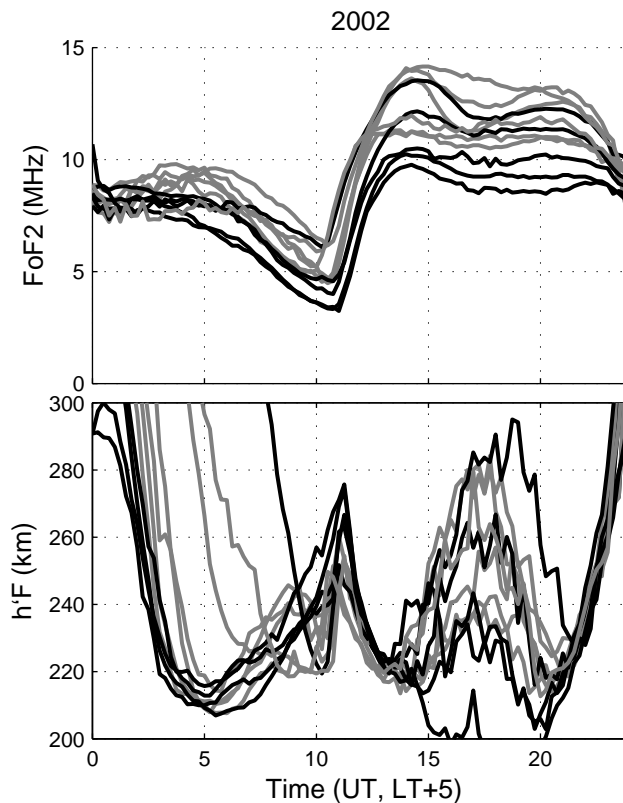
Figure 4.5: Monthly averages of f_0F2 (top) and $h'F$ (bottom) as measured by the Jicamarca digisonde. The black curves correspond to winter/summer data and the gray curves correspond to equinox data.

A similar plot as Figure 4.4 using the Jicamarca digisonde is shown in Figure 4.5. The data plotted here are from 2002, and each curve is a monthly average with the gray lines representing equinox months and the black lines representing winter/summer months. The uplifts are again evident in the post-midnight period (before 1000 UT) in the equinox months. The magnitude of the average uplifts are not much different than those measured at Palmas, despite the near-zero dip angle at Jicamarca. The uplifts should not be confused with the significant rise in $h'F$ after 1000 UT. This spike in $h'F$ may be caused by the low value of f_0F2 (near the lowest sounding frequency), which makes it nearly impossible to determine $h'F$.

4.4   Simulations of Post-Midnight Uplifts

In the preceding section, we showed evidence that post-midnight uplifts occur near the magnetic equator on a fairly regular basis. It is well-known that the zonal electric field is westward at night (e.g., *Fejer et al.*, 1979; *Kelley*, 1989) and there is no reason to think that the zonal electric field is changing sign at this time since such a trend does not show up in long-term averages except perhaps during summer solstice, solar minimum periods. We show some case studies with uplifts later that show indeed that a reversal does not occur. There is a general trend, however, of smaller fields for all seasons during solar minimum conditions.

The major forces that can drive the ionosphere upwards besides the effect of electric fields are those caused by neutral winds and the horizontal advection of plasma, while recombination can cause an apparent motion leading to an uplift as we have defined it (see the introduction). We show in this section that the daily uplifts discussed in Section 4.3 can be explained by including the role of recombination in the continuity equation. Off the equator, winds and diffusion become important and enhance the uplifts. At the equator, there is really no way that winds can directly produce an uplift. For reference, a meridional neutral wind of several hundred meters per second would be required to produce a local uplift of 50 km over the course of an hour at the dip latitude of Jicamarca. Such magnitudes are not observed (e.g., *Biondi et al.*, 1999). However, winds can indirectly produce an uplift through meridional advection of plasma, driven by a latitudinal gradient in electron density.

4.4.1   Recombination

The ionospheric response to recombination only is well-known (e.g., *Banks and Kockarts*, 1973; *Rishbeth and Garriott*, 1969). However, we present a discussion here in order

to illustrate the differences when a finite vertical drift is included.

For the Northern Hemisphere case, we define the $\hat{y}$ coordinate as parallel to the magnetic field, the $\hat{z}$ coordinate as perpendicular to the magnetic field and north (vertical at the equator), and the $\hat{x}$ coordinate as perpendicular to the magnetic field and east, and the vector velocity may be written as

$$\mathbf{v} = \mathbf{v}_\perp + \mathbf{v}_{||} = v_{\perp n}\hat{z} + v_{\perp e}\hat{x} + v_{||}\hat{y}. \tag{4.1}$$

The continuity equation is,

$$\frac{\partial n_e}{\partial t} + \nabla \cdot (n_e \mathbf{v}) = P - L \tag{4.2}$$

where P and L refer to production and loss terms, respectively. The continuity equation may be written as

$$\frac{\partial n_e}{\partial t} + n_e \left(\nabla \cdot \mathbf{v}_\perp\right) + \mathbf{v}_\perp \cdot (\nabla n_e) + n_e \frac{\partial v_{||}}{\partial x} + v_{||}\frac{\partial n_e}{\partial x} = P - L. \tag{4.3}$$

There is no production term at night and the loss term is due to recombination, which is controlled by the reactions that convert O^+ to molecular ions (which then quickly recombine dissociatively). The major reactions in the F-region are thus

$$O^+ + O_2 \rightarrow O_2^+ + O$$
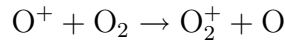
with reaction rate (*St.-Maurice and Torr*, 1978)

$$\gamma_1 = 2.82 \times 10^{-11} - 7.74 \times 10^{-12}(T_{eff}/300) + 1.073 \times 10^{-12}(T_{eff}/300)^2$$
$$-5.17 \times 10^{-14}(T_{eff}/300)^3 + 9.65 \times 10^{-16}(T_{eff}/300)^4 \quad \text{cm}^3\text{s}^{-1} \tag{4.4}$$

and

$$O^+ + N_2 \rightarrow NO^+ + N$$
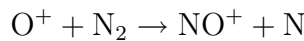
with reaction rate (*St.-Maurice and Torr*, 1978)

$$\gamma_2 = 1.53 \times 10^{-12} - 5.92 \times 10^{-13}(T_{eff}/300) + 8.6 \times 10^{-14}(T_{eff}/300)^2 \quad \text{cm}^3\text{s}^{-1} \tag{4.5}$$

where $T_{eff} = 0.667T_i + 0.333T_n$. The loss term can be written as

$$L = \beta n_e$$

where β is the recombination coefficient,

$$\beta = \gamma_1[O_2] + \gamma_2[N_2].$$

Then,

$$\frac{\partial n_e}{\partial t} + n_e \left(\nabla \cdot \mathbf{v}_\perp\right) + \mathbf{v}_\perp \cdot \left(\nabla n_e\right) + n_e\frac{\partial v_\|}{\partial x} + v_\|\frac{\partial n_e}{\partial x} = -\beta n_e. \tag{4.6}$$

For the case at the magnetic equator, we first make the assumptions that there are no parallel or perpendicular-east gradients in electron density. Then, we are left with the vertical velocity (perpendicular-north) term. Assuming no vertical velocity, we obtain the simplest continuity equation dominated by recombination,

$$\frac{\partial n_e}{\partial t} = -\beta n_e \tag{4.7}$$

with solution

$$n_e(z, t) = n_{e0}(z)e^{-\beta(z)t}$$

where $n_{e0}(z)$ is the initial density profile. The effect of recombination in the absence of a vertical drift is to eat away at the bottomside density, increasing the bottomside gradient, decreasing the peak density, and increasing the peak height.

If we let the initial density profile be a Chapman profile,

$$n_{e0}(z) = n_{m0} \exp\left[\frac{1}{2}\left(1 - \frac{z - z_{m0}}{H_{ch}} - e^{(z_{m0}-z)/H_{ch}}\right)\right] \tag{4.8}$$

(note the change in sign convention for z from previous chapters), then there is an interesting analytical solution for the peak height and density in the case that β is constant in time and decays exponentially in altitude with the Chapman scale height, i.e.

$$\beta(z) = \beta_0 e^{(z_{m0}-z)/H_{ch}} \tag{4.9}$$
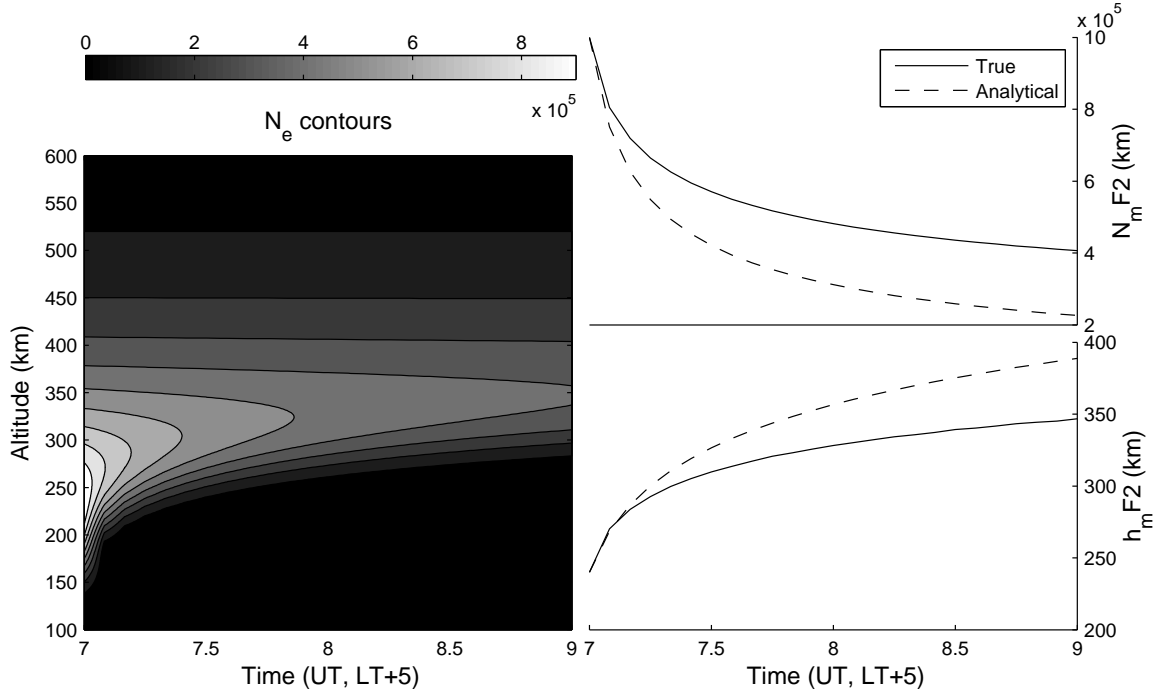
Figure 4.6: Electron density as a function of time and altitude for the case of recombination only. The left panel is a contour plot of n_e. The right panel is N_mF2 (top) and h_mF2 (bottom). The solid lines correspond to the values using the recombination rate calculated from MSIS and the dashed lines correspond to the analytical solution of Equations 4.10 and 4.11, which are based on the assumption of Equation 4.9.

where β_0 is the recombination coefficient at the peak. In this case, the altitude of the peak and the peak density can be shown to be

$$z_m(t) = z_{m0} + H_{ch} \ln\left[1 + 2\beta_0 t\right] \tag{4.10}$$

$$n_m(t) = \frac{n_{m0}}{\sqrt{1 + 2\beta_0 t}} \tag{4.11}$$

where n_{m0} and z_{m0} correspond to the peak density and altitude of the initial profile.

To demonstrate the behavior of the ionosphere under recombination only, we show an example in Figure 4.6. In this case, we have taken the initial electron density profile to be a Chapman layer with scale height $H_{ch} = 50$ km. The calculation is run for two hours and the neutral densities from the MSIS-90 model (*Hedin*, 1991a) are used to calculate the recombination coefficient for the conditions in the early morning of

October 8, 2002. The left-hand plot shows contours of electron density and the line plots show N_mF2 and h_mF2, along with n_m and h_m computed from Equations 4.10 and 4.11. It should be clear from these line plots that in general the recombination rate scale height is much smaller than the Chapman scale height, in contrast to the assumption of Equation 4.9. As can be seen from the figure, the ionosphere rapidly recombines for a short period. The height of the ionosphere increases and the peak density decreases. There is an observed uplift.

4.4.2 The Role of a Finite Vertical Drift

Now, let us consider the role that vertical motion plays in this process. Again at the magnetic equator, neglecting horizontal gradients, the continuity equation, Equation 4.6, becomes

$$\frac{\partial n_e(z,t)}{\partial t} + v_z(z,t)\frac{\partial n_e(z,t)}{\partial z} + n_e(z,t)\frac{\partial v_z(z,t)}{\partial z} = -\beta(z,t)n_e(z,t) \qquad (4.12)$$

where we have strictly included the time and altitude dependences. The velocity, v_z, in Equation 4.12 refers to the $\mathbf{E} \times \mathbf{B}$ drift caused by a zonal electric field. Experimental data show that v_z is approximately uniform with altitude in the F region in the post-midnight period so that the z dependence can be dropped. Physical analytical solutions to this equation are difficult to obtain, even for a constant drift, and we must turn to a numerical approach.

To illustrate the effect of a finite vertical drift, we have run numerical simulations for the case of a constant westward electric field (downward drift) with varying magnitudes, which are plotted in Figures 4.7 and 4.8. The initial profile was taken to be Chapman with a scale height of about 65 km and a peak density at 320 km of about 9.4×10^5 cm^{-3} corresponding approximately to the profile measured by Jicamarca at 0100 LT (0600 UT) on April 16, 2002. The simulations are run for 4 hours. Figure 4.7
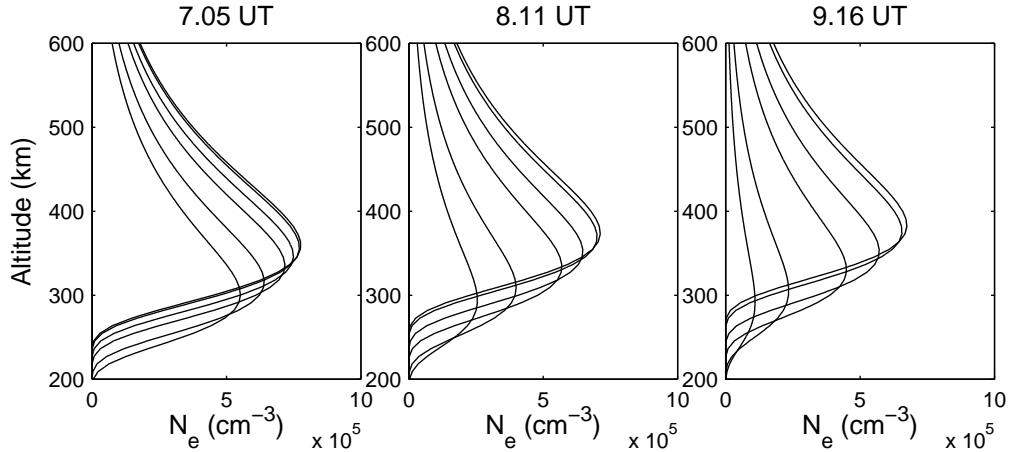
Figure 4.7: Profiles of electron density about 1, 2, and 3 hours into the simulation for constant downward velocities. The profiles with the lowest densities correspond to the highest downward velocities.

shows profiles at about 1, 2, and 3 hours into the simulation, for 6 different values of v_z of 0, -1, -5, -10, -20, and -30 m/s. Figure 4.8 shows contour plots for each of the cases. The major observation from these curves is that a downward drift leads to a faster decline in density (as one would expect) and at some critical velocity can overcome the uplift induced by recombination.

However, real drifts are a function of time and possibly height. In Section 4.5.1, we will include the effect of a time-dependent velocity.

4.4.3 Diffusion and Winds

Off the equator, in addition to the electric field, ambipolar diffusion, gravity, and neutral winds become important and their role in the vertical velocity must be included in the continuity equation. Equation 4.12 becomes (e.g., *Banks and Kockarts*, 1973)

$$\frac{\partial n_e}{\partial t} + \frac{\partial}{\partial z}\left[-D_a \sin^2 I \left(\frac{\partial n_e}{\partial z} + \frac{n_e}{H_p} \right) + v_z n_e \cos I - u_n n_e \sin I \cos I \right] = -\beta n_e \quad (4.13)$$

where $D_a = k_b T_p / m_i \nu_{in}$ is the ambipolar diffusion coefficient, I is the magnetic dip angle, $H_p = k_b T_p / m_i g$ is the plasma scale height, $T_p = T_i + T_e$, u_n is the northward
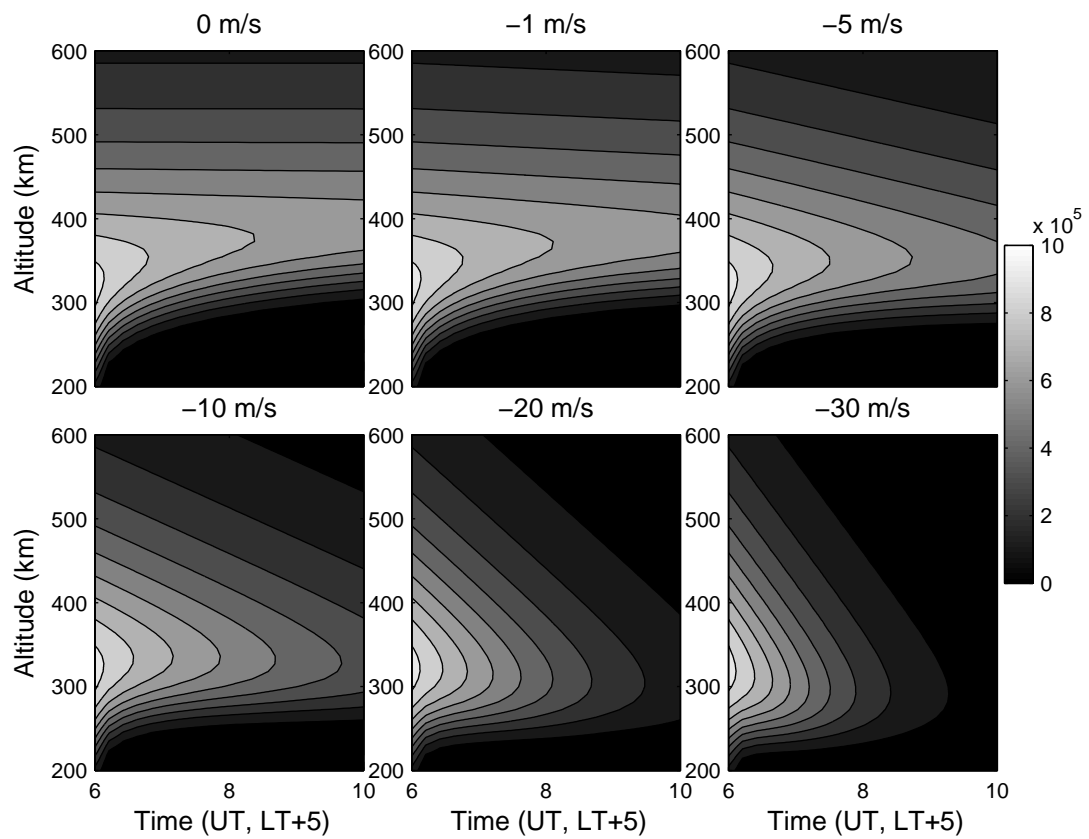
Figure 4.8: Contour plots of the electron density for the different values of a constant downward velocity.
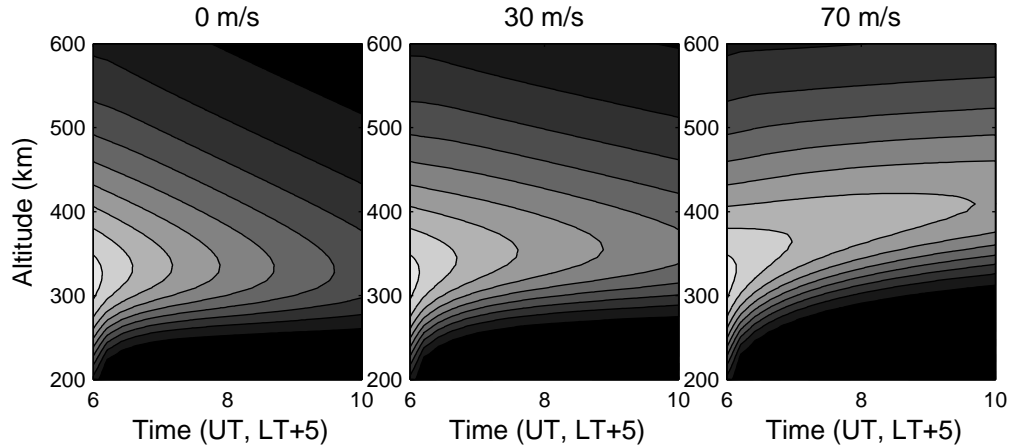
Figure 4.9: Contour plots of the electron density for the different values of a constant neutral wind as described in the text. The color scale is the same as that in Figure 4.8.

neutral wind, ν_{in} is the ion-neutral collision frequency, and we have ignored temperature gradients and other neutral motions. It can be expected that diffusion should reduce the magnitude of the uplifts but that neutral winds might enhance them in the case of an equatorward wind. Equatorward winds are observed at low and mid-latitudes after midnight (e.g., *Biondi et al.*, 1999), although there is an abatement of the wind (e.g., *Herrero et al.*, 1993) associated with the midnight pressure bulge (e.g., *Fesen*, 1996), which is related to the convergence of winds near the equator (e.g, *Faivre et al.*, 2006). Some analytical solutions to various simplified versions of this continuity equation have been obtained (e.g, *Banks and Kockarts*, 1973; *Duncan*, 1956; *Dungey*, 1956; *Martyn*, 1956; *Rishbeth and Garriott*, 1969; *Vlasov et al.*, 2005). However, in general a numerical approach is necessary.

Examples of the behavior with winds, diffusion, and a vertical velocity are shown in Figure 4.9 for a constant downward drift of 10 m/s and three different values of equatorward wind: 0 m/s, 30 m/s, and 70 m/s. The same initial profile as before was used and the simulation corresponds to the location of Palmas. At 0 m/s, we see a curve similar to that of Figure 4.8 except with slightly increased falling velocity due

to the inclusion of diffusion. At 30 m/s, we see a sizable uplift, and at 70 m/s, we see a huge uplift of almost 100 km.

4.5 Discussion

4.5.1 Comparison to Observations

In the previous section, we showed evidence that recombination induces an apparent uplift at the magnetic equator provided that the downward vertical drift (westward electric field) is sufficiently small. In this subsection, we compare our modeling results to some Jicamarca measurements.

On April 16, 2002, a mild uplift of 40-50 km was observed in the post-midnight period at Jicamarca. The radar was operating in the drifts (perpendicular) mode and densities were estimated using the differential phase approach (*Feng et al.*, 2004; *Kudeki et al.*, 1999). The measured velocity is shown in the top panel of Figure 4.10 as the solid line, and a polynomial fit used in our simulation is the dashed line. The drift was assumed constant as a function of altitude. An initial density profile corresponding to a fit to the measurements was used, which corresponded to a bottomside scale near 65 km and a larger topside scale. The altitude of the peak, h_mF2, as measured by Jicamarca is shown as the blue line in the second panel, and the model results are shown in black. N_mF2 as measured by Jicamarca is shown as the green line and the model results are shown in red. The lower panels show the modeled and measured densities as a function of height and time. We should note that we have increased the recombination coefficient slightly over the value given using the MSIS parameters for this case to match the observed density decrease.

The downward vertical drift velocity decreases after 0100 LT and reaches a minimum downward velocity of near 0 m/s at 0300 LT, at which point it increases again.
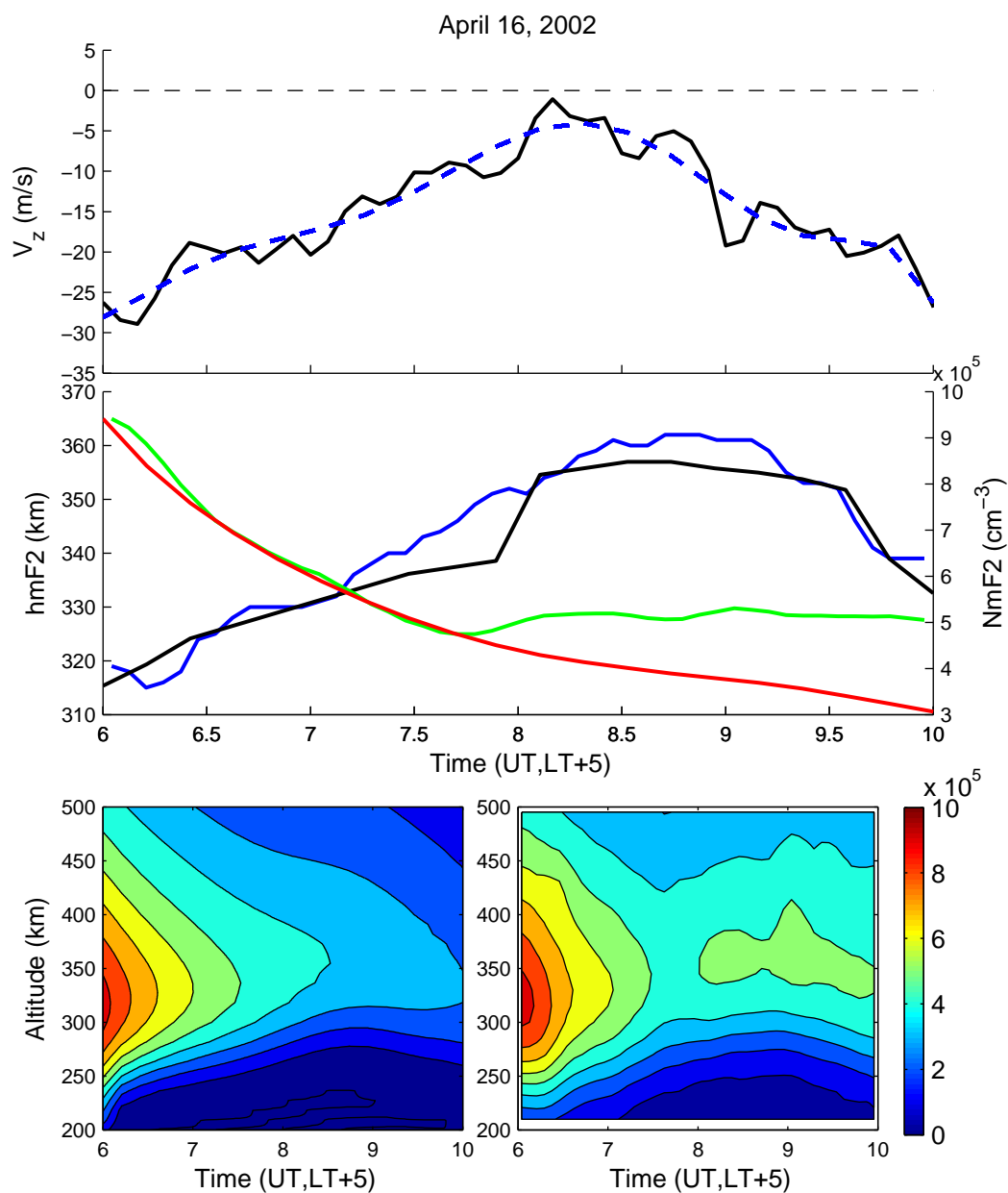
Figure 4.10: Data and simulations on April 16, 2002. The top panel is the vertical drift measured by Jicamarca (black solid) and the drift used in the model run (blue dashed). The second panel is h_mF2 (measured in blue, modeled in black) and N_mF2 (measured in green, modeled in red). The lower panel is a density contour plot of the model (left) and measurements (right).
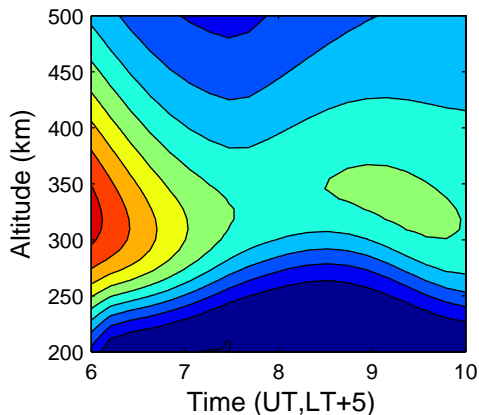
Figure 4.11: Contour plot of modeled densities including a horizontal plasma flux term as described in the text. The color scale is the same as in Figure 4.10.

This is a characteristic that is observed frequently during the uplifts. From the model behavior described in the preceding section, we would expect an uplift at this point and this is exactly what we see. The h_mF2 comparisons show that the model reproduces the uplift in height quite well. However, in comparing the densities, we see that up until about 0300 LT, they agree very well, but after that point, there is a large discrepancy. In fact, N_mF2 increases, which can be seen more clearly in the color plot in Figure 4.10 where we see a secondary maximum in density in the Jicamarca data. This maximum cannot be explained by including only recombination and the one-dimensional plasma motion.

In order to explain this increase, we must consider additional sources of ionization. Possibilities include actual production (which seems unlikely at night), a shear in the vertical drift (the drift would have to increase in magnitude with increasing altitude), or a gradient in horizontal plasma flux, corresponding to either a meridional or a zonal gradient in electron density. A meridional plasma flux could be interpreted as the horizontal advection of the equatorial anomaly into the equatorial region, which seems to be the most likely explanation. This advection may be associated with the midnight pressure bulge caused by a convergence of thermospheric winds at low

latitudes.

If we subtract the electron density data from the model to obtain the difference, and take the time derivative, we obtain an estimate of the ionization rate necessary for the model to agree with the data (this estimate is only approximate since it ignores recombination and is only calculated at the peak). We find that in this case the rate is close to constant after 0230 LT with a value near 20-25 cm^{-3} s^{-1}. Such an ionization rate seems too high to be caused by a shear in the vertical drift, implying that plasma flux must be the major source of ionization. Thus, the ionization rate gives us an estimate of the derivative (horizontal gradient) of the plasma flux. The total electron content transported to the equatorial region for such a horizontal plasma flux can be computed as 25 cm^{-3} s^{-1} multiplied by the vertical scale (about 100 km) multiplied by the time scale of the flux. This flux persists for at least 2.5 hours, giving a total electron content of about 2.25 TECU (1 TECU = 10^{12} cm^{-2}) for a gradient in flux of 25 cm^{-3} s^{-1}. This is a reasonable change in the vertically integrated electron density observed at at Jicamarca in the post-midnight period, which is typically greater than 10 TECU (e.g., *Valladares et al.*, 2001). We note that our estimate of the flux and associated TEC increase is probably an upper limit.

Figure 4.11 shows the results of incorporating the necessary horizontal gradient in plasma flux, and we now see very good agreement with the observed density behavior with the model N_mF2 variation matching the data almost exactly. The total electron content from 200-450 km for the two simulations (with and without flux) and for the data are compared in Figure 4.12. The results are in reasonable agreement with the estimations above. The source of this flux is likely a meridional density gradient.
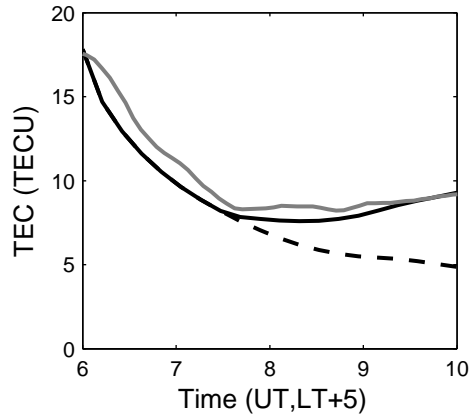
Figure 4.12: Total electron content (TEC) from 200 to 450 km for the simulation results presented in Figure 4.10 (dashed black) without flux, the simulation results presented in Figure 4.11 (solid black) with flux, and the data (gray).

4.5.2 Interpretation and Variation of Uplifts

We have shown that uplifts occur fairly regularly in the equatorial ionosphere. The uplifts are not caused by a reversal of the zonal electric field, as shown in the case study presented in the previous section and as can be seen by looking at other datasets. However, comparisons to Jicamarca drifts indicate they occur when the downward nighttime vertical drift is small or decreasing, which allows recombination to become significant.

The source of the variation in the zonal field is related to variations in the thermospheric wind driving the F-region dynamo. These variations are associated with the midnight temperature maximum, or midnight pressure bulge, and a convergence of winds at low latitudes (e.g., *Herrero et al.*, 1993; *Faivre et al.*, 2006; *Fesen*, 1996; *Sastri et al.*, 1994). Observations (e.g., *Burnside et al.*, 1981; *Herrero et al.*, 1993) have shown that there is an abatement in the meridional neutral wind associated with the pressure bulge. The F-region dynamo controls the magnitude of the zonal electric field and thus the decreasing zonal electric field is associated with the abatement in the dynamo winds. Presumably, the seasonal variations of the winds also contributes

to the seasonal variations of the uplifts described in Section 4.3.

We have mentioned the fact that the magnitude of the uplifts is related to auroral electrojet activity. Storm-time effects can cause variations in the equatorial electric fields through changes in the global wind system, penetrating electric fields (e.g., *Nishida et al.*, 1966; *Vasyliunas*, 1970; *Kelley et al.*, 1979b), and disturbance dynamo winds driven by Joule heating (e.g., *Blanc and Richmond*, 1980). It is unlikely that the effects we are observing are due to penetrating electric fields since there are no rapid variations in the interplanetary electric field for the days we have examined. In addition, the under-shielding effect would cause a penetrating electric field that would be westward at these times, and we observe an eastward shift in the zonal field. However, weak disturbance dynamo effects could be causing the variations. A recent study by *Richmond et al.* (2003) has shown that at night the disturbance dynamo tends to drive a current that leads to reductions or reversals in the equatorial zonal electric field. This behavior appears to be consistent with the observations, an uplift and a decrease in the magnitude of the zonal electric field caused by weak auroral electrojet activity. From this explanation, it is clear how enhanced uplifts can occur during times of higher magnetic activity, when the disturbance dynamo becomes enhanced. As shown in the data from October 1-2, 2002 presented in Section 4.3, enhanced uplifts occur in response to geomagnetic activity. Storm-time effects induced for example by variations in the dynamo wind system could lead to an enhancement of pre-existing irregularities, leading to the behavior shown in Figure 4.2.

It might be thought that the decrease in magnitude of the zonal electric field can be interpreted in terms of the reverse fountain effect (e.g., *King*, 1968). The so-called fountain effect is caused in the daytime by the zonal field which drives plasma upwards. The plasma can then fall down the field lines to low latitudes where it creates the equatorial anomalies. At night, the reverse effect can occur. Downward

drifts cause decreased plasma pressure on the topside, which can pull plasma from low latitudes to the equatorial region. When this reverse fountain effect decreases in magnitude due to a decrease in the magnitude of the downward drift, an uplift can be caused via the mechanisms described already. The inclusion of recombination is essential to reproducing this uplift.

While the effect of the post-midnight wind abatement and the disturbance dynamo can explain the uplifts, it does not explain the density increase that is observed. The interpretation of the density increase in terms of the reverse fountain effect is not satisfactory because at the time of the uplift, the westward electric field is at its weakest and thus the plasma flux caused by the reverse fountain effect is also at its lowest. In order to explain this density increase, we have invoked a horizontal gradient in the meridional plasma flux in Section 4.5.1. This is an inward flux that could be driven by a westward electric field or by a convergence of neutral winds. But, as we have just stated, the observed westward electric field is becoming smaller, which should reduce the plasma flux, not increase it. Thus, the major source of the flux appears to be the convergence of the low latitude winds associated with the midnight pressure bulge. Other studies have reported a density increase associated with the midnight temperature maximum or midnight pressure bulge (e.g., *Arduini et al.*, 1997). At this time, it is unclear whether the pressure bulge is significant enough to drive the gradient in plasma flux that is required for this interpretation.

4.5.3 Equatorial Spread F

One of the potential implications of the post-midnight uplifts described in this chapter is the generation of a secondary maximum in spread-F occurrence rates. Many papers have described a secondary maximum in ESF occurrence in the post-midnight period (*Abdu et al.*, 1981, 1983; *Fejer et al.*, 1999; *Hysell and Burcham*, 2002; *Mac-*

Dougall et al., 1998). During periods of high geomagnetic activity, electric fields can penetrate to low latitudes and cause the equatorial electric field to reverse in the post-midnight period, which is a source of ESF during periods of high geomagnetic activity (*Kelley et al.*, 1979b; *Fejer et al.*, 1999). *Hysell and Burcham* (2002) divide the pre-sunrise ESF into two categories. The first, as described by *Farley et al.* (1970) and *MacDougall et al.* (1998), occur just before sunrise near the F peak. The other may be due to "dead bubbles". Thus it seems possible that the uplifts described in this chapter could contribute to the secondary maximum in ESF occurrence that occurs in the pre-sunrise period.

To illustrate that there is indeed a secondary peak in the ESF occurrence rate, we show Palmas ESF statistics in Figure 4.13 for several equinox months. The top panel of each plot shows the statistics for each day of the given month, with range spreading distinguished from frequency spreading as described in the caption. The dominant occurrence peak can be seen between 2000 and 2200 LT with a decline in rate after that point. A secondary peak is seen in all but one of the curves (April 2004), with an occurrence rate of near 40%, most pronounced in October 2002 and March 2004. The peak occurs between 0200 and 0400 LT. This corresponds nicely to the time of the uplifts, as depicted in Figure 4.4. It is interesting to note that the ESF observed in the late morning is largely of the frequency type. This was also observed by *Abdu et al.* (1983).

4.5.4 Extracting Velocities from Density Measurements

Recently, *Woodman et al.* (2006) have compared vertical drifts deduced from digisonde measurements to Jicamarca observations of the vertical drifts. The authors find fair agreement at times when strong convection dominates, for example near the pre-reversal enhancement, but poor agreement at times when production and recombi-
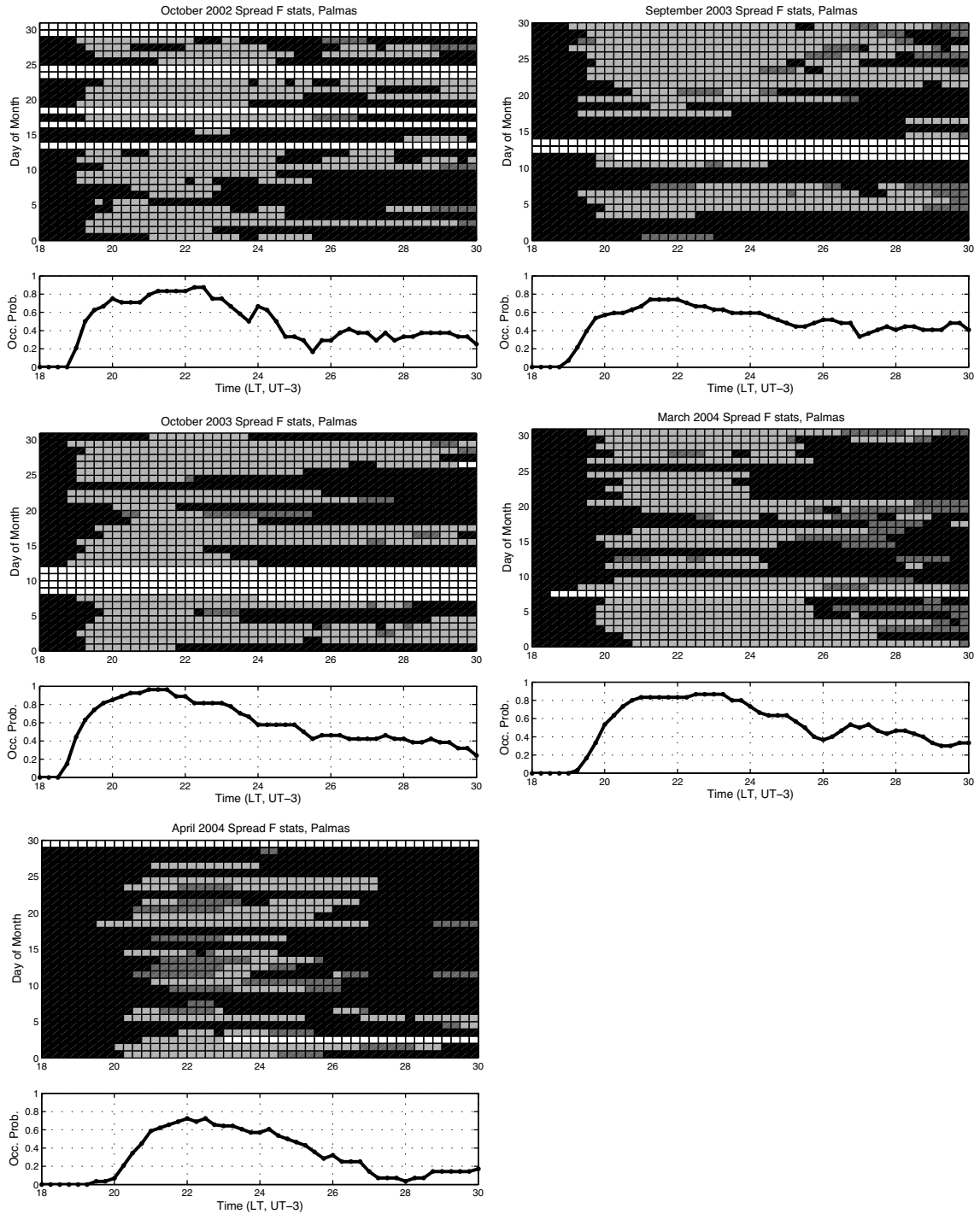
Figure 4.13: Spread-F statistics at Palmas for several equinox months in 2002, 2003, and 2004. The top panel is the spread-F statistics for the entire month as a function of local time and night of month. White corresponds to no data, black corresponds to no spread F, light gray corresponds to range spreading, and dark gray corresponds to frequency spreading. The lower panel is the averaged probability of occurrence of spread F for the month as a function of local time.

nation dominate. The digisonde drifts are deduced from the line-of-sight Doppler velocity, and such measurements have been relatively successful at high latitudes (e.g., *Scali et al.*, 1995). *Woodman et al.* (2006) show that the agreement is worst in the post-midnight period, and attribute this disagreement to the relative importance of recombination. There have been other studies on the role of recombination at the equator (e.g., *Bittencourt and Abdu*, 1981).

There exists a very simple method for estimating the drift from the continuity equation. Equation 4.12 can be solved for the vertical velocity with a horizontal plasma flux term included,

$$v_z = -\frac{\beta n_e + \partial n_e/\partial t + \partial(n_e v_x)/\partial x}{\partial n_e(z,t)/\partial z} \tag{4.14}$$

which is valid for the nighttime equatorial ionosphere. The plasma flux term can be due to either meridional or zonal gradients in density. Given bottomside density measurements, one can calculate the time and altitude gradients to estimate the vertical velocity. The plasma flux, of course, is more difficult to measure, although we have demonstrated in this chapter a simple method for estimating it given density measurements.

It is expected that digisonde drifts on average represent the motion of a constant density contour. Whether the drift is computed from the range rates of the echoes themselves or from the Doppler shifts shouldn't matter for total reflection. We show an example in Figure 4.14 for April 16, 2002. The top panel shows three constant density curves as a function of time from the model case study presented in Figure 4.11. The solid line with solid points in the bottom panel corresponds to the expected Doppler velocity that a digisonde would see, which corresponds to the change in height of a constant density contour as a function of time. This was averaged for the three contours in the top panel. The dashed line is the true velocity

used in the simulation. It is clear that the "Doppler" velocity is way off and unphysical - the velocity is not even the correct direction. The results are consistent with those presented by *Woodman et al.* (2006) which show a positive drift during this time period from the digisonde measurements, peaking between 0200 - 0400 LT. The crosses are the velocity estimates using Equation 4.14, including the plasma flux term, which fall exactly on top of the model curve. The small variation is due to errors in estimating the gradients. The circles are the calculations using Equation 4.14 but neglecting the plasma flux term, since that is in general difficult to estimate. Some error is induced by neglecting the flux, however the estimate is still very good compared to the Doppler result. Thus, it seems possible to estimate the vertical drifts using bottomside density profiles at times when the horizontal plasma flux is not too large. A similar technique was applied by *Bertoni* (2004) using the SUPIM model.

Note that both the recombination and the time derivative terms are quite important in general and neither should be neglected, at least in the post-midnight time period. During times of high convection (e.g., near the pre-reversal enhancement) recombination is negligible and the equation reduces to the motion of a constant density contour, as discussed by *Woodman et al.* (2006). Using Equation 4.14, the Doppler velocities can also be corrected for the effects of recombination and plasma flux in the form,

$$v_z = -v_D - \frac{\beta n_e + \partial(n_e v_x)/\partial x}{\partial n_e(z,t)/\partial z} \tag{4.15}$$

where v_D is the measured Doppler velocity.

4.6 Conclusion

We have shown observational evidence for post-midnight uplifts near the magnetic equator using data from a digital ionosonde in Palmas, Brazil and by a digisonde
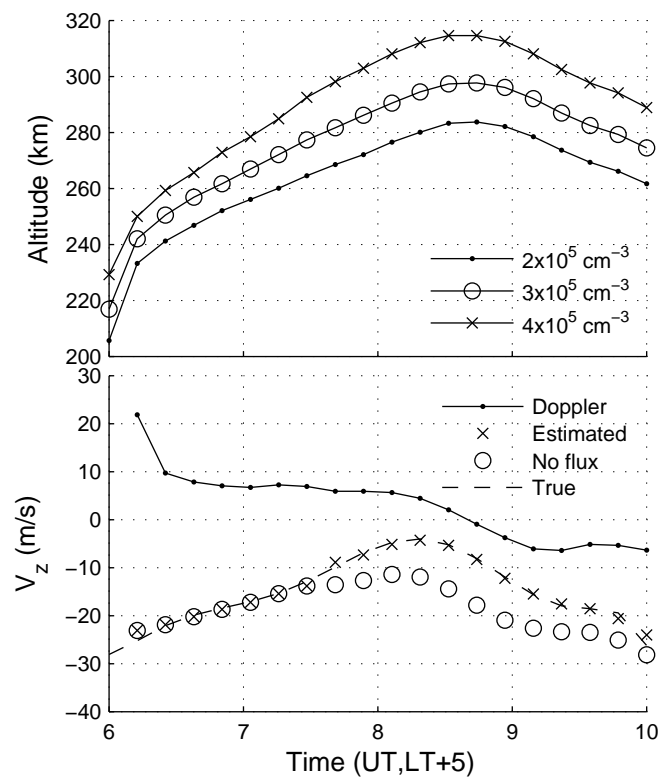
Figure 4.14: The top plot shows three constant density contours using the model results presented in Figure 4.11. The bottom plot shows the expected digisonde Doppler velocity (solid line with solid points), estimated velocity from density profiles (crosses), estimated velocity ignoring plasma flux (circles), and true velocity (dashed line).

at the Jicamarca Radio Observatory. These uplifts are in general not caused by a reversal in the zonal electric field, but such a reversal would enhance them, which may occur during active periods. During the time of uplift, the magnitude of the westward electric field decreases (but does not reverse) and recombination causes an apparent lifting of the layer, an increase in h_mF2. The change in the westward electric field during these time periods seems to be associated with an abatement of the equatorward neutral wind, induced by the midnight pressure bulge. Enhanced uplifts may be driven by auroral electrojet activity causing the disturbance dynamo to reduce the magnitude of the electric field, as studied by *Richmond et al.* (2003).

An interpretation of the uplift in terms of the reverse fountain effect cannot explain a density increase that is observed during the time of the uplift. In order to explain this increase, we have shown that horizontal plasma flux must be included in our model. These fluxes may be driven by meridional density gradients and a convergence of neutral winds at the equator associated with the midnight density maximum. Density and height data can be used to estimate the plasma flux in the post-midnight sector. Jicamarca-measured drifts in combination with digisonde density measurements could be used to study this flux. Our simple model can be combined with density curves, for example measured by a digisonde, to estimate vertical drifts at the magnetic equator in the post-midnight period.

In addition, we have shown that the uplifts may contribute to a secondary maximum in the equatorial spread-F occurrence rate that occurs in the post-midnight period. The extent of this maximum appears to agree quite well with the local time variation of the uplifts.

Acknowledgements

Chapter 5

The Spectral Properties of Low Latitude Daytime Electric Fields Inferred from Magnetometer Observations *

There is absolutely conclusive evidence against the supposition that terrestrial magnetic storms are due to magnetic actions of the sun; or to any kind of dynamical action taking place within the sun, or in connection with hurricanes in its atmosphere, or anywhere near the sun...

    - Lord Kelvin quoted in the *Proceedings of the Royal Society* in 1901, commenting on Kristian Birkeland's theories on the Sun-Earth connection. Quote from The Northern Lights by Lucy Jago.

5.1 Abstract

Four years of magnetometer data from two locations in Peru, one at the equator and one off the equator, have been converted to electric fields and their frequency

---

*This chapter based on the original work, currently under review, *Nicolls et al.* (2006b).

characteristics (fluctuation spectra) examined. In the frequency range from 0.1 to 30 cycles per hour, the average spectrum monotonically decreases. However, it deviates from a power law in the range 0.3 to 3 cycles per hour especially for high levels of activity. The integrated power above 0.15 cycles per hour is a strong function of K_p indicating that much of the fluctuations in the ionospheric equatorial field are of solar wind or magnetospheric origin. This result is in agreement with a previous power spectral study of low, middle, and high latitude fields using radars. The observed field strengths are lower than the ones observed in a previous study using balloon data at middle and high latitudes when the fields are projected to the equatorial plane. Simultaneous interplanetary electric field (IEF) data are compared to the equatorial field to determine how strong a relationship exists and to determine the amplitude and phase of their ratio as a function of frequency - an estimate of the average transfer function of the system. This function displays a bandpass-like form with a peak near 0.5 cycles per hour. This peak and evidence for a ringing of the time domain response suggests a weakly resonant system indicating some capacitance in the system in addition to the inductance of the ring current and the resistance of the ionosphere. Case studies show that application of this function to IEF data yields good results and support the notion that the response of the equatorial field to long-duration IEF polarities can last for many hours. Application of the function to test inputs such as pulses and triangle waves support this result. The magnitude of the average transfer function is only about 5 dB down from the maximum at a frequency corresponding to a 10-hour period. Thus, long-duration penetrating electric fields are captured by this empirical model. At high frequencies, we suggest that mapping of small-scale MHD turbulence is less effective than high frequency related transitions in the IEF.

5.2   Introduction

Ionospheric F-region $\mathbf{E} \times \mathbf{B}$ drifts have been studied for decades at equatorial latitudes, particularly using the powerful incoherent scatter radar (ISR) at the Jicamarca Radio Observatory (JRO) in Peru (e.g., *Fejer et al.*, 1979, 1989, 1991). In addition to the Jicamarca ISR observations, ionosondes (e.g., *Batista et al.*, 1996) and satellites (e.g., *Fejer et al.*, 1995) have also been used to study equatorial plasma drifts.

The average quiet-time behavior of the low latitude plasma drifts and its dependence on season and solar cycle have been studied in depth. Useful models of this quiet-time behavior have been developed (*Fejer*, 1997; *Richmond et al.*, 1980; *Scherliess and Fejer*, 1999). More recently, the behavior of the low latitude drifts during geomagnetically active periods has been studied in detail (e.g., *Fejer and Scherliess*, 1997; *Scherliess and Fejer*, 1997). The storm-time response of the low latitude fields is controlled by (a) the solar-wind/magnetosphere dynamo via penetration fields (e.g., *Fejer and Scherliess*, 1997; *Senior and Blanc*, 1984) and (b) the disturbance dynamo fields (e.g., *Blanc and Richmond*, 1980; *Scherliess and Fejer*, 1997). The former process is a prompt effect, associated with rapid turnings of the interplanetary magnetic/electric field (IMF and IEF, respectively) and operating on relatively short timescales of less than a few hours (e.g., *Fejer and Scherliess*, 1997). The latter process, on the other hand, is delayed for tens of hours and lasts for much longer, up to 30 hours (*Scherliess and Fejer*, 1997). *Scherliess and Fejer* (1999) have developed a global empirical model for the quiet-time equatorial vertical plasma drifts (eastward electric fields) based on Jicamarca ISR and AE-E satellite data, incorporating daily, seasonal, solar cycle, and longitudinal variations. This quiet-time model of the vertical plasma drift can be combined with the *Fejer and Scherliess* (1997) and *Scherliess and Fejer* (1997) models for penetration and disturbance dynamo fields, respectively,

to obtain a full empirical model of the vertical drift during geomagnetically active periods. Note that such a model does not include quiet-time fluctuations, which could be due to a number of sources. One must be cautious in separating the quiet-time fluctuations from the high latitude effects.

Direct electric field measurements at the equator are naturally sporadic in nature, as the Jicamarca ISR can realistically only operate a few days out of every month. However, recently a technique has been developed for inferring the daytime eastward electric field systematically from magnetometer data. *Gonzales et al.* (1979) showed that the eastward electric field could be inferred from the difference in the horizontal component of the magnetic field, ΔH, inferred from two low latitude magnetometers, one located at the magnetic equator and one located slightly off the magnetic equator. *Gonzales et al.* (1979) compared the result to simultaneous Jicamarca measurements. The subtraction is done to remove ring current contamination. *Rastogi and Klobuchar* (1990) developed this idea further. *Anderson et al.* (2002) demonstrated that there exists a quantitative relationship between ΔH and the eastward electric field, and *Anderson et al.* (2004) deduced these relationships in several forms, including a neural network trained on Jicamarca ISR measurements. *Anderson et al.* (2006) have extended these ideas to other longitude sectors. The intention is to incorporate this method into assimilative models (*Anderson et al.*, 2004, 2006). We should note that while the dominant contribution to ΔH is from the electrojet current, other sources, such as wind-driven currents (e.g., *Anderson et al.*, 2004; *Shume et al.*, 2005) and other current systems, are certainly significant at times and may add some limitations to this approach.

Due to the sporadic nature of the electric field measurements, studies of the relationship between the IEF and the electric fields at low latitudes have focussed on case studies (e.g., *Chakrabarty et al.*, 2005; *Earle and Kelley*, 1987; *Fejer et al.*, 1983; *Fejer*

and Scherliess, 1997; *Gonzales et al.*, 1979, 1980, 1983; *Kelley et al.*, 1979a, 2003b; *Kikuchi et al.*, 1996; *Nishida*, 1968; *Reddy et al.*, 1979; *Sastri*, 2002). Spectral studies of the ionospheric electric field at the equator are rare (e.g., *Chakrabarty et al.*, 2005; *Earle and Kelley*, 1987). In this chapter, we study the spectral properties of the several years of equatorial magnetometer data presently available in digital form and compare it to IEF data over the same period. Such a comparison serves to identify the sources of the electric fields at different fluctuation scales. We study both the average spectral properties in detail as well as some case studies. The linear relationship we find is not unrelated to a study by *Huang et al.* (2006), who developed a constant relationship between the IEF and the equatorward field for southward IMF. Our result has frequency response information, and can be used for either sign of the IEF. In *Kelley et al.* (2006), this method is used to investigate multi-longitude case studies and explore the effects of the disturbance dynamo.

5.3   Dataset Description

5.3.1   Equatorial Electric Field Data

The fluxgate magnetometers used in this study and their operations have been discussed by *Anderson et al.* (2004). One magnetometer is operated in Piura, Peru (5.18°S, 80.64°W) and the other at Jicamarca, Peru (11.92°S, 76.87°W). *Anderson et al.* (2004) presented several quantitative relationships between the vertical plasma drift at the equator and the ΔH value inferred from the magnetometers. Using measurements of the daytime $\mathbf{E} \times \mathbf{B}$ drifts from the 150-km region (*Chau and Woodman*, 2004) by the Jicamarca Unattended Long-term Ionosphere Atmosphere (JULIA) radar, they found the relationship between ΔH and the vertical plasma drift using a least-squares technique, a regression analysis, and a neural network approach. In
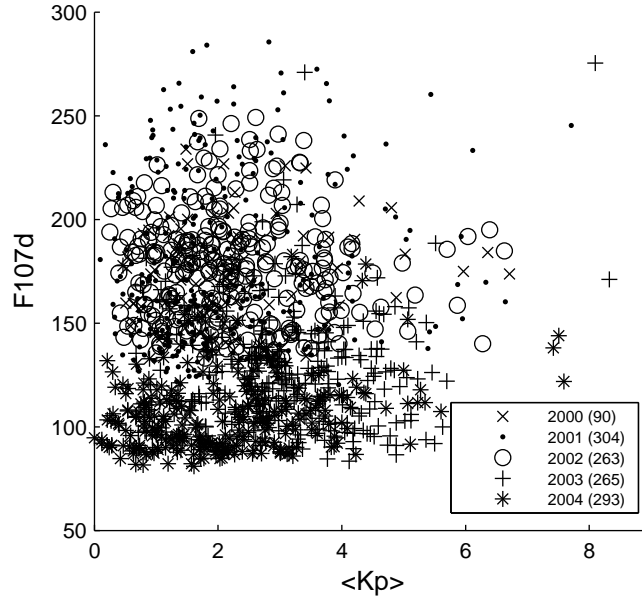
Figure 5.1: The data coverage of the magnetometer data from 2000-2004 as a function of daily $F10.7$ solar flux and average K_p index. The years are indicated by the different symbols.

the present study, we use the neural network, trained on data from 2001-2003, to estimate the vertical plasma drift from the ΔH measurements. The neural network is parameterized in terms of year, day of year (DOY), $F10.7$, $F10.7A$, the daily A_p index, the K_p index, the ΔH value, and local time. *Anderson et al.* (2004) showed that the $\mathbf{E} \times \mathbf{B}$ drifts predicted by the neural network have RMS errors of around 2.9 m/s, somewhat less that the RMS errors using the other approaches tested. The neural network is a multilayer, feed-forward network, trained using a gradient-descent back-propagation algorithm designed to minimize the mean square error between the training cases and the network output. The network consists of one hidden layer with 5 neurons. For more details, see *Anderson et al.* (2004).

We apply the neural network to magnetometer data from 2000-2004 to study the average spectral properties of the equatorial electric fields. The processed data have a time resolution of one minute, and only daytime data are used, between 0700 LT

(1200 UT) and 1700 LT (2200 UT). We also detrend the resulting drifts or electric fields using a representative quiet-time curve. This process will be discussed more later. Figure 5.1 shows the distribution of the data in terms of a proxy for magnetic activity, the daily K_p index averaged over the daytime period of interest, and the daily $F10.7$ solar flux.

5.3.2   Solar Wind Data

In this chapter, we compare the equatorial electric fields inferred from the magnetometer data to solar wind electric fields in the frequency and time domains. The solar wind electric field data come from the Advanced Composition Explorer (ACE) satellite, located at the L1 Libration point ($\delta \approx 1.41 \times 10^6$ km from Earth). The y-component of the IEF is calculated from

$$E_y = -V_z B_x + V_x B_z \tag{5.1}$$

where V and B refer to the solar wind velocity and magnetic field, respectively, in the GSM (geocentric solar magnetospheric) coordinate system (the x-axis is along the Sun-Earth line with the origin at the center of the Earth and x is positive towards the Sun; the y-axis is the cross product of the x-axis and the magnetic dipole axis, positive towards dusk, and thus the magnetic dipole axis is in the x-z plane; the z-axis is the cross product appropriate for a right-hand coordinate system, with positive z in the same sense as magnetic north). The electric field is delayed using a simple estimate for the time delay from the L1 point to the earth

$$\tau = \delta/V_x. \tag{5.2}$$

This time delay is of course only an approximation and much more detailed calculations are possible (e.g., *Ridley et al.*, 1998), including the travel time of the bow shock

to the magnetopause and the Alfven transit time from the subsolar magnetopause to the ionosphere .

The suggestion has been made that the effective electric field is proportional to $\sin^2(\theta/2)$ where θ is the clock angle measured from north (e.g., *Burton et al.*, 1975). The result is a half-wave rectification of the IEF such that the Region 1 currents are not dominated by the classic reconnection on the dayside. However, there are many examples in the literature and in this paper when a northward turning causes just as large of an effect at the equator as a southward turning. So, although the half-wave rectifier viewpoint may be a reasonable concept for energy input to the polar cap, it does not seem to work for electric field penetration. A reasonable explanation for this difference is that the clock angle dependence does not take into account residual Region 1 currents that flow due to the inductance of the ring current.

5.3.3   Spectral Density Estimation

In the next sections, we will present spectral density estimates as well as transfer function estimates. Spectral estimates are obtained using a simple periodogram where we apply a Hamming window to the data to reduce zero-point mismatch effects. The linear transfer function, or frequency response, is a signal processing or circuit analysis concept. It specifies the relationship between the input and output of a linear, time-invariant system in the frequency domain. Alternatively, the transfer function is defined as the impulse response of a system. Transfer functions are estimated using the estimated cross spectral density and the estimated power spectral density. For a linear time-invariant system, the transfer function estimate is

$$H_{xy} = \frac{P_{xy}}{P_x} \tag{5.3}$$

where P_{xy} refers to the cross spectral density for input signal x and ouput signal y and P_x is the input power spectral density (solar wind power spectral density) (e.g., *Oppenheim et al.*, 1999). H_{xy} is a complex quantity (magnitude and phase) since the cross spectral density is complex. We define the average transfer function as the average cross spectral density divided by the average input power spectral density. We will also present estimates of the coherency, defined as

$$C_{xy} = \frac{|P_{xy}|}{\sqrt{P_x P_y}}.$$
(5.4)

A coherency near one implies highly correlated signals at a given frequency. We again use our average cross spectral density and power spectral densities in determining the average coherency.

5.4 Average Spectra

In Figure 5.2, we show time series representing the average electric fields determined from the magnetometer ΔH, sorted by 'activity' level (dark lines). In addition, we plot the average curves using the *Scherliess and Fejer* (1999) quiet-time empirical model (light lines). The level of activity is defined by considering the integrated fluctuation power above 0.15 cycles per hour for an individual day. A quiet-time average integrated fluctuation power is computed by averaging the values for daily average K_p less than 3. The datasets are binned according to their integrated fluctuation power relative to that quiet-time average. An active day corresponds to one where the integrated fluctuation power is 5 dB above the quiet, for both the ionospheric data and the solar wind data. A mid-range day is one between -5 dB and 5 dB relative to the quiet, and a very quiet day is one less than -5 dB relative to the quiet. Defining the level of activity by integrated fluctuation power is useful (more useful than binning by K_p or AE index, for example) since a high level of fluctuation is indicative
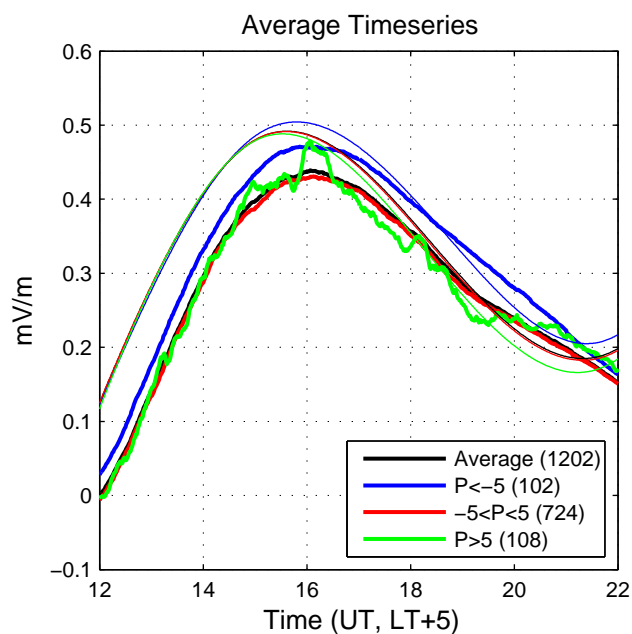
Figure 5.2: The average electric fields as a function of time for the datasets, sorted by integrated power as described in the text. The color corresponds to power interval, where the quantity P refers to the number of dB above or below the quiet day. The thick lines correspond to the magnetometer averages, and the thin lines correspond to averages of the *Scherliess and Fejer* (1999) curves over the same intervals. The number of datasets in each average is indicated in the legend.
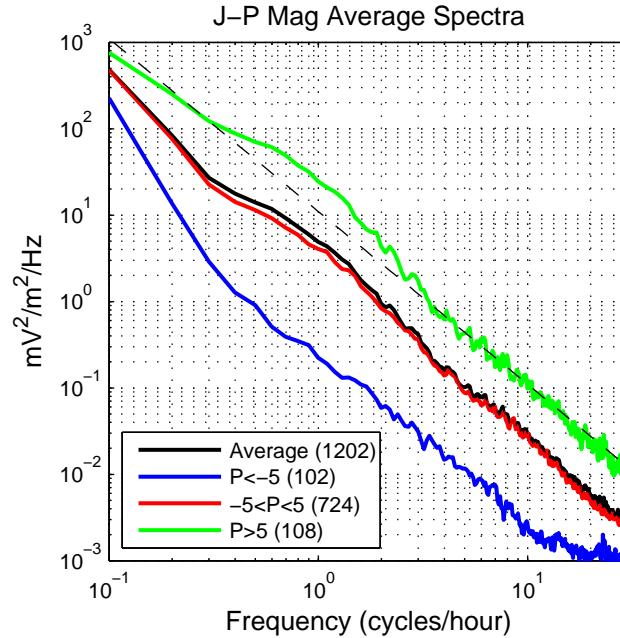
Figure 5.3: The average difference spectra from the magnetometer data sorted by integrated power. The quiet day model has been subtracted from the time series before the spectra were computed. The color corresponds to power interval, where the quantity P refers to the number of dB above or below the quiet day. The number of datasets in each average is indicated in the legend. The dashed line is a power law with a slope of -2 for reference.

of penetration events (*Earle and Kelley*, 1987). This activity level is similar to the one deduced by *Earle and Kelley* (1987) above which they argued solar wind and magnetospheric sources dominated the equatorial electric field spectra.

The thick blue curve in Figure 5.2 is the average electric field for the quiet periods as we have defined them. We see that the *Scherliess and Fejer* (1999) curves overestimate the magnetometer inferred fields slightly, especially in the morning hours. The averages for higher levels of activity, including the total average of all days (thick black), show somewhat smaller fields than the quiet day curve (thick blue). This may be the result of disturbance dynamo suppression of the daytime electric field. The high activity average electric field (thick green) fluctuates around the total average field (thick black). Thus, in studying the fluctuation spectra, we will detrend
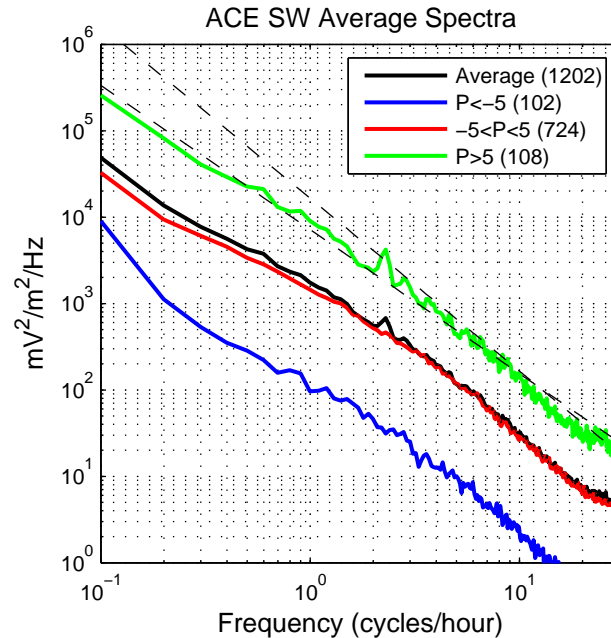
Figure 5.4: Same as Figure 5.3 except for the ACE solar wind electric field data. Two reference power law curves are shown here, one with slope -2 and one with slope -5/3.

using the total average field since it represents the nominal behavior of the vertical drift neglecting penetration fields and correcting to some extent for the effects of the disturbance dynamo.

Figures 5.3 and 5.4 show the averaged equatorial ionospheric and solar wind electric field fluctuation spectra for several levels of activity as we have defined it. Figure 5.3 shows the average spectra for the ionospheric data, and the increased power for higher levels of activity is clear. The number of datasets used in each average is indicated in the legend, and it should be noted that the higher variance in the high activity and low activity cases, especially at high frequencies, is mainly due to the fact that those averages contain fewer datasets than the mid-range curve. The equatorial spectra have a power law slope near -2 at high frequencies, as indicated by the dashed black line in the figure. The quiet-time difference spectra drop off sharply at low frequencies, in the range 0.1-0.3 cycles per hour, indicating that high frequency

fluctuations are not significant during these time periods. Instead, deviations from the quiet day averages tend to be relatively low frequency in nature, as one would expect (driven by day-to-day variability in the dynamo, for example). Some drop off is also observed in the mid-range and average spectra, but of smaller relative magnitude. However, the high activity spectrum does not show such a drop off. The high activity spectrum instead shows a power law behavior all the way to the lowest frequencies, but a deviation from that power law particularly in the few hour frequency range (between about 0.3 and 3 cycles per hour) where the spectrum is elevated by a few dB. This deviation is also observed in the mid-range spectrum to a much smaller extent.

Turning to the solar wind spectra in Figure 5.4, we again see the large change in power (of higher relative magnitude than the ionospheric spectra) when the data are binned in terms of level of activity (as previously defined). The quiet-time average spectrum has very small fluctuation levels at higher frequencies, dropping off steeply. The mid-range and high activity levels show similar trends, with the high activity level spectrum simply of higher magnitude. At high levels of activity, the fluctuation power is enhanced, on the average, at all frequencies. The dashed lines correspond to power law slopes of -2 and -5/3. At the lower frequencies (below about 10 cycles per hour), the slope of the average spectra is close to -5/3, which corresponds to the power law slope that has been observed in the solar wind (e.g., *Goldstein et al.*, 1994) and expected for MHD inertial range turbulence (e.g., *Ghosh et al.*, 1996). A flattening of this slope is expected at frequencies below about 10^{-2} cycles per hour (e.g., *Ghosh et al.*, 1996), which is beyond the resolution of our study. Above the ion cyclotron frequency, the spectra is expected to steepen as a result of Hall effects in MHD turbulence (*Ghosh et al.*, 1996). This is observed near 10 cycles per hour where the spectrum steepens to a slope higher than -2 before hitting the noise floor. We
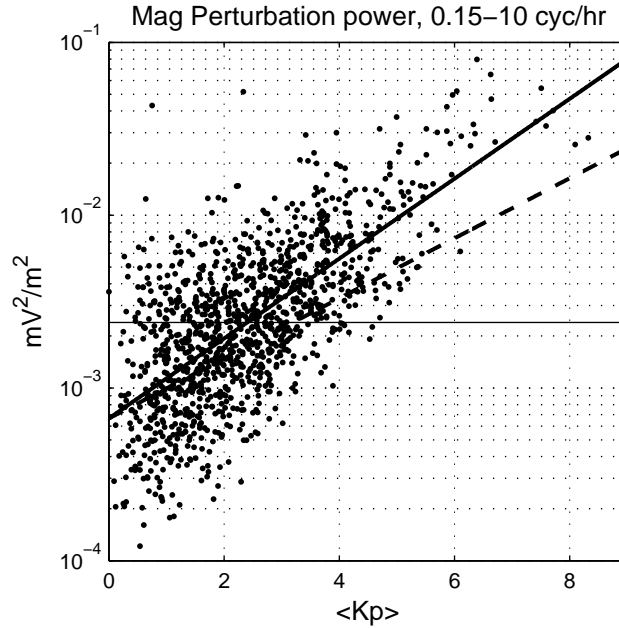
Figure 5.5: Scatter plot of the magnetometer difference spectra integrated from 0.15-10 cycles per hour as a function of average K_p index. The thin black horizontal line is the 0 dB point (corresponding to an average of values for $K_p \leq 3$). The solid black line is a line of best fit. The dashed line goes as $\exp(0.4K_p)$ as suggested by *Mozer* (1971).

note in passing that sharp edges may "contaminate" a pure MHD turbulence spectra at high frequencies and yield a k^{-2} type spectrum.

The integrated power in the equatorial data in the range 0.15 to 10 cycles per hour is plotted in Figure 5.5 as a function of the daily average K_p index along with a straight line fit. Recall that this parameter is used in our determination of the level of activity of a certain day. A clear increase is seen with magnetic activity. The dashed line is from a previous study of fluctuating electric fields using balloon data (*Mozer*, 1971), which is close to the dependence reported by *Earle and Kelley* (1987). The balloon measurements were made at middle to high latitudes and mapped to the equatorial plane, and a spectral form of (*Mozer*, 1971)

$$P = 100^{+200}_{-70} e^{0.4K_p} f^{-1.6 \pm 0.3} \tag{5.5}$$

was deduced, where f is in cycles per hour and P is in mV^2/m^2/Hz. The spectral slope of -1.6 is smaller than the value seen in Figure 5.3 (*Mozer* (1971) found a -5/3 spectrum rather than a -2 spectrum) but might be close near low frequencies. The power spectral density indicated by Equation 5.5 is nearly a factor of 100 higher than our results. Our results for the integrated power are in fairly good agreement with those of *Earle and Kelley* (1987). When *Earle and Kelley* (1987) compared spectra observed at Jicamarca to spectra observed at a higher L shells using radar data, they concluded that in general the fields were relatively uniform in the equatorial plane using the $L^{3/2}$ scaling (e.g., *Mozer*, 1970). *Earle and Kelley* (1987) found that the magnetospheric fields penetrate deep into the plasmasphere, virtually unatennuated down to about $L = 1.4$. From there, the fields decreased by about a factor of 2 from the uniform equatorial plane assumption to $L = 1.05$. The indication from the *Earle and Kelley* (1987) study is that in this frequency range the electric field in the equatorial plane of the magnetosphere is relatively uniform. The balloon observations of *Mozer* (1971) show much higher fluctuating field strengths for the cases studied.

The estimated average transfer function, as defined in the previous section, is shown in Figure 5.6. The estimate is essentially the average cross spectral density divided by the average solar wind power spectral density, for a given activity level. The magnitude and phase are plotted as a function of frequency. The average transfer function for low activities is essentially meaningless. As expected from the average spectra, the transfer for mid-range and high activity levels peaks in the frequency range 0.2 to 2 cycles per hour. As discussed earlier, this is the result of the deviation from the -2 power law shown in Figure 5.3 in this range, whereas the solar wind fluctuations do not show such a deviation on the average. The form of this average transfer function suggests a preferred response for the system in the few hour frequency range. That is to say that enhanced fluctuations in the solar wind electric field in general
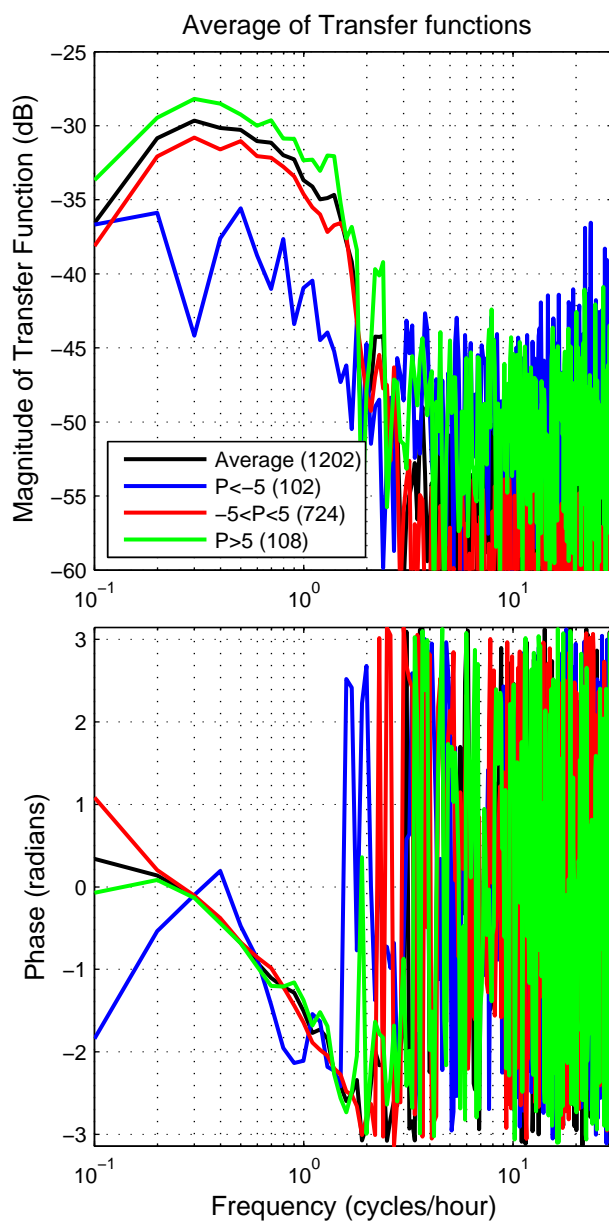
Figure 5.6: Average transfer function sorted by activity level using the windowed periodogram method to estimate the cross spectral densities and power spectral densities. The top panel is the magnitude of the average transfer function and the bottom panel is the phase.
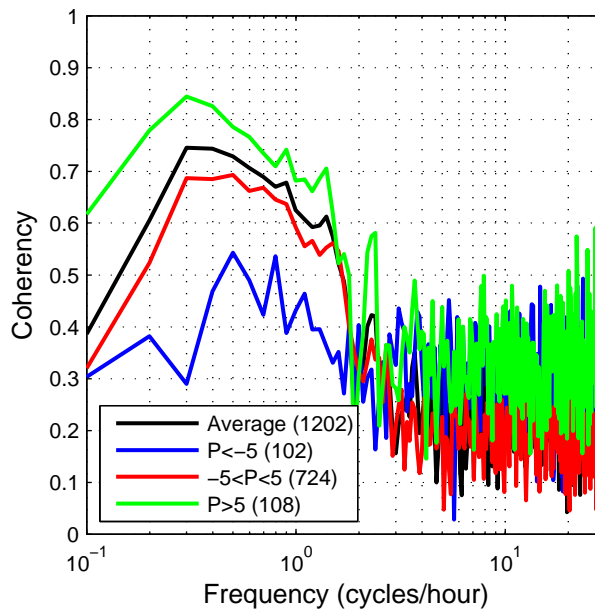
Figure 5.7: Average coherency sorted by activity.

occur at all frequencies given by a power law of slope near -5/3 for the time scales of interest. However, the low frequencies are attenuated somewhat by the system, and the very high frequencies do not transfer effectively. One must remember that these high frequency components are smaller in magnitude to begin with. However, in general, and on the average, these high frequency components do not get into the system, which implies a natural filtering process or scale-dependent mapping effects. Figure 5.7 shows the coherency (normalized magnitude of the cross spectral density, as defined earlier). These curves confirm the high degree of coherency in this range for high activity, indicating a close relationship between the IEF and the ionospheric field in the frequency range less than 1 cycle per hour. The transfer function and the coherency drop off drastically above about 2 cycles per hour indicating that the transfer of high frequencies is variable and must be treated on a case-by-case basis. This will be investigated later when we look at some case studies.

In Figure 5.8 we apply the average transfer function to four IEF inputs: a step
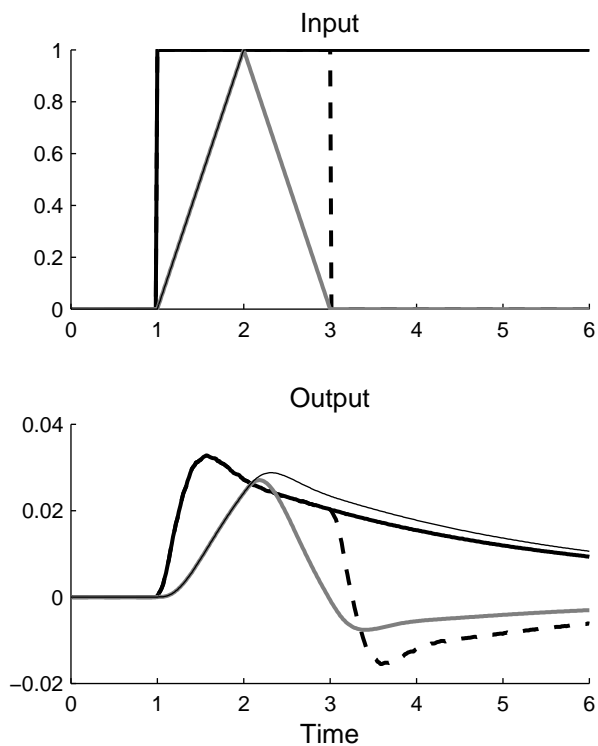
Figure 5.8: Results of applying the average transfer function to four different inputs. The dark solid black line corresponds to a step function. The dashed line is a two-hour square pulse, following the step function before turning off at $t = 3$ hours. The gray line is a triangular pulse of width two hours. The light black line is a ramp, following the triangular pulse until the maximum, where it joins the step function.

function, a two hour pulse, a triangle pulse lasting for two hours, and a ramp. See the figure caption for more details on the curves. This figure is meant to characterize the system's average response to various types of inputs, which represent to some degree the types of fluctuations that are observed in the solar wind. The square pulse is reproduced with a short time delay due to the high frequency cutoff in the bandpass characteristic. There is overshoot and a hint of ringing suggesting a weakly resonant response (with a low quality or Q factor), as indicated by the average transfer function curve in Figure 5.6. The response to the triangular pulse is reproduced with less overshoot and a smaller delay. The long-duration response to the step and ramp represent a slow decline from the response of the initial impulse. This response time constant is much longer than the 30-minute time constant that is typically quoted, but it is in agreement with the study of *Huang et al.* (2005). The slow response is a result of the fact that the average transfer function for the high activity cases is only a few dB down from the maximum at low frequencies (the drop off is faster for the lower activity levels). This property of the average transfer function allows it to reproduce some of the effects of long-duration penetration events, such as those reported by *Huang et al.* (2005). This property of the average transfer function, although in agreement with their measurements, seems to imply a much larger low frequency response than was thought to exist. This response may be due to a larger than expected inductance in the ring current. The explanation of long-duration events based on the SAMI model and quoted by *Huang et al.* (2006) does not seem to hold up. They input a square wave and found that it decayed within 30 minutes whereas a triangle wave input seemed to illicit a long-duration response. But, as we shall see in the next section, step function inputs in the IEF do not always decay quickly. As discussed by *Huang et al.* (2006), there is some theoretical basis for long penetration time scales (*Jaggi and Wolf*, 1973).

5.5 Case Studies

In this section, we explore several case studies where we examine the observed equatorial field and compare it to the prediction of the average transfer function approach. We begin by looking at some events that have been studied in detail in other publications: the March 31, 2001 event (*Maruyama et al.*, 2005; *Kelley et al.*, 2006) and the April 17, 2002 event (*Goncharenko et al.*, 2005; *Kelley et al.*, 2003b, 2006). We then move into other events, some of which have not been studied before.

The results of March 31, 2001 are shown in Figure 5.9. The upper two plots are the power spectra of the y component of the IEF and of the zonal ionospheric electric field inferred from the magnetometer observations. In the middle panel, the gray line shows the average transfer function while the dark line shows the actual (estimated) transfer function for the event. Note the sizable enhancement in the latter at high frequencies. The light black curve in the lower panel of the figure is the IEF scaled by a factor of 15, the dark black curve is the ionospheric electric field, and the gray curve is the result of applying the average transfer function. The factor of 15 was observed by *Kelley et al.* (2003b) to be the ratio of the IEF to the equatorial electric field measured by the Jicamarca incoherent scatter radar on April 17, 2002. This was suggested to be the ratio of the size of the magnetosphere to the length of the reconnection line at the magnetopause. We will use this factor of 15 in all future plots to display the solar wind electric field data on the same axis as the equatorial data. *Huang et al.* (2006) use a factor of 10 for similar comparisons.

The March 31, 2001 event was characterized by a square wave input with a one hour duration and near constant B_z northward near 1400 UT followed by a sharp reversal to strongly southward. The spectra of the IEF (top panel, top curves) and of the equatorial field (top panel, bottom curves) show power at all frequencies elevated
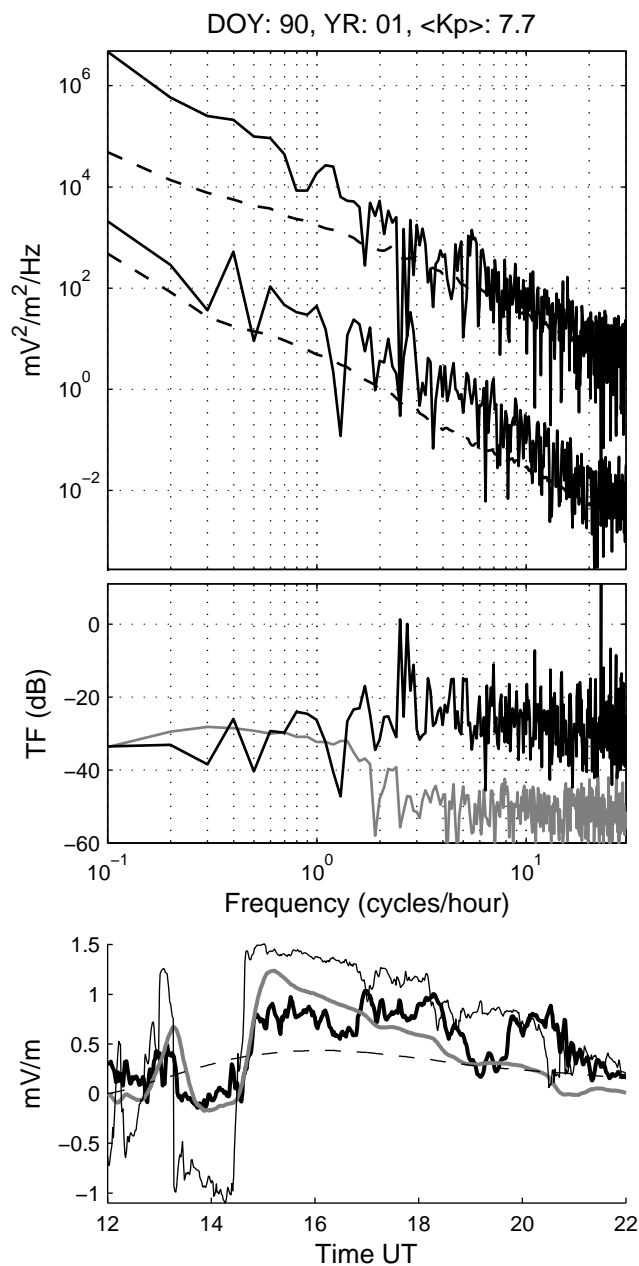
Figure 5.9: Series of plots corresponding to March 31, 2001. The top plot shows the solar wind and ionospheric spectra estimated using a windowed periodogram (black), along with the average spectra (dashed, black curves from Figures 5.3 and 5.4). The middle plot shows the average transfer function (gray) along with the transfer function estimated for this day in particular (black). The lower plot shows the solar wind electric field scaled by 15 (thin black), the magnetometer deduced ionospheric electric field (thick black), the electric field obtained by applying the average transfer function to the solar wind data (gray), and the quiet day average (dashed).

above the average. Applying the average transfer function to the IEF (gray curve in the lower panel, where the quiet day curve has been added) captures the equatorial response quite well although the edges on the data are a bit sharper than that predicted by the average transfer function. This effect is a result of the suppression of the high frequency components in the average transfer function. The southward turning causes the average transfer function estimate to overshoot, but the transfer function captures the slow decay of the ionospheric field quite well. This is an interesting event because typical time constants for penetration have been thought to be near 30 minutes or less (e.g., *Senior and Blanc*, 1984; *Huang et al.*, 2005), meaning that after pulses from southward IMF to northward IMF (or vice versa), the equatorial response should have decayed more rapidly. This rapid decay was recently also found using the SAMI model (*Huang et al.*, 2006) and seems not to be valid. Clearly, though, the equatorial field follows the solar wind electric field, which the average transfer function reproduces as described in the previous section. A small ramping effect is seen and a weak counter electrojet was predicted and is also observed. The IEF slowly recovered over the eight-hour period from 1400 UT to 2200 UT. This effect was seen in the equatorial data and in the prediction, although smaller-scale fluctuations are not captured. Turning to the transfer function in the middle panel (where we plot the magnitude of the average transfer function and the estimate for this day), we see that for this event, the actual transfer function had a very high response at frequencies above 1 cycle/hour which led to a rapid response to the square wave in the northward IMF, not seen in the transfer function response.

The results of the April 17, 2002 case study are shown in Figure 5.10 in the same format as Figure 5.9. This event was more oscillatory in nature, with a fluctuation period near one hour. Both the ionospheric and the solar wind data again show enhanced fluctuation power (above the average) at all frequencies above about 0.2
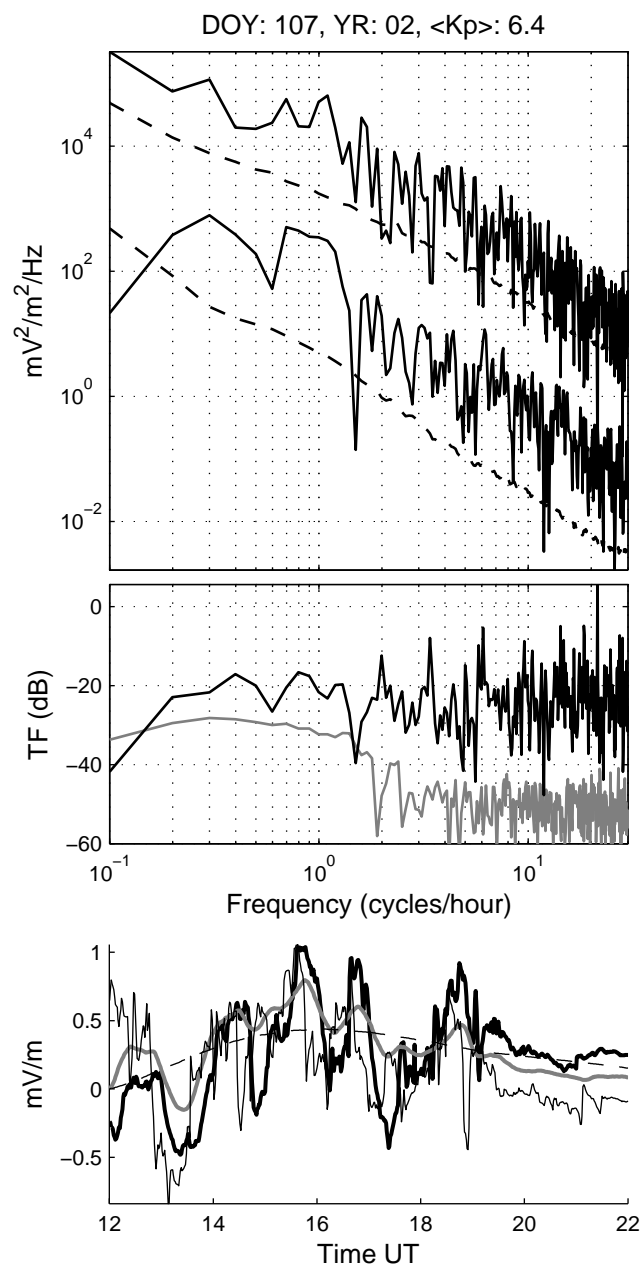
Figure 5.10: Same as Figure 5.9 except for April 17, 2002.

cycles per hour. The enhancement in the solar wind is near uniform with frequency, although there is a clear oscillation near one hour in the solar wind time series and a corresponding spike in the spectrum. The enhancement in the ionospheric data is much clearer, with a broad increase near a frequency of 1 cycle per hour and near 0.3 cycles per hour (which is also observed in the solar wind). The actual (estimated) transfer function for this day has a higher magnitude than the average transfer function and is nearly flat as a function of frequency, similar to the transfer function in Figure 5.9. There are peaks in the transfer function near 0.4 and 0.8 cycles per hour of magnitude near -20 dB, or a factor of 10 in electric field (similar to the factor of 15 reported by *Kelley et al.* (2003b)). The higher frequency components are about 30 dB down, or a factor near 30 in electric field. The average transfer function estimates a value near one hour of closer to a factor of -30 dB and a high frequency factor near -50 dB. The fact that the average transfer function underestimates the field is seen in the time series, where the true fluctuations are about 3 times the transfer function predicted fluctuations. The average transfer function predicted result is also smoother because of the suppression of the high frequency fluctuations. *Huang et al.* (2006) have studied equatorial field responses to southward turnings of the interplanetary magnetic field and find a factor of 10 difference between the dawn-to-dusk component of the IEF and the eastward electric field on the dayside, which in this case would agree fairly well. Note, however, that in the March 31, 2001 case a factor of 10 would have significantly overestimated the ionospheric response.

Several more examples are presented in Figures 5.11 and 5.12, where we show 16 cases of the time series plots, in the same format as the lower panels of Figures 5.9 and 5.10 (three curves - the solar wind electric field scaled by a factor of 15 in light black, the magnetometer-derived equatorial electric field in thick black, and the average transfer function predicted result in gray). Many of the events shown here

are oscillatory in nature, and many are quite unique.

Looking at Figure 5.11, one of our worst examples is at the top left (day 262 of 2000). Here, except for a few brief intervals, the IEF was dusk-to-dawn the whole period. The pulse in the y component of the IEF from negative to zero and back at the delayed time of 1500 UT was immediately seen at the equator with an eastward pulse. The transfer function responded with the usual delay discussed elsewhere in this paper. It seems curious that a null in the y component of the IEF would cause this response. Thus, we have investigated B_y, which turned sharply positive in this same period and with the same type of waveform. It seems likely that convection and Region 1 currents were enhanced but shifted from the noon meridian. B_y effects have recently been reported in penetration electric field events (*Kelley and Makela*, 2002). This may in turn have led to a disturbance dynamo field for times after 1600 UT, which seems to be consistent with substorm activity seen in the D_{st} and AE indices on this day.

Days 94 and 101 of 2001 in Figure 5.11 show oscillatory situations in which the observed fluctuations and their magnitudes were well reproduced. Day 95 of 2003 shows a case where the fluctuation magnitudes were reproduced but a DC component is not, possibly due to an enhanced disturbance dynamo. This interpretation is consistent with the AE index on this day. Day 98 of 2001 shows a positive spike near 1400 UT which is reproduced, and then a negative spike near 1500 UT. The average transfer function underestimates the magnitude of that negative bay. On this day, despite the fact that the IMF remains northward, we see the gradual decay in the ionospheric field with a time constant near 30 minutes, which is the classically expected shielding time constant (*Gonzales et al.*, 1983; *Senior and Blanc*, 1984; *Vasyliunas*, 1972). On day 212 of 2001, the fluctuations are also underestimated. Some unique cases are also evident, day 262 of 2000 (already discussed) and day 250
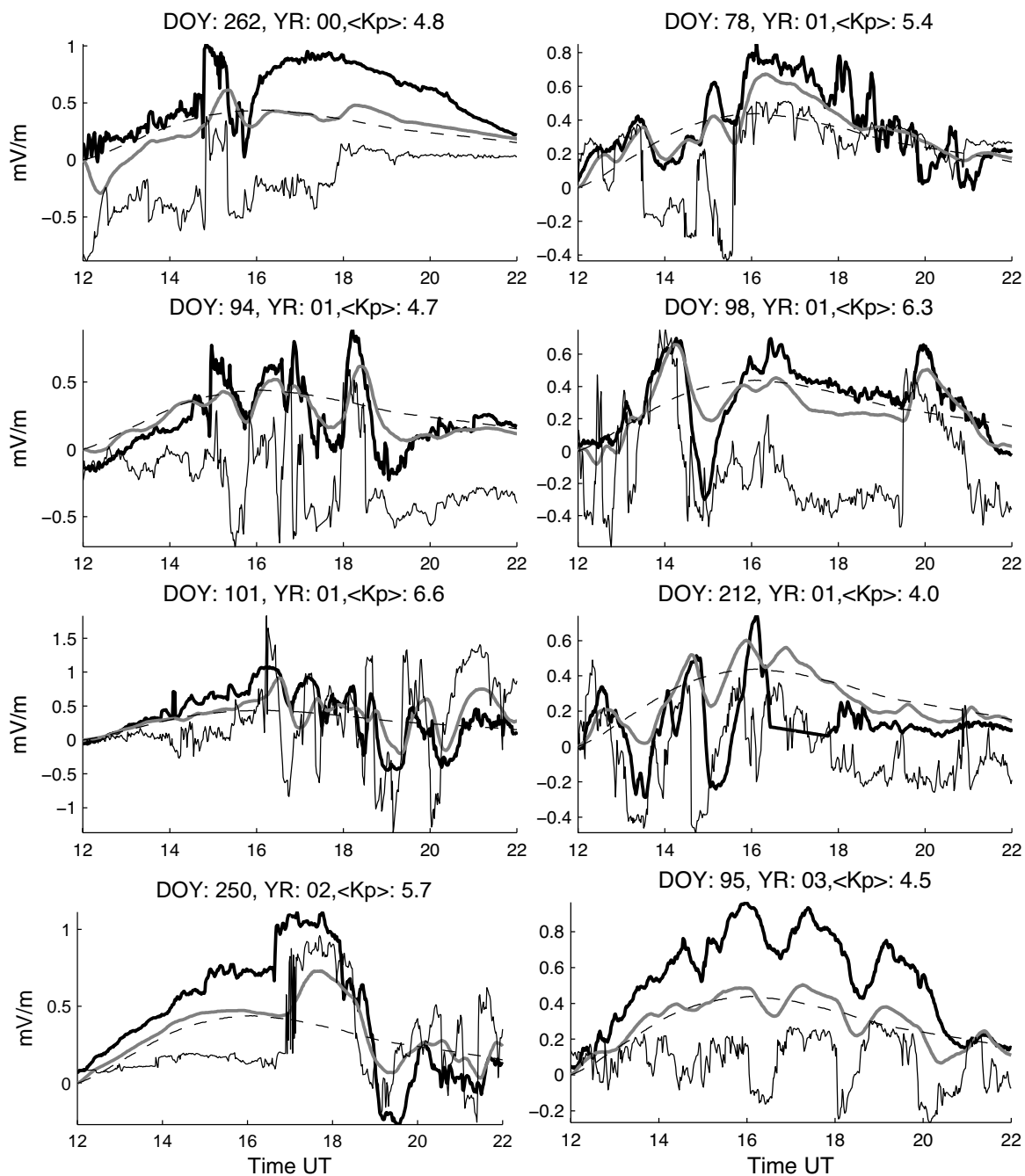
Figure 5.11: A series of 8 case studies. The thin black curve is the solar wind electric field divided by 15, the thick black curve is the equatorial electric field inferred from the magnetometer data, and the gray curve is the results of applying the average transfer function to the solar wind data. The dashed curve is the quiet-time field.

of 2002 (which has been discussed by *Huang et al.* (2005)). The former is a series of two pulses. The ionosphere reacts immediately to both pulses and the average transfer function cannot predict this because of the suppression of the high frequencies. The latter case is a strong southward spike in IMF that persists for over an hour. The ionospheric field reacts immediately in this case, and does not decay, similar to the March 31, 2001 event and an example of a long-duration event as reported by *Huang et al.* (2005). The IMF then turns northward and the system responds more classically.

Figure 5.12 shows more case studies, some of which the average transfer function does a good job on, others it does not. In general, there is a tendency for the average transfer function to underestimate the oscillations, which is simply the result of the averaging that went into creating it, although many of the features are recovered. We should note that none of the cases showed the degree of underestimation that was observed on April 17, 2001 in Figure 5.10, which was an event with particularly efficient transfer (*Kelley et al.*, 2003b). In addition, the average transfer function does not do a good job at capturing the very high frequency oscillations (above a few cycles per hour) when they are significant. In general, these higher frequencies are not as well represented by the average transfer function as the frequencies around one cycle per hour. We discuss a possible reason for this in the conclusion.

Since the work of *Vasyliunas* (1970), it has been known that the ring current shields the inner magnetosphere from external potentials for frequencies less than a few cycles per day. This high-pass filtering has also been discussed by *Kelley et al.* (1979a). Time constants for shielding have been derived by *Vasyliunas* (1972), and *Gonzales et al.* (1983) showed that the system could be represented as an equivalent resistor-inductor circuit (including the effects of ionospheric and ring current conductivity). The inductance of the ring current is nicely modeled by a loop of current. A weakly resonant system could be equivalently modeled by adding some small capaci-
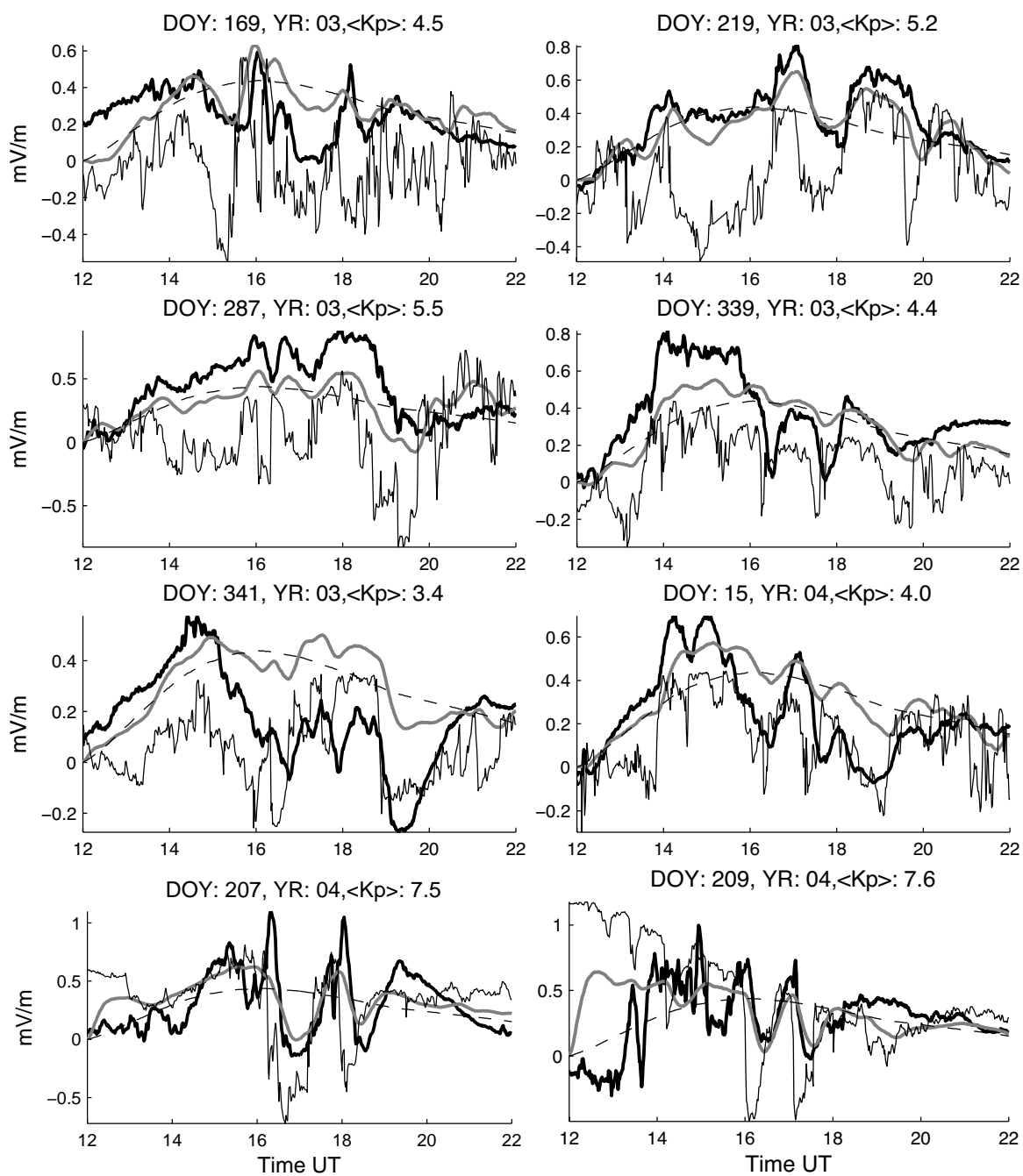
Figure 5.12: Same as Figure 5.11 for 8 more active days.

tance to the system. Such an addition would simply represent the general absence of very high frequency oscillations observed in the equatorial plane, which may or may not be physical in origin.

5.6 Conclusions

Fluctuations in the interplanetary electric field have a power law spectrum in the frequency range from 0.1 to 30 cycles per hour. The zonal component of the daytime equatorial electric field has a monotonically decreasing power spectrum in the same range with a power law slope of -2, but deviates from that power law between 0.5 to 3 cycles per hour, especially during active periods. Correspondingly, the average transfer function relating the two fields has a broad maximum centered near 0.5 cycles per hour. The magnitude of the average transfer function peaks at about 4% of the IEF. This is lower than the ratio reported by *Huang et al.* (2006). In some active case studies we find that the observed field is typically underestimated by a factor of two by the average transfer function. The integrated power in the equatorial field increases by a factor of 100 for K_p ranging from 0 to 8. This dependence is evidence that much of the variability of the equatorial field is of interplanetary origin, as suggested by *Earle and Kelley* (1987).

Often this linear transfer function relationship between the IEF and the equatorial field is remarkably good. A similar conclusion was found by *Huang et al.* (2006) who found that a simple multiplier could be used to predict the equatorial field for a southward interplanetary magnetic field. Our function is useful for either direction of the IMF.

Power spectra of the magnetospheric electric field have previously been published using radar data (*Earle and Kelley*, 1987) and balloon data (*Mozer*, 1971). In both

cases the spectral shape and K_p dependence of the fluctuating field strength are close to those presented here. The radar study is in better agreement with the results presented here and indicates that in this frequency range the electric field in the equatorial plane is relatively uniform and about 5% of the external electric field.

The form of the average transfer function and its time-domain response to an impulse function suggest a weakly resonant response of the system. The self-inductance of the ring current coupled with some capacitance and the ionospheric resistivity may provide such a response, although the physical mechanisms behind such an equivalent circuit have not been investigated. The average transfer function is only about 5 dB down from its peak value at a frequency corresponding to a 10-hour period. This is consistent with the penetration of electric fields for long durations, some of which have been shown here, in *Kelley et al.* (2006), and in *Huang et al.* (2005, 2006). During events with poor agreement between the average transfer function result and the data, gravity waves may provide a source of the fluctuations, as suggested by *Earle and Kelley* (1987). By comparing data for longitudes an hour or so apart, such events might be discriminated.

When a sharp transition occurs in the IEF, the equatorial ionosphere responds very quickly whereas the application of the average transfer function yields a sluggish response. One possible explanation is as follows. The sharp transitions, which often last an hour or more, are almost certainly associated with very large-scale IEF changes. Other solar wind conditions yielding similar power spectra may be due to turbulent fluctuations with much smaller scales. These smaller-scale electric fields may not couple well to the magnetosphere. Such effects may be separable using a wavelet analysis to isolate the edges in the IEF, parse them, and then perform the spectral analysis. We hope to investigate this idea in a future study.

Acknowledgements

Chapter 6

Investigation of the Nighttime Molecular Ion Composition at Middle and Low Latitudes using Airglow Measurements [*]

A knave; a rascal; an eater of broken meats; a base, proud, shallow, beggarly, three-suited, hundred-pound, filthy, worsted-stocking knave; a lily-livered, action-taking knave, a whoreson, glass-gazing, super-serviceable finical rogue; one-trunk-inheriting slave; one that wouldst be a bawd, in way of good service, and art nothing but the composition of a knave, beggar, coward, pandar, and the son and heir of a mongrel bitch: one whom I will beat into clamorous whining, if thou deniest the least syllable of thy addition.
    - Earl of Kent in <u>The Tragedy of King Lear</u> by William Shakespeare

6.1   Abstract

The 630-nm nighttime airglow is radiated by $O(^1D)$ atoms, which are produced by the dissociative recombination of O_2^+ ions. The typical approach used to calculate the

---

red line emission rate at night is based on the assumption that O_2^+ is mainly produced by the reaction of O^+ with molecular oxygen. In the case that the O_2^+ density is much smaller than the O^+ density, $[O^+] = n_e$ in the $F2$ region. Good agreement between measured nighttime integrated emission rates and the emission rates calculated by this typical approach, using both electron densities measured using incoherent scatter radars and given by the IRI model, has been shown. However, the O_2^+ densities given by the IRI model are much higher than the densities produced by the reaction of O^+ with O_2, and these densities do not correspond to the condition $[O^+] = n_e$. In this case, the typical approach cannot be applied and molecular ions must be included in the emission rate calculations. The integrated emission rates calculated including the molecular ion density given by the IRI model have been found to be much higher than the measured 630.0-nm emission rates. This discrepancy takes place at latitudes below about $\pm 30°$ in the western longitude sector, mainly for the period from March to November, and the disagreement is higher than one order of magnitude at the equator. In addition, we model the $F2$-region green line $O(^1S)$ emission at 557.7 nm due to the dissociative recombination of O_2^+. Using measurements of this volume emission rate made by the WINDII satellite, we are able to show that IRI overestimates the O_2^+ density (and ion fraction) on the bottomside. A revision of the ion composition in the IRI model on the bottomside seems to be needed based on the results. Airglow measurements may be useful in constraining such a revision. A revision could utilize the formulae for the relationship between the molecular ion densities and neutral densities derived here, using the MSIS neutral densities and the IRI electron density. These calculations are based on the assumption that O_2^+ and NO^+ are only produced through ion-molecular reactions. Such a revision would correct the magnitude and altitudinal dependence of the molecular ion fraction in the IRI model.

6.2 Introduction

The atomic oxygen red line at 630.0 nm is one of the strongest features in the visible nighttime airglow. Many ground-based, satellite, and rocket observations of the red line emission have been made. According to experimental data, the intensity of the nighttime emission does not exceed a few hundred Rayleighs (e.g., *Tohmatsu*, 1990). As shown in Chapter 2, the observed intensities are in good agreement (within 20%) with the calculations based on the excitation of this emission due to O_2^+ dissociative recombination in the $F2$ region (*Torr and Torr*, 1982; *Abreu et al.*, 1986; *Link and Cogger*, 1988). It is assumed in these calculations that the O_2^+ ions are only produced by the reaction of O^+ with molecular oxygen. According to this approach, the O_2^+ density is much smaller than the O^+ density and $[O^+] = n_e$ in the $F2$ region. This approach is used in most calculations of the red line emission rate.

Recently, *Vlasov et al.* (2005) (see Chapter 2) developed a formula for the red and green line volume emission rates including molecular ions. But, we showed, as expected, that for most conditions at middle and low latitudes the molecular ions are negligible. However, we did mention the fact that there is a problem with the ion composition and electron density given by the IRI model at latitudes below $\pm 30°$, which predict a 630.0-nm integrated emission rate of over 1000 R. The goal of this chapter is to consider in detail the impact of the ionospheric parameters given by the IRI model on the red line intensities. In addition, we use measurements of the 557.7-nm $F2$ region volume emission rate to estimate the O_2^+ density, and show that the IRI model overestimates the O_2^+ fraction in this region, which is the source of the high red line emission rate.

6.3 Model of F-region emissions

The optical red and green line emissions at 630.0 nm and 557.7 nm are radiated by atomic oxygen excited in the ^1D and ^1S metastable states, respectively. As discussed in Chapter 2, the main source of the metastable atoms in the nighttime upper atmosphere is dissociative recombination of O_2^+ (*Bates*, 1956; *Barbier*, 1957)

$$O_2^+ + e^- \rightarrow O(^3P) + O(^1D,^1S). \tag{6.1}$$
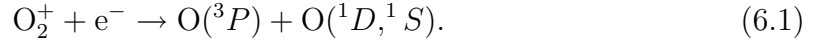
There is also the small additional production of $O(^1D)$ due to the dissociative recombination of NO^+ and the quenching of the $N(^2D)$ metastable atoms (*Rusch et al.*, 1978)

$$NO^+ + e^- \rightarrow N(^2D) + O \tag{6.2}$$

$$N(^2D) + O_2 \rightarrow NO + O(^1D). \tag{6.3}$$
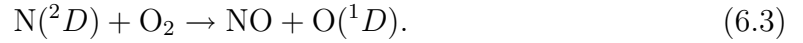
In Chapter 2, we derived the volume emission rate for the red and green lines including molecular ions,

$$I_R^\triangle = \frac{A_{1D}\left\{\mu_D \alpha_{O_2^+}^*[O_2^+]n_e + \frac{\beta \alpha_{NO^+}^*[NO^+]n_e \gamma_D[O_2]}{\gamma_D[O_2]+\gamma_O[O]}\right\}}{k_1[N_2] + k_2[O_2] + k_3[O] + A_{1D} + A_{2D}} \tag{6.4}$$

$$I_G^\triangle = \frac{A_{1S}\mu_S \alpha_{O_2^+}^*[O_2^+]n_e}{A_{1S} + A_{2S}}. \tag{6.5}$$

where μ_D and μ_S are the $O(^1D)$ and $O(^1S)$ yields, respectively, in Reaction 6.1; $\alpha_{O_2^+}^*$ is the rate coefficient of Reaction 6.1; β is the yield of the $N(^2D)$ atoms in Reaction 6.2; $\alpha_{NO^+}^*$ is the rate coefficient of Reaction 6.2; γ_O is the rate coefficient of the deactivation of the $N(^2D)$ atoms by atomic oxygen; γ_D is the rate coefficient of Reaction 6.3; k_1, k_2, and k_3 are the rate coefficients of $O(^1D)$ quenching by N_2, O_2 and O, respectively; A_{1D} and A_{2D} are the coefficients of the transitions $^1D_2 \rightarrow ^3P_2$ and $^1D_2 \rightarrow ^3P_1$, respectively; A_{1S} and A_{2S} are the coefficients of the transitions

$^1S_2 \rightarrow {}^1D_2$ and $^1S_2 \rightarrow {}^3P_1$, respectively. The comparative simplicity of Equation 6.5 is due to the fact that $O(^1S)$ deactivation by collisions with neutral constituents is negligible in the F region. The rate coefficients used in our model calculations were described in detail in Chapter 2. We should note, as mentioned in Chapter 2 and discussed by *Vlasov et al.* (2005) in more detail, that there is some uncertainty in the value of μ_S, perhaps a factor of 2 or so.

The modern method for calculating the intensities is based on the assumption that the O_2^+ and NO^+ ions are only produced by the ion-molecular reactions

$$O^+ + N_2 \rightarrow NO^+ + N \tag{6.6}$$

$$O^+ + O_2 \rightarrow O_2^+ + O \tag{6.7}$$

in the $F2$ region. In this case, the concentrations of the O_2^+ and NO^+ ions are given by

$$[NO^+] = \frac{\gamma_1[N_2]}{\alpha^*_{NO^+} n_e}[O^+] \tag{6.8}$$

$$[O_2^+] = \frac{\gamma_2[O_2]}{\alpha^*_{O_2^+} n_e}[O^+] \tag{6.9}$$

where γ_1 and γ_2 are the rate coefficients of Reactions 6.6 and 6.7, respectively. The most common method of calculating the volume emission rates uses Equations 6.8 and 6.9 with the assumption that $[O^+] = n_e$, which then reduce to

$$[NO^+] = \frac{\gamma_1[N_2]}{\alpha^*_{NO^+}} \tag{6.10}$$

$$[O_2^+] = \frac{\gamma_2[O_2]}{\alpha^*_{O_2^+}}. \tag{6.11}$$

Substituting Equations 6.10 and 6.11 into Equations 6.4 and 6.5, we obtain for the volume emission rates,

$$I_R = \frac{A_{1D}\left\{\mu_D\gamma_2[O_2]n_e + \frac{\beta\gamma_1[N_2]n_e\gamma_D[O_2]}{\gamma_D[O_2]+\gamma_O[O]}\right\}}{k_1[N_2] + k_2[O_2] + k_3[O] + A_{1D} + A_{2D}} \tag{6.12}$$

$$I_G = \frac{A_{1S}\mu_S\gamma_2[O_2]n_e}{A_{1S} + A_{2S}}. \tag{6.13}$$

These equations neglect molecular ions.

Using Equations 6.8 and 6.9 and the relation $n_e = [O^+] + [O_2^+] + [NO^+]$, it is possible to obtain for the ion densities

$$[O_2^+] = \frac{\gamma_2[O_2]}{\alpha^*_{O_2^+}}\left(1 + \frac{\gamma_1[N_2]}{\alpha^*_{NO^+}n_e} + \frac{\gamma_2[O_2]}{\alpha^*_{O_2^+}n_e}\right)^{-1} \tag{6.14}$$

$$[NO^+] = \frac{\gamma_1[N_2]}{\alpha^*_{NO^+}}\left(1 + \frac{\gamma_1[N_2]}{\alpha^*_{NO^+}n_e} + \frac{\gamma_2[O_2]}{\alpha^*_{O_2^+}n_e}\right)^{-1} \tag{6.15}$$

$$[O^+] = n_e\left(1 + \frac{\gamma_1[N_2]}{\alpha^*_{NO^+}n_e} + \frac{\gamma_2[O_2]}{\alpha^*_{O_2^+}n_e}\right)^{-1}. \tag{6.16}$$

Then, using Equations 6.4-6.5 and 6.12-6.13, along with the density formulations of Equations 6.14-6.16, the ratio of the volume emission rates excluding and including molecular ions can be written as

$$P = \frac{I_R}{I_R^\triangle} = \frac{I_G}{I_G^\triangle} = 1 + \frac{\gamma_1[N_2]}{\alpha^*_{NO^+}n_e} + \frac{\gamma_2[O_2]}{\alpha^*_{O_2^+}n_e}. \tag{6.17}$$

Note that in order to obtain this expression, the second term in the numerator of Equations 6.4 and 6.12 has been neglected because the $O(^1D)$ production due to NO^+ recombination is small at middle and low latitudes. According to Equation 6.17, P increases with the decreasing electron density and increasing molecular neutral density that occurs at lower altitudes. The influence of these parameters can be considered using the analytical model developed in Chapter 2. The height distribution of the ratio P can be written as

$$\begin{aligned} P &= 1 + \frac{\gamma_1[N_2]_0}{\alpha^*_{NO^+}n_{e0}}\exp\left[\frac{z}{H_{N_2}} - \frac{1}{2}\left(1 + \frac{z}{H_{Ch}} - e^{z/H_{Ch}}\right)\right] \\ &\quad + \frac{\gamma_2[O_2]_0}{\alpha^*_{O_2^+}n_{e0}}\exp\left[\frac{z}{H_{O_2}} - \frac{1}{2}\left(1 + \frac{z}{H_{Ch}} - e^{z/H_{Ch}}\right)\right] \end{aligned} \tag{6.18}$$

for a barometric distribution of the neutral constituents with H_{N_2} and H_{O_2} scales and a Chapman layer for the electron density with a scale H_{Ch}. Here, $z = 0$ at the altitude of the $F2$ peak and z increases below $h_m F2$. $[N_2]_0$, $[O_2]_0$, and n_{e0} are the densities at $h_m F2$. Equation 6.18 makes it possible to determine the altitude below which molecular ions must be taken into account. The height distribution of the ratio P is shown in Figure 6.1 for a typical set of parameters, along with the volume emission rates with and without molecular ions. As can be seen, a significant increase of the ratio occurs at altitudes below 250 km. However, because the volume emission rate is typically fairly low at these altitudes, as discussed by *Vlasov et al.* (2005) and in Chapter 2, the error does not induce a significant error in the calculation of the integrated emission rate. In such a case, the molecular ions can be neglected. The effect is more important on the green line emission because that emission occurs lower in altitude since it is controlled by the O_2 scale height, whereas the red line emission is also affected by the O and N_2 scale heights.

Measurements of the red line emission rate have been made many times at Arecibo in various geophysical conditions (see examples and references in *Vlasov et al.* (2005) and Chapter 2). In general, there is good agreement between the experimental data and the calculations. The red line integrated emission rate does not typically exceed a few hundred Rayleighs at low and middle latitudes, and these values are in agreement with the calculations by Equation 6.12 based on the assumption of negligible molecular ion densities.

6.4   Comparisons to IRI

In the previous section, we showed that the effects of molecular ions on the red and green line volume emission rates should not be significant at low and mid-latitudes.
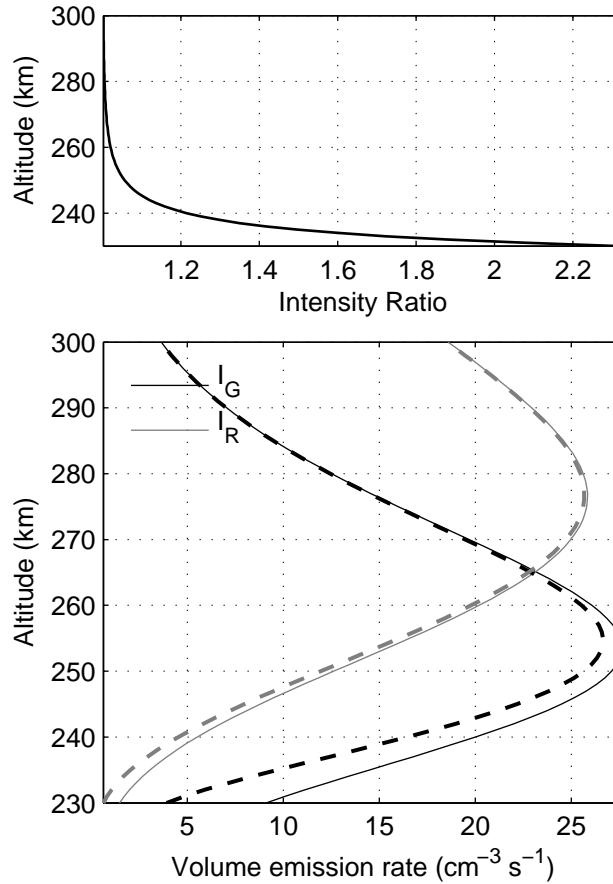
Figure 6.1: (Top) Volume emission rate ratio given by Equation 6.18 and (Bottom) volume emission rate altitude distributions for green (black) and red (gray) lines without moleculars (solid) and with moleculars (dashed). The parameters used in this calculation were: $h_mF2 = 300$ km, $n_{e0} = 5 \times 10^5$ cm^{-3}, $[N_2]_0 = 10^8$ cm^{-3}, $[O_2]_0 = 6 \times 10^6$ cm^{-3}, $[O]_0 = 7 \times 10^8$ cm^{-3}, $T_i = T_e = T_N = 1000$ K, and $H_{Ch} = H_{O_2}$.

This discussion was based on the assumption that O_2^+ and NO^+ are only produced by molecular reactions with O^+, Reactions 6.6 and 6.7. Figure 6.2 compares the ion densities predicted by the IRI model to the densities predicted by the ion-molecular reactions, Equations 6.14-6.16. Figure 6.3 shows the same results as Figure 6.2, except the ion fraction is plotted instead of the absolute density. The calculations are done at four different latitudes for a constant longitude, -70°E, and a constant time, 0500 UT (about 0100 LT). The longitude is approximately that of the western chain of ISRs. The electron density, electron temperature, and ion temperature given by the IRI-2001 model (*Bilitza*, 2001) and the neutral densities given by the MSIS-90 model (*Hedin*, 1991a) have been used in Equations 6.14-6.16. The Danilov-95 (*Danilov and Smirnova*, 1995) ion composition model and Gulyaeva (*Gulyaeva*, 1987) bottomside profiles have been used in the IRI calculations. The solid lines correspond to the IRI predictions and the dashed lines correspond to the predictions of Equations 6.14-6.16. The IRI model predicts much higher molecular ion densities than do Equations 6.14-6.16 with the MSIS neutral densities. At low latitudes, IRI estimates densities that are over an order of magnitude higher than our calculations. IRI also predicts a higher O_2^+ than NO^+ density for all latitudes, in disagreement with our calculations. The IRI densities seem to have a peak near 275 km at all latitudes, for which there is no evidence from the MSIS neutral densities. The disagreement clearly decreases with increasing latitude. At 45°N, the difference between the IRI predictions and the calculations are not significant, although there are clearly qualitative differences in the profile shapes, with the IRI profiles still showing a peak near 275 km. We will discuss the local time and seasonal dependencies later.

The large discrepancy between the IRI O_2^+ densities and those calculated using the MSIS neutral densities and Equations 6.14-6.16 have a significant effect on the predicted airglow emission rates. Thus, using airglow measurements, it should be
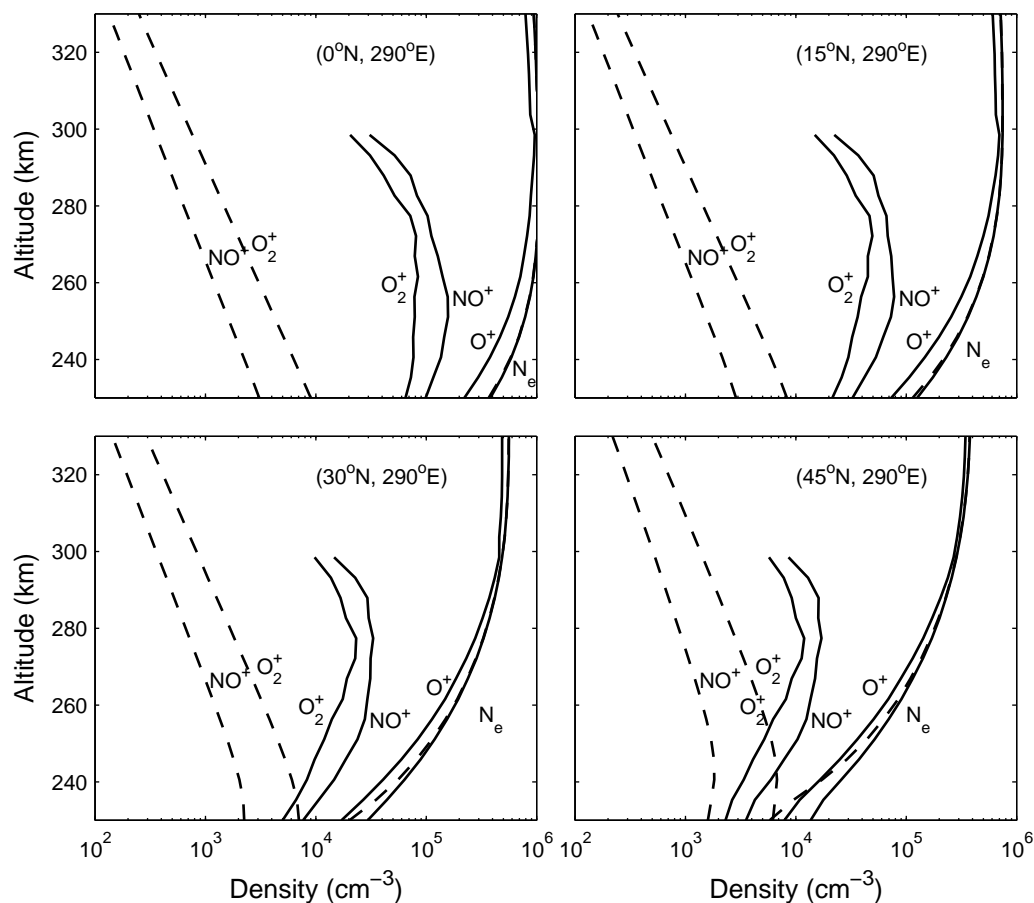
Figure 6.2: The height distributions of the electron and ion densities given by the IRI model (solid lines) and the ion densities calculated using Equations 6.14-6.16 (dashed lines) with the IRI electron density and the MSIS neutral densities, for four different latitudes. The calculations were run for the conditions at 0500 UT on October 1, 2002.
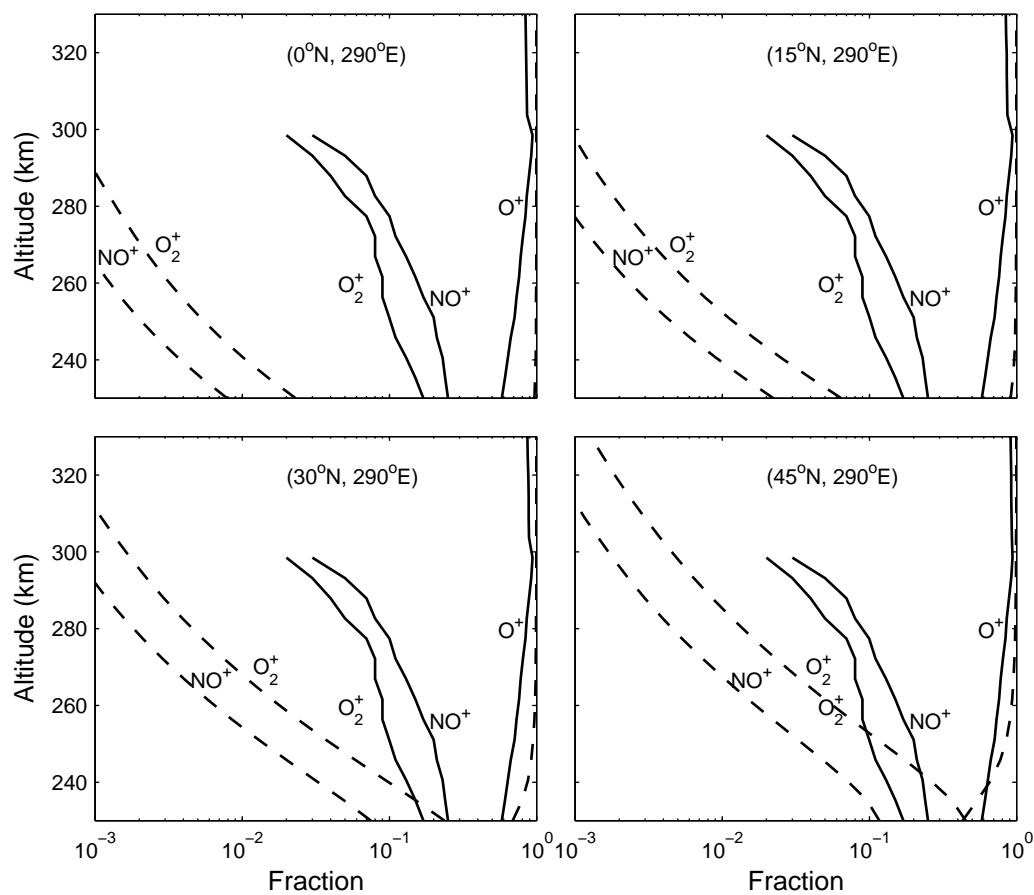
Figure 6.3: Height distributions of the ion fractions for the same cases as Figure 6.2. The solid lines correspond to the predictions of the IRI model and the dashed lines correspond to the ion fractions using Equations 6.14-6.16 with the IRI electron density.

possible to determine whether the IRI densities are reasonable. Figure 6.4 shows the predicted volume emission rates for the IRI profiles in Figures 6.2 and 6.3. Shown are the green line emission rates (black lines) and the red line emission rates (gray lines) for the case including the molecular ion densities (dashed lines) and neglecting the molecular ion densities (solid lines). This figure is in stark contrast to Figure 6.1, where we showed that the expected role of the molecular ions was to decrease the volume emission rate slightly on the bottomside. However, when we use the IRI ion densities, a much higher volume emission rate is predicted. The effect is much more significant at low latitudes. At the equator, an integrated red line emission rate of 11 kR is predicted, a factor of 20 higher than the emission rate predicted neglecting molecular ions. The green line ratio is of a similar magnitude. The ratio decreases as a function of latitude, and at 45°N the integrated emission rates are within a factor of 2, although there are again qualitative discrepancies in the emission profiles. We should note that the volume emission rates predicted from the IRI electron densities neglecting the molecular ions look fairly reasonable, and the magnitudes of the integrated emission rates are in approximate agreement with observations.

Such high red and green line F-region integrated emission rates have never been observed at low and mid-latitudes. Note that O_2^+ was absent in an older version of the ion composition in the IRI model. In Figure 6.5, we show the seasonal, latitudinal, and local time variation of the discrepancy. Plotted is the ratio of the 630.0-nm integrated emission rate including molecular ions to that neglecting molecular ions. The first row shows this ratio as a function of day of year (DOY) and latitude at constant times of 0200 UT (about 2200 LT) and 0500 UT (about 0100 LT). The bottom row shows the ratio as a function of DOY and UT time. All calculations are done at a longitude of -70°E, and are calculated every tenth day for every 5 degrees of latitude from 0 to 45°N and for every hour from 0100-0800 UT (about 2100-0400 LT).
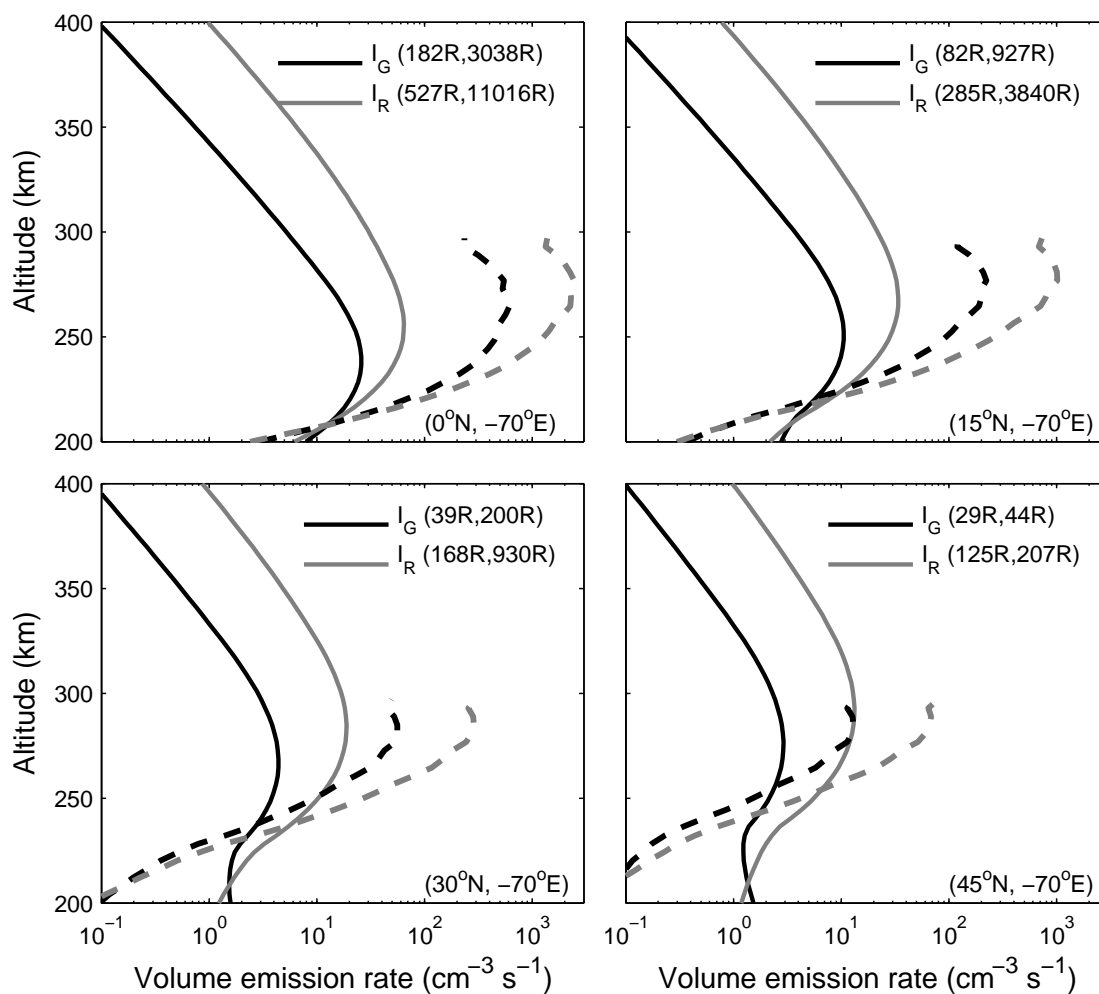
Figure 6.4: The height profiles of the 630.0-nm (gray) and 557.7-nm (black) volume emission rates calculated by the usual approach (solid) and with the ion densities given by the IRI model (dashed). The integrated emission rates in Rayleighs for the two curves are indicated in the legend (the first number corresponds to the usual approach, neglecting the ion composition).

Black portions of the plots indicate a ratio of 20-30, dark gray portions indicate a ratio of 10-20, and light gray portions are between about 5 and 10. Completely white portions correspond to times when IRI gives zero O_2^+ fraction - in that case, the ratio cannot be calculated. The calculations show that the discrepancy is the largest during equinox conditions at low latitudes. The discrepancy also exists off the equator during summer months and on the equator during winter months. The discrepancy is most pronounced around local midnight. The integrated emission rates corresponding to the largest ratios are in excess of 20 kR. We should point out that the discrepancy is mainly confined to the western longitude sector - at eastern longitudes greater than about 30°, the discrepancy seems to disappear.

Comparisons to ground-based airglow measurements are difficult because of the integrated nature of those measurements. Two volume emission profiles might be completely different but give the same integrated quantity, for example see Figure 6.4. Further understanding of the discrepancies that lead to such huge ratios of the integrated intensities can be gained by looking at actual measurements of the volume emission rates. The Wind Imaging Interferometer (WINDII) experiment, part of the Upper Atmosphere Research Satellite (UARS), made many measurements of green line volume emission profiles (e.g., *Shepherd et al.*, 1997). These profiles can be used to directly infer the O_2^+ density. Figure 6.6 shows two examples. The top panel corresponds to 4.62 UT (23.57 LT) on March 26, 1993, and the lower panel corresponds to 6.15 UT (23.13 LT) on September 20, 1992 at the locations indicated on the figures, both of which are near the equator. The volume emission rate profiles for both cases show the trend that we have been discussing. The IRI-predicted green line volume emission rate is much higher (a factor of 10-20) than the measured volume emission rate and the emission rate predicted using Equation 6.13 with the IRI electron density and the MSIS neutral densities. The volume emission rate also
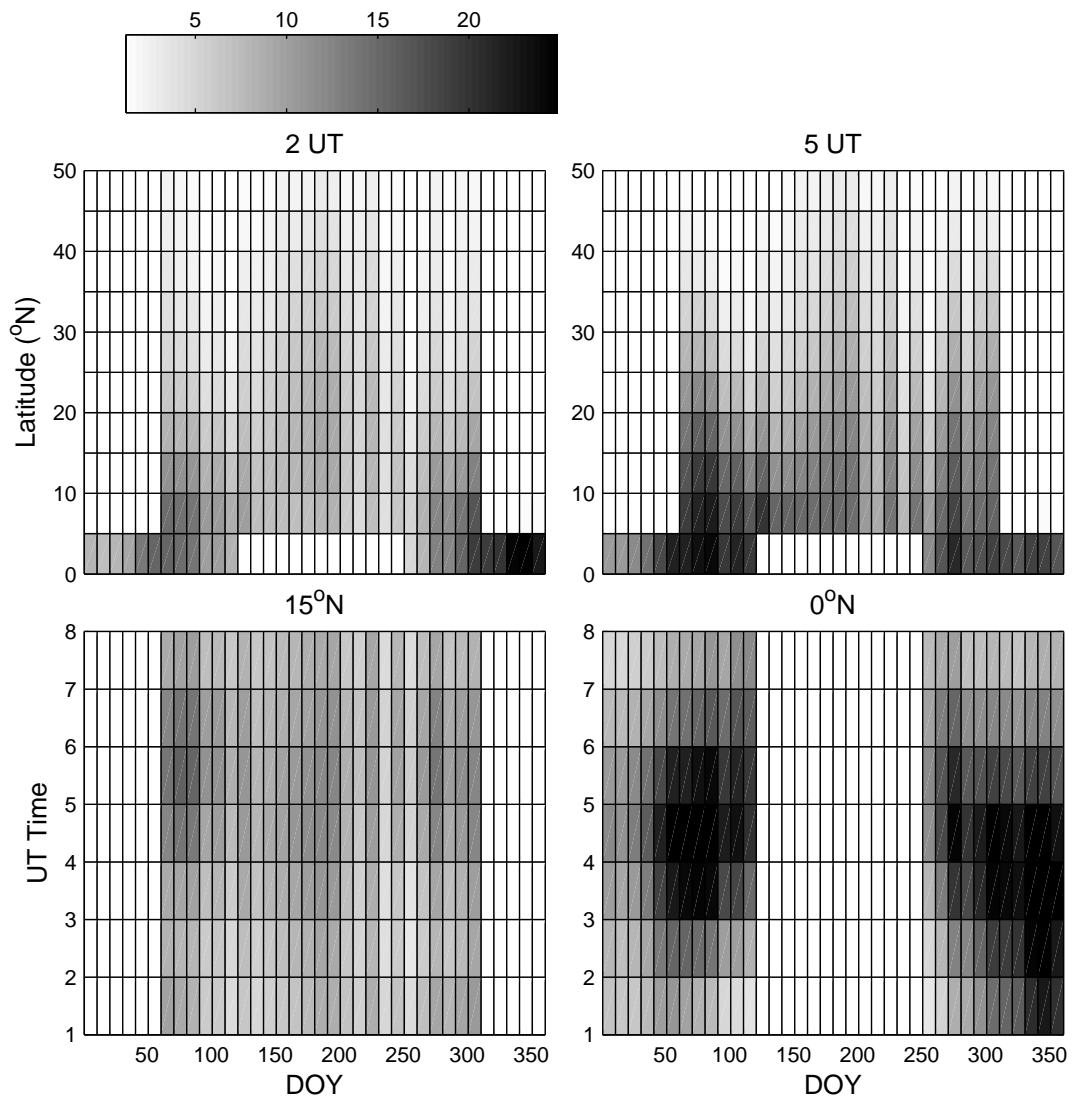
Figure 6.5: The ratio of the integrated red line emission rate including the IRI molecular ions to the integrated red line emission rate neglecting the molecular ions is plotted. The top row shows this ratio as a function of latitude and day of year for the year 2002 at two UT times, 0200 UT and 0500 UT. The bottom row shows the ratio as a function of UT time and day of year for two latitudes, 15°N and 0°. The longitude for all calculations is -70°E.

peaks at a much higher altitude, about 275 km as compared to about 240 km for the measurements. The calculations using Equation 6.13 underestimate the emission rate somewhat, perhaps by a factor of 2, but this discrepancy could easily be the result of errors in the electron density or the neutral density given by the models, or in the value of μ_S as mentioned earlier. The shapes of the profiles are in agreement. The second panels show the derived O_2^+ densities (solid are from the measurements, black dashed are from IRI, and gray dashed are using the MSIS neutral densities and the IRI electron density) along with the IRI electron density (dash-dotted). The IRI O_2^+ density is again much higher than that derived from the measurements and peaks at a much higher altitude, which leads to the enhanced volume emission rate at high altitudes. The MSIS-derived O_2^+ density is within about a factor of 2 of the "measured" density and has the same altitudinal trend, in sharp contrast to the IRI profiles. The discrepancy in magnitude is likely due to the bottomside IRI electron density for these specific conditions, although the difference is not too significant, and the profile shapes are in good agreement. The plots in the third panel of the O_2^+ fractions for the three curves show similar information. Both the measurements and the MSIS derivations show a decrease in the O_2^+ fraction to a negligible level by 250 km, whereas the IRI O_2^+ fraction decreases much more slowly.

Our conclusions are supported by our estimates of the ionization rates corresponding to the IRI parameters at latitudes below 30°N. The recombination rate of the molecular ions is given by the formula

$$L = \alpha_{O_2^+}^* [O_2^+] n_e + \alpha_{NO^+}^* [NO^+] n_e.$$

Using the IRI values at 250 km from the panel at 0°N in Figure 6.2 corresponding to $[O_2^+] = 8.2 \times 10^4$ cm^{-3}, $[NO^+] = 1.6 \times 10^5$ cm^{-3}, $n_e = 8.2 \times 10^5$ cm^{-3}, along with the rate constants of *Sheehan and St.-Maurice* (2004) with $T_e \approx 1000$ K, we obtain
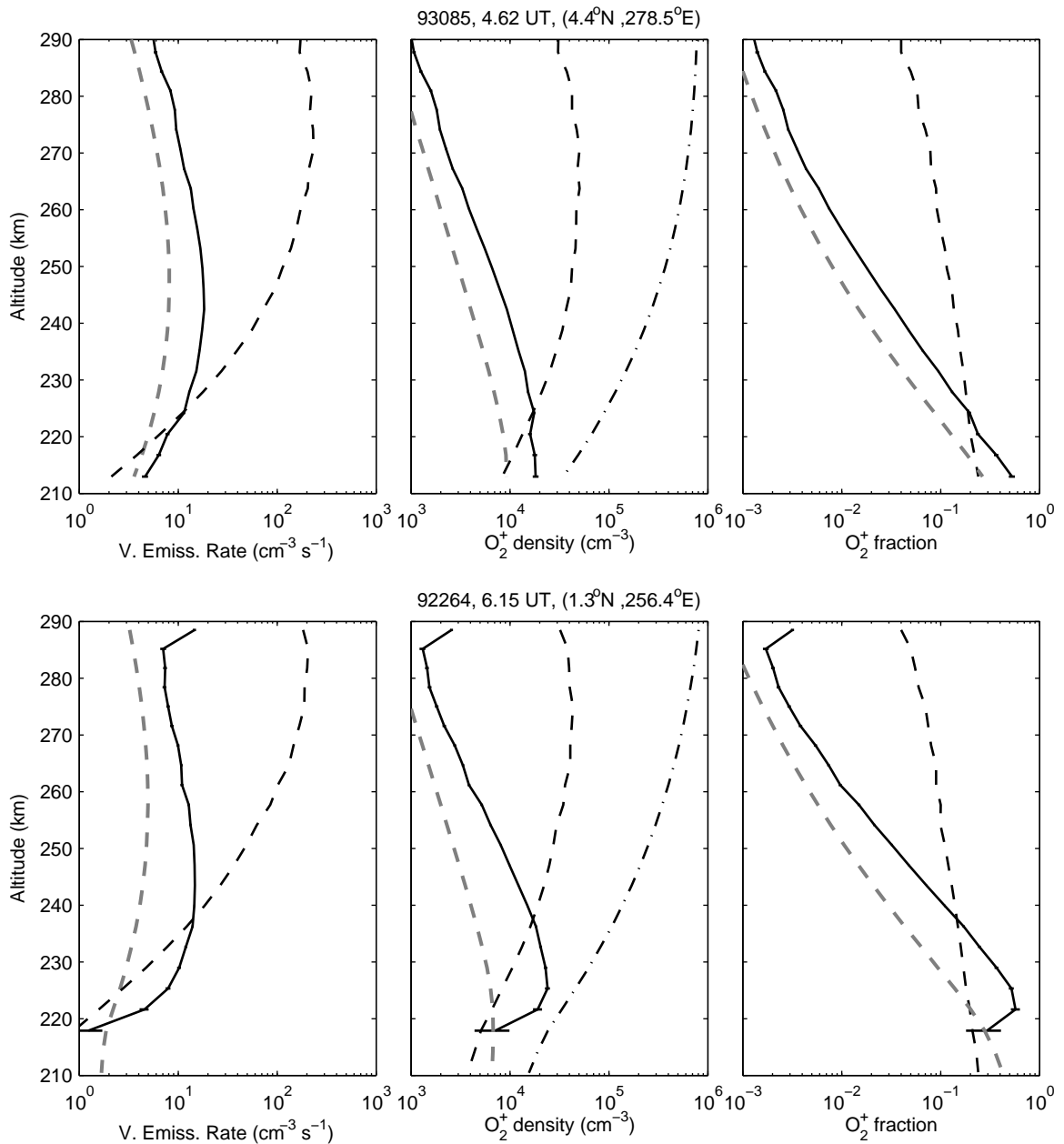
Figure 6.6: Two examples of WINDII volume emission rates (left), derived O_2^+ densities (middle), and ion fractions (right). In the left-hand panels, the solid curves are the WINDII measurements, the gray dashed curves are the derived emission rates using Equation 6.13 with the IRI electron density, and the black dashed curves are the volume emission rates from Equation 6.5 with the IRI ion densities. In the middle panels, the black lines are the O_2^+ densities derived from the measurements using Equation 6.5, the dashed black lines are the IRI O_2^+ densities, the dash-dotted lines are the IRI electron densities, and the dashed gray lines are the MSIS-predicted O_2^+ densities from Equation 6.14 using the IRI electron densities. The right-hand panels are the ion fractions for the 3 curves computed using the IRI electron densities.

$L = 2.6 \times 10^4$ cm^{-3}s^{-1} (5.6×10^3 cm^{-3}s^{-1} for only O$_2^+$). The same calculation at 15°N yields $L = 5.5 \times 10^3$ cm^{-3}s^{-1} (1.2×10^3 cm^{-3}s^{-1} for only O$_2^+$) and at 30°N yields $L = 5.8 \times 10^2$ cm^{-3}s^{-1} (1.2×10^2 cm^{-3}s^{-1} for only O$_2^+$). The recombination lifetimes for these examples ($\tau_j = 1/\alpha_j^* n_e$) are $\tau_{\text{O}_2^+} = 15$ s, $\tau_{\text{NO}^+} = 8$ s at 0°N; $\tau_{\text{O}_2^+} = 32$ s, $\tau_{\text{NO}^+} = 17$ s at 15°N; and $\tau_{\text{O}_2^+} = 98$ s, $\tau_{\text{NO}^+} = 54$ s at 30°N. These times are much shorter than the time of any transport processes in the $F2$ region and thus there is local equilibrium for the molecular ions. This means that the production rate of the molecular ions is equal to the recombination rate. However, a production rate of 10^4 cm^{-3}s^{-1} is close to or greater than the maximum value of the daytime ionization rate in the $F2$ region at the equator, which is unrealistic at night.

The ion composition model in IRI (*Bilitza*, 2001; *Danilov and Smirnova*, 1995) is based mainly on rocket and satellite data. As noted by *Bilitza* (2001), the limitations of the IRI ion composition are due to the limited database used in the model. The techniques discussed here could be used to improve the nighttime ion composition model.

6.5   Conclusions

The red and green line emission rates calculated by the usual approach (neglecting molecular ions) with the electron density predicted by IRI seem to be in fairly good agreement with measured emission rates. These models for the emission rates have been validated before with actual measurements, for example from Arecibo (*Vlasov et al.*, 2005). The role of non-negligible molecular ions should be to decrease the red and green line volume emission rates at low altitudes. This behavior is predicted from the assumption that O$_2^+$ and NO$^+$ ions are only produced by the O$^+$ reactions with N$_2$ and O$_2$, a reasonable assumption at night at low and mid-latitudes. However, the

molecular ion densities given by the IRI model are much higher than the predictions of that theory with the MSIS neutral densities. The IRI molecular ion densities show a much different altitudinal dependence than the MSIS-predicted molecular ion densities. In turn, the emission rates calculated with the molecular ion densities given by the IRI model are much higher than any measured emission rates, by over an order of magnitude at low and mid-latitudes at western longitudes. The discrepancy between the emission data and the IRI model is most important at latitudes below $30°$ during the period from March to November. Measurements of the green line volume emission rate as a function of altitude by the WINDII instrument confirm that the discrepancy is likely due to an overestimation of the O_2^+ fraction.

These results may help with a revision of the ion composition in the IRI model. A first revision might incorporate volume emission rate measurements such as those by WINDII and consistency with ground-based integrated measurements. Alternatively, the MSIS neutral densities could be used with Equations 6.14-6.16 and the IRI electron density as a nighttime molecular ion density model.

Acknowledgements

Chapter 7

Deriving Neutral Parameters from Incoherent Scatter Radar Observations using Ion Energy Balance[*]

Most people use statistics the way a drunkard uses a lamp post, more for support than illumination. - Mark Twain

7.1   Abstract

Ion energy balance studies using incoherent scatter radar (ISR) data involve the estimation of the neutral density and exospheric temperature from the ISR-measured parameters using theoretical collision cross sections. The ratio $[O]_{\mathrm{radar}}/[O]_{\mathrm{MSIS}}$ in long-term averages is an estimate of the so-called Burnside factor and can be derived from these studies. This parameter is thought to be associated with errors in the O^{+}-

---

[*]This chapter based on the original work, currently in press, *Nicolls et al.* (2006a). Reproduced by permission of the American Geophysical Union.

O collision cross section. The most recent comparison between MSIS neutral atomic oxygen densities and values derived from Arecibo ISR measurements using ion energy balance shows large discrepancies for high solar flux conditions (*Burnside et al.*, 1991). In contrast to ion momentum studies, which typically lead to a Burnside factor greater than one (usually near 1.2-1.3), the discrepancies between MSIS densities and radar-derived values tend to result in low values (near 0.8) for the Burnside factor. Various interpretations of this discrepancy have been put forward. We have re-analyzed the Arecibo ISR World Day data from 1988 to 1994, corresponding to the moderate to high solar flux period of solar cycle 22. By extending the analysis to the upper F region/lower topside (and explicitly including the role of H^+, which is often neglected) we obtain consistent results for the neutral density and exospheric temperature that show no significant long-term discrepancy from the MSIS predictions. For this period, we obtain a median ratio $[O]_{radar}/[O]_{MSIS}$ of 1.26 ± 0.02 using the O^+-O collision cross section from *Banks* (1966b). The standard deviation of the data is about 0.35. This ratio is close to the most recently published theoretical simulations of the collision cross section within the uncertainties. Knowing the correct O^+-O collision cross section allows one to extract the neutral parameters from the radar data and study short-term (day-to-day) variations in those parameters.

7.2   Introduction

Studies of the ion energy budget based on incoherent scatter radar (ISR) measurements have been used often in the past to infer neutral atmospheric parameters (e.g., *Bauer et al.*, 1970; *Swartz and Nisbet*, 1971; *Burnside et al.*, 1988; *Oliver and Glotfelty*, 1996). The technique is particularly simple in the vicinity of the F-region electron density peak, where atomic oxygen ions (O^+) make up nearly 100% of the

ion density. In this region, one can estimate the temperature of the neutrals and the density of neutral atomic oxygen by combining ISR measurements from several altitudes. The results of this method, however, depend on the O^+-O collision cross section used in the study. This parameter has been under debate for more than a decade (e.g. *Salah*, 1993; *Oliver and Glotfelty*, 1996) and remains a topic of investigation (*Omidvar et al.*, 1998b). Since the O^+-O energy transfer rate is proportional to the neutral density of atomic oxygen and the collision cross section, uncertainties in the cross section lead to uncertainties in the neutral densities derived from the ion energy balance.

The uncertainties in the O^+-O collision cross section or collision frequency have historically been expressed in the form of a ratio between a value for that parameter determined experimentally (or theoretically) and the theoretical value from *Banks* (1966b). The *Banks* (1966b) collision frequency is quite close to other commonly used collision frequencies such as those of *Schunk and Walker* (1973) and *Dalgarno* (1964). The *Schunk and Walker* (1973) value has the same temperature dependence as the *Banks* (1966b) value but is about 5% higher, based on the calculations of *Schunk and Walker* (1970). Here we will report the values relative to that of *Banks* (1966b) despite the fact that the study of *Burnside et al.* (1987) computed a factor using the *Schunk and Walker* (1973) collision frequency. We report the results in this way to be consistent with the historical definition of the Burnside factor as a multiplier of the *Banks* (1966b) result. The ratio has been dubbed the "Burnside factor" (or F) following the study by *Burnside et al.* (1987), which concluded that an increase in Banks' result by 70% ($F = 1.7$) was necessary for neutral winds derived from Arecibo ISR measurements and the ion momentum budget to agree with 630-nm neutral winds measured by a Fabry-Perot interferometer (note that this value should really be closer to 1.8 relative to the *Banks* (1966b) baseline). Of course, the term

"Burnside factor" did not come about until after this study, but it is still useful to express the early theoretical work in terms of a Burnside factor.

We point the interested reader to the paper by *Salah* (1993) where many of the early theoretical expressions for the momentum transfer collision frequency are tabulated. Theoretical calculations of the O^+-O collision cross sections have been attempted since the late 1950's, when *Dalgarno* (1958a) estimated the diffusion coefficient of O^+ based on the theoretical resonance cross section estimates of *Dalgarno* (1958b). *Dalgarno* (1964) scaled this value to agree with the laboratory measurements of *Stebbings et al.* (1964). The *Dalgarno* (1964) value corresponds to a Burnside factor of about 1.03 at 500 K and about 1.0 at 2000 K (the temperature here refers to the mean ion-neutral temperature). The formulation of *Banks* (1966b) ($F=1$) was based on the theoretical work of *Knof et al.* (1964) and is in reasonable agreement with an extrapolation of the *Stebbings et al.* (1964) laboratory measurements. *Stubbe* (1968) introduced a correction to the *Banks* (1966b) extrapolation of the *Stebbings et al.* (1964) curve, corresponding to $F \approx 1.35$ at 500 K and $F \approx 1.25$ at 2000 K. The next theoretical developments were made in the 1990's, when *Stallcop et al.* (1991) and *Pesnell et al.* (1993) computed the collision frequency using different quantum mechanical simulations (but the same potential energy curves) with nearly identical results. The *Pesnell et al.* (1993) results correspond to $F \approx 1.36$ at 500 K and $F \approx 1.28$ at 2000 K, quite close to the *Stubbe* (1968) formulation. The latest results of *Hickman et al.* (1997), who considered the effects of fine structure in the theoretical calculations using the *Stallcop et al.* (1991) potential energy curves, correspond to $F \approx 1.33$ at 500 K and $F \approx 1.22$ at 2000 K.

Meanwhile, many attempts have been made to infer the Burnside factor from aeronomical measurements. There are two commonly used techniques for making these indirect measurements, one based on the ion momentum budget and one based on the

ion energy budget, both of which have been described in the preceding paragraphs. *Roble* (1975) used a different approach, using a one dimensional model and varying the diffusion coefficient until good agreement was obtained between the model and the electron density observed at Millstone Hill - he found $F \approx 1.5$. Following the study of *Burnside et al.* (1987) (which derived the Burnside factor of $F = 1.7^{+0.7}_{-0.3}$), many subsequent studies were also done using the ion momentum balance technique. The results of *Sipler et al.* (1991) ($F \approx 1.9 \pm 0.15$) and *Buonsanto et al.* (1992) ($F \approx 1.7 \pm 0.07$) seemed to confirm the correction suggested by *Burnside et al.* (1987). These results led to the adoption of a new collision frequency by the CEDAR community (*Salah*, 1993), which corresponds to $F \approx 1.68$ at 500 K and $F \approx 1.85$ at 2000 K. However, *Reddy et al.* (1994) was later able to show that the results of *Burnside et al.* (1987) could be explained by an inherent positive bias in the estimate of the F factor resulting from the least squares fitting method used to determine the factor. Later, *Hines et al.* (1997) expanded and generalized this analysis, and *Omid-var et al.* (1998a) illustrated how different estimators could result in different values of F. Since these studies, the F factor from ion momentum studies has begun to converge on values close to the most recent theoretical simulations (*Hickman et al.*, 1997; *Pesnell et al.*, 1993). A re-analysis of much of the Millstone Hill data (including those used by *Sipler et al.* (1991)) with careful attention paid to the error analysis was done by *Buonsanto et al.* (1997), and they found $F = 1.4 \pm 0.3$. A re-analysis of EISCAT data by *Davis et al.* (1995) also led to F values between 1.2 and 1.4. Although these results are convincing, with the ion momentum results showing good agreement with the theoretical values, there has never been any definitive consensus on this issue, as other experimental results (e.g. *Dyson et al.*, 1997) and recent lab measurements (e.g. *Lindsay et al.*, 2001) point to values closer to 2.0.

On the other hand, studies of the ion energy balance have pointed to values of F

below one. This alternative interpretation of the Burnside factor has been considered by *Oliver and Glotfelty* (1996), who looked at the ratio of experimentally determined atomic oxygen densities to MSIS densities derived from the ion energy balance at Millstone Hill. Under the assumption that in a long-term average MSIS densities are correct, and using Banks' collision cross section, the ratio of the radar O density to the MSIS value can be considered an estimate of the Burnside factor. When *Oliver and Glotfelty* (1996) applied this interpretation to Millstone Hill estimates of [O], they found a Burnside factor of 0.75, with the possibility of it being up to 0.91 if light ions (not accounted for in the analysis) were present in the data. Moreover, by reinterpreting the results of previous studies at other facilities (*Hedin and Alcaydé*, 1974; *Alcaydé and Bauer*, 1977; *Carlson and Harper*, 1977; *Burnside et al.*, 1991) taking into account possible errors in the analysis (most of which had to do with an overestimation of the Coulomb logarithm in the electron-ion heat transfer rate by about 10%), they argue that these similar studies would also yield a ratio $[O]_{\mathrm{radar}}/[O]_{\mathrm{MSIS}}$ below one. For example, the original study of *Carlson and Harper* (1977) at Arecibo reported a Burnside factor of about $F = 1.28 \pm 0.15$, but the reinterpretation by *Oliver and Glotfelty* (1996) corrected this value to $F = 0.75 \pm 0.1$ (note that this correction did not have to do with the Coulomb logarithm used by *Carlson and Harper* (1977) but with the neutral density used). In particular, these authors find that a reinterpretation of the neutral atomic density results of *Burnside et al.* (1991) leads to a Burnside factor of $F = 0.82 \pm 0.1$. These results led *Oliver* (1997) to propose the possibility that a reservoir of 1-2% $\sim$4000 K hot oxygen (e.g., *Yee et al.*, 1980) could explain the values of F lower than 1 and the discrepancy with the ion momentum results.

However, in the study of *Burnside et al.* (1991), the discrepancies between $[O]_{\mathrm{radar}}$ and $[O]_{\mathrm{MSIS}}$ grew quite large during solar maximum conditions due to very low values

of $[\mathrm{O}]_{\mathrm{radar}}$, which perhaps biased the ratio $[\mathrm{O}]_{\mathrm{radar}}/[\mathrm{O}]_{\mathrm{MSIS}}$ towards values less than one. Since the study by *Burnside et al.* (1991), the Arecibo F-region World Day data from solar cycle 22 has been re-analyzed taking into account light ions ($\mathrm{H^+}$ and $\mathrm{He^+}$). The details of the analysis technique are described in Section 7.7 (Appendix A). The availability of these newer, more accurate datasets prompted us to revisit the results of *Burnside et al.* (1991). By careful consideration of the errors in the energy balance equations, and by extending the analysis to higher altitudes including the effects of $\mathrm{H^+}$, we are able to obtain estimates of the neutral parameters that show consistency with the MSIS results. In addition, if we interpret the ratio $[\mathrm{O}]_{\mathrm{radar}}/[\mathrm{O}]_{\mathrm{MSIS}}$ as a Burnside factor, the results are consistent with the most recent theoretical formulations of *Stallcop et al.* (1991), *Pesnell et al.* (1993), and *Hickman et al.* (1997) for the $\mathrm{O^+}$-O collision cross section.

7.3 Calculating Neutral Parameters Using Energy Balance

Near the $F2$ peak, atomic oxygen ions mainly interact collisionally with two gases: the electrons and the parent neutral atomic oxygen. During the day, when the electron gas ends up with most of the energy in excess of the photoionization threshold, Coulomb collisions between the electrons and ions effectively heat the ion gas. The ions then pass this energy to the parent neutral gas (thermospheric O).

The ion energy balance equation for a species i can be written as (e.g., *Bailey and Sellek*, 1990)

$$\frac{3}{2}k_B n_i \left(\frac{\partial T_i}{\partial t} + \mathbf{v}_i \cdot \nabla T_i \right) = Q_i - k_B n_i T_i \nabla \cdot \mathbf{v}_i + \nabla \cdot (\kappa_i \nabla T_i) + F_{in} \qquad (7.1)$$

where the net heating rate is given by

$$Q_i = Q_{e,i} - \sum_{j \neq i} Q_{i,j} - \sum_k \left(Q_{i,k}^{el} + Q_{i,k}^{inel} \right) = Q_{e,i} - \sum_{j \neq i} Q_{i,j} - Q_{i,n} \tag{7.2}$$

and T_i is ion temperature, n_i is ion density, k_B is Boltzmann's constant, $\mathbf{v}_i$ is the species velocity, κ_i is the thermal conductivity, and F_{in} is frictional (Joule) heating. In the equation for Q_i, we have defined

$$Q_{i,n} = \sum_k \left(Q_{i,k}^{el} + Q_{i,k}^{inel} \right). \tag{7.3}$$

In the above expressions, $Q_{e,i}$ represents the total electron-ion heat transfer rate, $Q_{i,j}$ represents the total heat transfer from ion i to ion j, $Q_{i,k}^{el}$ represents the heat transfer from ion i to neutral k due to elastic collisions, and $Q_{i,k}^{inel}$ represents the heat transfer from ion i to neutral k due to inelastic collisions.

In Equation 7.1, the left-hand side can be set to 0 since the time rate of change of T_i is small relative to the integration period, and the gradient of T_i is small relative to the beam size. The second term on the right-hand side is always small since the divergence of the plasma velocity is negligible. In the case where thermal conductivity and Joule heating are negligible, which is valid under most conditions at Arecibo, Q_i must be 0 so that for the O^+ ions,

$$Q_{e,O^+} - Q_{O^+,n} = 0 \tag{7.4}$$

where the $Q_{i,j}$ term has been dropped since we have assumed all ions to be at the same temperature T_i (and those terms are proportional to the difference in ion temperatures (e.g., *Banks and Kockarts*, 1973; *Bailey and Sellek*, 1990)). This assumption is not exactly true in the topside ionosphere, where different H^+ and O^+ temperatures have been measured (*Sulzer and González*, 1996).

The electron-ion heat transfer rate, Q_{e,O^+}, can be written as (e.g., *Banks*, 1966a;

Banks and Kockarts, 1973)

$$Q_{e,O^+} = A_{e,O^+} n_e^2 (1 - p_{H^+})(T_e - T_i) T_e^{-3/2} \quad \text{eV cm}^{-3} \text{s}^{-1} \tag{7.5}$$

where T_e is electron temperature in Kelvins, p_{H^+} is the H^+ ion fraction, n_e is the electron density in cm^{-3}, and

$$A_{e,O^+} = C_{e,O^+} \ln \Lambda, \quad C_{e,O^+} = 3.1970 \times 10^{-8} \quad \text{eV K}^{1/2} \text{ cm}^3 \text{ s}^{-1}. \tag{7.6}$$

In Equation 7.5, we have used the fact that the O^+ ion density is given by the O^+ ion fraction times the electron density, and used the assumption that the only other ion species is H^+ (while the IS analysis does fit for the He^+ fraction in the topside, we have assumed that it is negligible at the altitudes and local times that we study, which is a good assumption). The Coulomb logarithm, $\ln \Lambda$, is given by *Itikawa* (1975) as

$$\ln \Lambda = \ln \left[\frac{16\pi n_e \lambda_D^3}{\gamma^2} \right] - 0.5 \tag{7.7}$$

where $\ln \gamma = 0.57722$ is Euler's constant, and λ_D is the electron Debye length,

$$\lambda_D = \frac{1}{10} \left(\frac{\epsilon_0 k_B T_e}{n_e e^2} \right)^{1/2} \quad \text{cm} \tag{7.8}$$

where ϵ_0 is the permittivity of free space, e is the electron charge, and where all quantities in these formulae are MKS, except the electron density, which is in cm^{-3}.

The ion-neutral heat transfer rate is given by

$$Q_{O^+,n} = \sum_k \left(Q_{O^+,k}^{el} + Q_{O^+,k}^{inel} \right). \tag{7.9}$$

The dominant term is due to pseudo-elastic collisions with atomic oxygen, a resonant interaction (e.g., *Banks and Kockarts*, 1973; *Schunk and Nagy*, 2000). Most studies neglect the other terms, however we include the (usually) small corrections due to elastic collisions with N_2, O_2, He, and H as well as the correction due to inelastic

collisions with H. This allows us to extend the analysis to higher altitudes and include the lower topside region. The heat transfer rate becomes,

$$Q_{O^+,n} = \sum_k Q^{el}_{O^+,k} + Q^{inel}_{O^+,H}. \tag{7.10}$$

The inelastic term is given by (*Bailey*, 1983; *Raitt et al.*, 1975),

$$
\begin{aligned}
Q^{inel}_{O^+,H} &= C^{inel}_{O^+,H}\sqrt{T_n}[\text{H}][\text{O}^+]\left(T_i - \frac{8[\text{O}][\text{H}^+]}{9[\text{H}][\text{O}^+]}\sqrt{T_nT_i}\right), \quad C^{inel}_{O^+,H} = 3.8\times 10^{-15} \\
&= C^{inel}_{O^+,H}n_e\left\{[\text{H}](1-p_{H^+})T_i\sqrt{T_n} - \frac{8}{9}[\text{O}]p_{H^+}T_n\sqrt{T_i}\right\} \tag{7.11}
\end{aligned}
$$

and the elastic terms are given by (*Banks*, 1966b; *Banks and Kockarts*, 1973; *Bailey and Sellek*, 1990; *Schunk and Nagy*, 2000),

$$
\begin{aligned}
Q^{el}_{O^+,n} &= Q^{el}_{O^+,O} + Q^{el}_{O^+,N_2} + Q^{el}_{O^+,O_2} + Q^{el}_{O^+,H} + Q^{el}_{O^+,He} \tag{7.12} \\
Q^{el}_{O^+,O} &= C^{el}_{O^+,O}F[\text{O}]n_e(1-p_{H^+})\sqrt{T_i+T_n}(T_i-T_n), \quad C^{el}_{O^+,O} = 2.1\times 10^{-15} \tag{7.13} \\
Q^{el}_{O^+,N_2} &= C^{el}_{O^+,N_2}[\text{N}_2]n_e(1-p_{H^+})(T_i-T_n), \quad C^{el}_{O^+,N_2} = 6.6\times 10^{-14} \tag{7.14} \\
Q^{el}_{O^+,O_2} &= C^{el}_{O^+,O_2}[\text{O}_2]n_e(1-p_{H^+})(T_i-T_n), \quad C^{el}_{O^+,O_2} = 5.8\times 10^{-14} \tag{7.15} \\
Q^{el}_{O^+,H} &= C^{el}_{O^+,H}[\text{H}]n_e(1-p_{H^+})(T_i-T_n), \quad C^{el}_{O^+,H} = 3.3\times 10^{-14} \tag{7.16} \\
Q^{el}_{O^+,He} &= C^{el}_{O^+,He}[\text{He}]n_e(1-p_{H^+})(T_i-T_n), \quad C^{el}_{O^+,He} = 2.8\times 10^{-14}. \tag{7.17}
\end{aligned}
$$

All heat transfer rates are in units of eV cm^{-3} s^{-1} with the densities in cm^{-3} and the temperatures in Kelvins. $C^{el}_{O^+,O}$ has units of eV cm^3 K$^{-3/2}$ s^{-1} and the other constants have units of eV cm^3 K^{-1} s^{-1}. Note that the weak temperature dependence of the O$^+$-O collision cross section has been ignored, which may add an error on $C^{el}_{O^+,O}$ of near $\pm2\%$ (*Banks*, 1966b; *Oliver and Glotfelty*, 1996). The equations above use the *Banks* (1966b) collision cross sections, however we have included the Burnside factor scaling, F, to $Q^{el}_{O^+,O}$. In our analysis, we set $F = 1$ and study it later by comparing our results to MSIS, as we will discuss.

With these definitions, the problem then comes down to solving the simplified energy balance equation, Equation 7.4, to infer neutral atmospheric parameters. In order to develop a suitable least squares problem, we assume model functions for the atomic oxygen density, $[O]$, and the neutral temperature, T_n, and fit for the atomic oxygen density at some altitude along with the exospheric temperature, T_∞.

The neutral atmospheric model that we use is the analytical model given by *Bates* (1959) and *Walker* (1965), which is also used to formulate the MSIS model. The model for the neutral temperature assuming diffusive equilibrium (and neglecting thermal diffusion) is a Bates-Walker profile,

$$T_n(\zeta) = T_\infty - (T_\infty - T_{n0})e^{-s\zeta} \tag{7.18}$$

where T_{n0} is the neutral temperature at a reference altitude z_0, s is an inverse scale height given by

$$s = \frac{1}{T_\infty - T_{n0}} \frac{\partial T_n}{\partial z}\bigg|_{z_0} \equiv \frac{ks}{T_\infty - T_{n0}} \tag{7.19}$$

(defining ks to be the gradient in neutral temperature evaluated at z_0), ζ is geopotential height (e.g., *Banks and Kockarts*, 1973),

$$\zeta = \int_{z0}^{z} \frac{g(z')}{g(z_0)} dz' = \frac{z - z_0}{1 + (z - z_0)/R_e}, \tag{7.20}$$

g is gravity, and R_e is the radius of the Earth.

The atomic oxygen density is given by (e.g., *Banks and Kockarts*, 1973)

$$[O](z) = [O]_0 \frac{T_{n0}}{T_n(z)} \exp\left[-\int_{z_0}^{z} \frac{dz'}{H(z')}\right] \tag{7.21}$$

where $[O]_0$ is the density at the reference height, the neutral scale height is

$$H(z) = \frac{k_B T_n(z)}{m_O g(z)}, \tag{7.22}$$

and m_O is the mass of atomic oxygen. Converting the integral above into one over geopotential height,

$$\int_{z_0}^{z} \frac{dz'}{H(z')} = \frac{mg_0}{k_B} \int_{0}^{\zeta} \frac{d\zeta'}{T_n(\zeta')}, \tag{7.23}$$

where g_0 is gravity at z_0, one can analytically compute the scale-height integral, and the expression for the neutral density may be written in closed form as

$$[\text{O}](\zeta) = [\text{O}]_0 \left[\frac{T_{n0}}{(e^{s\zeta} - 1)T_\infty + T_{n0}} \right]^{1+\gamma} e^{s\zeta} \tag{7.24}$$

where

$$\gamma = \frac{m_O g_0}{k_B T_\infty s}. \tag{7.25}$$

We estimate T_{n0} and ks from the MSIS-90 model (*Hedin*, 1991a) at an altitude z_0=120 km. Then, given an exospheric temperature and a neutral atomic oxygen density at z_0, one can compute the neutral temperature and density at all altitudes. We will report exospheric temperatures along with atomic oxygen densities at an arbitrary altitude of 400 km.

We should point out that our formulation is slightly different than the one employed by *Burnside et al.* (1991), who assumed that since T_n is approximately constant with altitude in the F region, the integrand in the exponent of Equation 7.21 could be written as $(z - z_0)/H$. We have tested this approach and find it to be reasonable, giving similar results for the exospheric temperature and neutral atomic oxygen density.

The problem is thus one of minimizing the squared residual of the weighted function in a least squares sense by adjusting $[\text{O}]_0$ and T_∞,

$$\chi^2 = \sum_{k=1}^{N_{alt}} \frac{(Q_{e,O^+} - Q_{O^+,n})_k^2}{\sigma_k^2} \tag{7.26}$$

for measurements at N_{alt} altitudes, where $1/\sigma_k^2$ is an altitude-dependent weight determined by the error in the functional being minimized.

7.4   Description of Data and Analysis Technique

ISR measurements from several heights (N_{alt}) and weights, $1/\sigma_k^2$, given by estimated variances in the modeled expression $Q_{e,O^+} - Q_{O^+,n}$, are used in the energy balance analysis. The temperatures, electron density, and H$^+$ ion fraction, along with the errors in those parameters, are determined from the incoherent scatter analysis, and a discussion of that technique is given in Section 7.7. The electron density has been carefully and consistently calibrated using data from an on-site ionosonde. All data (T_e, T_i, N_e, p_{H^+}) that went into the analysis come from World Day observations at Arecibo between 1988 and 1994, and in total 43 days were used in this study. The standard World Day F-region experiment has 37-km height resolution and approximately one-minute time resolution. For this study, we have averaged the data in one hour intervals. Local time at Arecibo is Atlantic Standard Time, i.e. UT-4. Figure 7.1 puts into perspective the conditions for the days used in this study, showing the h_mF2 value, the H$^+$ fraction, and the $F10.7$ solar flux for the datasets. We will refer to this figure more later.

The Arecibo ISR data come from heights between about 145 km and 665 km. However, the actual altitude window used in the least squares fitting in this study varies with solar flux and season, beginning roughly at the electron density peak and continuing up to the lower topside. We do not formally limit the altitude range of the data we use in our analysis to a prescribed window. Instead, we constrain the altitudes to satisfy the conditions that $T_i > T_n$ and $T_e > T_i$ (so that $Q_{e,O^+} > 0$). The only upper limits that we include are to require that Q_{e,O^+} be greater than 10 eVcm^{-3}s^{-1}, since the effects of thermal conductivity and other terms are perhaps between 0 and 10 eV cm^{-3}s^{-1}, and that $Q_{O^+,O}^{el}$ be greater than twice the sum of all the other "cooling terms" (elastic and inelastic). Thus, the altitude window used in

our study moves with the $F2$ peak, however extends into the topside region, which significantly enhances the quality of the fits since the difference $T_i - T_n$ increases with altitude. We will give an example of the fitting procedure shortly, after discussing the weights.

The errors used for the weights, σ_k in Equation 7.26, correspond to the errors in the functional being minimized, $Q_{e,O^+} - Q_{O^+,n}$. These errors are not trivial to evaluate since the model, $Q_{O^+,n}$, is a function of measured parameters, and the terms cannot be separated. The errors in Q_{e,O^+} are easy to evaluate using the errors from the IS analysis. To compute the errors σ_k, we first do a fit given errors calculated using the MSIS parameters, to get close to a solution and avoid convergence issues. We then do an iterative fit, adjusting the weights at each iteration. Some expressions for the errors and more information are given in Section 7.8. We do not assume any errors in the neutral parameters from MSIS that are used in the fitting (T_{n0}, ks, and the neutral densities not including atomic oxygen). We have experimented, however, in including arbitrary uncertainties in the MSIS parameters and obtain similar results. Our results, of course, will be sensitive to the values of T_{n0}, ks, and the neutral densities that are used. We have performed a sensitivity analysis of the technique to errors in T_{n0}, ks, and the neutral densities by performing various Monte Carlo simulations where the three parameters are varied independently assuming Gaussian distributed variables with a standard deviation of 20% of the MSIS-given values. We have done this for several different profiles, and find that the errors induced in the determination of O and T_∞ are usually negligible.

An example fit is shown in Figure 7.2, corresponding to the profile at 10.5 LT on March 20, 1988, which is a fairly typical case. The peak height, h_mF2, for this example was near 290 km. In the left-hand panel, the relevant terms in the energy balance equation are shown. The circles are the calculated values of Q_{e,O^+}, and the dots are
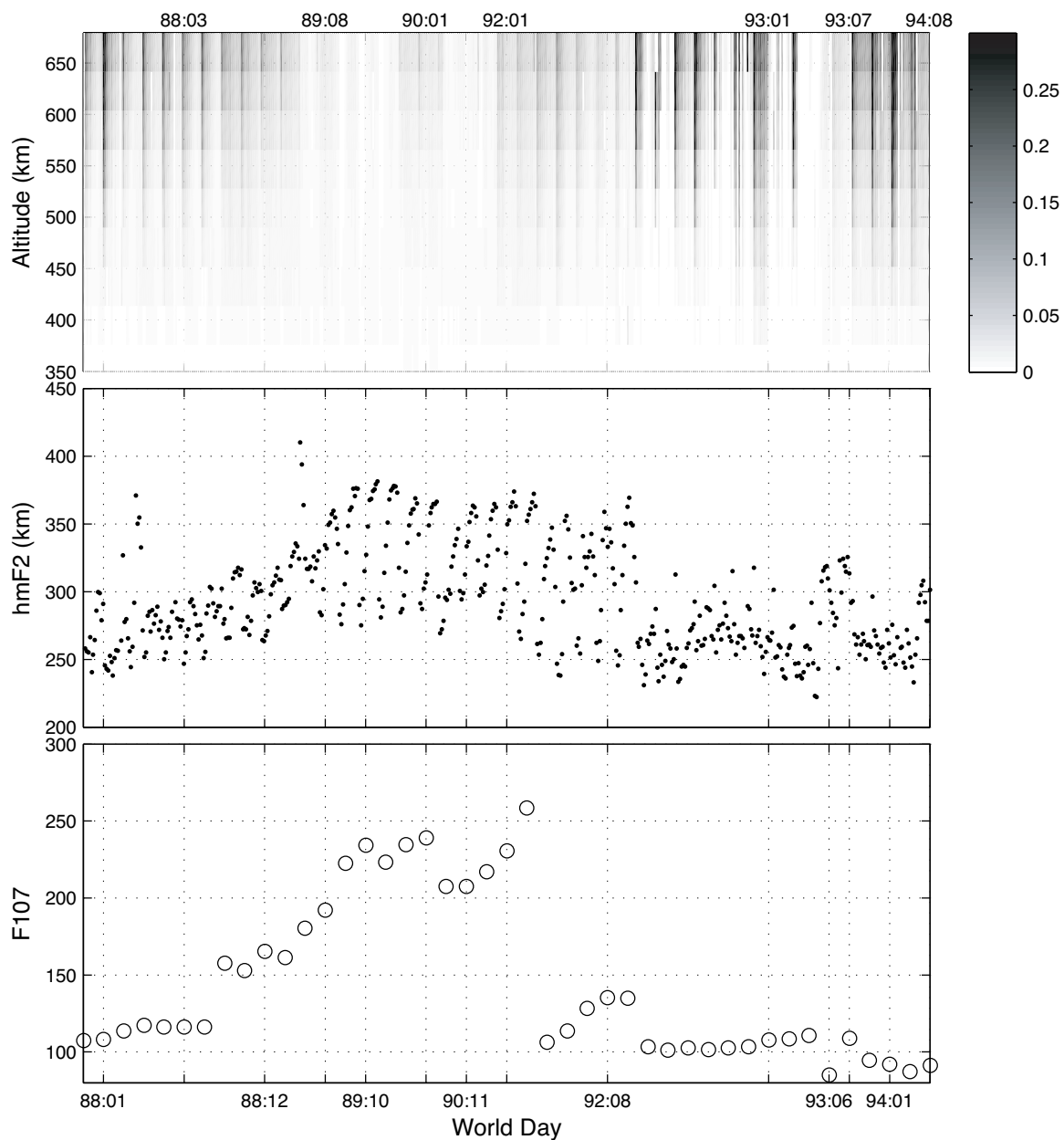
Figure 7.1: Daytime hydrogen fraction (top), h_mF2 (middle), and daily $F10.7$ (bottom) for Arecibo World Days between 1988 and 1994. Note that the x-axis does not represent actual time, but rather the data were plotted sequentially and a date stamp (in the form Year:Month) was assigned to each particular World Day period.
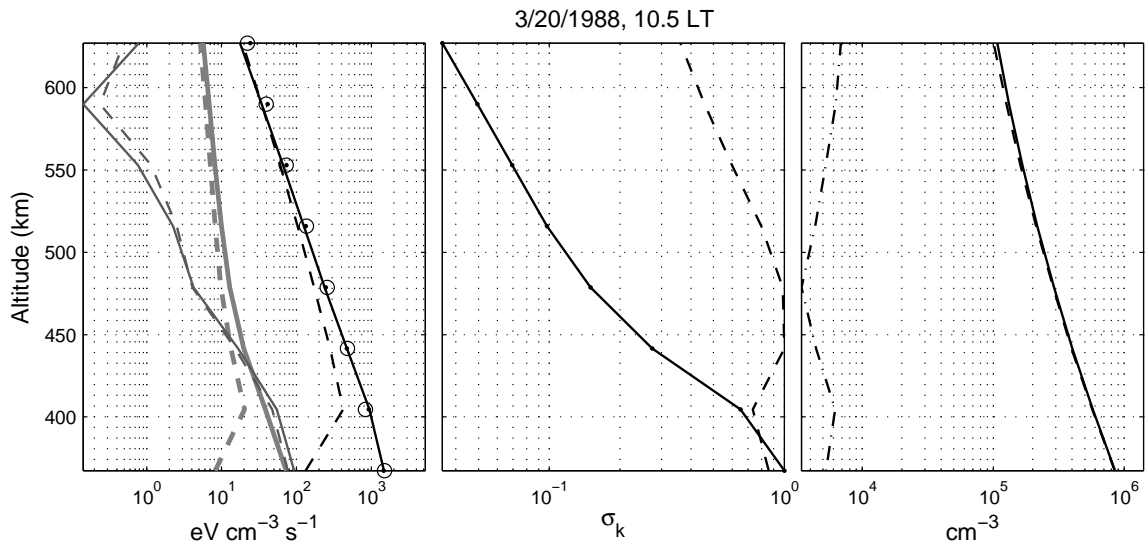
Figure 7.2: An example of a fitted profile. The left plot compares the relevant terms in the energy balance equation. All solid lines correspond to fitted results, and all dashed lines correspond to MSIS results. The black circles are the computed values of Q_{e,O^+}, the black dots are the final values of $Q_{O^+,n}$ determined from the fitting process, the black lines are $Q^{el}_{O^+,O}$ (the dominant term), the thick gray lines are $\sum_{k \neq O} Q^{el}_{O^+,k}$, and the thin, darker gray lines are $Q^{inel}_{O^+,H}$. The solid line in the middle panel shows the normalized σ_k, the inverse square root of the weights used in the fitting. The dashed line corresponds to normalized $Q_{e,O^+}/\sigma_k$, corresponding to the square root of the functional being minimized. The right panel shows the H$^+$ density, the O$^+$ density, and the electron density.

the values of $Q_{O^+,n}$ derived from the fitting procedure. They are in good agreement. The black lines correspond to the $Q_{O^+,O}^{el}$ terms, the thick gray lines correspond to the sum of all the other elastic terms, and the thin, darker lines correspond to the absolute value of the inelastic H term, where the solid lines are calculated using the fitted parameters, and the dashed lines are calculated using the MSIS parameters. The curves show the dominance of the O elastic term at all altitudes, with the other elastic terms becoming more important at high altitudes (due mainly to the H elastic term). The inelastic H term is smaller at all altitudes, and is most important at low altitudes. This is because even though the H^+ fraction is small (near 1%) at these altitudes, the ratio of the atomic oxygen density to the atomic hydrogen density decreases faster than the ratio of H^+ to O^+ increases, so that at higher altitudes the term is in fact smaller. The panel on the right shows the H^+ density (dash-dotted), the O^+ density (dashed) and the electron density for this example. The H^+ density increases to near 10% at the highest altitudes. The middle panel shows some of the effects of the weights. The solid curve is the normalized error, σ_k, in $Q_{e,O^+} - Q_{O^+,n}$ as a function of altitude. The error decreases with altitude, but the value of the function being minimized also decreases. The dashed line is the normalized $Q_{e,O^+}/\sigma_k$, which shows a peak near 450 km, meaning that the errors in these points contribute most to the residual and thus to the minimization procedure. These altitudes also correspond to those where $Q_{O^+,O}^{el}$ is the most dominant over the other terms.

A second example is shown in Figure 7.3 which has a higher fraction of H^+. In this case, the highest altitudes have H^+ fractions of over 30%, and these altitudes were eliminated from the analysis since the charge exchange term, $Q_{O^+,H}^{inel}$ became more important. That term is more important than the minor species elastic terms at these altitudes, however it is still lower than the elastic O term. Nevertheless, we eliminate those altitudes so that they don't affect our results due to possible errors
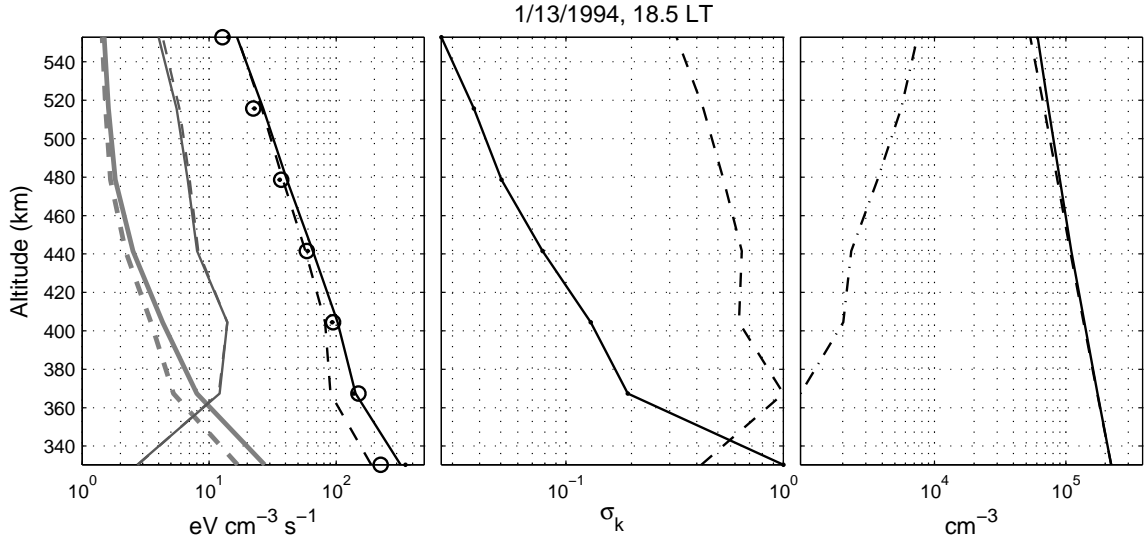
Figure 7.3: Same as Figure 7.2 for a different profile.

in the MSIS atomic hydrogen densities (which are likely less reliable than the atomic oxygen densities because they are derived from charge exchange equilibrium and are thus susceptible to the combined errors of the Atmospheric Explorer satellite [O$^+$] and [H$^+$] measurements). The upper altitudes included in the fit have H$^+$ fractions over 10%, and the fits look good. In this case, we see that the lower altitudes were weighted somewhat less because of errors there.

Weighting the fits properly is important. As an example, and as a method of confirming our error estimates, we performed a Monte Carlo simulation of our results for a particular profile, corresponding to the profile shown in Figure 7.2. The technique comprised of assuming normally distributed variables for the parameters measured by the radar and the neutral parameters from MSIS. Standard deviations were given by the measurement errors or by an assumed 20% uncertainty in the MSIS parameters. The fits were performed 10000 times for 3 cases: (1) where the weights are ignored - i.e., $\sigma_k = 1$ in Equation 7.26, (2) where the weights are given only by the errors in Q_{e,O^+} - i.e., the errors in $Q_{O^+,n}$, due to both the neutral and radar-measured parame-
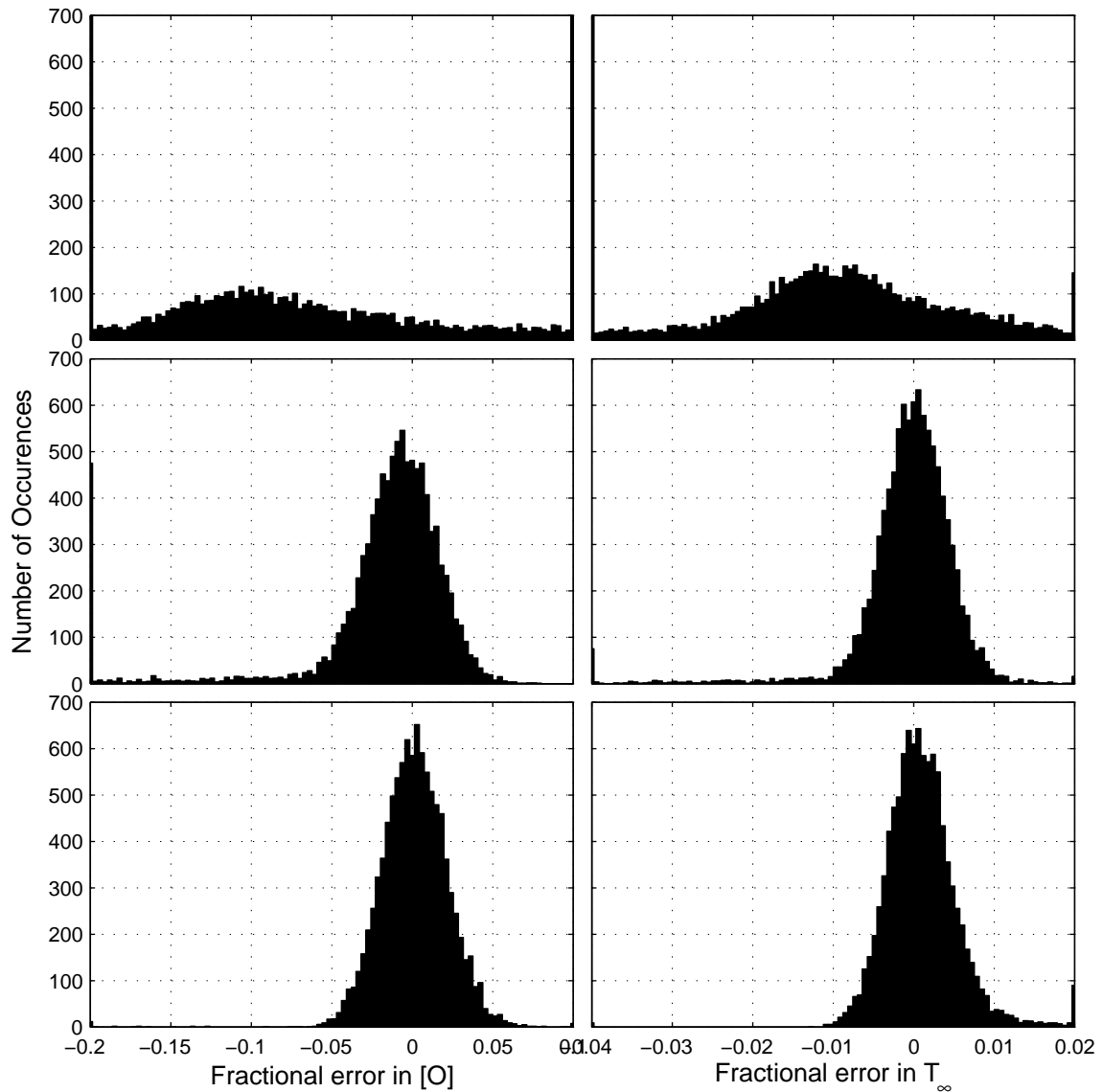
Figure 7.4: Monte Carlo simulation results, for the case of unity weights (top row), weights given by the error in Q_{e,O^+} (middle row), and weights given by errors in $Q_{e,O^+} - Q_{O^+,n}$ (bottom row). The left column shows the distribution functions for [O], and the right column shows the distribution functions for T_∞. The axes are normalized by the "true" value (determined from the original fit). The bin size for the [O] simulation is about 0.003 and the bin size for the T_∞ simulation is about 0.0006.

ters, are ignored, and (3) where the full error estimate as described is included in the weights. The results are summarized in Figure 7.4. The top panels show the results for case (1), the middle panels show the results for case (2), and the bottom panels show the results for case (3), where the plot in the left column corresponds to the [O] distribution and the plot in the right column corresponds to the T_∞ distribution. The axes have been normalized to the "true" values, determined from the original fit. In this case, the error from the fitting technique gave a fractional error in [O] of about 0.03 and a fractional error in T_∞ of about 0.005. These results correspond reasonably well to the widths of the distributions shown in the third row of the figure. T_∞ is determined much more accurately than [O], which has been noted before (e.g., *Bauer et al.*, 1970). Ignoring the weights (top row) leads to an underestimation of [O] and T_∞, a bias towards lower values, and a much broader distribution. For this particular profile, the bias is about 10% for [O] and 1-2% for T_∞. The bias decreases significantly when errors in Q_{e,O^+} are included in the fits (middle row). Including the full errors seems to remove the bias completely. Note that the bias could be more or less depending on the altitudes used in the fits. If lower altitudes were included in the fits, or the upper altitudes were excluded, then the bias would presumably increase further. These results correspond only to this particular profile and other features can be seen if one examines different profiles. However, the general conclusion is that the best fits are obtained when we include all the error terms as described.

7.5   Results and Discussion

Using a method similar to that described, except neglecting all terms other than the $Q^{el}_{O^+,O}$ term, limiting the altitude range, and assuming an isothermal atmosphere, *Burnside et al.* (1988) computed neutral atomic oxygen densities using Arecibo ISR

data corresponding to low solar flux conditions (October 1985 - July 1986). For low solar flux conditions at Arecibo, the $F2$ peak may go as low as 200 km in the afternoon, and light ions may reach a 5% level at altitudes slightly below 500 km. Figure 7.1 shows the variation of H^+/n_e, the height of the $F2$ peak, and the $F10.7$ index for Arecibo World Days between 1988 and 1994. Under the low solar flux conditions, the choice made by *Burnside et al.* (1988) of using data between 290-475 km implies that their analysis mostly included data between the F-region peak and the level where light ions become important. The interpretation of their results, however, is not completely straightforward since their experimental values were computed with a 1.7 increase in $Q_{O^+,n}$ ($F = 1.7$), partly offset by their assumption of $\ln \Lambda = 15$ (perhaps 9% too high) in Q_{e,O^+}, as discussed in detail by *Oliver and Glotfelty* (1996). The technique of *Burnside et al.* (1988) was later applied to Arecibo World Day data from 1985-1989 (*Burnside et al.*, 1991). In Figure 13 of this last reference, they show a comparison of experimental neutral atomic oxygen densities along with the corresponding MSIS densities. The difference between experimental and MSIS values becomes extremely large for the World Days with the higher solar flux (June 1989 - October 1989). We have re-analyzed the high solar flux data that went into that study and have found that if one only considers data from the altitude range 290-475 km (as done by *Burnside et al.* (1991)), the results of the fit depart quite considerably from MSIS values. This discrepancy occurs because there exists a relationship between the height of the $F2$ peak and $F10.7$, as shown in Figure 7.1. Namely, as the solar flux increases, the $F2$ peak rises as well.

The problem with including only heights near or below h_mF2 is that the difference in $T_i - T_n$ is small and error prone. The fitter does not have much leeway to decrease T_n while maintaining a positive difference $T_i - T_n$ in the ion cooling term. At some point, in order to achieve convergence, the fitter must decrease [O] to reduce the

difference $Q_{e,O^+} - Q_{O^+,n}$ at the lower altitudes. Furthermore, other cooling terms can be significant at these altitudes, and neglecting them may not be justified.

As described in the previous sections, we have attempted to avoid this difficulty by not choosing a fixed altitude window from which to fit. Instead, we attempt to include all the important terms in the O^+ energy balance equation and pay careful attention to the errors as a function of altitude. In general, this leads to the smaller emphasis of altitudes where $T_i - T_n$ is small and where other terms become significant enough to make the [O] and T_∞ determination inaccurate. A full re-analysis of the IS data, including the effects of the light ions and a careful density calibration, has no doubt also improved the quality of the radar parameters used in the fits. As shown in Figure 7.1, despite the fact that we go to quite high altitudes, the role of H^+ does not become too important, as for most days used in this study the H^+ fraction has an upper limit of 10%. As we discussed in Section 7.4, careful consideration of the errors used in the fitting leads to weighting altitudes depending on the ratio of the functional being minimized to the net error (the altitudes where this ratio is the largest are the most important ones). The most important altitudes tend to be ones above h_mF2 but where the heating term Q_{e,O^+} is still large and where the elastic atomic oxygen term $Q_{O^+,O}^{el}$ is larger than the other cooling terms.

In Figures 7.5 and 7.6 we show two examples of fit results for specific days, March 17, 1988 and January 28, 1992. The top plots show the derived [O] at 400 km and T_∞ (solid) along with error bars given by the fitter. The dashed lines are the corresponding MSIS values. The bottom plots show the altitude profiles of the important terms and fitting results for the different times, as described in the caption and discussed below. For the 1988 case, we see that the MSIS values and radar values of [O] are fairly close in the late morning, but begin to diverge in the afternoon, where the radar-derived parameter exceeds the MSIS parameter by a factor of about 1.2. The

exospheric temperature for this case is a few tens of Kelvins below the MSIS value in the morning, and very close to the MSIS value in the afternoon. The general trend of enhanced exospheric temperature in the afternoon, peaking at about 1500-1600 LT, is seen. For the 1992 case, the [O] densities again diverge in the afternoon, with the radar parameters exceeding the MSIS parameters by a factor of 1.3-1.4. The exospheric temperature, on the other hand, exceeds the MSIS value, by perhaps 100 K, but again has a similar shape and trend. Note that the exospheric temperature was much higher on this day (the solar flux was significantly higher, about 230 compared to about 117).

These two days exhibit significantly different conditions, yet it is clear that we can obtain good fits for both days. The differences can be seen in the plotted profiles. The circles correspond to values of Q_{e,O^+}, the dots correspond to fitted values of $Q_{O^+,n}$, the dashed lines correspond to $Q_{O^+,n}$ from MSIS, and the dash-dotted lines are a proxy for the "most important" heights (for the fitter). They correspond to the ratio $Q_{e,O^+}/\sigma_k$, where σ_k is the estimated error in the expression $Q_{e,O^+} - Q_{O^+,n}$, normalized to a value of 10^4 (to fit on the axes). Error bars in the parameters Q_{e,O^+} and $Q_{O^+,n}$ are also shown (note that the error bars are symmetric - the log scale distorts them). The 1988 day corresponds to moderate solar flux where h_mF2 was between 250 and 300 km for most of the day. This allows the fitter to extend to lower altitudes successfully, where $T_i - T_n$ is not too small. The most important altitudes nevertheless correspond to slightly higher heights, which was discussed in Section 7.4. In some cases, the upper altitudes were eliminated from the fits because of the importance of other cooling terms, such as the charge exchange term, which becomes more important at the higher altitudes when h_mF2 is low. The 1992 case, on the other hand, is a higher solar flux day where h_mF2 became as high as 370 km. The altitudes below h_mF2 are not formally excluded from the fits, however the
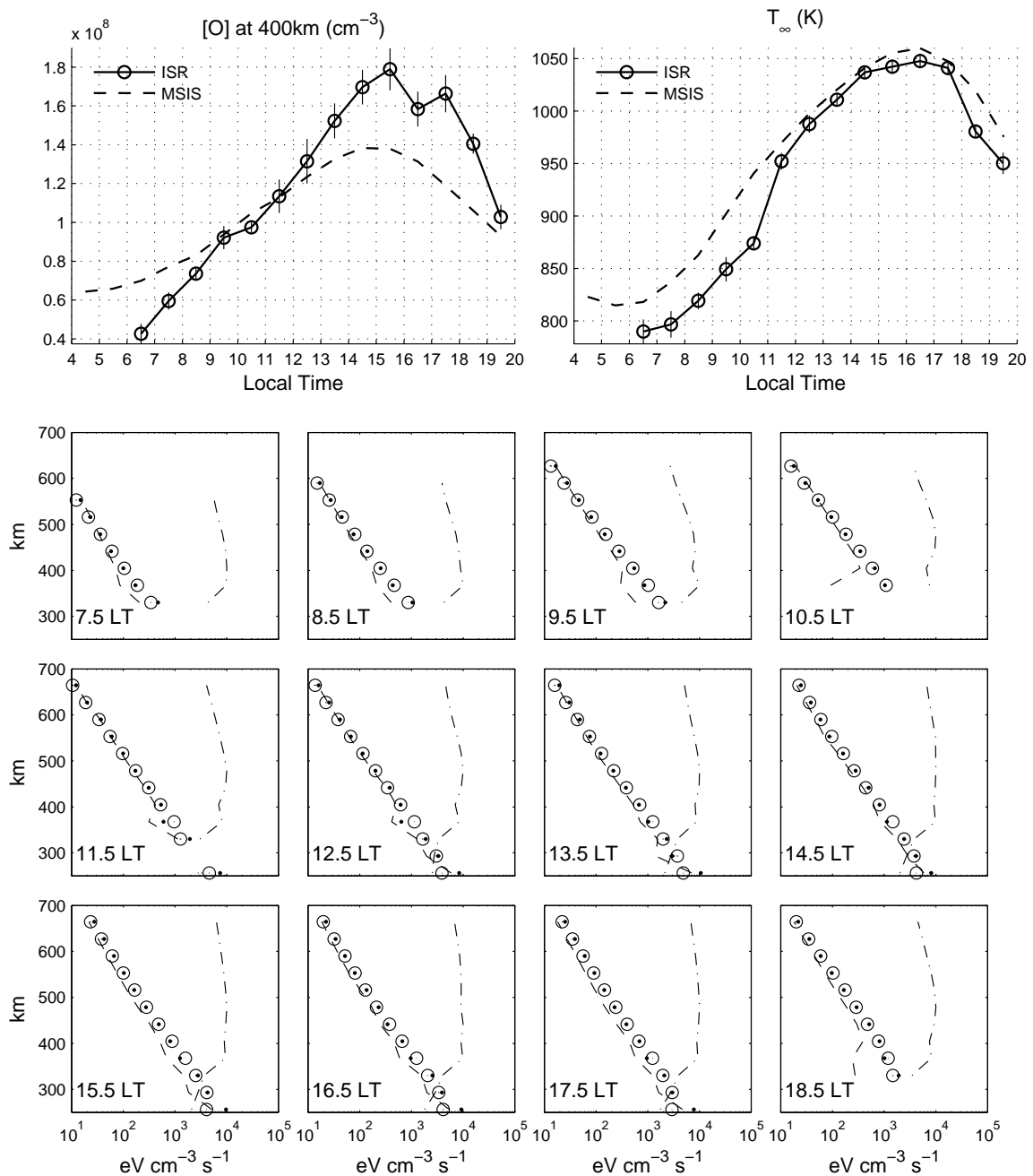
Figure 7.5: Summary of fits for March 17, 1988. The top left plot shows the fitted atomic oxygen density at 400 km, and the top right plot shows the fitted exospheric temperature, along with the MSIS values. In the profiles, the circles are Q_{e,O^+}, the dots are $Q_{O^+,n}$ from the fits, the dashed lines are the MSIS values of $Q_{O^+,n}$, and the dash-dotted values is the ratio $Q_{e,O^+}/\sigma_k$ normalized to a maximum of 10^4. Also plotted are error bars on Q_{e,O^+} and $Q_{O^+,n}$, which are only visible at the lowest altitudes.
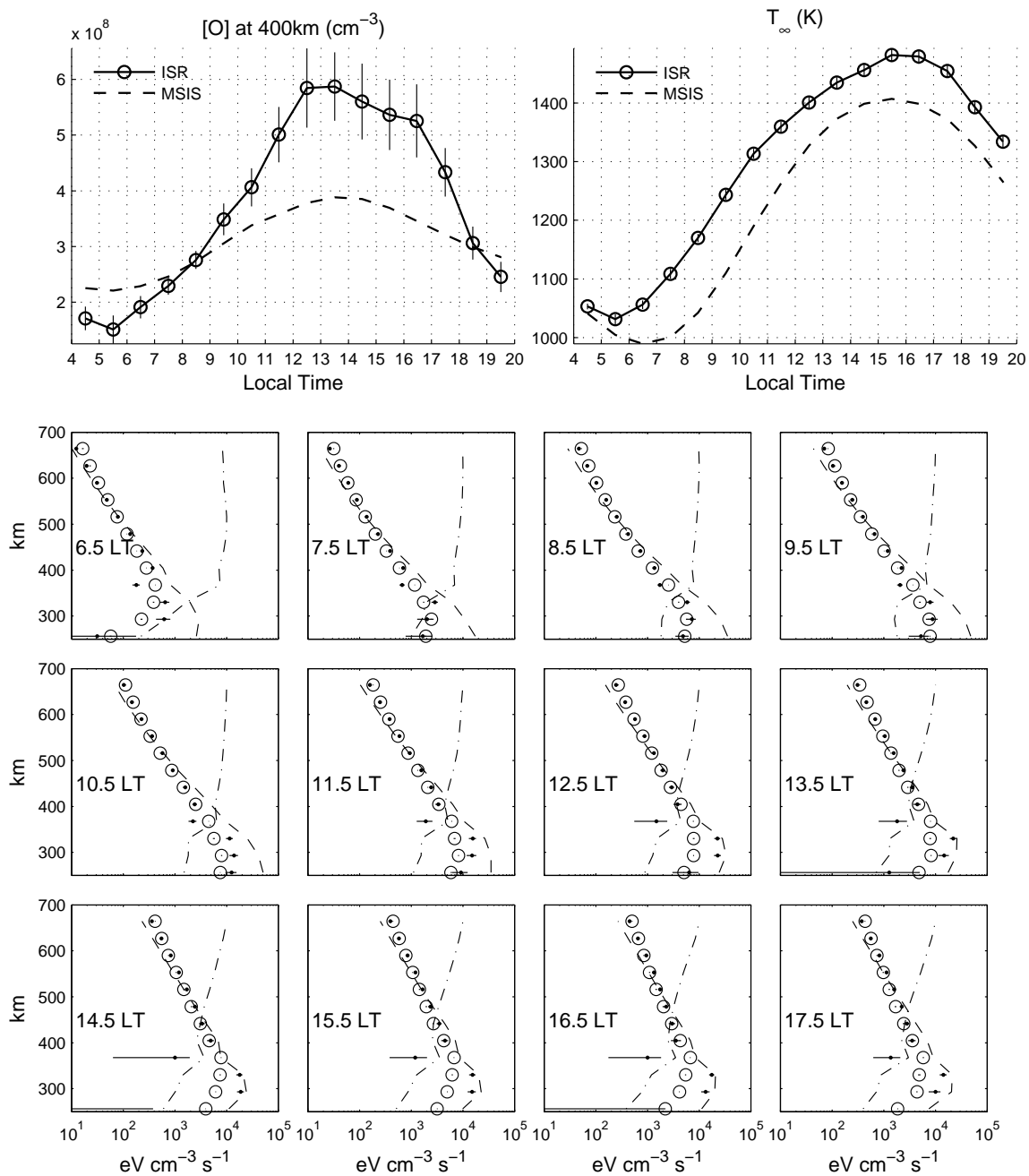
Figure 7.6: Same as Figure 7.5, except for January 28, 1992.

errors are larger and those altitudes are weighted down so that they don't contribute as much to the residual. The altitudes with the largest impact are the higher ones. The fitter can extend to much higher altitudes because the H$^+$ fraction is small and $Q^{el}_{O^+,O}$ is still much greater than the other cooling terms. It is cases like these where our technique is much improved over restricting the fits to low altitudes. Restricting the fits to a specific altitude window of 290-475 km would imply mainly including heights near and below the $F2$ peak.

Some averaged results of the analysis for the atomic oxygen density are shown in Figure 7.7. While we call these monthly averages, we should point out that really there are only a few days in each month in these averages. January 1990, January 1992, and August 1989 include 2 days, January 1994 and October 1989 include 3 days, and January 1993 includes 9 days. Plotted are the derived [O] at 400 km (circles) for 6 different months spanning the dataset, where the curves correspond to unweighted averages and the error bars correspond to unweighted averages of the errors. The black dots with gray error bars correspond to averaged fits using the fixed window method, as done by *Burnside et al.* (1991). The MSIS values are the solid line. The asterixes correspond to h_mF2, which is noted on the right-hand axis. It is apparent that at higher h_mF2, corresponding to the higher solar flux data, the atomic oxygen density is higher, as dictated by the fits and the MSIS values. The curves tend to deviate from MSIS during the afternoon, when h_mF2 is the highest and the atomic oxygen density increases. During the high solar flux cases (top row, bottom row), it is clear that the fixed window method does not work, giving low densities in the afternoon (when h_mF2 rises) and poor fits (taking the error bar on the fit to be a proxy for the quality of the fit). The lower two periods (August and October 1989) were included in the analysis of *Burnside et al.* (1991) (see the lower row of Figure 13 in that reference). Our result using the fixed window analysis seems to agree with the
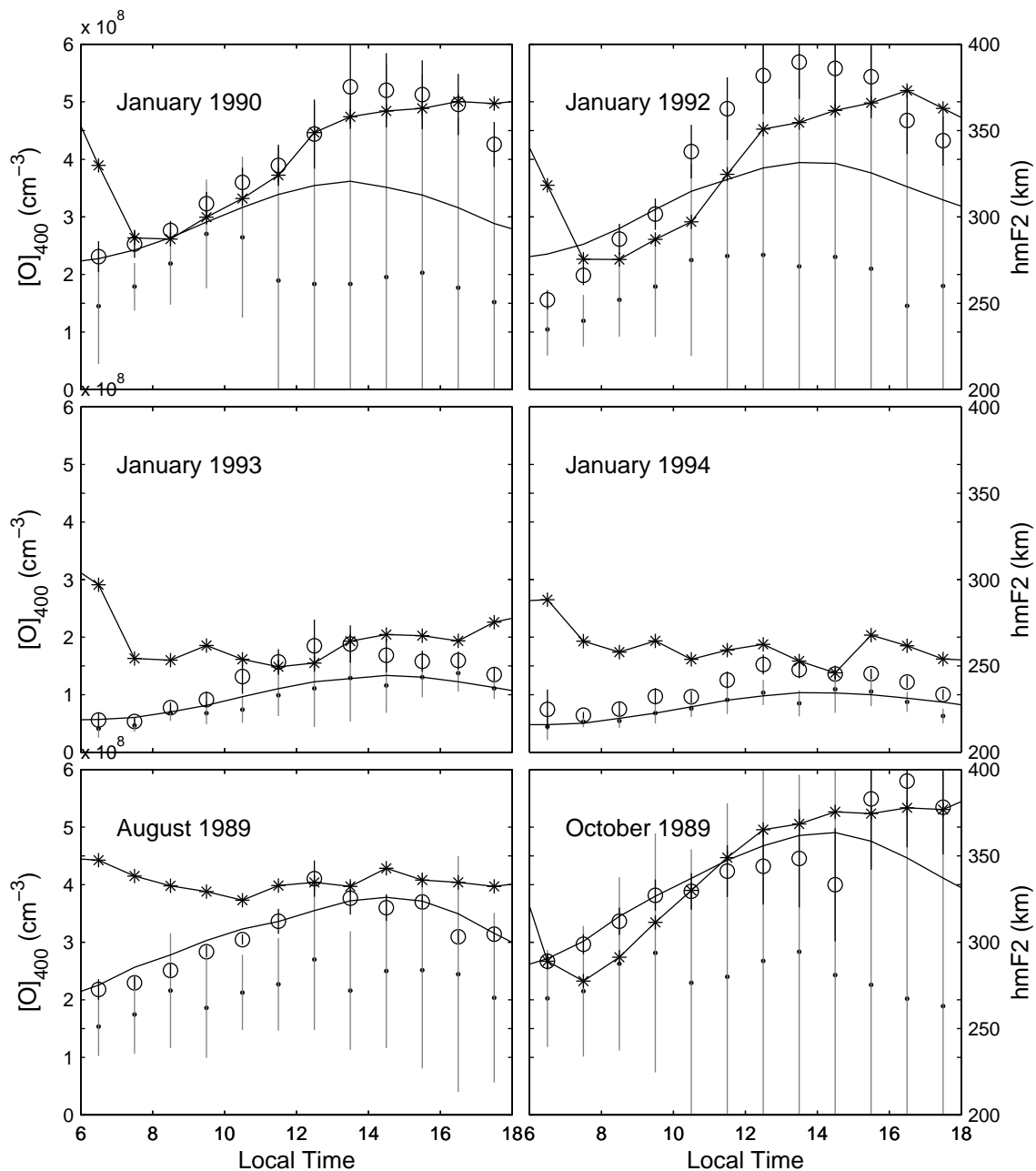
Figure 7.7: Several period averages of [O] for the dataset. The open circles are the radar-derived atomic oxygen densities at 400 km using the methods described in the text, with error bars corresponding to unweighted averaged errors. The black dots with gray error bars are the same densities inferred using a limited altitude range and a different error analysis, as described in the text. The solid line is the MSIS value. The stars are values of h_mF2 (corresponding to the right axis).
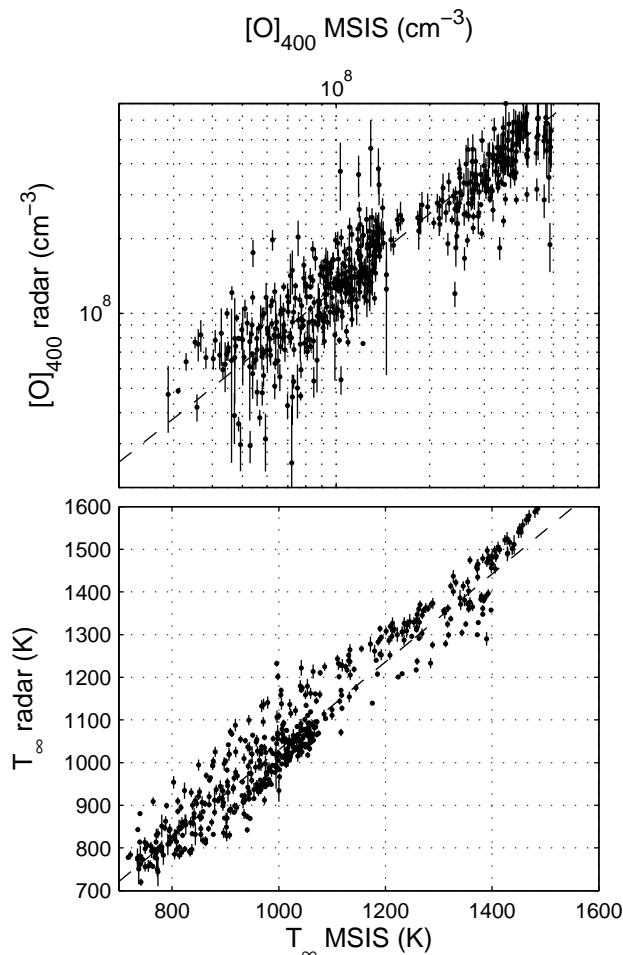
Figure 7.8: Scatter plots of the derived parameters versus the MSIS parameters, with error bars. The dashed line in the upper plot ([O]) corresponds to a slope of 1.26, and the dashed line in the lower plot (T_∞) corresponds to a slope of 1.03.

Burnside et al. (1991) curves. However, the fits become much better with the atomic oxygen densities increasing in the afternoon if the higher altitudes are included. We point out that the fixed window analysis works better for the lower solar flux periods (middle row of Figure 7.7) for the reasons described already.

We turn now to overall averages, to compare the results to the MSIS predictions and to estimate a value of F, the Burnside factor. A scatter plot of all the [O] (400 km) and T_∞ values versus their MSIS equivalents is shown in Figure 7.8, along with error bars. We have considered data points only between the times of 6.5 and 17.5

LT for this and future plots. A dashed line is also plotted, which is a slope of 1.26 for the [O] case and a slope of 1.03 for the T_∞ case. How these numbers were obtained will be discussed shortly. Most points lie close to these lines, and the points that are farther away tend to have larger error bars. There is very little scatter for the T_∞ points and indeed, as discussed earlier, the T_∞ error bars are much smaller than the [O] error bars. The histogram of the ratio of the radar parameters to the MSIS parameters is shown in Figure 7.9. The [O] distribution shows a peak above 1. The T_∞ distribution shows a fairly uniform distribution around 1.

In order to deduce an overall Burnside factor as other studies have done, we have considered various estimators for F. These include the median value of the F distribution (as done by *Oliver and Glotfelty* (1996)), the mean value of the F distribution, a weighted average of the F values, and a ratio of the weighted averages (the weighted average of the radar [O] divided by the weighted average of the MSIS [O]). For the histograms in Figure 7.9, the median values are 1.26 for [O] and 1.03 for T_∞; the mean values are 1.30 for [O] and 1.04 for T_∞; the weighted averages of F are 1.26 for [O] and 1.04 for T_∞, and the ratios of the weighted averages vary depending on the weights chosen but are in general near the median value or slightly lower. We have found that the median is the most insensitive to outliers and most representative of the asymmetric distribution. In order to estimate an error on the median, we fit a log-normal distribution to the data, as plotted in Figure 7.9, and compute the standard deviation on the median by generating many lognormally distributed datasets using the fitted mean and variance. Note that the error on the median is greater than the error on the mean by about 20%. Using this estimator, our value of the Burnside factor is $\tilde{F} = 1.26 \pm 0.02$. For the same technique applied to the exospheric temperature ratio, we find 1.03 ± 0.003, a value very close to one, indicating that in the long-term average the radar-derived exospheric temperature does not depart significantly from
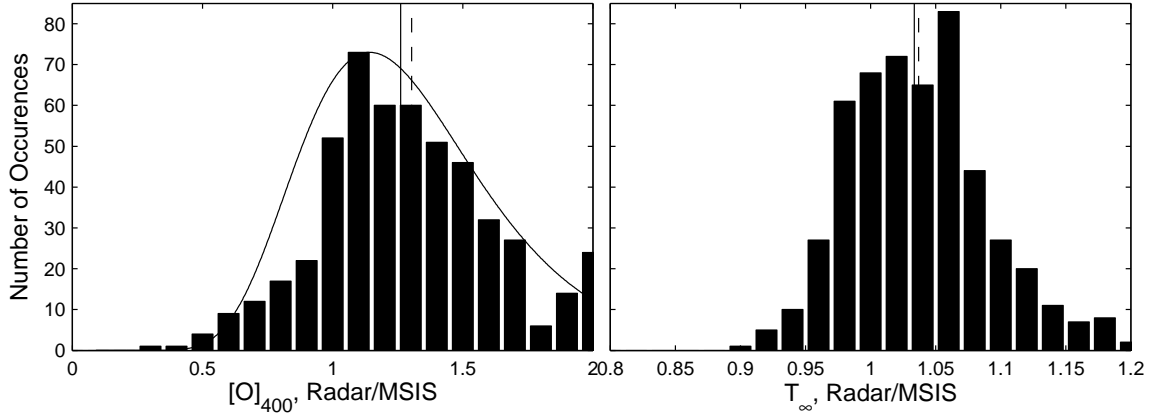
Figure 7.9: Histogram of $[O]_{\mathrm{radar}}/[O]_{\mathrm{MSIS}}$ (left) and $T_\infty^{\mathrm{radar}}/T_\infty^{\mathrm{MSIS}}$ (right) for the datasets used in this study. The solid line corresponds to the median value and the dashed line corresponds to the unweighted mean. The model distribution function on the left-hand plot is a lognormal fit to the data. The bin sizes are given by 0.1 for $[O]$ and 0.02 for T_∞.

the MSIS-predicted exospheric temperature. Note that the error bars correspond to the error on the medians, not the standard deviation of the distributions (which are about 0.35 for the $[O]$ ratio and 0.05 for the T_∞ ratio). Our estimate of F is close to the collision frequency calculations of *Stallcop et al.* (1991), *Pesnell et al.* (1993) and *Hickman et al.* (1997). As mentioned in the introduction, the *Hickman et al.* (1997) value of F would be about 1.26 at a mean ion-neutral temperature of 1000 K (1.23 at 1500 K).

We should briefly compare our results to what would be obtained if we had done the analysis in different ways. We should consider the effects of (a) the extra terms in the energy balance equation, (b) the weighting, and (c) the fixed window approach (as done by *Burnside et al.* (1991)). If we had neglected the extra terms in $Q_{O^+,n}$ (the extra elastic terms and the H^+ inelastic term), and done the fits in the same way, we would have obtained a factor of $F = 1.20$. So, the effect of including the extra terms was to increase the value of F slightly, by about 5%, over the analysis neglecting the minor terms. If we had done the fits weighting the terms only by the errors in Q_{e,O^+},

we would have obtained a value of $F \approx 1.05$. If we had done the analysis using the fixed-window approach (window from 290-475 km), with weights corresponding to errors in Q_{e,O^+}, we would have obtained a factor $F \approx 0.85$. This factor is in very good agreement with the reinterpretation done by *Oliver and Glotfelty* (1996) of the *Burnside et al.* (1991) results, which gave a factor of $F = 0.82$. Thus, we see that weighting the fits properly and extending the fits to higher altitudes (not using the fixed window approach) were both significant in obtaining our value of F, with the most important correction being the latter one. The inclusion of the minor correction terms at the higher altitudes was a more minor effect.

Figure 7.10 shows the unweighted long-term average as a function of local time, along with the MSIS values multiplied by the derived scaling factors. We note that we should be dividing the radar-derived density by F instead of multiplying the MSIS values by F in order to obtain the true values in the long-term average, however for the sake of simplifying the plot we scale the curves the other way. The error bars on this plot correspond to standard deviations of the derived neutral parameters in a particular time bin. As we have noted, intrinsic to deriving a value of F via the ion energy budget approach is the assumption that MSIS is correct in a long-term average. A good test of whether this assumption holds true is to check how close the average curve $[O]_{\text{radar}}$ is to the average curve $F[O]_{\text{MSIS}}$, as indicated by the upper dashed line in Figure 7.10. As shown by that curve, this assumption is fairly good. For $[O]$, the ratio of the curves is very close to 1 in the afternoon (the radar curve is about 2% higher) and close in the morning (the radar curve is about 8-9% lower). For T_∞, the curves are within 1% for all local times. Thus, for our study, the assumption that MSIS is correct in the long-term average seems to be a reasonable one. However, as noted by *Oliver and Glotfelty* (1996), this is an important point to consider, because if this assumption breaks down the interpretation of F as a scaling of the collision
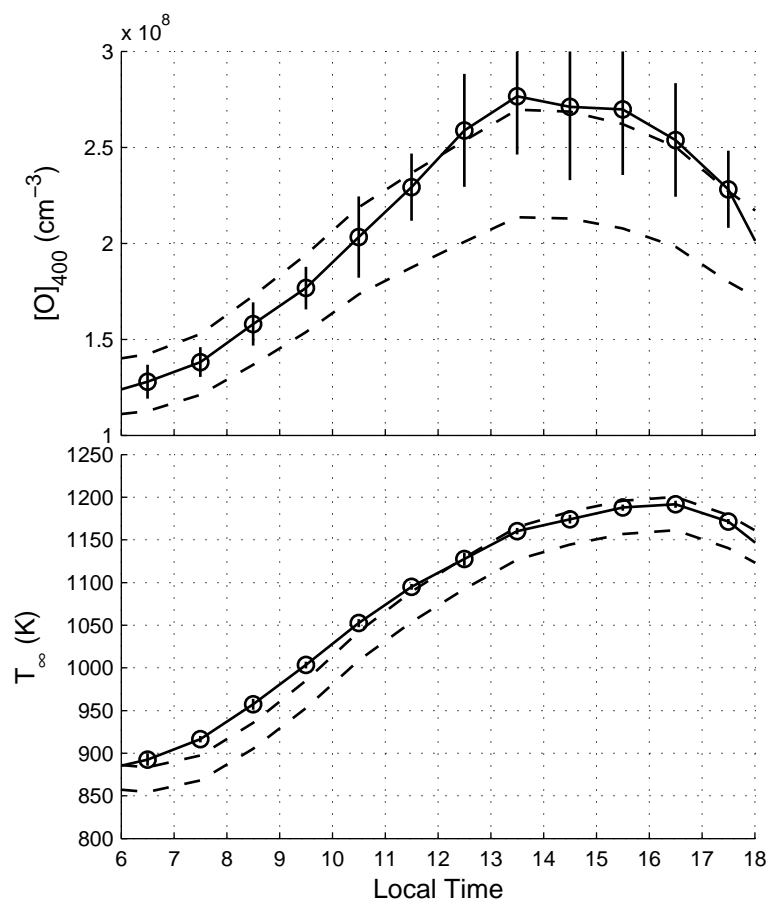
Figure 7.10: Unweighted average of [O] (top) and T_∞ (bottom) for the entire dataset. The solid line with circles is the radar-derived parameters, the lower dashed line is the MSIS value, and the upper dashed line is the MSIS value times our best estimate of the correction factor.

cross section is no longer valid. Instead, F includes a scaling of the MSIS neutral atomic oxygen density. To emphasize this point, in the upper panel of Figure 7.11 we plot a time series of the [O] and T_∞ ratios, corresponding to daily medians (and daily median errors). The [O] values have been scaled by the $F = 1.26$ factor derived from the long-term analysis (in reality, we should now redo the analysis using the most recent theoretical collision cross sections and compare those results to MSIS - this approach will be used in future derivations of neutral parameters). The time axis corresponds to the same as that in Figure 7.1. We see that whereas the T_∞ ratio is fairly consistent on a day-to-day basis, the [O] ratio changes considerably on a day-to-day basis. This feature was discussed by *Oliver and Glotfelty* (1996). Plotted in the lower panel is the $F10.7$ index (circles, left axis) and the daily average K_p index (dots, right axis). Some of the fluctuations in the [O] ratio may be correlated with these indices, but in general the correlation is very weak. For example, the large change in the [O] ratio around the August 1992 World Day period seems to be associated with an $F10.7$ rise in a largely low solar flux time period. Perhaps in this situation MSIS (which takes in the daily and 3-month average $F10.7$ as input parameters) does not effectively capture the change in [O] that takes place with the increase in solar flux. However, we can see that the exospheric temperature given by MSIS is correct in this period, telling us that the temperature change associated with the solar flux increase is captured. In any case, we can see that there is clearly significant day-to-day variability in the [O] ratio that is not captured by the empirical model. This variability is presumably associated with day-to-day changes in mixing in the mesopause region. Knowing the correct O^+-O collision cross section (or correct value of F), day-to-day variations in the O density can be studied using radar-derived parameters.
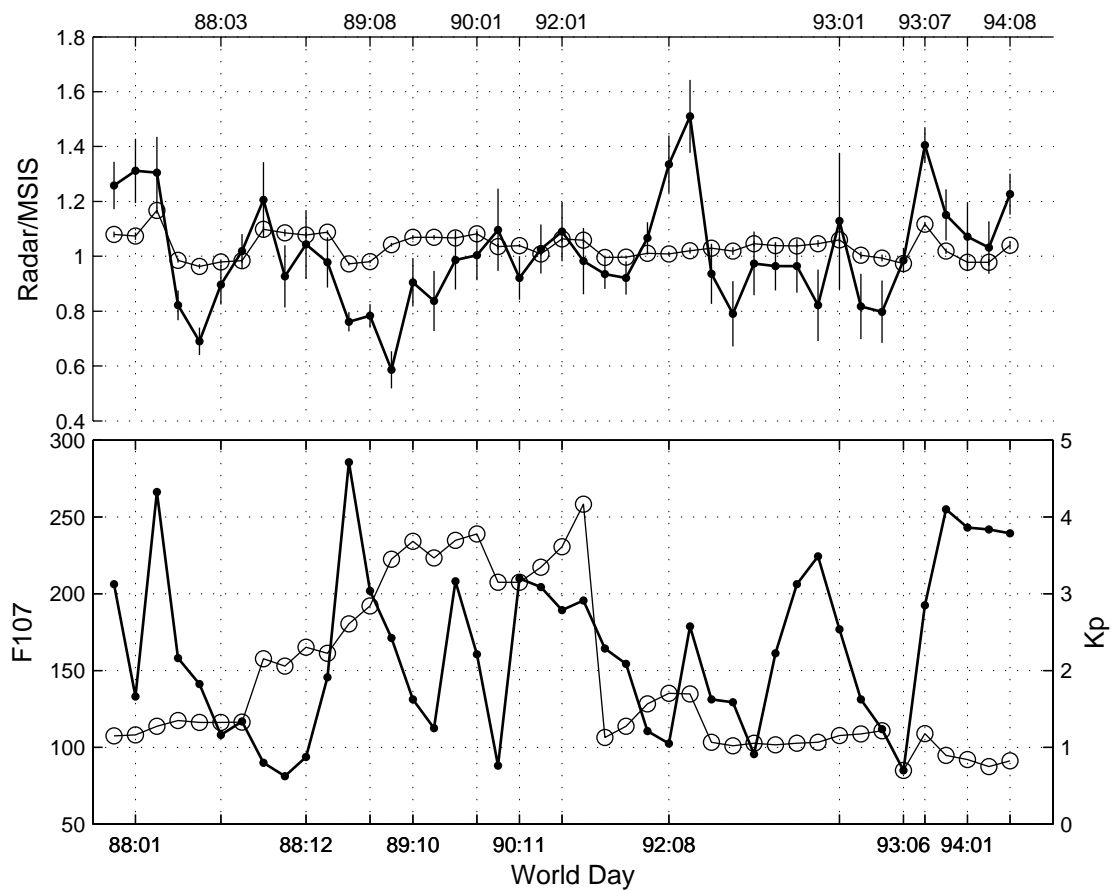
Figure 7.11: The top panel shows a time series of the ratio of the radar-derived values to the MSIS values, with [O] indicated by the solid points and T_∞ indicated by the circles. These values correspond to the daily median values, and the error bars are the median errors (not the error on the median). The [O] values have been scaled (divided) by the derived long-term F factor (1.26). The bottom panel shows the daily $F10.7$ index (circles, left axis) and the daily average K_p index (solid points, right axis). The time axis is the same as that in Figure 7.1.

7.6 Summary and Conclusions

The main purpose of this study has been to demonstrate that the apparent large discrepancies between MSIS and Arecibo neutral oxygen densities at high solar flux found by *Burnside et al.* (1991) were mainly caused by the use of ISR data from heights below the F-region peak. By extending the energy balance analysis to higher altitudes, and by carefully considering the altitude-dependent weights, good results can be obtained. Fortunately, as the F layer rises near solar maximum, light ions do not become significant during the day below about 620 km, so there are enough range gates where the temperatures can be measured accurately to perform the least squares fitting analysis. Using this scheme, we obtain much better experimental estimates for the neutral atomic oxygen density at Arecibo at high solar flux, which agree with the trends and magnitudes predicted by MSIS. Nevertheless, as also shown by *Oliver and Glotfelty* (1996), there is significant day-to-day variability in the atomic oxygen density. The exospheric temperature, on the other hand, agrees very well with the MSIS parameters, both in the long-term averages and on a day-to-day basis.

If long-term MSIS averages of [O] can be regarded as correct, then we find a Burnside factor of $F = 1.26 \pm 0.02$ from Arecibo ISR measurements and the ion energy budget. When this revised Burnside factor is applied to the *Banks* (1966b) collision cross section, reasonable agreement with the most recent theoretical collision cross sections is obtained. The results of this analysis thus do not require hot oxygen or any other heat source to reproduce the observed ion temperature values using the MSIS neutral densities. This is in contrast to the previous analysis of *Burnside et al.* (1991), which would have required hot oxygen or some other heat source. The main factor in this change is the choice of altitude region. In light of these results, we recommend a re-analysis of other data sets to examine whether hot oxygen is

still needed as a heat source to bring the radar-derived collision cross sections into agreement with the theoretical calculations.

7.7 Appendix A: Analysis of Arecibo World Day Data, October 1986 to Present

The radar technique used for the World Day observations at Arecibo beginning in October 1985 and continuing until the present is described in *Sulzer* (1986). However, the improved analysis that has been done on the Arecibo World Day that is in the NCAR CEDAR database is described here. Seven frequencies are transmitted by phase modulating the carrier with a repeating binary waveform. The frequencies are spaced by about 35 kHz, and a 250-kHz bandwidth containing the returns from the seven frequencies is analyzed. Figure 7.12a shows sets of seven spectra from the highest four ranges of the experiment where the noise baseline has not yet been removed. The low electron density and the rapid increase in H^+ fraction versus altitude that is apparent in this figure are typical of low solar flux conditions. These spectra might appear unusual to those familiar with only the nearly rectangular shape of an O^+ spectrum from the middle of the F region, but it is our intention to show more difficult cases, since the easy cases do not require the techniques described here. The data in the figure are from 3:16 LT on April 25, 1995. The data from lower heights, which have a much higher signal-to-noise ratio, show little effect of the filter shape and are not presented since there is less difficulty in preparing them for fitting. The actual filter shape is very flat but does not fall off quickly enough to prevent the folding in of a significant amount of noise from outside the clear bandwidth. This is the explanation for the rising baseline near the edges of the bandpass. The method for removing the noise baseline is discussed below, which is more difficult than one

might expect because no noise samples were taken along with these data (World Days between November 1985 and December 1994). Thus, the amplitude of the noise spectrum is not known. However, the shape is known because it changes slowly with time and can be determined from times possibly several hours from the time of the measurements, when the transmitter is not operating but the data-taking program is, typically with the receiver connected to a load rather than the antenna.

Figure 7.12b shows the same spectra after the removal of the noise baseline. The variations in amplitude among the seven spectra from a single range are the result of the imperfect binary phase code used to generate the frequencies and of imperfections in the transmitter, resulting in the asymmetry about 430 MHz. The larger, narrower spectra are from the lower heights. As altitude increases, the amount of O^+ decreases quickly, leaving the wider H^+ spectrum. The shape of this latter spectrum is not completely resolved because the spectra are too close together. That any shape at all is apparent is due to the low temperature of the solar minimum night. After sunrise, the shape becomes completely flat, and we rely entirely upon the level of the spectrum to determine the fraction of H^+. Although we can get good estimates of H^+ in this fashion, getting a temperature measurement without a significant fraction of O^+ is not possible. For cases when it is important to obtain the temperatures at these altitudes, we use a different method, discussed in *Sulzer and González* (1996).

Figure 7.12c shows the spectra after the seven frequencies have been combined into a single right-half spectrum shifted to zero frequency. This is the spectrum used in the modeling. It is the Fourier transform of the truncated autocorrelation function, where the lags all have uniform weighting. Although the non-linear least squares fitting program works equally well irrespective of what form the data are in (as long as all effects are accounted for), we have found that the spectrum based on the uniformly weighted truncated ACF is most convenient for visual inspection of the

results because it shows the most information to the human observer.

7.8 Appendix B: Partial Derivatives for Error Estimates

The errors in the modeled electron-ion heat transfer rate are due to errors in the determination of electron temperature, ion temperature, ion fraction, and electron density. Neglecting correlation terms, the error can be written as,

$$\sigma_{e,O^+} = \sqrt{\left(\sigma_{T_e}\frac{\partial Q_{e,O^+}}{\partial T_e}\right)^2 + \left(\sigma_{T_i}\frac{\partial Q_{e,O^+}}{\partial T_i}\right)^2 + \left(\sigma_{n_e}\frac{\partial Q_{e,O^+}}{\partial n_e}\right)^2 + \left(\sigma_{p_{H^+}}\frac{\partial Q_{e,O^+}}{\partial p_{H^+}}\right)^2}$$

$$(7.27)$$

where

$$\frac{\partial Q_{e,O^+}}{\partial T_e} = \frac{C_{e,O^+} n_e^2 (1 - p_{H^+}) \left[3(T_e - T_i) - (T_e - 3T_i)\ln\Lambda\right]}{2T_e^{5/2}} \tag{7.28}$$

$$\frac{\partial Q_{e,O^+}}{\partial T_i} = \frac{Q_{e,O^+}}{T_i - T_e} \tag{7.29}$$

$$\frac{\partial Q_{e,O^+}}{\partial n_e} = \frac{C_{e,O^+} n_e (1 - p_{H^+})(T_e - T_i)\,(4\ln\Lambda - 1)}{2T_e^{3/2}} \tag{7.30}$$

$$\frac{\partial Q_{e,O^+}}{\partial p_{H^+}} = \frac{Q_{e,O^+}}{p_{H^+} - 1}. \tag{7.31}$$

The errors in the modeled ion-neutral heat transfer rate are due to errors in the ion temperature, electron density, and ion fraction. Errors are also caused by uncertainties in the neutral parameters from MSIS: the neutral temperature at the lowest altitude, the estimated gradient for the temperature profile, and the neutral densities. We ignore these effects. The total error in the heat transfer rate is thus:

$$\sigma_{O^+,n} = \left[\sigma_{T_i}^2\left(\frac{\partial Q_{O^+,n}}{\partial T_i}\right)^2 + \sigma_{n_e}^2\left(\frac{\partial Q_{O^+,n}}{\partial n_e}\right)^2 + \sigma_{p_{H^+}}^2\left(\frac{\partial Q_{O^+,n}}{\partial p_{H^+}}\right)^2\right]^{0.5} \tag{7.32}$$

with
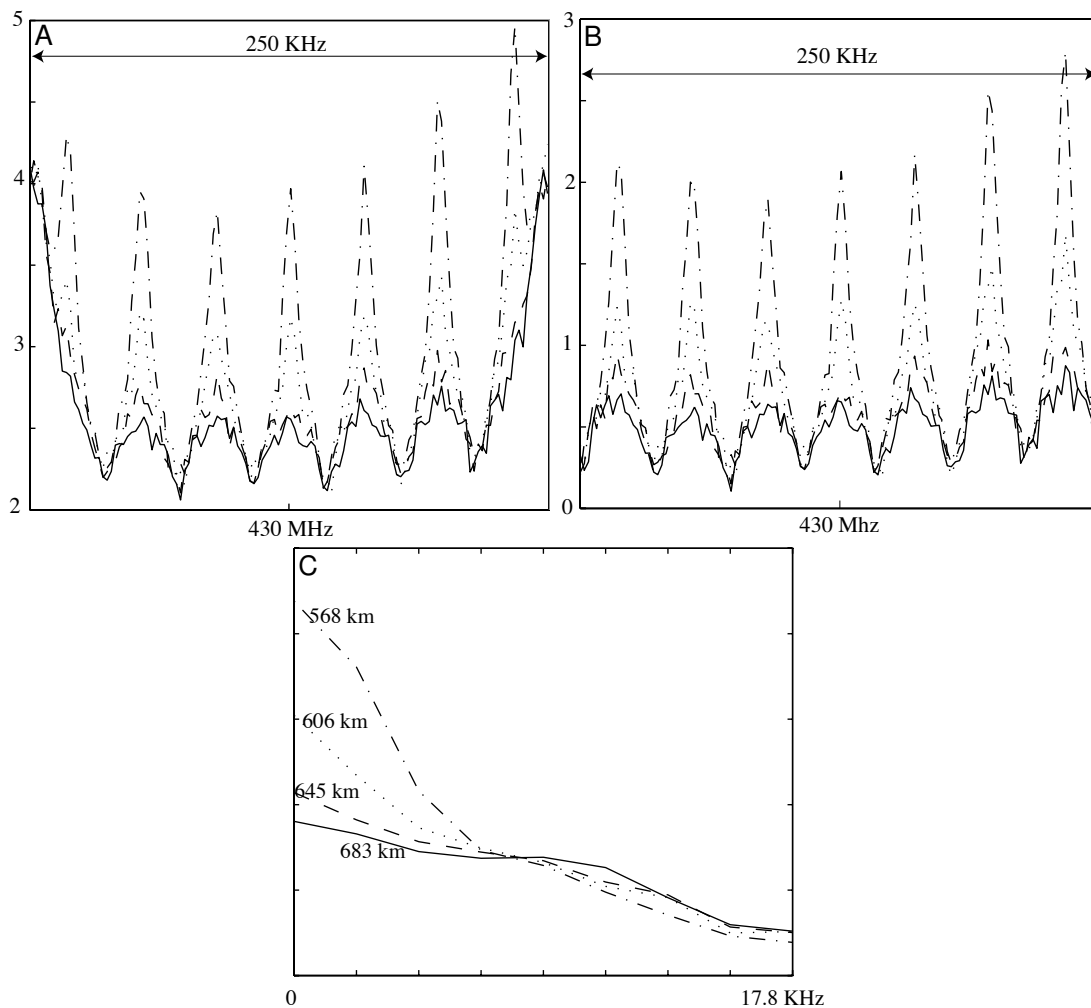
Figure 7.12: Panel A shows spectra from the four highest ranges taken with the regular World Day mode used at Arecibo: 568 km (dashed-dotted line), 606 km (dotted line), 645 km (dashed line), and 683 km (solid line). The noise baseline has not yet been removed. Its two dominant features are raising the entire level of the spectrum well above the level of the ionospheric spectra, and causing the level to rise at the edges of the spectrum. Panel B shows the same data but with the noise baseline level removed. The spectra are still (apparently) above the baseline; this is caused by the presence of H^+. The wide spectra of H^+ are incompletely separated and thus cause the entire set of spectra to appear raised above the zero level. Panel C shows the same data but after the seven spectra have been combined into one. This is the form used in the fitting process.

$$\frac{\partial Q_{O^+,n}}{\partial T_i} = Q_{O^+,O}^{el}\frac{3T_i + T_n}{2(T_i - T_n)(T_i + T_n)} \tag{7.33}$$

$$+ C_{O^+,H}^{inel} n_e \left\{ \sqrt{T_n}[\mathrm{H}](1 - p_{H^+}) - \frac{4}{9}p_{H^+}[\mathrm{O}]\frac{T_n}{\sqrt{T_i}} \right\} + \sum_{k \neq O} \frac{Q_{O^+,k}^{el}}{T_i - T_n}$$

$$\frac{\partial Q_{O^+,n}}{\partial p_{H^+}} = \sum_k \frac{Q_{O^+,k}^{el}}{p_{H^+} - 1} - C_{O^+,H}^{inel} n_e \left\{ [\mathrm{H}]T_i\sqrt{T_n} + \frac{8}{9}[\mathrm{O}]T_n\sqrt{T_i} \right\} \tag{7.34}$$

$$\frac{\partial Q_{O^+,n}}{\partial n_e} = \sum_k \frac{Q_{O^+,k}^{el}}{n_e} + \frac{Q_{O^+,H}^{inel}}{n_e} \tag{7.35}$$

If desired, analytical partial derivatives necessary to construct the Jacobian can also be derived in a straightforward manner. The error in the function to be minimized, Equation 7.4, corresponding to the weights in the least squares analysis, are given by (neglecting correlation terms)

$$\sigma_j = \left[\sigma_{T_e}^2 \left(\frac{\partial Q_{e,O^+}}{\partial T_e} \right)^2 + \sigma_{T_i}^2 \left(\frac{\partial Q_{e,O^+}}{\partial T_i} - \frac{\partial Q_{O^+,n}}{\partial T_i} \right)^2 + \sigma_{n_e}^2 \left(\frac{\partial Q_{e,O^+}}{\partial n_e} - \frac{\partial Q_{O^+,n}}{\partial n_e} \right)^2 \right.$$

$$\left. + \sigma_{p_{H^+}}^2 \left(\frac{\partial Q_{e,O^+}}{\partial p_{H^+}} - \frac{\partial Q_{O^+,n}}{\partial p_{H^+}} \right)^2 \right]^{0.5} \tag{7.36}$$

where the index j refers to a specific altitude.

Acknowledgements

Chapter 8

Future Work

Reisner's Rule of Conceptual Inertia: If you think big enough, you'll never have to do it.

This thesis has covered a diverse set of topics, and the conclusions on individual studies have been included at the end of each chapter. Here we briefly summarize some future work (work in progress) that pertains to the ideas related in this thesis. Most of this discussion focusses on the daytime molecular ion composition, but some other topics are briefly mentioned.

Daytime $F1$-Region Ion Composition

Measurements of molecular ion composition are fairly sparse compared to other ionospheric measurements, mainly because of the difficulty of measuring the composition with ground-based instrumentation. Many rocket experiments have measured ion composition, and some satellites, such as the Atmospheric Explorer satellites, have made measurements of ionospheric composition below 250 km. Some of the satellite and rocket data were used in the development of the IRI model (*Danilov and Smirnova*, 1995; *Bilitza*, 2001), as mentioned earlier in Chapter 6. Comparisons be-
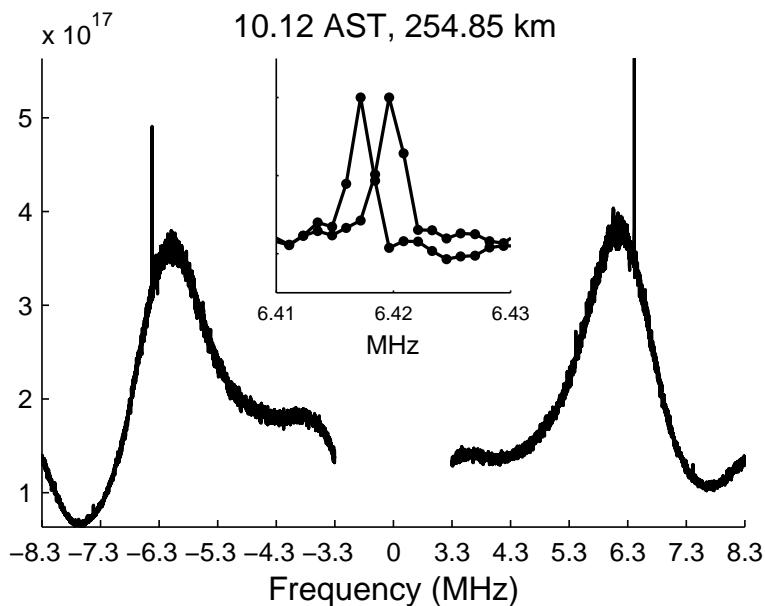
Figure 8.1: Example of full plasma line spectrum measured on April 1, 2006. The y axis corresponds to unnormalized power. The inset is a zoomed-in plot of the normalized peak with the down-shifted line folded over to positive frequencies.

tween satellite data and photochemical models (e.g, *Torr et al.*, 1979) have been fairly successful. However, even today, there does not exist an empirical or semi-empirical model of the molecular ion composition that is useful and reliable for scientific studies. The IRI-predicted molecular ion composition has some interesting features to say the least. The nighttime composition problem was discussed in Chapter 6. The daytime composition predicted by IRI has some discontinuities and unphysical behavior.

ISR measurements of the molecular ion composition in the $F1$ region are particularly difficult. This difficulty arises from the fact that there is a temperature-composition ambiguity in the incoherent scatter theory, making fitting of the ion line for both temperatures and ion composition nearly impossible. Because of this difficulty, additional information must be added to the problem to make the fitting possible. Early work in this area focussed on constraining the fits by assuming that $T_i = T_n$ in this region, which is a reasonable assumption owing to the strong col-

lisional coupling between the ions and neutrals at lower altitudes (e.g., *Banks and Kockarts*, 1973). Constraining the ion temperature to be equal to the neutral temperature, and using a neutral temperature from some model atmosphere, as done by *Evans* (1967), is certainly reasonable, but is of course not very desirable. Another approach was to assume smooth functions for the ionospheric parameters, as done by *Waldteufel* (1970). A description of the problem and the different types of techniques to constrain the problem was given by *Oliver* (1979). An excellent idea was put forth by *Waldteufel* (1971), who suggested using measurements of the plasma line to determine n_e very accurately, and use this measurement in combination with the power from the ion line to determine the ratio T_e/T_i. This ratio was then used in the fits of the ion line spectra, along with an empirical relation for the molecular ion fraction. This approach is very similar to the one we are beginning to use for the analysis of Arecibo data. We use high resolution measurements of the plasma line using the coded long pulse technique (*Djuth et al.*, 1994; *Aponte et al.*, 2006), which give the absolute ionospheric densities with up to 75-meter altitude resolution and about 10-second time resolution during the daytime. An example of the full plasma line spectrum (up- and down-shifted lines) is shown in Figure 8.1. The broad increase in frequency is due to randomized clutter from the coded long pulse mode. The information is in the frequency of the narrow spikes, which corresponds to the frequency predicted by the linear dispersion relation for Langmuir waves (e.g., *Yngvesson and Perkins*, 1968)

$$f_r^2 = f_p^2 + \frac{3k^2}{4\pi^2} \frac{k_b T_e}{m_e} + f_c^2 \sin^2 \theta$$

where f_p is the plasma frequency ($\approx 9\sqrt{n_e}$, for n_e in m^{-3}), k_b is Boltzmann's constant, k is the radar wavenumber ($4\pi/\lambda$), m_e is the electron mass, f_c is the electron gyrofrequency, and θ is the angle between the radar wave vector and the magnetic field. In the equation for the resonance frequency above, the second and third terms
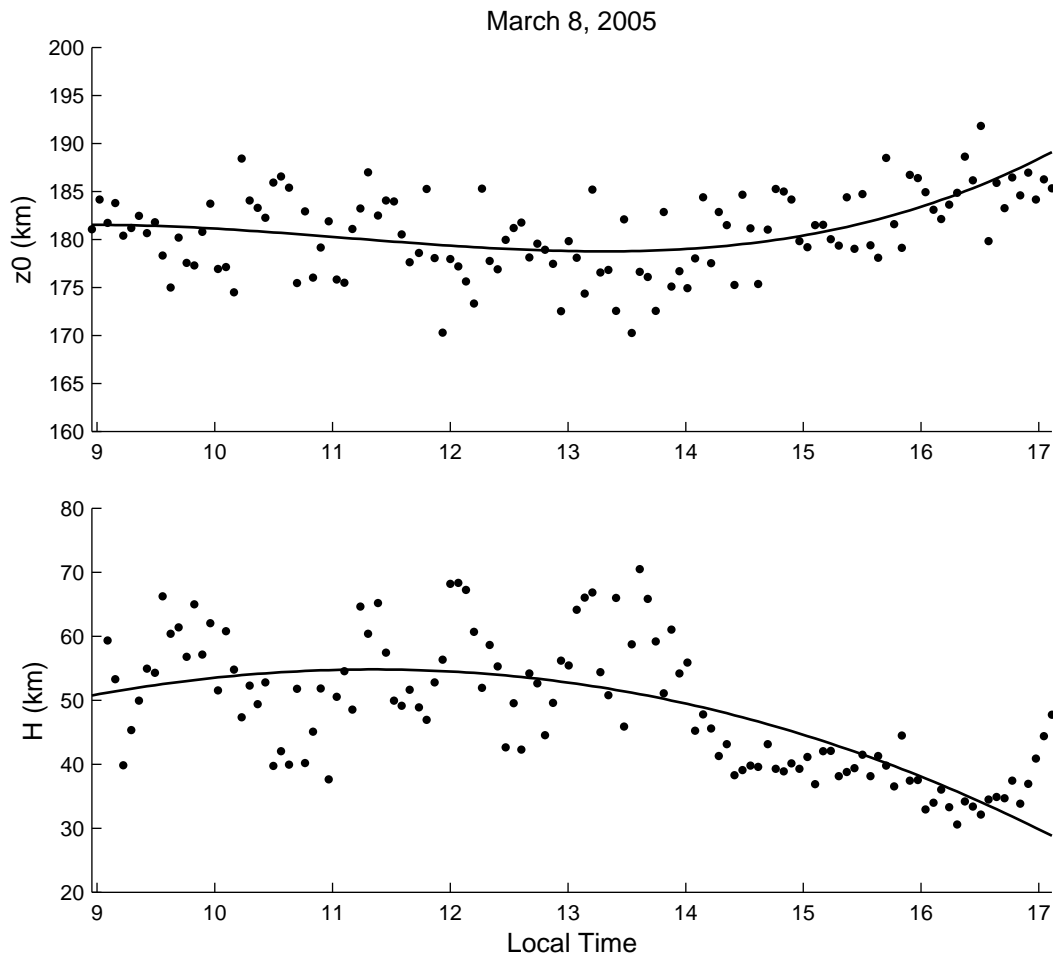
Figure 8.2: Measured z_0 and H on March 8, 2005. The dots are data points and the solid lines are polynomial fits.

are always nearly negligible (or a very small, perhaps 2%, correction), allowing us to directly infer the electron density from the resonance frequency.

The first results of our technique are to be published in *Aponte et al.* (2006) and are shown in Figure 8.2. Our fitting method assumes a hyperbolic tangent model for the molecular fraction,

$$p(z) = \frac{1}{2}\left[1 - \tanh\left(\frac{z - z_0}{H}\right)\right] \tag{8.1}$$

where z_0 is the transition height (50% moleculars) and H is a scale height. H and z_0 as measured are plotted in Figure 8.2 (the dots) along with polynomial fits to the data.
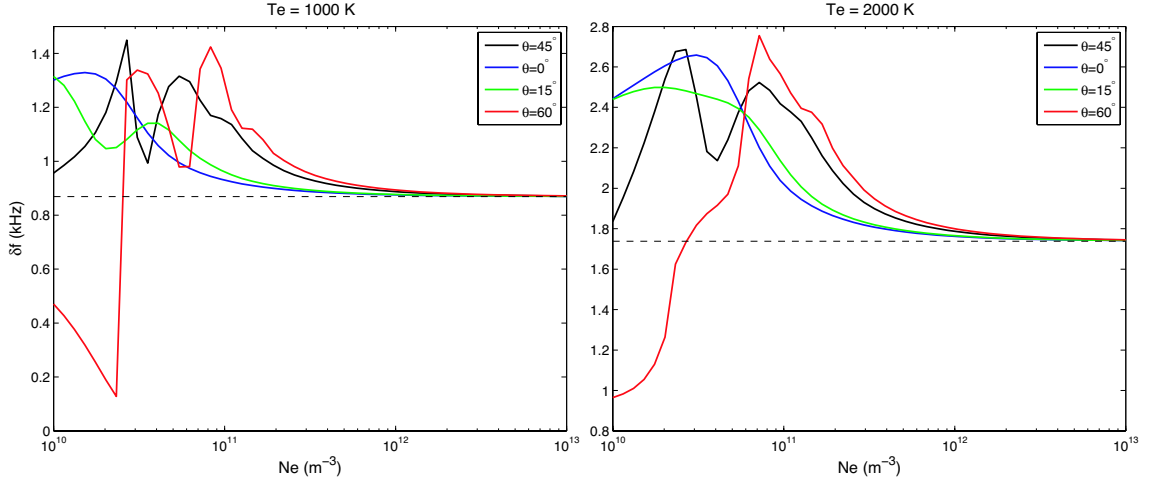
Figure 8.3: Difference between up- and down-shifted plasma line frequencies predicted by the linear dispersion relation (dashed), the kinetic theory neglecting the magnetic field (blue), and the kinetic theory including the magnetic field, for three different values of the angle between the radar **k** vector and the magnetic field (black, green, red). The left panel corresponds to T_e=1000 K and the right panel corresponds to T_e=2000 K.

A clear solar zenith angle dependence is seen in z_0, which is anticorrelated with H, as has been observed at EISCAT (*Litvine et al.*, 1998). There are short-term fluctuations in H and z_0 which are associated with electron density and temperature fluctuations. These are the first true measurements of the molecular fraction in the $F1$ region at Arecibo (some measurements have been made at EISCAT, but these are largely model driven and involve a full profile type fit). These measurements also yield the temperatures in this region for the first time, and the results are interesting, with the ion temperature showing a scale that is quite different from that predicted by MSIS. We are also developing a photochemical model, as briefly described in Chapter 1, to explain the observed variations. Initial results show fairly good agreement with the measurements. In the future, we plan to incorporate true measurements of the solar irradiance into our model calculations.

Further improvements to the technique described may involve using additional information from the plasma line. It turns out that the plasma line asymmetry

(difference between up- and down-shifted plasma line frequencies) is a good tracer for the electron temperature (or possibly currents, depending on how large you think they are) (*Showen*, 1979). As shown in Figure 8.3, the difference in the two lines, as predicted by kinetic theory, is in the range of 1-2 kHz, and depends strongly on the electron temperature (because of changes in the radar **k** vector for the up- and down-shifted lines), the electron density (because of kinetic effects), and the angle between the **k** vector and the magnetic field (because of kinetic effects including the magnetic field). If this difference can be measured successfully, then the theory can possibly be used to back out the electron temperature with the very precise electron density measurements afforded by the plasma line (statistical accuracy of better than 0.02%). This would allow for a very high resolution diagnostic of the electron temperature without having to measure the ion line, and would significantly improve our estimates of the F1-region composition. The first results of extracting T_e from the plasma line asymmetry are to be published in *Nicolls et al.* (2006d).

As an example, we show a profile measured on April 1, 2006 near 1000 LT in Figure 8.4. In this experiment, we used a configuration where the line feed was pointed towards the vertical ($\theta = 45°$) and we measured the up- and down-shifted plasma line frequencies along with the ion line (using a new MRACF mode described in *Nikoukar et al.* (2006)). The left panel shows the electron density from the plasma line and the electron temperature processed from the ion line (with no molecular model assumed), and the right panel shows the measured δf (black), which is a few-minute average, the predicted δf using linear fluid theory (green), the predicted δf using kinetic theory but neglecting the magnetic field (red), and the predicted δf using kinetic theory but including the magnetic field (blue). We note that there was a 1-kHz offset that we believe to be system-related (but have yet to track down) that we have removed from the measured δf. Near the F peak, the linear relation does
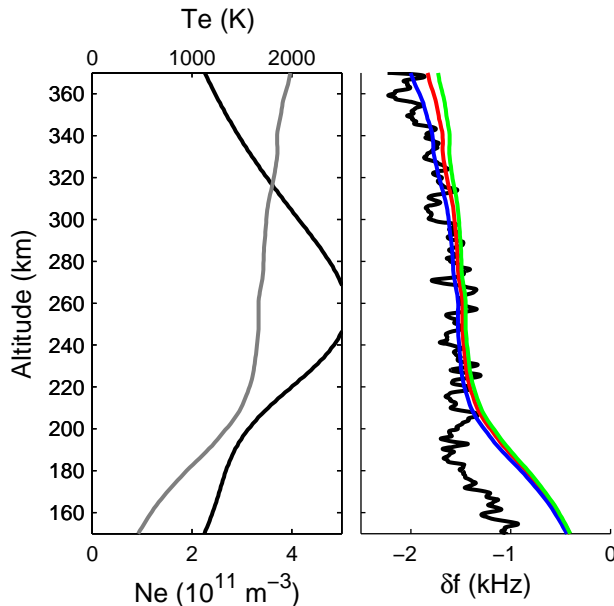
Figure 8.4: Example of measurements on April 1, 2006, near 1000 LT. The left panel shows a plasma density profile inferred from the plasma line offset (black curve, lower axis) along with the electron temperature from the ion line (gray curve, top axis). No moleculars were used in the ion line fit. The right panel is the measured plasma line frequency difference (black), the prediction from linear theory (green), the prediction from kinetic theory neglecting the magnetic field (red), and the prediction from kinetic theory with $\alpha = 45°$ (blue).

fine since the plasma density is sizable. Above the F peak, the kinetic effects become important, and we see that the theory including the magnetic field does an excellent job of reproducing the observed δf. These results are not only useful for measuring the electron temperature (and in turn the molecular fraction), but are also turning out to be a sensitive test of kinetic effects including the magnetic field! Below 200 km the curves diverge, for a combination of a few reasons. First of all, the ACFs were processed neglecting the moleculars, which is incorrect, and including the moleculars would have the effect of increasing the electron temperature (increasing the predicted plasma line offset). Secondly, we have recently shown that the MRACF mode is not satisfactory at low altitudes (*Aponte et al.*, 2006) where the range smearing effects of the long pulse cannot be corrected by the linear regularization approach employed in

the technique of *Nikoukar et al.* (2006). In the future we will combine this mode with a coded long pulse ion line technique at low altitudes.

We are attempting a similar measurement at Jicamarca of the molecular ion fraction. The approach is very similar, except instead of plasma line measurements we use the absolute density from Faraday rotation. We then use this density to get the estimate of T_e/T_i. We have recently performed an experiment that should tell us whether this technique is feasible.

There are several important scientific reasons for studying molecular ions, in particular with ISRs. These include:

1. To obtain good temperature estimates (and temperature ratio estimates in the daytime), which depend on the composition that one assumes in the IS fitting process (often one assumes that $n_e = [O^+]$).

2. To improve empirical model estimates of ion fractions.

3. To increase understanding of ionospheric phenomena that occur on the bottomside and E region, such as intermediate layers, metallic layers, 150-km echoes, recombination processes, airglow, etc.

Nighttime Composition

The techniques described in the previous section do not work at night because the plasma line is not enhanced above thermal levels (and thus requires long integration times to detect). New ideas are being explored for investigating the nighttime ion composition. These include constraining the temperatures or combining with other measurements (Lidar measurements of temperatures at the lower boundary, or airglow volume emission rate measurements). These techniques may allow us to explore the composition of nighttime intermediate layers and sporadic E layers, where the relative

abundance of moleculars as compared to metallics is uncertain, as well as to further investigate the discrepancy discussed in Chapter 6.

Neutral Coupling Studies

Further investigations of the neutral composition using different techniques including that discussed in Chapter 7 are necessary. We plan to apply the technique described in Chapter 7 to the full set of Arecibo data. This should give a seasonal and solar cycle description of the atomic oxygen density and the exospheric temperature, as well as a measure of the day-to-day variability, that can be used to improve the MSIS model. The long-term study will also allow us to investigate possible secular changes in the atomic oxygen density and exospheric temperature. These secular changes have been predicted to occur as a result of increased CO_2 levels, which increases thermospheric cooling leading to a gradual decline in the thermospheric atomic oxygen levels (S. Solomon, personal communication, 2006). These trends may be anthropogenic in origin, and can be studied using the long-duration ISR databases. The day-to-day variability is another issue that is likely related to day-to-day changes in mixing in the mesopause region. These changes will also be interesting to study using ISR data.

A further study of neutral coupling focusses on the neutral wind. We have recently developed a technique (*Aponte et al.*, 2005) to measure the eastward electric field and the parallel ion velocity with very high time resolution, which gives ISR-based neutral wind estimates with very high resolution. These measurements, when combined with Fabry-Perot measurements of the wind, can give insight into the coupling of the neutral and ion gases. In particular, two FPIs can be used to measure the neutral wind along the magnetic meridian simultaneously with the radar measurements to investigate any discrepancies. Such a study could investigate and possibly resolve the debate of the Burnside factor (see Chapter 7) which was originally based on ion

momentum budget measurements (*Burnside et al.*, 1987). If we can show that the neutral winds from radar measurements and FPIs agree, and can derive a Burnside factor close to 1.25, the results will be very satisfying in light of the recent neutral energy balance results presented in Chapter 7.

In addition, long-term FPI measurements have indicated a shift in the meridional neutral wind over time (over many years of observations). Such trends can be validated with ISR measurements. The high resolution neutral wind measurements afforded by ISRs can also be used to investigate storm-time effects, including vertical shear in the wind. A case study of shear observed during the April 2002 geomagnetic storm is currently being investigated in conjunction with a global modeling effort using the TIMEGCM.

Mid-Latitude Instabilities

A further topic of investigation is related to the observation of mid-latitude instabilities. Figure 8.5 shows examples of what are thought to be related to mid-latitude instabilities, as observed through all-sky images. There are different types of structures. The top panel in Figure 8.5 shows plumes reminiscent of images of equatorial spread F, which is usually observed as structures moving in from the equator, with perhaps secondary structuring growing in the local mid-latitude ionosphere (e.g., *Makela et al.*, 2006). These events are thought to be associated with equatorial instabilities. A second class of instabilities are thought to be related to the Perkins mechanism (*Perkins*, 1973), which are the TIDs in the lower panel. These are essentially bands of raised and lowered portions of the ionosphere ("alternating bands of rising low density regions and falling high density regions") that propagate in the low and mid-latitude ionosphere. Japanese observations of the conjugate ionosphere have shown that these TIDs are electrified, as predicted, and shown in the lower panel of
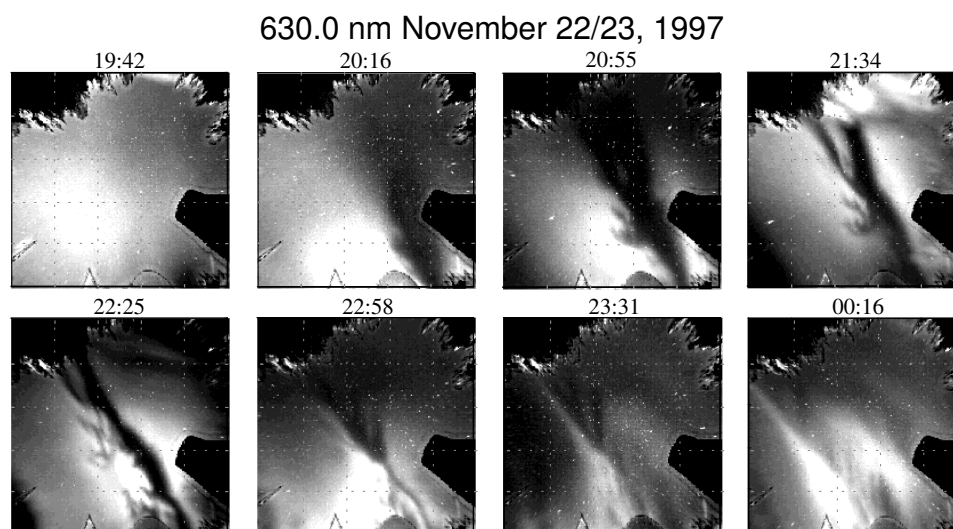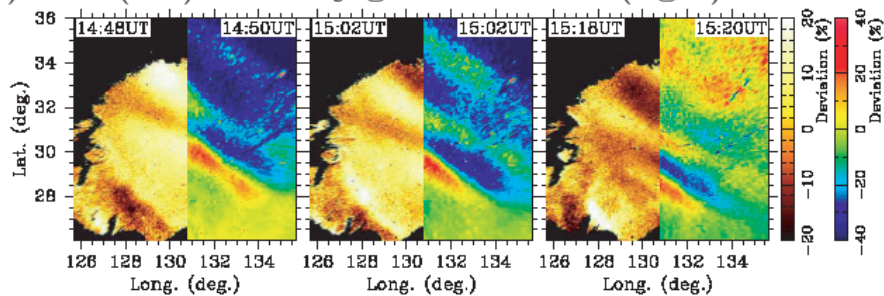
Figure 8.5: Examples of mid-latitude structuring as observed using airglow imaging. The top panel is from *Makela* (2003) and shows plumes measured in the 630.0-nm emission. The bottom panel shows evidence for electrical structuring in mid-latitude TIDs, from *Otsuka et al.* (2004).

Figure 8.5. There are many unanswered questions relating to mid-latitude instability. The instability has yet to be modeled in three dimensions; the effect of E-region coupling is unclear; the growth rates are too low and require a seed mechanism (gravity waves or perhaps sporadic E or some other instability); and there are some aspects of the theory that disagree with the measurements (such as the propagation direction, which may have to do with TID polarization fields as described by *Kelley and Makela* (2001)). Thus, there is a lot of work to do regarding the modeling and measurements of the mid-latitude instability. An additional area of interest is observations of quasiperiodic echoes in sporadic E at mid-latitudes.

Penetration Electric Fields

A final topic of investigation is the further study of penetration electric fields. In Chapter 5 we developed a transfer function model for penetration electric field effects. While the model works fairly well, the physical properties of the system are not understood. The physical explanation for long-duration penetration fields, for example, is unclear. Further studies of the global (multi-longitude as well as multi-latitude) effects of penetration fields are necessary, as well as studies of the role of B_y fluctuations in the solar wind (related to field-aligned currents).

Appendix A

Small-Scale Structure on the Poleward Edge of a Stable Auroral Red Arc *

One Ring to rule them all, One Ring to find them,
One Ring to bring them all and in the darkness bind them
  - J. R. R. Tolikien, in <u>The Fellowship of the Ring</u> (translated from the Elvish)

A.1 Abstract

Here we present all-sky images of a stable auroral red arc collocated with the low-density trough. Small-scale, dynamic structure is observed on the poleward edge of the arc that may be caused by a crossed density/temperature gradient or by a collisional Kelvin-Helmholtz shear-flow instability in conjunction with a sufficient density gradient.

---

*This chapter based on the original published work, *Nicolls et al.* (2005). ©2005 IEEE. Reprinted, with permission, from *IEEE Transactions on Plasma Science.*
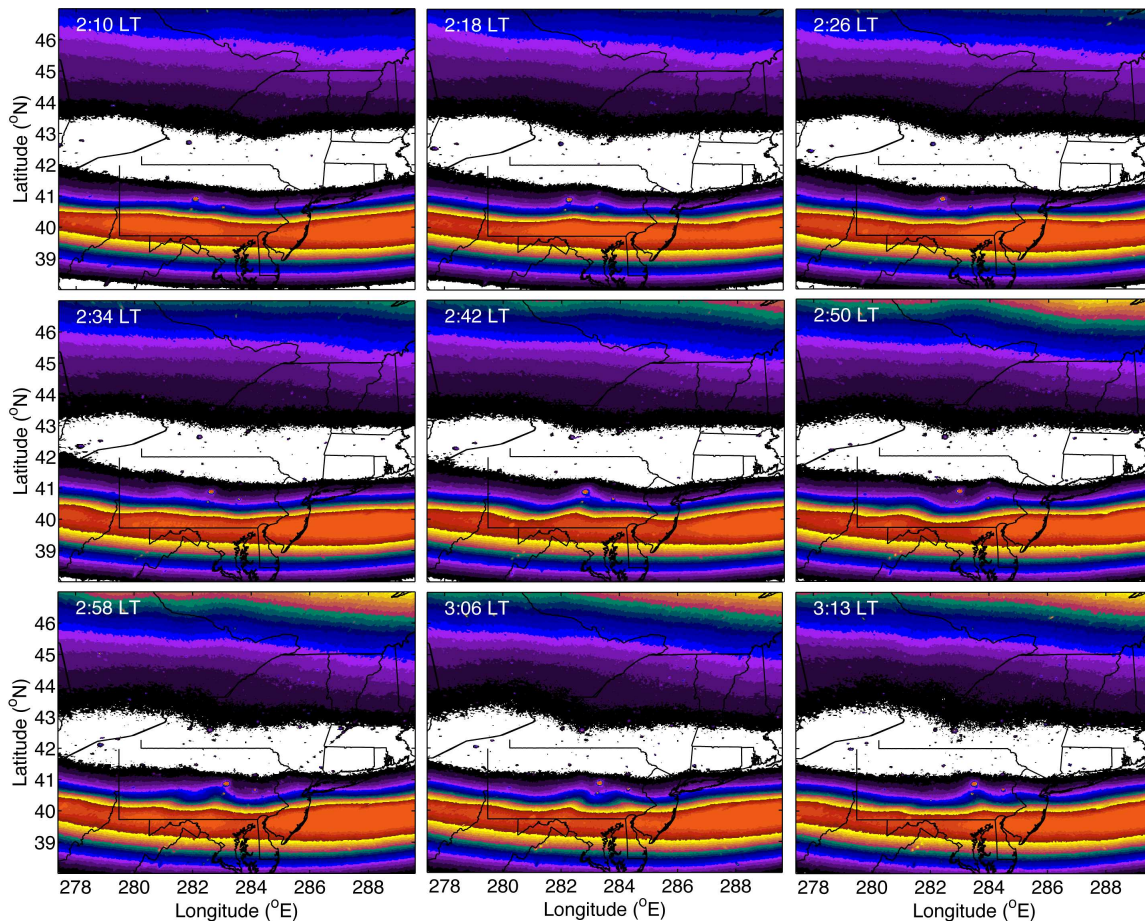
Figure A.1: Series of images of SAR arcs on a banded color scale observed from Ithaca, NY on October 28-29, 2000.

A.2   Observations

Stable auroral red (SAR) arcs are auroral bands that occur equatorward of the main diffuse aurora in the mid-latitude region. The arcs weren't discovered until the mid 1900s because, unlike the polar aurora, they are typically not visible to the unaided eye. SAR arcs are stable and long-lived and are associated with energy transfer from trapped ring-current particles during storm recovery (*Kozyra et al.*, 1997). The arcs are generally thought to be nearly homogeneous as a function of longitude. Here we present images from a sensitive CCD camera that show wave-like features on the poleward edge of a SAR arc and discuss possible origins.
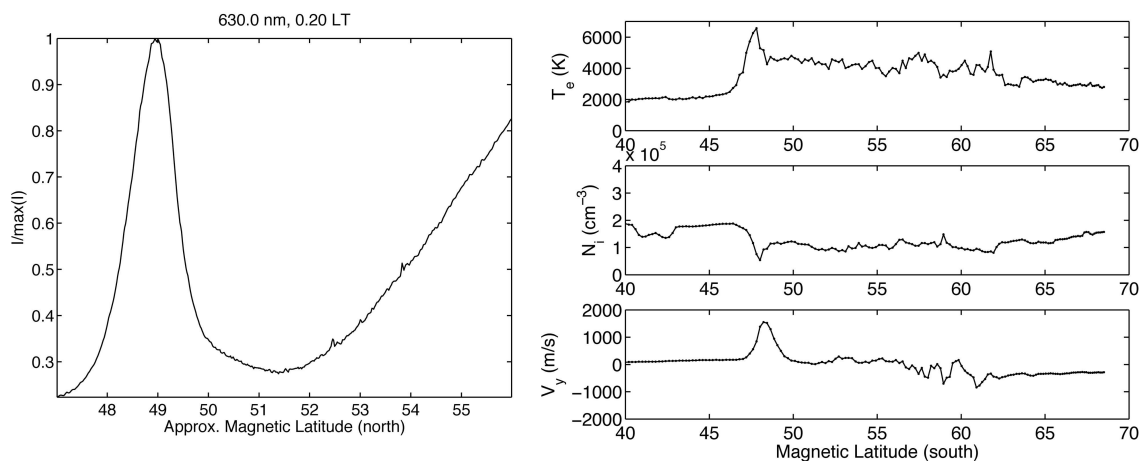
Figure A.2: A cut across one of the images (left) along with DMSP-measured electron temperature, ion density, and cross-track drift (right).

Figure A.1 shows a series of images at 630.0 nm taken from Ithaca, NY (42.5°N, 283.5°E) on the night of October 28-29, 2000. The images were taken with the Cornell All-Sky Imager, a CCD camera with an all-sky lens, telecentric optics, and five-position filterwheel. The 90-s images have been unwarped onto a latitude-longitude grid assuming an emission height of 400 km and a horizontal extent of 1000 km. The arcs are distinctly seen south of the diffuse aurora at a latitude of 40° and persist for the entire night. Although the camera was not calibrated for absolute intensity, the intensity of the arc was often well over 5 times the lower latitude airglow, implying a peak emission of over 1 kR.

SAR arcs are formed when energy that has been deposited into the plasma at high altitudes is conducted along the field lines, leading to excitation of atomic oxygen to the ^1D state. The emission peaks in the F region due to the lower efficiency of quenching at these altitudes. On the night shown, the D_{st} index indicates that a storm began late on the 28th, peaking at -130 nT near 3 UT on the 29th.

The right panel of Figure A.2 shows data from a DMSP satellite pass ($\sim$800 km) near the magnetic conjugate point. Plotted are the electron temperature, the ion

density, and the cross-track drift velocity. Peaks in T_e and V_y and a narrow trough in N_i are observed at about 48-49° magnetic latitude, the signature of the arc. The left panel is a cut across one of the images as a function of magnetic latitude. The large density depletion leads to a huge surge in electron temperature, up to almost 7000 K. In addition, westward drifts of over 1500 m/s are observed, characteristic of a sub-auroral ion drift event. While the processes that cause the low density trough are thought to be unrelated to the formation of SAR arcs (*Kozyra et al.*, 1997), the region is important because it allows for the high temperatures and thus high red-line intensity.

The images in Figure A.1 also show evidence for billow-like structure moving along the poleward edge of the arcs with scale sizes less than 100 km. Longer-wavelength undulations are evident in the edge of the diffuse aurora, which have been observed before (*Kelley*, 1986). The shorter-wavelength structures on the poleward edge of the arc may be due to a crossed density/temperature gradient instability (*Hudson and Kelley*, 1976; *Keskinen*, 2002). Close examination of Figure A.2 shows that on the poleward edge of the SAR arc the two gradients are large and anti-correlated, as required for instability. The equatorward edge has a weaker density gradient. In addition, a collisional Kelvin-Helmholtz instability has recently been discussed as a contributing factor in the structuring of ionospheric density gradients in this scale size range (*Hysell and Kudeki*, 2004). The shear in the plasma flow in Figure A.2 aligns well with the poleward density gradient, but less well on the equatorward edge.

Bibliography

Abdu, M. A., I. S. Batista, and J. A. Bittencourt (1981), Some characteristics of spread F at the magnetic equatorial station Fortaleza, *J. Geophys. Res.*, *86*(A8), 6836–6842.

Abdu, M. A., R. T. de Medeiros, and Y. Nakamura (1983), Latitudinal and magnetic flux tube extension of the equatorial spread F irregularities, *J. Geophys. Res.*, *88*(A6), 4861–4868.

Abreu, V. J., J. H. Yee, S. C. Solomon, and A. Dalgarno (1986), The quenching rate of O(^1D) by O(^3P), *Planet. Space Sci.*, *34*(11), 1143–1145.

Alcaydé, D., and P. Bauer (1977), Modelisation des concentrations d'oxygene atomique observées par diffusion incohérente, *Ann. Geophys.*, *33*(3), 305–320.

Anderson, D., A. Anghel, K. Yumoto, M. Ishitsuka, and E. Kudeki (2002), Estimating daytime vertical $\mathbf{E} \times \mathbf{B}$ drift velocities in the equatorial F-region using ground-based magnetometer observations, *Geophys. Res. Lett.*, *29*(12), 1596, doi:10.1029/2001GL014562.

Anderson, D., A. Anghel, J. Chau, and O. Veliz (2004), Daytime vertical $\mathbf{E} \times \mathbf{B}$ drift velocities inferred from ground-based magnetometer observations at low latitudes, *Space Weather*, *2*(11), S11001, doi:10.1029/2004SW000095.

Anderson, D. N., A. Anghel, J. Chau, and K. Yumoto (2006), Global, low latitude vertical $\mathbf{E} \times \mathbf{B}$ drift velocities inferred from daytime magnetometer observations, *Space Weather*, *In Press*.

Andrews, D. G., J. R. Holton, and C. B. Leovy (1987), *Middle Atmosphere Dynamics*, Academic Press., San Diego, CA.

Angstrom, A. J. (1868), *Recherches sur le Spectre Solaire*, W. Schultz, Upsala, Sweden.

Aponte, N., M. J. Nicolls, S. A. González, M. P. Sulzer, M. C. Kelley, E. Robles, and C. A. Tepley (2005), Instantaneous electric field measurements and derived neutral winds at Arecibo, *Geophys. Res. Lett.*, *32*(12), L12107, doi:10.1029/2005GL022609.

Aponte, N., M. P. Sulzer, M. J. Nicolls, R. Nikoukar, and S. A. González (2006), Molecular ion composition measurements in the $F1$ region at Arecibo, *J. Geophys. Res.*, *To be submitted.*

Appleton, E. V. (1927), The existence of more than one ionised layer in the upper atmosphere, *Nature*, *120*, 330.

Arduini, C., G. Laneve, and F. A. Herrero (1997), Local time and altitude variation of equatorial thermosphere midnight density maximum (MDM): San Marco drag balance measurements, *Geophys. Res. Lett.*, *24*(4), 377–380.

Bailey, G. J. (1983), The effect of a meridional $\mathbf{E} \times \mathbf{B}$ drift on the thermal plasma at $L = 1.4$, *Planet. Space Sci.*, *31*(4), 389–409.

Bailey, G. J., and R. Sellek (1990), A mathematical model of the earth's plasmasphere and its application in a study of He$^+$ at L=3, *Ann. Geophys.*, *8*(3), 171–189.

Baluja, K. L., and C. J. Zeippen (1988), M1 and E2 transition probabilities for states within the $2p^4$ configuration of the OI isoelectronic sequence, *J. Phys. B: At. Mol. Opt. Phys.*, *21*(9), 1455–1471.

Banks, P. (1966a), Collision frequencies and energy transfer: Electrons, *Planet. Space Sci.*, *14*(11), 1085–1103.

Banks, P. M. (1966b), Collision frequencies and energy transfer: Ions, *Planet. Space Sci.*, *14*(11), 1105-1122.

Banks, P. M. (1967), Ion temperature in the upper atmosphere, *J. Geophys. Res.*, *72*(13), 3365–3385.

Banks, P. M., and G. Kockarts (1973), *Aeronomy*, Academic Press, San Diego, CA.

Barbier, D. (1957), Interprétation de la luminescence nocturne de la raie rouge d'oxygène, *Comptes rendus, Acad. Sciences Paris*, *244*(15), 2077–2080.

Barth, C. A. (1961), 5577-Angstrom airglow, *Science*, *134*(348), 1426.

Barth, C. A. (1964), Three-body reactions, *Ann. Geophys.*, *20*(2), 182–196.

Bates, D. R. (1956), Recombination in the ionosphere, in *Solar Eclipses and the Ionosphere*, edited by W. J. Beynon and G. M. Brown, p. 191, Pergamon, New York.

Bates, D. R. (1959), Some problems concerning the terrestrial atmosphere above about the 100 km level, *Proc. Roy. Soc. London*, *253*(1275), 451–462.

Bates, D. R. (1988), Excitation of 557.7 nm OI line in nightglow, *Planet. Space. Sci.*, *36*(9), 883–889.

Bates, D. R. (1992), Nightglow emissions from oxygen in the lower thermosphere, *Planet. Space Sci.*, *40*, 211–221.

Batista, I. S., R. T. de Medeiros, M. A. Abdu, J. R. de Souza, G. J. Bailey, and E. R. de Paula (1996), Equatorial ionospheric vertical plasma drift model over the Brazilian region, *J. Geophys. Res.*, *101*(A5), 10,887–10,892.

Bauer, P., P. Waldteufel, and D. Alcayde (1970), Diurnal variations of the atomic oxygen density and temperature determined from incoherent scatter measurements in the ionospheric *F* region, *J. Geophys. Res.*, *75*(25), 4825–4832.

Baumgardner, J., B. Flynn, and M. Mendillo (1993), Monochromatic imaging instrumentation for applications in aeronomy of the Earth and planets, *Opt. Eng.*, *32*(12), 3028–3032.

Bertoni, F. (2004), Derivas ionsfericas em latitudes equatoriais: Observacoes e modelagem, Ph.D. thesis, Instituto Nacional de Pesquisas Espaciais.

Bilitza, D. (2001), International Reference Ionosphere 2000, *Radio Sci.*, *36*(2), 261–276.

Biondi, M. A., S. Y. Sazykin, B. G. Fejer, J. W. Meriwether, and C. G. Fesen (1999), Equatorial and low latitude thermospheric winds: Measured quiet time variations with season and solar flux from 1980 to 1990, *J. Geophys. Res.*, *104*(A8), 17,091–17,106.

Bittencourt, J. A., and M. A. Abdu (1981), A theoretical comparison between apparent and real vertical ionization drift velocities in the equatorial *F* region, *J. Geophys. Res.*, *86*(A4), 2451–2454.

Blanc, M., and A. D. Richmond (1980), The ionospheric disturbance dynamo, *J. Geophys. Res.*, *85*(A4), 1669–1686.

Bowles, K. L. (1958), Observations of vertical incidence scatter from the ionosphere at 41 Mc/s, *Phys. Rev. Lett.*, *1*(12), 454–455.

Buonsanto, M. J. (1999), Ionospheric storms: A review, *Space Sci. Rev.*, *88*, 563–601.

Buonsanto, M. J., Y. K. Tung, and D. P. Sipler (1992), Neutral atomic oxygen density from nighttime radar and optical wind measurements at Millstone Hill, *J. Geophys. Res.*, *97*(A6), 8673–8679.

Buonsanto, M. J., D. P. Sipler, G. B. Davenport, and J. M. Holt (1997), Estimation of the O^+, O collision frequency from coincident radar and Fabry-Perot observations at Millstone Hill, *J. Geophys. Res.*, *102*(A8), 17,267–17,274.

Burnside, R. G., J. W. Meriwether, and M. R. Torr (1977), Contamination of ground-based measurements of OI (6300 Å) and NI (5200 Å) airglow by OH emissions, *Planet. Space Sci.*, *25*(10), 985–988.

Burnside, R. G., F. A. Herrero, J. W. Meriwether, and J. C. G. Walker (1981), Optical observations of thermospheric dynamics at Arecibo, *J. Geophys. Res.*, *86*(A7), 5532–5540.

Burnside, R. G., C. A. Tepley, and V. B. Wickwar (1987), The O^+ - O collision cross section: Can it be inferred from aeronomical measurements?, *Ann. Geophys.*, *5*(6), 343–349.

Burnside, R. G., M. P. Sulzer, and J. C. G. Walker (1988), Determination of thermospheric temperatures and neutral densities at Arecibo from the ion energy balance, *J. Geophys. Res.*, *93*(A8), 8642–8650.

Burnside, R. G., C. A. Tepley, and M. P. Sulzer (1991), World Day observations at Arecibo: 1985 to 1989, *J. Geophys. Res.*, *96*(A3), 3691–3710.

Burton, R. K., R. L. McPherron, and C. T. Russell (1975), Terrestrial magnetosphere: A half-wave rectifier of the interplanetary electric field, *Science*, *189*(4204), 717–718.

Campbell, W. W. (1895), A note on the spectrum of the aurora borealis, *Astrophys. J.*, *2*, 162.

Carlson, H. C., and R. M. Harper (1977), An experimental estimate of O^+-O resonant charge transfer cross section, collision frequency, and energy transfer rate, *J. Geophys. Res.*, *82*(7), 1144–1148.

Chakrabarti, S. (1999), Ground based spectroscopic studies of sunlit airglow and aurora, *J. Atmos. Solar-Terr. Phys.*, *60*(14), 1403–1423.

Chakrabarty, D., R. Sekar, R. Narayanan, C. V. Devasia, and B. M. Pathan (2005), Evidence for the interplanetary electric field effect on the OI 630.0 nm airglow over low latitude, *J. Geophys. Res.*, *110*, A11301, doi:10.1029/2005JA011221.

Chapman, S. (1931), The absorption and dissociative or ionizing effect of monochromatic radiation in an atmosphere on a rotating earth, *Proc. Phys. Soc.*, *43*, 1047–1055.

Chau, J. L., and R. F. Woodman (2004), Daytime vertical and zonal velocities from 150-km echoes: Their relevance to *F*-region dynamics, *Geophys. Res. Lett.*, *31*(17), L17801, doi:10.1029/2004GL020800.

Chimonas, G., and C. O. Hines (1970), Atmospheric gravity waves launched by auroral currents, *Planet. Space Sci.*, *18*(4), 565.

Coker, C., E. E. Henderlight, K. F. Dymond, S. E. Thonnard, S. E. McDonald, A. C. Nicholas, S. A. Budzien, and R. P. McCoy (2004), Comparison of ionospheric observations from UV limb scans and radar altimetry, *Radio Sci.*, *39*, RS6003, doi:doi:10.1029/2003RS003012.

Coster, A. J., J. C. Foster, and P. J. Erickson (2003), Space weather: Monitoring the ionosphere with GPS, *GPS World*, *May*, 40–45.

Crary, D. J., and J. M. Forbes (1986), The dynamic ionosphere over Arecibo: A theoretical investigation, *J. Geophys. Res.*, *91*(A1), 249–258.

Dalgarno, A. (1958a), Ambipolar diffusion in the $F2$-layer, *J. Atmos. Terr. Phys.*, *12*, 219–220.

Dalgarno, A. (1958b), The mobilities of ions in their parent gases, *Phi. Trans. Roy. Soc.*, *250*(982), 426–439.

Dalgarno, A. (1964), Ambipolar diffusion in the F-region, *J. Atmos. Terr. Phys.*, *26*(9), 989.

Danilov, A., and N. Smirnova (1995), Improving the 75 to 300 km ion composition model of the IRI, *Adv. Space Res.*, *15*(2), 171–177.

Davies, K., and D. M. Baker (1965), Ionospheric effects observed around the time of the Alaskan earthquake of March 28, 1964, *J. Geophys. Res.*, *70*(9), 2251–2253.

Davis, C. J., A. D. Farmer, and A. Aruliah (1995), An optimised method for calculating the $O^{+}-O$ collision parameter from aeronomical measurements, *Ann. Geophys.*, *13*(5), 541–550.

Djuth, F. T., M. P. Sulzer, and J. H. Elder (1994), Application of the coded long-pulse technique to plasma line studies of the ionosphere, *Geophys. Res. Lett.*, *21*(24), 2725–2728.

Dougherty, J. P., and D. T. Farley (1960), A theory of incoherent scattering of radio waves by a plasma, *Proc. Roy. Soc.*, *259*(1296), 79–99.

Duncan, R. A. (1956), The behaviour of a chapman layer in the night F_2 region of the ionosphere, under the influence of gravity, diffusion, and attachment, *Australian J. Phys.*, *9*, 436–439.

Dungey, J. W. (1956), The effect of ambipolar diffusion in the night-time F layer, *J. Atmos. Terr. Phys.*, *9*, 90–102.

Dyson, P. L., T. P. Davies, M. L. Parkinson, A. J. Reeves, P. G. Richards, and C. E. Fairchild (1997), Thermospheric neutral winds at southern mid-latitudes: A comparison of optical and ionosonde $h_m F2$ methods, *J. Geophys. Res.*, *102*(A12), 27,189–27,196.

Earle, G. D., and M. C. Kelley (1987), Spectral studies of the sources of ionospheric electric fields, *J. Geophys. Res.*, *92*(A1), 213–224.

Ebel, A. (1980), Eddy diffusion models for the mesosphere and lower thermosphere, *J. Atmos. Terr. Phys.*, *42*(7), 617–628.

Emery, B. A., R. M. Harper, S. Ganguly, J. C. G. Walker, and G. A. Giles (1981), Arecibo ionospheric data: August 1972 - May 1977, *Tech. rep.*, National Astronomy and Ionosphere Center.

Evans, J. V. (1967), Electron temperature and ion composition in the $F1$ region, *J. Geophys. Res.*, *72*(13), 3343–3355.

Faivre, M., J. W. Meriwether, C. G. Fesen, and M. A. Biondi (2006), Climatology of the midnight temperature maximum phenomenon at Arequipa, Peru, *J. Geophys. Res.*, *111*, A06302, doi:10.1029/2005JA011321.

Farley, D. T., and T. Hagfors (2006), *Incoherent scatter: Theory and experiment*, The photocopier in Laurie's office, Ithaca, NY.

Farley, D. T., B. B. Balsley, R. F. Woodman, and J. P. McClure (1970), Equatorial spread F: Implications of VHF radar observations, *J. Geophys. Res.*, *75*(34), 7199–7216.

Fejer, B. G. (1997), The electrodynamics of the low-latitude ionosphere: Recent results and future challenges, *J. Atmos. Terr. Phys.*, *59*(13), 1456–1482.

Fejer, B. G., and L. Scherliess (1997), Empirical models of storm time equatorial zonal electric fields, *J. Geophys. Res.*, *102*(A11), 24,047–24,056.

Fejer, B. G., D. T. Farley, R. F. Woodman, and C. Calderon (1979), Dependence of equatorial F-region vertical drifts on season and solar cycle, *J. Geophys. Res.*, *84*(A10), 5792–5796.

Fejer, B. G., M. F. Larsen, and D. T. Farley (1983), Equatorial disturbance dynamo electric fields, *Geophys. Res. Lett.*, *10*(7), 537–540.

Fejer, B. G., E. R. de Paula, I. S. Batista, E. Bonelli, and R. F. Woodman (1989), Equatorial F region vertical plasma drifts during solar maximum, *J. Geophys. Res.*, *94*(A9), 12,049–12,054.

Fejer, B. G., S. A. Gonzalez, E. R. de Paula, and R. F. Woodman (1991), Average vertical and zonal F region plasma drifts over Jicamarca, *J. Geophys. Res.*, *96*(A8), 13,901–13,906.

Fejer, B. G., E. R. de Paula, R. A. Heelis, and W. B. Hanson (1995), Global equatorial ionospheric vertical plasma drifts measured by the AE-E satellite, *J. Geophys. Res.*, *100*(A4), 5769–5776.

Fejer, B. G., L. Scherliess, and E. R. de Paula (1999), Effects of the vertical plasma drift velocity on the generation and evolution of equatorial spread F, *J. Geophys. Res.*, *104*(A9), 19,859–19,869.

Fejer, J. A. (1960), Scattering of radio waves by an ionized gas in thermal equilibrium, *Can. J. Phys.*, *38*(8), 1114–1133.

Feng, Z. M., E. Kudeki, R. F. Woodman, J. Chau, and M. Milla (2004), *F* region plasma density estimation at Jicamarca using the complex cross-correlation of orthogonal polarized backscatter fields, *Radio Sci.*, *39*(3), RS3015, doi: 10.1029/2003RS002963.

Fennelly, J. A., and D. G. Torr (1992), Photoionization and photoabsorption cross sections of O, N_2, and N for aeronomic calculations, *At. Data and Nucl. Data Tables*, *51*(2), 321–363.

Fesen, C. G. (1996), Simulations of the low-latitude midnight temperature maximum, *J. Geophys. Res.*, *101*(A12), 26,863–26,874.

Foster, J. C., P. J. Erickson, A. J. Coster, J. Goldstein, and F. J. Rich (2002), Ionospheric signatures of plasmaspheric tails, *Geophys. Res. Lett.*, *29*(13), 1623, doi:10.1029/2002GL015067.

Froese-Fischer, C., and H. P. Saha (1983), Multiconfiguration Hartree-Fock results with Breit-Pauli corrections for forbidden transitions in the $2p^4$ configuration, *Phys. Rev. A*, *28*(6), 3169–3178.

Fuller-Rowell, T. J., M. V. Codrescu, R. J. Moffett, and S. Quegan (1994), Response of the thermosphere and ionosphere to geomagnetic storms, *J. Geophys. Res.*, *99*(A3), 3893–3914.

Fuller-Rowell, T. J., M. V. Codrescu, H. Rishbeth, R. J. Moffett, and S. Quegan (1996), On the seasonal response of the thermosphere and ionosphere to geomagnetic storms, *J. Geophys. Res.*, *101*(A2), 2343–2353.

Fuller-Rowell, T. J., M. V. Codrescu, R. G. Roble, and A. D. Richmond (1997), How does the thermosphere and ionosphere react to a geomagnetic storm?, in *Magnetic Storms*, edited by B. T. Tsurutani, W. D. Gonzalez, Y. Kamide, and J. K. Arballo, p. 203, Geophysical Monograph 98, American Geophysical Union, Washington, D.C.

Garcia, F. J. (1999), Atmospheric studies using all-sky imaging of airglow layers, Ph.D. thesis, Cornell University.

Garcia, F. J., M. J. Taylor, and M. C. Kelley (1997), Two-dimensional spectral analysis of mesospheric airglow image data, *Applied Optics*, *36*(29), 7374–7385.

Ghosh, S., E. Siregar, D. A. Roberts, and M. L. Goldstein (1996), Simulation of high-frequency solar wind power spectra using Hall magnetohydrodynamics, *J. Geophys. Res.*, *101*(A2), 2493–2504.

Goldstein, M. L., D. A. Roberts, and C. A. Fitch (1994), Properties of the fluctuating magnetic helicity in the inertial and dissipation ranges of solar wind turbulence, *J. Geophys. Res.*, *99*(A6), 11,519–11,538.

Goncharenko, L. P., J. E. Salah, A. van Eyken, V. Howells, J. P. Thayer, V. I. Taran, B. Shpynev, Q. Zhou, and J. Chau (2005), Observations of the April 2002 geomagnetic storm by the global network of incoherent scatter radars, *Ann. Geophys.*, *23*(1), 163–181.

Gonzales, C. A., M. C. Kelley, B. G. Fejer, J. F. Vickrey, and R. F. Woodman (1979), Equatorial electric fields during magnetically disturbed conditions, 2, Implications of simultaneous auroral and equatorial measurements, *J. Geophys. Res.*, *84*(A10), 5803–5812.

Gonzales, C. A., M. C. Kelley, D. L. Carpenter, T. R. Miller, and R. H. Wand (1980), Simultaneous measurements of ionospheric and magnetospheric electric fields in the outer plasmasphere, *Geophys. Res. Lett.*, *7*(7), 517–520.

Gonzales, C. A., M. C. Kelley, R. A. Behnke, J. F. Vickrey, R. Wand, and J. Holt (1983), On the latitudinal variations of the ionospheric electric field during magnetic disturbances, *J. Geophys. Res.*, *88*(A11), 9135–9144.

González, S. A., M. P. Sulzer, M. J. Nicolls, and R. Kerr (2004), Solar cycle variability of nighttime topside helium ion concentrations over Arecibo, *J. Geophys. Res.*, *109*(A7), A07302, doi:10.1029/2003JA010100.

Gordiets, B. F., Y. N. Kulikov, M. M. N, and M. Y. Marov (1982), Numerical modelling of the thermospheric heat budget, *J. Geophys. Res*, *87*(A6), 4504–4514.

Gordon, W. E. (1958), Incoherent scattering of radio waves by free electrons with applications to space exploration by radar, *Proc. IRE*, *46*(11), 1824–1829.

Guberman, S. L. (1987), The production of $O(^1S)$ from dissociative recombination of O_2^+, *Nature*, *327*(6121), 408–409.

Guberman, S. L. (1988), The production of $O(^1D)$ from dissociative recombination of O_2^+, *Planet. Space Sci.*, *36*(1), 47–53.

Guberman, S. L., and A. Giusti-Suzor (1991), The generation of $O(^1S)$ from the dissociative recombination of O_2^+, *J. Chem. Phys.*, *95*(4), 2602–2613.

Gulyaeva, T. (1987), Progress in ionospheric informatics based on electron density profile analysis of ionograms, *Adv. Space Res.*, *7*(6), 39–48.

Hagfors, T. (1961), Density fluctuations in a plasma in a magnetic field, with applications to the ionosphere, *J. Geophys. Res.*, *66*(6), 1699–1712.

Haldoupis, C., M. C. Kelley, G. C. Hussey, and S. Shalimov (2003), Role of unstable sporadic-E layers in the generation of midlatitude spread F, *J. Geophys. Res.*, *108*(A12), 1446, doi:10.1029/2003JA009956,.

Harper, R. M. (1972), Observation of a large nighttime gravity wave at Arecibo, *J. Geophys. Res.*, *77*(7), 1311–1315.

Hedin, A. E. (1991a), Extension of the MSIS thermosphere model into the middle and lower atmosphere, *J. Geophys. Res.*, *96*(A2), 1159–1172.

Hedin, A. E. (1991b), Revised global model of thermosphere winds using satellite and ground-based observations, *J. Geophys. Res*, *96*(A5), 7657–7688.

Hedin, A. E., and D. Alcaydé (1974), Comparison of atomic oxygen measurements by incoherent scatter and satellite-borne mass spectrometer techniques, *J. Geophys. Res.*, *79*(10), 1579–1581.

Herrero, F. A., N. W. Spencer, and H. G. Mayr (1993), Thermosphere and F-region plasma dynamics in the equatorial region, *Adv. Space Res.*, *13*(1), 201–220.

Hickman, A. P., M. Mediri-Napade, C. D. Chapin, and D. L. Huestis (1997), Fine structure effects in the O^+-O collision frequency, *Geophys. Res. Lett.*, *24*(2), 119–122.

Hierl, P., I. Dotan, J. V. Seeley, J. M. V. Doren, R. Morris, and A. A. Viggiano (1997), Rate constants for the reactions of O^+ with N_2 and O_2 as a function of temperature (300-1800 K), *J. Chem. Phys.*, *106*(9), 3540 – 3544.

Hines, C. O. (1960), Internal atmospheric gravity waves at ionospheric heights, *Can. J. Phys.*, *38*(11), 1441–1481.

Hines, C. O., H. G. Mayr, and C. A. Reddy (1997), On the analysis of geophysical data for an unknown constant, exemplified by the problem of the $O^+ - O$ collision cross-section, *J. Atmos. Solar-Terr. Phys.*, *59*(2), 181–189.

Ho, C. M., A. J. Mannucci, U. J. Lindqwister, X. Pi, and B. T. Tsurutani (1996), Global ionosphere perturbations monitored by the worldwide GPS network, *Geophys. Res. Lett.*, *23*(22), 3219–3222.

Ho, C. M., A. J. Mannucci, L. Sparks, X. Pi, U. J. Lindqwister, B. D. Wilson, B. A. Iijima, and M. J. Reyes (1998), Ionospheric total electron content perturbations monitored by the gps global network during two northern hemisphere winter storms, *J. Geophys. Res.*, *103*(A11), 26,409–26,420.

Hocke, K., and K. Schlegel (1996), A review of atmospheric gravity waves and travelling ionospheric disturbances: 1982-1995, *Ann. Geophys.*, *14*(9), 917–940.

Huang, C. S., and M. C. Kelley (1996), Nonlinear evolution of equatorial spread F 2. Gravity wave seeding of Rayleigh-Taylor instability, *J. Geophys. Res.*, *101*(A1), 293–302.

Huang, C. S., C. A. Miller, and M. C. Kelley (1994), Basic properties and gravity wave initiation of the midlatitude F region instability, *Radio Sci.*, *29*(1), 395–405.

Huang, C. S., J. C. Foster, and M. C. Kelley (2005), Long-duration penetration of the interplanetary electric field to the low-latitude ionosphere during the main phase of magnetic storms, *J. Geophys. Res.*, *110*(A11), A11309, doi:10.1029/2005JA011202.

Huang, C. S., S. Sazykin, J. L. Chau, N. Maruyama, and M. C. Kelley (2006), Penetration electric fields: Efficiency and characteristic time scale, *J. Atmos. Solar-Terr. Phys.*, *Submitted*.

Hudson, M. K., and M. C. Kelley (1976), The temperature gradient drift instability at the equatorward edge of the ionospheric plasma trough, *J. Geophys. Res.*, *81*(22), 3913–3918.

Hunsucker, R. D. (1982), Atmospheric gravity waves generated in the high-latitude ionosphere: A review, *Rev. Geophys.*, *20*(2), 293–315.

Hysell, D. L., and J. D. Burcham (1998), JULIA radar studies of equatorial spread F, *J. Geophys. Res.*, *103*(A12), 29,155–29,167.

Hysell, D. L., and J. D. Burcham (2002), Long term studies of equatorial spread F using the JULIA radar at Jicamarca, *J. Atmos. Solar-Terr. Phys.*, *64*(12-14), 1531.

Hysell, D. L., and E. Kudeki (2004), Collisional shear instability in the equatorial F region ionosphere, *J. Geophys. Res.*, *109*(A11), A11301, doi:10.1029/2004JA010636.

Itikawa, Y. (1975), Electron-ion energy-transfer rate, *J. Atmos. Terr. Phys.*, *37*(12), 1601–1602.

Jaggi, R. K., and R. A. Wolf (1973), Self-consistent calculation of the motion of a sheet of ions in the magnetosphere, *J. Geophys. Res.*, *78*(16), 2852–2866.

Kagan, L. M., M. J. Nicolls, M. C. Kelley, H. C. Carlson, V. V. Belikovich, N. V. Bakhmeteva, G. P. Komrakov, T. S. Trondsen, and E. Donovan (2005), Observation of radio-wave-induced red hydroxyl emission at low altitude in the ionosphere, *Phys. Rev. Lett.*, *94*(9), 095004, doi:10.1103/PhysRevLett.94.095004.

Kella, D., L. Vejby-Christensen, P. J. Johnson, H. B. Pedersen, and L. H. Andersen (1997), The source of green light emission determined from a heavy-ion storage ring experiment, *Science*, *276*(5318), 1530–1533.

Kelley, M. C. (1986), Intense sheared flow as the origin of large-scale undulations at the edge of the diffuse aurora, *J. Geophys. Res.*, *91*(A3), 3225–3230.

Kelley, M. C. (1989), *The Earth's ionosphere: Plasma physics and electrodynamics*, Academic Press, San Diego, CA.

Kelley, M. C., and S. Fukao (1991), Turbulent upwelling of the midlatitude ionosphere: 2. Theoretical framework, *J. Geophys. Res.*, *96*(A3), 3747–3754.

Kelley, M. C., and J. J. Makela (2001), Resolution of the discrepancy between experiment and theory of midlatitude *F*-region structures, *Geophys. Res. Lett.*, *28*(13), 2001, doi:10.1029/2000GL012777.

Kelley, M. C., and J. J. Makela (2002), B_y-dependent prompt penetrating electric fields at the magnetic equator, *Geophys. Res. Lett.*, *29*(7), 1153, doi: 10.1029/2001GL014468.

Kelley, M. C., K. D. Baker, and J. C. Ulwick (1979a), Late time barium cloud striations and their possible relationship to equatorial spread *F*, *J. Geophys. Res.*, *84*(A5), 1898–1904.

Kelley, M. C., B. G. Fejer, and C. A. Gonzales (1979b), Explanation for anomalous equatorial ionospheric electric fields associated with a northward turning of the interplanetary magnetic field, *Geophys. Res. Lett.*, *6*(4), 301–304.

Kelley, M. C., M. F. Larsen, C. A. LaHoz, and J. P. McClure (1981), Gravity wave initiation of equatorial spread *F*: A case study, *J. Geophys. Res.*, *86*(A11), 9087–9100.

Kelley, M. C., R. Livingston, and M. McCready (1985), Large amplitude thermospheric oscillations induced by an earthquake, *Geophys. Res. Lett.*, *12*(9), 577–580.

Kelley, M. C., J. J. Makela, B. M. Ledvina, and P. M. Kintner (2002), Observations of equatorial spread-*F* from Haleakala, Hawaii, *Geophys. Res. Lett.*, *29*(20), 2003, doi:10.1029/2002GL015509.

Kelley, M. C., C. Haldoupis, M. J. Nicolls, J. J. Makela, A. Belehaki, S. Shalimov, and V. K. Wong (2003a), Case studies of coupling between the *E* and *F* regions during unstable sporadic-*E* conditions, *J. Geophys. Res.*, *108*(A12), 1447, doi: 10.1029/2003JA009955.

Kelley, M. C., J. J. Makela, J. L. Chau, and M. J. Nicolls (2003b), Penetration of the solar wind electric field into the magnetosphere/ionosphere system, *Geophys. Res. Lett.*, *30*(4), 1158, doi:10.1029/2002GL016321.

Kelley, M. C., M. J. Nicolls, D. Anderson, A. Anghel, R. Sekar, K. S. V. Subbarao, and A. Bhattacharya (2006), Multi-longitude case studies comparing the interplanetary and equatorial ionospheric electric fields using an empirical model, *J. Atmos. Solar-Terr. Phys.*, *Submitted*.

Kenner, R. D., and E. A. Ogryzlo (1983), Quenching of $O_2(c^1\Sigma_u^-)\nu=0$ by $O(^3P)$, $O_2(a^1\Delta_g)$, and other gases, *Can. J. Chem.*, *61*(5), 921–926.

Keskinen, M. J. (2002), Enhancement or suppression of irregularities in the high-latitude trough ionosphere using high-power radio waves, *Radio Sci.*, *37*(4), 1065, doi:10.1029/2001RS002541.

Kikuchi, T., H. Luhr, T. Kitamura, O. Saka, and K. Schlegel (1996), Direct penetration of the polar electric field to the equator during a DP2 event as detected by the auroral and magnetometer chains and the EISCAT radar, *J. Geophys. Res.*, *101*(A8), 17,161–17,174.

Kil, H., and R. A. Heelis (1998), Global distribution of density irregularities in the equatorial ionosphere, *J. Geophys. Res.*, *103*(A1), 407–417.

King, J. W. (1968), Airglow observations and the decay of the ionospheric equatorial anomaly, *J. Atmos. Terr. Phys.*, *30*(3), 391–397.

Kirchengast, G. (1996), Elucidation of the physics of the gravity wave-TID relationship with the aid of theoretical simulations, *J. Geophys. Res*, *101*(A6), 13,353–13,368.

Kirchengast, G. (1997), Characteristics of high-latitude TIDs from different causative mechanisms deduced by theoretical modeling, *J. Geophys. Res*, *102*(A3), 4597–4612.

Klostermeyer, J. (1978), Nonlinear investigation of the spatial resonance effect in the nighttime equatorial F region, *J. Geophys. Res.*, *83*(A8), 3753–3760.

Knof, H., E. A. Mason, and J. T. Vanderslice (1964), Interaction energies, charge exchange cross sections and diffusion cross sections for N^+-N and O^+-O collisions, *J. Chem. Phys.*, *40*(12), 3548–3553.

Kozyra, J. U., A. F. Nagy, and D. W. Slater (1997), High-altitude energy source(s) for stable auroral red arcs, *Rev. Geophys.*, *35*(2), 155–190.

Kudeki, E., S. Bhattacharyya, and R. F. Woodman (1999), A new approach in incoherent scatter F region E×B drift measurements at Jicamarca, *J. Geophys. Res.*, *104*(A12), 28,145–28,162.

Langford, A. O., V. M. Bierbaum, and S. R. Leone (1986), Branching ratios for electronically excited oxygen atoms formed in the reaction of N^+ with O_2 at 300 K, *J. Chem. Phys.*, *84*(4), 2158–2166.

Lewis, R. V., P. J. S. Williams, G. H. Millward, and S. Quegan (1996), The generation and propagation of atmospheric gravity waves from activity in the auroral electrojet, *J. Atmos. Terr. Phys.*, *58*(6), 807–820.

Lindsay, B. G., D. R. Sieglaff, K. A. Smith, and R. F. Stebbings (2001), Charge transfer of keV O^+ ions with atomic oxygen, *J. Geophys. Res.*, *106*(A5), 8197–8203.

Link, R., and L. L. Cogger (1988), A reexamination of the OI 6300-Å nightglow, *J. Geophys. Res*, *93*(A9), 9883–9892.

Link, R., and P. K. Swaminathan (1992), $N(^2D)+O_2$: A source of thermospheric 6300 Å emission?, *Planet. Space Sci.*, *40*(5), 699–705.

Litvine, A., W. Kofman, and B. Cabrit (1998), Ion composition measurements and modelling at altitudes from 140 to 350 km using EISCAT measurements, *Ann. Geophys.*, *16*(10), 1159–1168.

Lopez-Gonzalez, M. J., J. J. Lopez-Moreno, and R. Rodrigo (1992a), Altitude profiles of the atmospheric system of O_2 and of the green line emission, *Planet. Space Sci.*, *40*(6), 783–795.

Lopez-Gonzalez, M. J., J. J. Lopez-Moreno, and R. Rodrigo (1992b), Atomic oxygen concentrations from airglow measurements of atomic and molecular oxygen emissions in the nightglow, *Planet. Space Sci.*, *40*(7), 929–940.

MacDougall, J. W., M. A. Abdu, P. T. Jayachandran, J. F. Cecile, and I. S. Batista (1998), Presunrise spread *F* at Forteleza, *J. Geophys. Res.*, *103*(A10), 23,415–23,425.

Macpherson, B., S. A. González, G. J. Bailey, R. J. Moffett, and M. P. Sulzer (1998), The effects of meridional neutral winds on the O^+-H^+ transition altitude over Arecibo, *J. Geophys. Res.*, *103*(A12), 29,183–29,198.

Makela, J. J. (2003), Midlatitude ionospheric studies using the global positioning system and airglow cameras, Ph.D. thesis, Cornell University.

Makela, J. J., and M. C. Kelley (2003), Field-aligned 777.4-nm composite airglow images of equatorial plasma depletions, *Geophys. Res. Lett.*, *30*(8), 1442, doi: 10.1029/2003GL017106.

Makela, J. J., S. A. González, B. MacPherson, X. Pi, M. C. Kelley, and P. J. Sultan (2000), Intercomparisons of total electron content measurements using the Arecibo incoherent scatter radar and GPS, *Geophys. Res. Lett.*, *27*(18), 2841–2844.

Makela, J. J., M. C. Kelley, S. A. Gonzalez, N. Aponte, and R. P. McCoy (2001a), Ionospheric topography maps using multiple-wavelength all-sky images, *J. Geophys. Res.*, *106*(A12), 29,161–29,174.

Makela, J. J., M. C. Kelley, J. J. Sojka, X. Pi, and A. J. Mannucci (2001b), GPS normalization and preliminary modeling of total electron content during a midlatitude space weather event, *Radio Sci.*, *36*(2), 351–361.

Makela, J. J., M. C. Kelley, S. A. González, N. Aponte, and J. J. Sojka (2003), Mid-latitude plasma and electric field measurements during space weather month, September 1999, *J. Atmos. Solar-Terr. Phys*, *65*(10), 1077–1085, doi: 10.1016/j.jastp.2003.07.002.

Makela, J. J., M. C. Kelley, and M. J. Nicolls (2006), Optical observations of the development of secondary instabilities on the eastern wall of an equatorial plasma bubble, *J. Geophys. Res.*, *In Press.*

Martyn, D. F. (1956), Processes controlling ionization distribution in the F_2 region of the ionosphere, *Australian J. Phys.*, *9*, 161–165.

Maruyama, N., A. D. Richmond, T. J. Fuller-Rowell, M. V. Codrescu, S. Sazykin, F. R. Toffoletto, R. W. Spiro, and G. H. Millward (2005), Interaction between direct penetration and disturbance dynamo electric fields in the storm-time equatorial ionosphere, *Geophys. Res. Lett*, *32*(17), L17105, doi:10.1029/2005GL023763.

McDade, I. C., D. P. Murtagh, R. G. H. Greer, P. H. G. Dickinson, G. Witt, J. Stegman, E. J. Liewellyn, L. Thomas, and D. B. Jenkins (1986), ETON 2: Quenching parameters for the proposed precursors of $O_2(b^1 \Sigma_g^+)$ and $O(^1S)$ in the terrestrial nightglow, *Planet. Space Sci.*, *34*(9), 789–800.

Melendez-Alvira, D. J., D. G. Torr, P. G. Richards, W. R. Swift, M. R. Torr, T. Baldridge, and H. Rassoul (1995), Sensitivity of the 6300 Å twilight airglow to neutral composition, *J. Geophys. Res.*, *100*(A5), 7839–7853.

Melendez-Alvira, D. J., R. R. Meier, J. M. Picone, P. D. Feldman, and B. M. McLaughlin (1999), Analysis of the oxygen nightglow measured by the Hopkins Ultraviolet Telescope: Implications for ionospheric partial radiative recombination rate coefficients, *J. Geophys. Res.*, *104*(A7), 14,901–14,913.

Meriwether, J. W. (1989), A review of the photochemistry of selected nightglow emissions from the mesopause, *J. Geophys. Res.*, *94*(A12), 14,629–14,646.

Meriwether, J. W., D. G. Torr, J. C. G. Walker, and A. O. Nier (1978), The $O^+(^2P)$ emission at 7320 Å in twilight, *J. Geophys. Res.*, *83*(A7), 3311–3319.

Miller, C. A. (1996), On gravity waves and the electrodynamics of the mid-latitude ionosphere, Ph.D. thesis, Cornell University.

Miller, C. A. (1997), Electrodynamics of midlatitude spread F 2. A new theory of gravity wave electric fields, *J. Geophys. Res.*, *102*(A6), 11,533–11,538.

Miller, S. M., and M. Hunter (2004), $O(^1D)$ branching fraction from the reaction $N(^2D) + O_2 \rightarrow NO(^2\pi,v,J) + O(^3P,^1D)$, *J. Phys. Chem. A*, *108*(26), 5588–5599, doi:10.1021/jp031340k S1089-5639(03)01340-9.

Millward, G. H. (1994), A resonance effect in AGWs created by periodic recurrent bursts in the auroral electric field, *Ann. Geophys.*, *12*(1), 94–96.

Millward, G. H., R. J. Moffett, S. Quegan, and T. J. Fuller-Rowell (1993a), Effects of an atmopsheric gravity wave on the midlatitude ionospheric *F* layer, *J. Geophys. Res.*, *98*(A11), 19,173–19,179.

Millward, G. H., S. Quegan, R. J. Moffett, T. J. Fuller-Rowell, and D. Rees (1993b), A modelling study of the coupled ionospheric and thermospheric response to an enhanced high-latitude electric field event, *Planet. Space Sci.*, *41*(1), 45–56.

Mozer, F. S. (1970), Electric field mapping in the ionosphere at the equatorial plane, *Planet. Space Sci.*, *18*(2), 259.

Mozer, F. S. (1971), Power spectra of the magnetospheric electric field, *J. Geophys. Res.*, *76*(16), 3651.

Nicolls, M. J., and M. C. Kelley (2005), Strong evidence for gravity wave seeding of an ionospheric plasma instability, *Geophys. Res. Lett.*, *32*(5), L05108, doi: 10.1029/2004GL020737.

Nicolls, M. J., M. C. Kelley, A. J. Coster, S. A. González, and J. J. Makela (2004), Imaging the structure of a large-scale TID using ISR and TEC data, *Geophys. Res. Lett.*, *31*(9), L09812, doi:10.1029/2004GL019797.

Nicolls, M. J., M. C. Kelley, and C. Erdogan (2005), Small-scale structure on the poleward edge of a stable auroral red arc, *IEEE Trans. Plasma Sci.*, *33*(2), 412–413, doi:10.1109/TPS.2005.845008.

Nicolls, M. J., N. Aponte, S. A. González, M. P. Sulzer, and W. L. Oliver (2006a), Daytime *F*-region ion energy balance at Arecibo for moderate to high solar flux conditions, *J. Geophys. Res.*, *In Press.*

Nicolls, M. J., M. C. Kelley, J. L. Chau, O. Veliz, D. Anderson, and A. Anghel (2006b), The spectral properties of low latitude daytime electric fields inferred from magnetometer observations, *J. Atmos. Solar-Terr. Phys.*, *Submitted.*

Nicolls, M. J., M. C. Kelley, M. N. Vlasov, Y. Sahai, J. L. Chau, D. L. Hysell, P. R. Fagundes, F. Becker-Guedes, and W. L. C. Lima (2006c), Observations and modeling of post-midnight uplifts near the magnetic equator, *Ann. Geophys.*, *24*(5), 1317–1331.

Nicolls, M. J., M. P. Sulzer, N. Aponte, and S. A. González (2006d), High resolution electron temperature measurements using the plasma line asymmetry, *Geophys. Res. Lett.*, *Submitted.*

Nicolls, M. J., M. N. Vlasov, M. C. Kelley, and G. G. Shepherd (2006e), Discrepancy between the nighttime molecular ion composition given by the international reference ionosphere model and airglow measurements at low latitudes, *J. Geophys. Res.*, *111*(A3), A03304, doi:10.1029/2005JA011216.

Nikoukar, R., M. P. Sulzer, F. Kamalabadi, and E. Kudeki (2006), A two-step lag-profile based approach to the inversion of incoherent scatter radar data, *J. Geophys. Res.*, *To be submitted.*

Nishida, A. (1968), Coherence of geomagnetic DP 2 fluctuations with interplanetary magnetic variations, *J. Geophys. Res.*, *73*(17), 5549–5559.

Nishida, A., N. Iwasaki, and T. Nagata (1966), The origin of fluctuations in the equatorial electrojet: A new type of geomagnetic variation, *Ann. Geophys.*, *22*(3), 478–484.

Oliver, W. L. (1979), Incoherent scatter radar studies of the daytime middle thermosphere, *Ann. Geophys.*, *35*(3), 121–139.

Oliver, W. L. (1997), Hot oxygen and the ion energy budget, *J. Geophys. Res.*, *102*(A2), 2503-2511.

Oliver, W. L., and K. Glotfelty (1996), O^+-O collision cross section and long-term *F* region O density variations deduced from the ionospheric energy budget, *J. Geophys. Res.*, *101*(A10), 21,769-21,784.

Omidvar, K., R. Menard, and M. J. Buonsanto (1998a), Empirical determination of the O^+O collision frequency, *Ann. Geophys.*, *60*(15), 1485–1496.

Omidvar, K., R. Menard, and M. J. Buonsanto (1998b), Validation of empirical determination of the O^+ - O collision frequency, *The CEDAR Post*, *35*, 14.

Oppenheim, A. V., R. W. Schafer, and J. R. Buck (1999), *Discrete-Time Signal Processing*, 2nd ed., Prentice-Hall, Inc., Englewood Cliffs, NJ.

Otsuka, Y., K. Shiokawa, T. Ogawa, and P. Wilkinson (2004), Geomagnetic conjugate observations of medium-scale traveling ionospheric disturbances at midlatitude using all-sky airglow imagers, *Geophys. Res. Lett.*, *31*(15), L15803, doi:10.1029/2004GL020262.

Perkins, F. W. (1973), Spread *F* and ionospheric currents, *J. Geophys. Res*, *78*(1), 218–226.

Pesnell, W. D., K. Omidvar, and W. R. Hoegy (1993), Momentum transfer collision frequency of O^+ - O, *Geophys. Res. Lett.*, *20*(13), 1343-1346.

Peverall, R., S. Rosen, M. Larsson, J. R. Peterson, R. Bobbenkamp, S. L. Guberman, H. Danared, M. af Ugglas, A. Al-Khalili, A. N. Maurellis, and W. J. van der Zande (2000), The ionospheric oxygen green airglow: Electron temperature dependence and aeronomical implications, *Geophys. Res. Lett.*, *27*(4), 481–484.

Prölss, G. W. (1997), Magnetic storm associated perturbations of the upper atmosphere, in *Magnetic Storms*, edited by B. T. Tsurutani, W. D. Gonzalez, Y. Kamide, and J. K. Arballo, p. 227, Geophysical Monograph 98, American Geophysical Union, Washington, D.C.

Raitt, W. J., R. W. Schunk, and P. M. Banks (1975), A comparison of the temperature and density structure in high and low speed thermal proton flow, *Planet. Space Sci.*, *23*(7), 1103–1117.

Rastogi, R. G., and J. A. Klobuchar (1990), Ionospheric electron content within the equatorial $F2$ layer anomaly belt, *J. Geophys. Res.*, *95*(A11), 19,045–19,052.

Rayleigh, R. J. (1930), Absolute intensity of the auroral line in the night sky and the number of atomic transitions, *Proc. R. Soc. London A*, *129*(811), 458–467.

Reddy, C. A., V. V. Somayajulu, and C. V. Devasia (1979), Global scale electrodynamic coupling of the auroral and equatorial dynamo regions, *J. Atmos. Terr. Phys.*, *41*(2), 189–201.

Reddy, C. A., W. R. Hoegy, W. D. Pesnell, H. G. Mayr, and C. O. Hines (1994), Accuracy of the $O^+ - O$ collision cross-section deduced from ionosphere-thermosphere observations, *Geophys. Res. Lett.*, *21*(22), 2429-2432.

Rees, D. (1995), Observations and modeling of ionospheric and thermospheric disturbances during major geomagnetic storms: A review, *J. Atmos. Terr. Phys.*, *57*(12), 1433–1457.

Rees, M. H. (1989), *Physics and chemistry of the upper atmosphere*, Cambridge University Press, Cambridge.

Richards, P. G., J. A. Fennelly, and D. G. Torr (1994), EUVAC: A solar EUV flux model for aeronomic calculations, *J. Geophys. Res.*, *99*(A5), 8981–8992.

Richmond, A. D. (1978), Gravity wave generation, propagation, and dissipation in the thermosphere, *J. Geophys. Res.*, *83*(A9), 4131–4145.

Richmond, A. D. (1979), Large-amplitude gravity wave energy production and dissipation in the thermosphere, *J. Geophys. Res.*, *84*(A5), 1880–1890.

Richmond, A. D., and Y. Kamide (1988), Mapping electrodynamic features of the high-latitude ionosphere from localized observations: Technique, *J. Geophys. Res.*, *93*(A6), 5741–5759.

Richmond, A. D., and S. Matsushita (1975), Thermospheric response to a magnetic substorm, *J. Geophys. Res.*, *80*(19), 2839–2850.

Richmond, A. D., M. Blanc, B. A. Emery, R. H. Wand, B. G. Fejer, R. F. Woodman, S. Ganguly, P. Amayenc, R. A. Behnke, C. Calderon, and J. V. Evans (1980), An empirical model of quiet-day ionospheric electric fields at middle and low latitudes, *J. Geophys. Res.*, *85*(A9), 4658–4664.

Richmond, A. D., C. Peymirat, and R. G. Roble (2003), Long-lasting disturbances in the equatorial ionospheric electric field simulated with a coupled magnetosphere-ionosphere-thermosphere model, *J. Geophys. Res.*, *108*(A3), 1118, doi:10.1029/2002JA009758.

Ridley, A. J., G. Lu, C. R. Clauer, and V. O. Papitashvili (1998), A statistical study of the ionospheric convection response to changing interplanetary magnetic field conditions using the assimilative mapping of ionospheric electrodynamics technique, *J. Geophys. Res.*, *103*(A3), 4023–4040.

Rishbeth, H., and O. K. Garriott (1969), *Introduction to ionospheric physics*, Academic Press, New York, NY.

Roble, R. G. (1975), Calculated and observed diurnal variation of the ionosphere over Millstone Hill on 23-24 March 1970, *Planet. Space Sci.*, *23*(7), 1017–1033.

Rosenbluth, M. N., and N. Rostoker (1962), Scattering of electromagnetic waves by a non-equilibrium plasma, *Phys. Fluids*, *5*(7), 776–788.

Rottger, J. (1973), Wave-like structures of large-scale equatorial spread-F irregularities, *J. Atmos. Terr. Phys.*, *35*(6), 1195–1206.

Row, R. V. (1967), Acoustic-gravity waves in the upper atmosphere due to a nuclear detonation and an earthquake, *J. Geophys. Res.*, *72*(5), 1599–1610.

Rusch, D. W., J. C. Gerard, and W. E. Sharp (1978), The reaction of $N(^2D)$ with O_2 as a source of $O(^1D)$ atoms in aurorae, *Geophys. Res. Lett.*, *5*(12), 1043–1046.

Sahai, Y., J. A. Bittencourt, N. R. Teixeira, and H. Takahashi (1981), Simultaneous observations of OI 7774-Å and OI 6300-Å emissions and correlative study with ionospheric parameters, *J. Geophys. Res.*, *86*(A5), 3657–3660.

Saito, A., S. Fukao, and S. Miyazaki (1998), High resolution mapping of TEC perturbations with the GSI GPS network over Japan, *Geophys. Res. Lett.*, *25*(16), 3079–3082.

Salah, J. E. (1993), Interim standard for the ion-neutral atomic oxygen collision frequency, *Geophys. Res. Lett.*, *20*(15), 1543-1546.

Salpeter, E. E. (1960), Electron density fluctuations in a plasma, *Phys. Rev.*, *120*(5), 1528–1535.

Sardon, E., A. Rius, and N. Zarraoa (1994), Estimation of the transmitter and receiver differential biases and the ionospheric total electron content from Global Positioning System observations, *Radio Sci.*, *29*(3), 577–586.

Sastri, J. H. (2002), Penetration of electric fields at the nightside dip equator associated with the main impulse of the storm sudden commencement of 8 July, 1991, *J. Geophys. Res.*, *107*(A12), 1448, doi:10.1029/2002JA009453.

Sastri, J. H., H. N. Rao, V. V. Somayajulu, and H. Chandra (1994), Thermospheric meridional neutral winds associated with equatorial midnight temperature maximum (MTM), *Geophys. Res. Lett.*, *21*(9), 825–828.

Scali, J. L., B. W. Reinisch, C. J. Heinselman, and T. Bullet (1995), Coordinated digisonde and incoherent scatter radar F region drift measurements at Sondre Stromfjord, *Radio Sci.*, *30*(5), 1481–1498.

Scherliess, L., and B. G. Fejer (1997), Storm time dependence of equatorial disturbance dynamo zonal electric fields, *J. Geophys. Res.*, *102*(A11), 24,037–24,046.

Scherliess, L., and B. G. Fejer (1999), Radar and satellite global equatorial F region vertical drift model, *J. Geophys. Res.*, *104*(A4), 6869–6842.

Schubert, G., R. L. Walterscheid, M. P. Hickey, and C. A. Tepley (1999), Observations and interpretation of gravity wave induced fluctuations in the OI (557.7 nm) airglow, *J. Geophys. Res.*, *104*(A7), 14,915–14,924.

Schunk, R. W., and A. F. Nagy (2000), *Ionospheres: Physics, Plasma Physics, and Chemistry*, Cambridge University Press, New York.

Schunk, R. W., and J. C. G. Walker (1970), Thermal diffusion in the F2-region of the ionosphere, *Planet. Space Sci.*, *18*(4), 535–557.

Schunk, R. W., and J. C. G. Walker (1973), Theoretical ion densities in the lower ionosphere, *Planet. Space Sci.*, *21*(11), 1875–1896.

Senior, C., and M. Blanc (1984), On the control of magnetospheric convection by the spatial distribution of ionospheric conductivities, *J. Geophys. Res.*, *89*(A1), 261–284.

Sheehan, C. H., and J. P. St.-Maurice (2004), Dissociative recombination of N_2^+, O_2^+, and NO^+: Rate coefficients for ground state and vibrationally excited ions, *J. Geophys. Res.*, *109*(A3), A03302, doi:10.1029/2003JA010132.

Shepherd, G. G., R. G. Roble, C. McLandress, and W. E. Ward (1997), WINDII observations of the 558 nm emission in the lower thermosphere: The influence of dynamics on composition, *J. Atmos. Solar-Terr. Phys.*, *59*(6), 655–667.

Shiokawa, K., Y. Otsuka, T. Ogawa, S. Kawamura, N. Balan, K. Igarashi, A. J. Ridley, D. J. Knipp, A. Saito, and K. Yumoto (2002), A large-scale traveling ionospheric disturbance during the magnetic storm of 15 September 1999, *J. Geophys. Res.*, *107*(A6), 1088, doi:10.1029/2001JA000245.

Shiokawa, K., Y. Otsuka, T. Ogawa, S. Kawamura, M. Yamamoto, S. Fukao, T. Nakamura, T. Tsuda, N. Balan, K. Igarashi, G. Lu, A. Saito, and K. Yumoto (2003), Thermospheric wind during a storm-time large-scale traveling ionospheric disturbance, *J. Geophys. Res.*, *108*(A12), 1423, doi:10.1029/2003JA010001.

Showen, R. L. (1979), The spectral measurement of plasma lines, *Radio Sci.*, *14*(3), 503–508.

Shume, E. B., D. L. Hysell, and J. L. Chau (2005), Zonal wind velocity profiles in the equatorial electrojet derived from phase velocities of Type II radar echoes, *J. Geophys. Res.*, *110*(A12), A12308, doi:10.1029/2005JA011210.

Sipler, D. P., M. E. Hagan, M. E. Zipf, and M. A. Biondi (1991), Combined optical and radar wind measurements in the F-region over Millstone Hill, *J. Geophys. Res.*, *96*(A12), 21,555–21,262.

Slanger, T. G., B. J. Wood, and G. Black (1972), The temperature dependence of $O(^1S)$ quenching by O_2, *Chem. Phys. Lett.*, *17*(3), 401–403.

Smith, S. M., M. Mendillo, J. Baumgardner, and R. R. Clark (2000), Mesospheric gravity wave imaging from a sub-auroral site: First results from Millstone Hill, *J. Geophys. Res.*, *105*(A12), 27,119–27,130.

Sobral, J. H. A., H. Takahashi, M. M. A. Abdu, P. Muralikrishna, Y. Sahai, and C. J. Zamlutti (1992), $O(^1S)$ and $O(^1D)$ quantum yields from rocket measurements of electron densities and 557.7 and 630.0 nm emissions in the nocturnal F-region, *Planet. Space Sci.*, *40*(5), 607–619.

Solomon, S. C. (1991), Optical aeronomy, *Rev. Geophys.*, *29*, 1089–1109.

St.-Maurice, J. P., and D. G. Torr (1978), Nonthermal rate coefficients in the ionosphere: The reactions of O^+ with N_2, O_2, and NO, *J. Geophys. Res.*, *83*(A3), 969–977.

Stallcop, J. R., H. Partridge, and E. Levin (1991), Resonance charge transfer, transport cross-sections, and collision integrals for N^+ and O^+ interactions, *J. Chem. Phys*, *95*(9), 6429–6439.

Stebbings, R. F., A. C. H. Smith, and H. Ehrhardt (1964), Charge transfer between oxygen atoms and O^+ and H^+ ions, *J. Geophys. Res.*, *69*(11), 2349–2355.

Streit, G. E., C. J. Howard, A. L. Schmeltekopf, J. J. A. Davidson, and H. I. Schiff (1976), Temperature dependence of $O(^1D)$ rate constants for reactions with O_2, N_2, CO_2, O_3 and H_2O, *J. Chem. Phys.*, *65*(11), 4761–4764.

Strickland, D. J., J. S. Evans, and L. J. Paxton (1995), Satellite remote sensing of thermospheric O/N_2 and solar EUV 1. Theory, *J. Geophys. Res.*, *100*(A7), 12,217–12,226.

Stubbe, P. (1968), Frictional forces and collision frequencies between moving ion and neutral gases, *J. Atmos. Terr. Phys.*, *30*(12), 1965–1985.

Sulzer, M. P. (1986), A phase modulation technique for a sevenfold statistical improvement in incoherent scatter data-taking, *Radio Sci.*, *21*(4), 737-744.

Sulzer, M. P., and S. A. González (1996), Simultaneous measurements of O^+ and H^+ temperatures in the topside ionosphere over Arecibo, *Geophys. Res. Lett.*, *23*(22), 3235–3238.

Sun, Y., and A. Dalgarno (1992), Collisional excitation of metastable $O(^1D)$ atoms, *J. Chem. Phys.*, *96*(7), 5017–5019.

Swartz, W. E., and J. S. Nisbet (1971), Diurnal variation of the neutral temperature profile at Arecibo from incoherent scatter measurements and its relevance to the 1400-hour density maximum, *J. Geophys. Res.*, *76*(1), 185-196.

Testud, J., and G. Vasseur (1969), Gravity waves in the thermosphere, *Ann. Geophys.*, *25*(2), 525–546.

Thome, G. (1966), A study of large-scale traveling ionospheric disturbances in the ionosphere using the Arecibo UHF radar, Ph.D. thesis, Cornell University.

Thome, G. (1968), Long-period waves generated in the polar ionosphere during the onset of magnetic storms, *J. Geophys. Res.*, *73*(19), 6319–6331.

Tinsley, B. A., A. B. Christensen, J. Bittencourt, H. Gouveia, P. D. Angreji, and H. Takahashi (1973), Excitation of oxygen permitted line emissions in the tropical nightglow, *J. Geophys. Res.*, *78*(7), 1174–1186.

Titheridge, J. E. (1996), Direct allowance for the effect of photoelectrons in ionospheric modeling, *J. Geophys. Res.*, *101*(A1), 357–369.

Titheridge, J. E. (1997), Model results for the ionospheric E region: Solar and seasonal changes, *Ann. Geophys.*, *15*(1), 63–78.

Tohmatsu, T. (1990), *Compendium of Aeronomy*, Terra Scientific Publishing Company, Tokyo, Japan.

Torr, D. G., M. R. Torr, H. C. Brinton, L. H. Brace, N. W. Spencer, A. E. Hedin, W. B. Hanson, J. H. Hoffman, A. O. Nier, J. C. G. Walker, and D. W. Rusch (1979), An experimental and theoretical study of the mean diurnal variation of O^+, NO^+, O_2^+, and N_2^+ ions in the mid-latitude F_1 layer of the ionosphere, *J. Geophys. Res.*, *84*(A7), 3360–3372.

Torr, M. R., and D. G. Torr (1982), The role of metastable species in the thermosphere, *Rev. Geophys. Space Phys.*, *20*(1), 91–144.

Torr, M. R., D. G. Torr, and R. R. Laher (1985), The O_2 atmospheric O-O band and related emissions from Spacelab 1, *J. Geophys. Res.*, *90*(A9), 8525–8538.

Tsugawa, T., A. Saito, Y. Otsuka, and M. Yamamoto (2003), Damping of large-scale traveling ionospheric disturbances detected with GPS networks during the geomagnetic storm, *J. Geophys. Res.*, *108*(A3), 1127, doi:10.1029/2002JA009433.

Valladares, C. E., S. Basu, K. Groves, M. P. Hagan, D. Hysell, A. J. Mazzella, and R. E. Sheehan (2001), Measurement of the latitudinal distributions of total electron content during equatorial spread F events, *J. Geophys. Res.*, *106*(A12), 29,133.

Vasyliunas, V. M. (1970), Mathematical models of magnetospheric convection and its coupling to the ionosphere, in *Particles and Fields in the Magnetosphere*, edited by M. McCormac, pp. 60–71, D. Reidel, Norwell, MA.

Vasyliunas, V. M. (1972), The interrelationship of magnetospheric processes, in *Earth's Magnetospheric Processes*, edited by B. M. McCormack, pp. 29–38, D. Reidel.

Vickrey, J. F., W. E. Swartz, and D. T. Farley (1979), Ion transport in the topside ionosphere at Arecibo, *J. Geophys. Res.*, *84*(A12), 7307–7314.

Vlasov, M. N., and V. E. Davydov (1993), Splitting of atomic oxygen height profiles by eddy diffusion, *J. Atmos. Terr. Phys.*, *55*(10), 1361–1363.

Vlasov, M. N., and T. V. Korobeinikova (1991), Effect of turbulence, infrared radiation, and mass-averaged transport on the height distribution of temperature in the middle latitude and high latitude thermosphere, *Cosmic Res.*, *29*, 469–474.

Vlasov, M. N., M. C. Kelley, J. J. Makela, and M. J. Nicolls (2003), Intense nighttime flux from the plasmasphere during a modest magnetic storm, *J. Atmos. Solar-Terr. Phys.*, *65*(10), 1099–1105, doi:10.1016/j.jastp.2003.07.003.

Vlasov, M. N., M. J. Nicolls, M. C. Kelley, S. M. Smith, N. Aponte, and S. A. González (2005), Modeling of airglow and ionospheric parameters at Arecibo during quiet and disturbed periods in October, 2002, *J. Geophys. Res.*, *110*(A7), A07303, doi:10.1029/2005JA011074.

Waldteufel, P. (1970), A study of seasonal changes in the lower thermosphere and their implications, *Planet. Space Sci.*, *18*(5), 741.

Waldteufel, P. (1971), Combined incoherent-scatter *F*1-region observations, *J. Geophys. Res.*, *76*(28), 6995–6999.

Walker, J. C. G. (1965), Analytic representation of upper atmosphere densities based on Jacchia's static diffusion models, *J. Atmos. Sci.*, *22*(4), 462–463.

Wilson, B. D., C. H. Yinger, W. A. Feess, and C. Shank (1999), New and improved - the broadcast inter-frequency biases, *GPS World*, *10*, 56–66.

Woodman, R. F., J. L. Chau, and R. R. llma (2006), Comparison of ionosonde and incoherent scatter drift measurements at the magnetic equator, *Geophys. Res. Lett.*, *33*(1), L01103, doi:10.1029/2005GL023692.

Woods, T. N., F. G. Eparvier, S. M. Bailey, P. C. Chamberlin, J. Lean, G. J. Rottman, S. C. Solomon, W. K. Tobiska, and D. L. Woodraska (2005), Solar EUV Experiment (SEE): Mission overview and first results, *J. Geophys. Res.*, *110*, A01312, doi: doi:10.1029/2004JA010765.

Yee, J. H., J. W. Meriwether, and P. B. Hays (1980), Detection of a corona of fast oxygen atoms during solar maximum, *J. Geophys. Res.*, *85*(A7), 3396–3400.

Yngvesson, K. O., and F. W. Perkins (1968), Radar thomson scatter studies of photo-electrons in the ionosphere and Landau damping, *J. Geophys. Res.*, *73*(1), 97–110.